

**Preparation of Bulk High Temperature
Superconductors by Textured Growth Techniques,
and their Characterization**

By

M. R. GONAL

CHEM01200604026

BHABHA ATOMIC REASERCH CENTRE

*A thesis submitted to the
Board of Studies in Chemical Sciences*

In partial fulfillment of requirements

For the Degree of

DOCTOR OF PHILOSOPHY

of

HOMI BHABHA NATIONAL INSTITUTE



November, 2012

Homi Bhabha National Institute

Recommendation of the Viva Voce Board

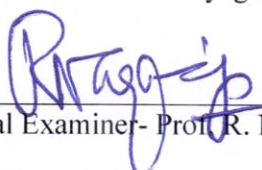
As members of the Viva Voce Board, we certify that we have read the dissertation prepared by Shri M. R. Gonal entitled "PREPARATION OF BULK HIGH TEMPERATURE SUPERCONDUCTORS BY TEXTURED GROWTH TECHNIQUES, AND THEIR CHARACTERISATION" and recommended that it may be accepted as fulfilling the dissertation requirement for the Degree of Doctor of Philosophy.



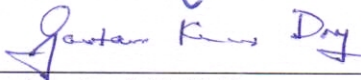
Chairman- Prof. D. Das Date: 15-03-2013



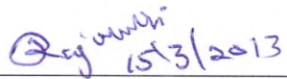
Convener- Prof. A. K. Tyagi Date: 15-03-2013



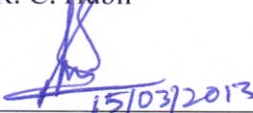
External Examiner- Prof. R. Nagarajan Date: 15-03-2013



Member- Prof. G. K. Dey Date: 15-03-2013



Co-guide- Prof. R. C. Hubli Date: 15-03-2013



Member- Prof. S. K. Mukherjee Date: 15-03-2013



Member- Prof. R. K. Vatsa Date: 15-03-2013

Final approval and acceptance of this dissertation is contingent upon the candidate's submission of the final copies of the dissertation to HBNI.

I hereby certify that I have read this dissertation prepared under my direction and recommend that it may be accepted as fulfilling the dissertation requirement.

Date: 15-03-2013
Place: BARC, Mumbai


(A. K. Tyagi)

STATEMENT BY AUTHOR

This dissertation has been submitted in partial fulfillment of requirements for an advanced Doctor of Philosophy degree at Homi Bhabha National Institute (HBNI) and is deposited in the library to be made available to borrowers under rules of the HBNI.

Brief quotations from this dissertation are allowable without special permission, provided that accurate acknowledgement of source is made. Requests for permission for extended quotation from or reproduction of this manuscript in whole or in part may be granted by the Competent Authority of HBNI when in his or her judgment the proposed use of the material is in the interests of scholarship. In all other instances, however, permission must be obtained from the author.



(M. R. Gonal)

DECLARATION

I, hereby declare that the investigations presented in the thesis have been carried out by me. The work is original and has not been submitted earlier as a whole or in part for a degree / diploma at this or any other Institution / University.



(M. R. Gonal)

Dedicated to my dear mother

ACKNOWLEDGEMENTS

It is a great pleasure in presenting my thesis on completion of my project and in expressing my deepest regards and deep sense of gratitude and sincere thanks to my research guide Dr. A. K. Tyagi,, Head, Solid State Chemistry Section, Chemistry Division, and co-guide Dr. R.C.Hubli, Head, Materials Processing Division, BARC for their valuable guidance in hours of need, constant encouragement, keen interest, good wishes and valuable suggestions throughout my entire research tenure. I am also grateful to them for critically reviewing this thesis.

It gives me great pleasure to thank Dr. G.P.Kothiyal, Head, Glass and Advanced Ceramics Division, BARC for his support in carrying out the research work.

It is also my great pleasure to thank Dr. A. K. Suri, Director, Materials Group, BARC for his support in carrying out the research work.

It gives me immense pleasure to acknowledge Dr. G.K. Dey, Head, Materials Science Division, BARC for his constant support and also for providing the facilities in his Division as well as helping me to get interesting data (OIM) from Prof. Samazdar, IIT Mumbai and valuable suggestions for completion of this work.

I also wish to thank Prof. Istvan Vazda, Head, Department of Electric and Power Engineering and Dr A.Gyore, Budapest University of Technology and Economics, Budapest, Hungary for their support during my stay at their laboratory.

I also wish to extend my heart filled thanks to my colleagues Dr. Abhijit Ghosh, Dr. Sahu, Shri Sachin Zinge and Shri Shoieb from Advanced Ceramics Section, GACD, BARC helping me in my experimental work and providing constructive suggestions throughout the work.

I wish to express my sincere gratitude and indebtedness to my mother, late Smt. Gangamma for her blessings. I am extremely thankful to my wife Smt. Pushpa for her patience and understanding.

CONTENTS

	Page Number
SYNOPSIS	xv
LIST OF FIGURES	xxxii
LIST OF TABLES	xxxviii
Chapter 1: Introduction	1-29
1.1 History of high temperature superconductors	1
1.2. Properties of superconductors	2
1.2.1. Meissner Oschenfeld Effect	2
1.2.2 Penetration Depth	3
1.2.3 Coherence Length	4
1.2.4 Type-I & Type-II Superconductors	4
1.2.4.1 Type-I or Soft Superconductors	5
1.2.4.2. Type-II or Hard Superconductors	5
1.2.5 Isotope Effect	7
1.2.6 Specific Heat	7
1.2.7 BCS Theory	8
1.3. High-Temperature oxide superconductors	12
1.3.1 Different systems of high temperature superconductors	12
1.4 YBCO (Y-123) System	13
1.4.1 Crystal structure of Y-123 oxide	13

1.4.2	RE-123 system	16
1.4.3	Anisotropy in the Material	17
1.5	Applications of HTSC materials	18
1.5.1	Factors influencing critical current density	23
1.6	Sintering Method	26
1.6.1	Melt Processing	26
1.7	Conclusion	29
Chapter-2 : Instrumentation and Experimental Techniques		30-69
2.1	Furnace fabrication	31
2.2	Liquid nitrogen T_c measurement system	32
2.3.	Compaction	34
2.3.1	Uniaxial pressing	34
2.3.2	Isostatic Pressing	35
2.3.2.1	Compaction studies	36
2.4	Particle size distribution	37
2.5	X-ray diffraction	38
2.6	Morphology and compaction characterization	39
2.6.1	Scanning electron microscope	39
2.6.2	Energy dispersive X-ray spectrometry	44
2.6.3	Electron Probe Micro-Analyzer (EPMA)	46
2.6.4	Transmission electron microscope (TEM)	51
2.6.5	Orientation Imaging Microscope (OIM)	53

2.7	Magnetic measurements	58
2.7.1	SQUID magnetometer	58
2.7.2	Trapped magnetic field and Levitation force measurement system	61
2.7.3	The levitation force measurement system	62
2.8.	Critical Current Density Measurements	64
2.9.	Determination of oxygen content	67
Chapter 3 : Bulk Powder processing, densification and characterization of Y-123 and Y-211 Powders		70-89
3.1	Synthesis	71
3.1.1	Ceramic method	71
3.1.2	Co-precipitation technique	74
3.1.3	Aerosol techniques	75
3.1.4	Sol-Gel processing	75
3.1.5	Other Processing methods	76
3.2	Experimental	77
3.2.1	Synthesis of Bulk Y-123 and Y-211 powder by solid state route	77
3.2.2	Synthesis of Y-211 by nitrate decomposition route	79
3.3	Characterization of powder	80
3.3.1	Particle size distribution	80
3.3.2	XRD studies	81
3.4	Sintering and characterization of sintered Y-123 oxide	82
3.4.1	Sintering	82
3.4.2	Critical transition temperature	82

3.4.3	SEM characterization	83
3.5	Quenching study of Y-123	84
3.5.1	High Temperature X-ray diffraction studies	85
3.6	Conclusion	89

**Chapter 4: Preparation and characterization of different composites for
MTG components 90-107**

4.1	Preparation of sample composite powders for fabrication of components	91
4.2	Addition of Y-211 phase	92
4.2.1	Addition of silver	92
4.2.2	Addition of platinum and ceria	93
4.2.3	Preparation of composites	93
4.3	Granulation of composite powders	94
4.4	Sintering of composites	95
4.5	Characterization of sintered and quenched composites	95
4.5.4	Critical transition temperature measurement	106
4.6	Conclusion	106

Chapter 5: Fabrication of components using MTG technique 108-141

5.1	Melt Processing of YBCO	109
5.1.1	Melt-Texture Processing	109
5.1.2	Techniques used for melt processing	111
5.2	The Y-123 Pseudo-Binary Phase Diagram	117
5.2.1	The Y-123 peritectic reaction	119

5.2.2	Mechanism of Y diffusion growth model	121
5.3	Compaction of composites	122
5.3.1	Preparation of preform and densification	123
5.3.1.1	Designing of rubber mould for fabricating different shapes	124
5.3.2	Densification of composites using CIP	125
5.4	Solidification of compacts using MTG and TSMTG technique	128
5.4.1	Sintering of compacts	129
5.4.2	Melt texture growth technique (MTG) of compacts	130
5.5	Machining of MTG compacts	135
5.5.1	Machined MTG components	136
5.7	Surface protection	139
5.8	Conclusion	140
Chapter 6 : Characterization of fabricated MTG components		142-180
6.1	Characterization of TSMTG samples	143
6.1.1	Critical transition temperature	143
6.1.2	XRD studies of sintered and TSMTG SSR-PL-1 plate	145
6.1.3	Microstructure analysis	145
6.1.3.1	Etching of TSMTG for microstructure analysis	145
6.1.3.2	Scanning electron microscope analysis of TSMTG grown SSR-PL-1	146
6.1.3.3	EPMA studies	147
6.1.3.4	Orientation Imaging Microscope (OIM) study of SSR-PL-1 plate	150
6.1.4	Magnetic measurements of TSMTG samples	151

6.1.4.1	Trapped magnetic field measurements	151
6.1.4.2	Levitation force measurement	152
6.1.5	Critical current density measurement	153
6.2	Characterization of superconducting properties TSMTG components fabricated using composite B – (1) NDR-PL-2,(2) NDR-CY-2, (3) NDR-PI- 1 and (4) NDR-CY-3	155
6.2.1	Microstructure analysis of TSMTG NDR-PL-2 plate	156
6.2.1.1	Scanning electron microscope analysis of TSMTG grown NDR-PL-2	156
6.2.1.2	OIM study of TSMTG NDR-PL-2 plate	157
6.2.1.3	HRTEM study	158
6.2.2	Magnetic measurements of TSMTG NDR-PL-2 plate	161
6.2.2.1	Trapped magnetic field measurement	161
6.2.2.2	Levitation force measurement	162
6.2.2.3	SQUID measurement of NDR-PL-2 plate	163
6.2.3	Critical current density measurement	164
6.2.4	Characterization of TSMTG NDR-CY-3 cylinder	166
6.3	Effect of Pt and Ceria in Y-123 on TSMTG superconducting properties	169
6.3.1	Characterization of TSMTG Pt-CY-5 samples	169
6.3.1.1	Microstructure study of TSMTG Pt-CY-5	169
6.3.1.1.1	SEM of TSMTG Pt-CY-5sample	169
6.3.1.1.2	EPMA of TSMTG Pt-CY-5 sample	170
6.3.2	J_c measurement of TSMTG Pt-CY-5 cylinder	172
6.4	Characterization of TSMTG Ce-CY-6 sample	173
6.4.1	SEM of TSMTG Ce-CY-6 cylinder	173

6.4.2	EPMA of TSMTG Ce-CY-6 plate	174
6.4.3	J_c measurement of TSMTG Ce-CY-6 hollow cylinder	176
6.5	Conclusion	177
CHAPTER 7 : Conclusions and future scope		181-187
7.1	Conclusion	181
7.2	Future scope of this work	186
Appendix		188-193
A.1	Supply of MTG components of different shapes	188
A.2	Characterization of MTG components	189
A.2.1	Levitation Force Measurement of YBCO Pins	189
A.3	Application of MTG components as rotor in prototype HTSC motor	190
A.4	Test report	193
References		194-205

**SYNOPSIS OF THE THESIS TO BE SUBMITTED TO THE HOMI
BHABHA NATIONAL INSTITUTE FOR THE DEGREE OF DOCTOR
OF PHILOSOPHY IN CHEMICAL SCIENCE**



Name of the Candidate : M. R. Gonal

Name of the Guide : Prof. A.K.Tyagi
Chemical Science, Homi Bhabha
National Institute, Mumbai - 400094, INDIA

Name of the Co-Guide : Prof. R.C.Hubli
Metallurgy, Homi Bhabha National
Institute, Mumbai - 400094, INDIA

Registration Number : CHEM01200604026

Date of Registration : 22-02-2007

Title of the Thesis : Preparation of Bulk High Temperature
Superconductors by Textured Growth
Techniques, and their Characterisation

Place of Research Work : Glass & Advanced Ceramics
Division, Bhabha Atomic Researc Centre,
Mumbai - 400 085, INDIA

Signature of the Candidate :

Signature of the Guide :

Signature of the Co-Guide :

SYNOPSIS

Preparation of Bulk High Temperature Superconductors by Textured Growth Techniques, and their Characterization

Preamble

About twenty five years ago in a series of amazing discoveries, it was found that a large family of ceramic cuprate materials exhibited superconductivity at temperatures above, and in some cases well above, that of liquid nitrogen. Imaginations were energized by the thought of applications for zero-resistance conductors cooled with an inexpensive and readily available cryogen. Early optimism, however, was soon dampened by the hard realities of these new materials: viz. brittle ceramics and not easily formed into long flexible conductors; high current levels require near-perfect crystalline and – the downside of high transition temperature – performance drops rapidly in a magnetic field. Despite these formidable obstacles, thousands of kilometers of high-temperature superconducting wire have now been manufactured for demonstrations of transmission cables, motors and other electrical power components [1-5]. Most research has been in the electric power areas for applications such as magnets, motors and power-transmission lines; all power applications share a common requirement that the superconducting material be formed into a long, strong and flexible conductor so that it can be used like the copper wire it is intended to replace. And, this is where the problems began because the HTS materials are ceramics that are more like a piece of chalk than the ductile copper metal.

Objective of the present studies:

The objective of the present investigation is to develop viable technologies to process the brittle ceramic High temperature superconductors (HTSC) $\text{YBa}_2\text{Cu}_3\text{O}_{7-\delta}$ (**YBCO or Y-123**) into commercially exploitable forms. To achieve this objective, efforts were concentrated in areas such as synthesis of powders through different routes, detailed study of sintering and phase conversion process with time, optimizing the fabrication process to achieve highly oriented/textured poly-crystals materials to improve the critical current density (J_c) using various solidification and texturing employing Top Seeded Melt Texture Growth Technique (TSMTG).

The details of the above mentioned studies including general introduction and experimental techniques have been arranged in four different chapters of the thesis, in addition to Introduction, experimental and conclusion chapters.

Chapter 1: Introduction

A brief introduction to discovery of superconductors with short historical background of oxide superconductors has been given. Literature survey on the progress of high temperature oxide superconductors, from the fabrication point of view has been summarized. The key requirement for practical use of this material is the critical current density (J_c), which is a very important technical parameter required for the applications. In order to overcome the 'weak links' at grain boundaries in YBCO samples, and to improve the properties of YBCO samples, the

melt textured growth (MTG) method was developed [6] which offers an effective way for the preparation of YBCO bulk superconductors with high critical current. Numerous modified melt growth methods such as quench melt growth (QMG) [7], partial melt process (PMP) [8] and melt process melt growth (MPMG) [9] have been developed to optimize values of the parameters and to obtain high quality YBCO bulk superconductors. As of now, top seeded melt growth method is widely used to grow large and well oriented single-domain YBCO samples [10-13]. Krabbes et al. [14] have reported that the Y_2O_3 addition to Y-123 may influence the mechanism of melt texturing of YBCO and the process window for YBCO for YBCO stable growth condition can be extended. Some of the dominant factors that affect the production of High J_c materials in Y-123 system i.e. multi-components system, less weak links, complex crystal structure, highly oriented structure, effective pinning centers [15-16] and oxygen stoichiometry etc. are mentioned in the thesis.

Chapter 2: Instrumentation

The experimental techniques which have been used during this research work are described in this chapter. This include fabrication of six side heating furnace (heating zone of 6 inch cube with an accuracy of $\pm 1^\circ C$ and cooling rate of 0.2 - 0.5 $^\circ C /h$). Low temperature (77K liquid nitrogen) critical transition temperature (T_c) measurement setup was designed and developed for multi-samples measurements in a single run. Silicon rubber molds were designed for compacting different shapes in cold isostaic press.

It is not easy to characterize these relatively large superconductors by conventional methods such as transport current density measurement. These methods are not only destructive but also applicable only to small samples. In this thesis, an automatic system was developed to characterize the levitation force and trapped magnetic field of large samples in a relatively short period.

The iodometric technique used for the determination of oxygen stoichiometry has been elaborated.

Critical current densities (J_c) of these samples were measured at Budapest University of Technology and Economics (BUTE), Budapest, Hungary. The calculation of the J_c was based on the measurement of the inductive type superconducting fault current limiter (iFCL) with SC ring. The activation current of the iFCL refers to the AC critical current of the superconducting ring. Assuming that the magnetic coupling between the two sides of the FCL is full; such the AC critical current of the SC ring is calculated from the activation current and the number of turns of the iFCL.

Other techniques like such as X-ray diffraction (High temperature XRD) for phase transition, phase purity and texturing, Laser particle size distribution unit for particle size distribution, Orientation Imaging Microscope (OIM) for orientation mapping of the surface, Scanning Electron Microscope (SEM) for microstructural examination, Electron Probe Microscope Analyzer (EPMA) for micro structural, elemental analyses, Superconducting Quantum Interference Device (SQUID), High Resolution Transmission Electron Microscope (HRTEM) are also be discussed briefly.

Chapter 3: Bulk Powder processing, densification and characterization of Y-123 and Y_2BaCuO_5 (Y-211) powders

$YBa_2Cu_3O_{7-\delta}$ (YBCO or Y-123) superconductor, has been chosen as the main focus for the research and development of real applications, due to the following reasons:

- (a) Its critical temperature (T_c) is higher than liquid nitrogen temperature (77 K)
- (b) Several processing techniques have been developed to achieve high J_c for practical uses.
- (c) The intrinsic properties and phase diagrams, which guide the appropriate direction for materials processing, are well documented.

Since Y-123 oxide is a multi-component compound, while synthesizing large scale powder care has to be taken to produce phase pure powder. The initial particle size plays an important role in achieving superconducting properties like critical current density (J_c) and critical magnetic field (H_c). This chapter describes the bulk powder synthesis of phase pure Y-123 and Y_2BaCuO_5 (Y-211) powder by different routes. These powders were characterized by X-ray diffraction, particle size distribution. Oxygen estimation (iodimetry titration) was performed by quenching the Y-123 pellet at different temperature and correlated with critical temperature (T_c). The changes in crystal structure at each temperature was studied by high temperature X-ray diffraction.

Synthesis of Bulk Y-123 powder by solid state route :- Stoichiometric amounts of AR grade Y_2O_3 , CuO and $BaCO_3$ were weighed and mixed in planetary ball mill in wet media using zirconia bowls and balls for 15-20 min. The powder mixture was subjected to multiple calcinations at 900° C for 10 h.

Synthesis of Y-211 by nitrate decomposition route :- Stoichiometric amounts of AR grade Y_2O_3 , CuO and $BaCO_3$ were weighed and dissolved in dilute nitric acid and evaporated to dryness with in situ stirring. The nitrated slurry was then subjected to heat treatment at 300 °C for 1h. The calcined Y-211 powders obtained by both solid state route as well as by nitrate decomposition route powders were characterized for X-Ray diffraction that showed the formation of phase pure material. The particle size of powder was studied by laser particle size measurement unit. The average particle size distribution of powder synthesized by nitrate decomposition was 3-5 microns whereas powder synthesized by solid state route was 15-20 microns. Large scale synthesis of nearly one kg batch of phase pure powder of Y-123 and Y-211 powders was achieved.

The Y-123 powder was compacted and sintered at 930°C for 10h. The electrical and structural changes have been studied for sintered samples of different oxygen content by quenching the sintered samples at different temperatures. It has been found that the T_c and the unit cell lattice parameters change smoothly with oxygen content. Oxygen rich samples are found to have better superconducting properties and are orthorhombically distorted. As they become oxygen deficient, superconducting properties get suppressed and unit cell changes to tetragonal symmetry. A series of compounds have been synthesized with oxygen content between two extremes i.e. $O_{7.0}$ to $O_{6.4}$ and they were characterized by X-ray diffraction, T_c and oxygen stoichiometry measurements. The superconducting samples transformed to semiconducting below the oxygen stoichiometry $O_{6.4}$. The occupation of oxygen vacancies create holes in the structure and with increase in

hole concentration by oxygen pick up, T_c increases up to the upper limit 90K. At this stage oxygen content is found to be ≈ 6.9 . Prolonged annealing in oxygen at low temperature where rate of oxygen pick up is maximum does not yield higher T_c . This suggests that the saturation point for oxygen content in Y-123 compound is ≈ 7.0

Critical current density (J_c) is strongly microstructure dependent rather than an intrinsic properties of the superconductor. Furthermore, some of the characteristic features of HTSC materials, such as the two-dimensional crystal structure and the very short coherence length, posed severe difficulties in J_c enhancement. Therefore, for achieving high J_c , the control of the microstructure is very important. Hence it is essential to acquire a structurally textured/oriented matrix of Y-123, with homogeneously dispersed defects or inclusions of impurities, acting as magnetic flux pinning centers. Components were fabricated using the above graded Y-211 powders and their impact on the superconducting properties of Y-123 were studied. The other composites have also been studied and characterized. Details of these components will be discussed in next chapters.

Chapter 4: Preparation and characterisation of different composites for MTG Components

This chapter describes the composite selection for fabrication of components of different shapes using the above powders. Zirconia bowl and zirconia balls in planetary ball mill are used to mix the powders. The mixed powder was then granulated by pressing, crushing, grinding and sieving. Samples have been fabricated to address the above issues by following approaches:

Examining the relative stability of solidification growth fronts by using different varieties of composites namely :

- 1) Y-123 + 25 wt % Y-211 (solid state route) + 5 Wt % Ag
- 2) Y-123 + 25 wt % Y-211 (nitrate decomposition route) + 5 Wt % Ag
- 3) Y-123 + 25 wt % yttria + 1 wt % Pt
- 4) Y-123 + 25 wt % yttria + 1 w % ceria

The inclusion of Y-211 particles has several advantages to the growth and properties of bulk Y-123 components, such as :

- a) It prevents the liquid flow so as to decrease the amount of pores.
- b) It shortens the space between the Y-211 particles to help growing the Y-123 crystal as well as creating the Y-123/Y-211 boundaries which are effective flux pinning sites.
- c) Volume fraction of Y-211 particles is approximately constant: the current density (J_c), value is an inverse measure of the mean size of Y-211 phase [17-18]. The high critical density values could be achieved by controlling volume fraction and particle size of the Y-211 phase.
- d) Y-211 also acts as reinforcement to the melt due to which the shape of the component is retained.

Owing to its selective permeability to oxygen, the addition of silver produces two-fold effects. Firstly, it provides highly diffusive pathways for the material transport via the capillary action and leads to particle rearrangement with a better packing density. It also improves the thermal conductance and reduces the local temperature rise which otherwise can weaken the pinning.

Platinum and cerium oxide powders were added for suppressing the Ostwald ripening (grain coarsening) of Y-211 particles.

Chapter 5: Fabrication of components using melt texture growth (MTG) technique

Unlike metals, ceramics are generally shaped (using different techniques like cold isostatic pressing, hot isostatic pressing etc.) prior to heating. This is due to their brittle nature which makes them difficult to machine, but also because pressure is normally required before subjecting them to thermal cycle so as to ensure large areas of surface contact between the grains. Large areas of surface contact not only increases reaction rates, but also tend to increase the density and strength of the components.

This chapter describes the fabrication of components of different shapes following various steps such as densification by using Cold Isostatic Press (CIP), sintering and then subjecting the compact to thermal cycle through melt texture growth (MTG) technique .

Compaction study has been carried out to achieve maximum green density by varying the pressure in CIP. The effects of pressure are (i) to reduce pores size (ii) to break up particles at surfaces in contact (iii) to introduce strain and plastic flow to achieve maximum green density.

Granulation along with vibration is carried out to ensure that the charge completely fills the mold to ensure good packing density. Since the components are of larger size, uniaxial pressing cannot be used, L/D ratio cannot be maintained and

also complex shapes cannot be pressed using uniaxial pressing. Therefore to maintain L/D ratio and to achieve uniform density throughout the sample, we have used cold isostatic pressing (CIP). The compacts using CIP are generally more homogeneous i.e. a uniform density is maintained in the entire compact shape and it is free of microcracks compared to the axially pressed counterparts. CIP is applied hydrostatically. The material is sealed in flexible membrane, such as rubber mold, and inserted into an oil mixed water bath. Mould was designed in such a way that it takes care of shrinkage while pressing and sintering as well as when it is subjected to melt texture growth technique (MTG) [detail of MTG is given subsequently]. The reduction in dimension at all the three stages had to be back calculated to design the mould.

During MTG process the compact attains higher temperature than the melting point of Y-123, the upper portion partially melts and shrinks. The lower portion of the compact also partially melts, reacts with base material due to which the shape is distorted at the bottom where the sample is in contact with base material. Therefore in order to decrease the loss of material and to retain optimum shape of the compact, a pre-sintering step is introduced before it is subjected to MTG in which the compact is slowly heated (to avoid thermal shock due to which cracks may be generated in the sample) to near melting point for a short period, It ensures the maximum shrinkage in the components while sintering.

At this stage an MgO crystal of preferred orientation (001) used as seed, placed on the compact while pressing. The compacts along with the seed are

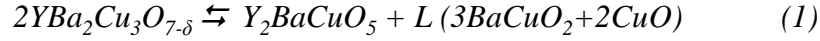
subjected to the MTG (details given subsequently) thermal cycle. Further prolonged oxygenation annealing is carried out at 425 °C for 150-200h.

Top seed melt texture growth technique (TSMTG)

This method uses natural tendency of Y-123 crystals to grow preferentially in ab plane. The cylinder/plate is subjected to the following thermal cycle. Y-123 dissociates at 1060°C into solid Y-211 and liquid of Ba and Cu oxides (reaction 1). During slow cooling from 995-940 °C (peritectic temperature) the Y-123 nucleates from undercooled mixture of Y-211 particles and melt consisting of BaCuO₂ and CuO (reaction 2). Thus to facilitate the growth of Y-123, the dissolution of Y-211 is essential so that additional Y³⁺ ions are supplied to Y-123 solidification front. The solidification front will engulf Y-211 particles, this depends upon the particle size of Y-211, velocity of the growth front and interface energies between Y-123, Y-211 and the melt. Therefore it was decided to add 25 wt % of Y-211 to Y-123 before melt processing. This ensures the formation of defects, which are necessary for pinning, as well as enough supply of Y³⁺ so that loss of liquid during melting is prevented. Y-211 recombines with BaCuO₂ liquid at around 1000 °C to form Y-123 subsequently it is slowly cooled through peritectic point to 930°C, which is followed by oxygenation at 425-450°C for 150-200 h.

The following critical parameters were optimized while executing MTG :

- i) The maximum temperature and its duration up to which the charge is heated
- ii) Cooling rate
- iii) Oxygen annealing duration.



The compacts using all the four composites were fabricated in hollow cylindrical and plate shapes. These compacts were then subjected to MTG, followed by prolonged annealing in oxygen atmosphere. Their detailed characterization is discussed in the next chapter.

Chapter 6: Characterization of fabricated MTG components

X-ray diffraction analysis of MTG sample reveals that the sample is highly textured along (001) planes.

The Scanning Electron Microscope (SEM) images of TSMTG fabricated sample using initial precursor of solid state route (initial powder average particle size 10-15 microns) show 15-20 microns of Y-211 particles. The SEM image of TSMTG fabricated sample using nitrate decomposition powder (initial powder average particle size 3-5 microns) show 3-5 micron size of Y-211 particles along with their distribution in the matrix of YBCO.

Electron Probe Micro-Analyzer (EPMA) image and corresponding elemental mapping show particle size distribution of Y-211 phase in the matrix of YBCO. These experiments also reveal the line profile of the variation of individual elements from matrix of Y-123 (superconducting) and Y-211 (non-superconducting) phases. The line profile shows the sudden discrete variation in the atomic percentage corresponding to Y, Cu and Ba.

Orientation Imaging Microscope (OIM) image shows Y-211 particle to be distributed in the matrix of YBCO and the color coding shows that all red color in the matrix are 001 oriented YBCO and the green color corresponds to Y-211 phase, which is randomly oriented. This OIM orientation is in corroboration with XRD analysis where the pattern shows all the peaks corresponds to 00l oriented plane.

TEM of Y-123 sintered powder is compared with TSMTG powder. The TEM of sintered powder showed that the grains are not aligned. The MTG powder shows two types of grains which are aligned with an angle of approximate 3-4 degree. This shows that crystals of Y-123 grains are textured and aligned.

Critical current density measurements were carried out at Budapest University of technology and Economics (BUTE), Budapest, Hungary. The J_c of sintered Y-123 compact was only 600 mA/cm². Remarkably, the critical current density (J_c) was found to be 838 A.cm⁻² for Y-123 samples containing Y-211 prepared by solid state route and 4032 A.cm⁻² for Y-211 by nitrate decomposition route. The five-times increase in current density is mainly attributed to the finer size of the Y-211 phase obtained by the nitrate decomposition route. The J_c values measured for other TSMTG samples generated using Pt, ceria added additives were found to be lower as compared to Y-211 addition.

The maximum trapped field values for TSMTG plate prepared by solid state route and for TSMTG sample prepared from nitrate decomposition route were 0-200 gauss and 0-800 gauss, respectively. Levitation force measured at 1 mm distance from magnet of TSMTG plate prepared by solid state route show force of 8 N and

whereas in TSMTG sample prepared by Y-211 synthesized by nitrate decomposition route show force of 28 N.

Chapter 7: Conclusions and future scope

The salient findings of the present work are as follows:

- A system for measurement of trapped magnetic field and levitation force of large MTG samples was designed and developed. It has an advantage of generating data in relatively very short period and the results reveal about the quality of the MTG sample. The technique developed can be used for measuring trapped magnetic field and levitation force of a sample size of 25 x 25 mm in 90-120 min without destroying the shape .
- Synthesis of bulk Y-123 and graded Y-211 phase pure powders in one Kg. size batch.
- Melt textured HTS components were fabricated with finer size of non-superconducting (Y-211) phase which act as flux pinning centers.
- Besides texturing of the Y-123 phase the smaller Y-211 second phase grains have enhanced the superconducting properties.
- MTG cylinders were fabricated with dimension 36 mm (ID) x 46 mm (OD) x 50 mm (length), also in size of 30 mm (length) x 20 mm (ID) and 30 mm (OD)
- HRTEM of MTG samples show textured grains with an angle of 4-5 °.
- OIM images and XRD show the orientation in the MTG samples

- Trapped magnetic field is observed 4-5 times higher in case of finer size Y-211 compared to coarser size Y-211 whereas levitation force 3-4 times.
- These results give same signature which are measured in J_c values of MTG ring samples, where J_c are 4-5 times higher for finer size Y-211 powder.
- The J_c measured in other TSMTG samples generated using Pt, ceria added additives were found to be lower as compared to Y-211 addition.
- Melt-texture growth of polycrystalline $YBa_2Cu_3O_{7-\delta}$ superconductor using MgO as seed crystal created an essentially highly dense structure consisting of cm long, plates shaped crystals preferably aligned parallel to the ab plane. The new microstructure, which completely replaces the previous granular and random structure in the sintered bodies, exhibits improved transport J_c values at 77 K of 4032 A/cm^2 in zero field (compared to 500 mA/cm^2 in sintered bodies). The remarkable improvement in J_c is attributed to the combined effects of graded Y-211 particles, compaction, thermal cycle, alignment of crystals, formation of cleaner grain boundaries.

Future scope of this work

- Fabrication of components of better HTSC properties.
- Synthesis of nano Y-211 powders will be carried out choosing proper variation in process parameters.
- Extension of the present work will be to fabricate components such as rotors in HTSC motors, fault current limiting devices, current leads etc. However,

this engineering work is out of scope of the present thesis and hence it will be taken up subsequently.

- Attempts will also be made to fabricate similar components from Bi-Ca-Sr-Cu-O based oxide superconductors.

Appendix

Control Instrumentation Division (CnID) BARC had been assigned the task of designing a prototype HTSC motor. As per the design requirement, a consignment of MTG components of hollow cylinder, plates and pins, was prepared by the top seeded melt texture growth (TSMTG) technique described in this thesis.

TSMTG plates, pins and hollow cylinders were supplied for testing in the prototype motor. In the appendix details of design and testing of the motor has been discussed.

References:

1. J.R. Hull et al., J. Appl. Supercond. 2 (1994) 449.
2. Q.Y. Chen et al., J. Appl. Supercond. 2 (1994) 457.
3. H. Tesihma et al., Physica C 256 (1996) 142.
4. P. Gornert, Cryst. Res. Technol. 32 (1997) 7.
5. I. Yoshikata, Y. Yousuke, Y. Masaaki et al., Jpn. J. Appl. Phys. 34 (1995) 5574.
6. S. Jin, T.H. Teifel, R.C. Sherwood, M.E. Davis, R.B. Van Dove, G.W. Kammolttm, R.A. Sasrnacht, H.D. Keith et al., Appl. Phys. Lett. 54 (1989) 584.
7. K. Salama, V. Selvmanickam, L. Gao, K. Sun, Appl. Phys. Lett. 54 (1989) 2352.
8. Z. Lian, Z. Pingziang, J. Ping, W. Keguang, W. Xiaozu, Supercond. Sci. Technol. 3 (1990) 490.
9. M. Murakami, Mod. Phys. Lett. B 4 (1990) 163.
10. C. Varanasi, P.J. McGinn, V. Pavate, E.P. Kvam, J. Mater. Res. 10 (1995) 2251.
11. S. Marinel. J. Wang, I. Monot, M.P. Delamare, J. Provost, G. Desgardin, Supercond. Sci. Technol. 10 (1997) 147.
12. W.M. Yang, L. Zhou, J.R. Wang, C.P. Zhang, Y. Feng, P.X. Zhang, X.Z. Wu, Physica C 282 – 287 (1997) 529.
13. W.M. Yang, L. Zhou, J.R. Wang, C.P. Zhang, Y. Feng, P.X. Zhang, X.Z. Wu, Physica C 282-287 (1997) 529.
14. G. Krabbes, P. Schatzle, W. Bieger, U. Wiesner, G. Stover, M. Wu, T. Strasser, A. Kohler, D. Litzkendorf. K. fischer, P. Gornert, Physica C 244 (1995) 145.
15. Z. Lian, Z. Pingziang, J. Ping, W. Keguang, W. Xiaozu, Supercond. Sci. Technol. 3 (1990) 490.
16. M. Murakami, Mod. Phys. Lett. B 4 (1990) 163.
17. M.Murakami,H.Fujitomo, S.Gotoh,K.Yamaguchi, N.Koshizuka, S Tanaka, Phisica C 1991, 321-6 (1991) 185.
18. S.Kohyashi,S. Hirano, S.nagaya, Kojima, Phisica C 254 (1993) 249.

LIST OF FIGURES

Fig. 1.1 History of superconducting critical temperatures in metals, non oxide ceramics, alloys, oxide ceramics.(Ref. Wikipedia)	2
Fig.1.2 On passing below the transition temperature the magnetic lines of force are expelled, showing Meissner Oschenfeld effect	4
Fig.1.3 The behaviour of Type I superconductor in an applied magnetic field	7
Fig.1.4 The superconducting magnetisation curve of Type II superconductor	7
Fig.1.5 Crystal structure of YBCO (a) tetragonal phase ($\delta=1$), (b) Orthorhombic phase ($\delta=0$)	15
Fig.1.6 Temperature dependence of the resistivity for orthorhombic and tetragonal phase in YBCO	15
Fig.1.7 Dependence of T_c on oxygen content ($7-\delta$) in YBCO	16
Fig.1.8 Calculated oxygen content in Y-123 compared with experimental data (open squares) [19] at various temperature and oxygen pressures [18]. Broken line indicates the solid phase orthorhombic to tetragonal phase transition	17
Fig.1.9 Dependence of RE-(III) ionic radius on lattice constant and peritectic temperature in RE-123. The RE-(III) ionic radii used for coordination number of eight	18
Fig 1.10 Schematic illustration of magnetic flux lines repelled by a superconductor with pinning centers	22
Fig.1.11 lattice constant vs. Temp. for Y-123 phase and for various substrates	23
Fig. 2.1 Schematic diagram of four- probe T_c measurement setup	35
Fig.2.1a Sample holder with samples affixed for four probe T_c measurement	35
Fig.2.2 A schematic drawing of Cold isostatic press	38
Fig.2.3 Schematic drawing of the various interactions of electron beam	41

Fig.2.4 Schematic diagram of an SEM	44
Fig.2.5 Schematic of EPMA system	50
Fig.2.6 Schematic of Proportional counter detector of EPMA unit	51
Fig. 2.7 The schematic diagram of a transmission electron microscope	54
Fig.2.8 Schematic of OIM	56
Fig.2.9 Typical setup of EBSD with Kikuchi bands	56
Fig.2.10 Kikuchi bands and corresponding indexing patterns	57
Fig.2.11 Inverse pole figure mapping	59
Fig.2.13 Magnetic measurement in SQUID	62
Fig.2.14 Trapped magnetic field and levitation force measurement system	65
Fig.2.15 Magnetising system	65
Fig.2.16 Schematic of trapped magnetic and levitation force measurement system	66
Fig.2.17 Data collection mapping of trapped magnetic field by hall probe of MTG samples	66
Fig.2.18 Hysteresis loops at 77K for (a) a sintered Y-123 and (b) a zone melt textured Y-123 showing the increase in magnetization due to texturing.	68
Fig.3.1 Flow sheet of synthesis (solid state route) Y-211 & Y-123	81
Fig.3.2 Flow sheet of synthesis (nitrate decomposition route) of Y-123	81
Fig.3.3 Y-123 powder in a alumina boat	82
Fig. 3.4 Y-211 powder in a alumina boat	83
Fig.3.5 Particle size distribution of Y-211 powder (a) synthesised by solid state route (b) nitrate decomposition route	83
Fig.3.6 XRD of Y-211 powder synthesized by solid state route	84
Fig.3 7 XRD of Y-211 synthesized by nitrate decomposition route	84

Fig.3.8 XRD of Y-123 powder synthesized by solid state route	85
Fig.3.9 R vs T of sintered Y-123 pellet	86
Fig.3.10 SEM image of fractured surface sintered Y-123 pellet	86
Fig.3.11 High temperature XRD of sintered Y-123 powder	89
Fig.3.12 R Vs T plot of Y-123 samples quenched from different Temperatures to liq.N ₂	90
Fig.3.13 T _c as a function of oxygen content in Y-123	92
Fig.4.1 XRD of sintered Y-123 powder	101
Fig.4.2 XRD of composite B, (B1) - as mixed powder. (B2) - sintered powder. (B3) – Quenched powder	101
Fig.4.3 XRD of composite C. (C1) as mixed powder, (C2) sintered powder, (C3) Quenched powder	102
Fig.4.4 XRD of composite D. (D1) as mixed powder. (D2) sintered powder. (D3) Quenched powder	102
Fig.4.5 SEM micrograph of fractured surface of sintered pure Y-123 pellet	104
Fig.4.6 SEM micrograph of fractured surface of sintered pellet of composite A	104
Fig.4.6a SEM micrograph of fractured surface of sintered pellet of composite B	105
Fig. 4.7 SEM micrograph of fractured surface of sintered pellet of composite C	105
Fig.4.8 SEM micrograph of fractured surface of sintered pellet of composite D	105
Fig.4.9 SEM micrograph of fractured surface of quenched pellet of composite B	106
Fig.4.10 SEM micrograph of fractured surface of quenched pellet of composite C	106
Fig.4.11 SEM micrograph of fractured surface of quenched pellet of composite D	106
Fig.4.12 BSE image and corresponding X-ray mapping of sintered composite B	108
Fig.4.13 BSE image and corresponding X-ray mapping of sintered composite C	109

Fig.4.14 BSE image and corresponding X-ray mapping of sintered composite D	109
Fig.5.1 Section of the Y-123 ternary phase diagram	122
Fig.5.2 Mechanism of Y-211 diffusion to solid Y-123 front growth in MTG tech.	126
Fig.5.3 Picture of moulds for fabricating components :- (1)-Mould for hollow cylinder 1, (2)- Mould for plates, (3)-Moulds for PINS,(4)-Moulds for hollow cylinder 2, (5)- Mould for hollow cylinder 3.	130
Fig.5.4 Typical picture of mould and filling composite powder in mould with vibrating	130
Fig.5.5 Typical thermal schedule for fabricating MTG components	133
Fig.5.6 Flow chart of typical MTG technique	136
Fig 5.7 Picture of cylinder during stages of fabrication using mould size hollow cylinder (1) Compacted cylinder, (2) Sintered cylinder, (3) MTG cylinder	137
Fig 5.8 Pictures of plate during various stages of fabrication using mould size plate 1, (1) Compacted plates, (2) Sintered plates, (3) TSMTG plates	137
Fig 5.9 Pictures of pin during various stages of fabrication using mould size pin 1 (1) Compacted pin, (2) Sintered pin, (3) MTG pin	138
Fig 5.10 Pictures of cylinder during various stages of fabrication using mould size hollow cylinder 2, (1) Compacted cylinder, (2) Sintered cylinder, (3) TSMTG cylinder	138
Fig 5.11 Machined TSMTG cylinders	142
Fig.5.12 Machined TSMTG plates	142
Fig.5.13 Machined TSMTG pins using composite B (NDR-PI-1)	142
Fig 5.14 Picture of rubber mould used to fabricate MTG components	144
Fig.6.1 Critical transition temperature R Vs T plot of sintered & TSMTG SSR-PL-1plate	149
Fig.6.2 XRD of sintered pellet	149

Fig.6.3 XRD of MTG NDR-PI-2 plate	150
Fig.6.4 SEM and EDS of TSMTG SSR-PL-1 plate	152
Fig.6.5 BSE and corresponding X-ray mapping of sintered MTG SSR-PL-1 plate	154
Fig 6.6 SEM image of TSMTG SSR-PL-1 and corresponding elemental line profile	154
Fig.6.7 OIM image of SSR-PL-1 plate	155
Fig.6.8 TSMTG SSR-PI-1 plate was cut as shown in figure, the cut black portion was used for measuring for trapped magnetic field (a) and graph shows plot of SSR-PL-1 plate (b)	157
Fig.6.9 Levitation force measurement of SSR-PL-1 plate	158
Fig.6.10 Critical current density of SSR-CY-1 TSMTG hollow cylinder	159
Fig.6.10a XRD pattern of TSMTG NDR-PL-2 plate	161
Fig.6.11 SEM micrograph of NDR-PL-1 plate	162
Fig. 6.12 OIM image of TSMTG NDR-PL-2 plate	163
Fig. 6.13 HRTEM image of sintered Y-123 powder	165
Fig. 6.14 HRTEM image TSMTG NDR-PL-2 powder	165
Fig.6.15 Trapped magnetic field measurement of TSMTG NDR-PL-1 plate	167
Fig.6.16 Levitation force of NDR-PL-1 plate	168
Fig.6.17 SQUID plot of NDR-PL-2 plate	169
Fig.6.18 J_c measurement of NDR-CY-2 cylinder	170
Fig.6.18a J_c measurement of MTG hollow cylinder NDR-CY-2a fabricated using composite –B with similar process used as in TSMTG NDR-CY-2 cylinder	171
Fig.6.19 J_c of top portion of NDR-Cy-3 cylinder	173
Fig.6.20 J_c of bottom portion of NDR-CY-3 cylinder	173
Fig.6.21 SEM and corresponding EDS of Pt-CY-5 TSMTG sample	175

Fig.6.22 BSE and corresponding X-ray mapping of sintered SSR-PL-1 plate	176
Fig.6.23 J_c measurement of TSMTG Pt-Cy-5 cylinder	177
Fig.6.24 SEM and EDS spectrum of TSMTG Ce-CY-6 plate	178
Fig.6.25 EPMA of TSMTG Ce-CY-6 plate	179
Fig.6.26 J_c measurement TSMTG of Ce-CY-6 cylinder	181
Fig. A.1 Levitation force measured at a distance of 1mm from magnet and pins for 7 pins bunched was found to be 17 N	189
Fig. A.2 Levitation force measured at a distance of 1mm from magnet and pins for 19 pins bunched was found to be 34 N	190
Fig.A.3 (A) Schematic drawing of rotor, (B) parts of rotor with HTSC plates, (C) assembled plate type rotor	191
Fig.A.4 (a) Schematic drawing of rotor, (b) parts of rotor with HTSC pins, (c) assembled pin type rotor	191
Fig. A.5 HTSC hollow cylinder fixed inside the rotor and assembly of hollow cylinder type rotor	192
Fig. A.6 HTSC motor assembly	192
Fig.A-7 Levitating magnet on TSMTG pellet	193

LIST OF TABLES

Table 1.1 Characteristics of metallic and oxide superconductors	13
Table 1.2 Application of HTSC materials	19
Table 1.3 Progress and necessary factors for high J_c HTSC materials	25
Table 3.1 Oxygen content, T_c and lattice parameters of Y-123, quenched from various temperature to liquid nitrogen	85
Table 5.1 Required final dimensions of MTG components	124
Table 5.2 Various moulds with shapes and sizes designed for fabricating components with corresponding photographs	127
Table 5.3 Components fabricated using composites in rubber moulds	127
Table 5.4 Shrinkage in size of the compacts while pressing, after sintering and after subjected to MTG	137
Table 6.1 Critical current density of TSMTG hollow cylinders	179
Table 6.2 Comparison of magnetic properties of TSMTG plates	180

Publications

Journal

- 1) Experimental Analysis of Different Type HTS Rings in Fault Current limiter
A.Gyore, I . Vajda, **M R Gonal**, K. P. Muthe, S C Kashyap, and D K Pandya.
IEEE transactions on Applied Superconductivity 17, 2. (2007),1899.

- 2) Bulk High Temperature Superconductors Prepared by Melt Textured Growth
Technique- Effect of Y_2BaCuO_5 Particle Size
M. R. Gonal, R.C. Hubli and A.K. Tyagi
AIP Conf. Proc. **1349**, (2011) 833

- 3) Study of Superconducting Properties in Melt Textured YBCO samples
M. R. Gonal, K.G.Bhushan, S Ramanathan, R.C. Hubli, A.K. Tyagi, and
G.P.Kothiyal
AIP Conf. Proc. 1447, 911

- 4) The Effect of Addition of Y-211 with two Different Particle Sizes on the
Properties of Melt Processed $YBa_2Cu_3O_{7-\delta}$ (YBCO) Bulk Superconductors
M. R. Gonal, R.C. Hubli, A.K.Suri, A.K. Tyagi, Atila Gyore and Istvan
Vajda
IEEE transactions on Applied Superconductivity (Communicated)

Symposium

- 1) Characterisation of Bulk High Temperature Superconductors Prepared by
Melt Textured Growth Technique
M. R. Gonal, R.C. Hubli and A.K. Tyagi[†]
Proceedings of the 54th DAE Solid State Physics Symposium (2009)

Chapter 1

Introduction

1.1 History of High Temperature Superconductors

The scientific community witnessed a path breaking discovery of high critical temperature (T_c) oxide superconductors (HTSC) in La-Ba-Cu-O system by Bednorz and Müller [1,2] about 25 years ago. This Noble prize winning discovery resulted in great excitement and ever since, continuous efforts have been made to explore more of such materials with critical temperature well above liquid Nitrogen temperature (77K). Materials with higher T_c have since been explored and the chronology is depicted summarily in Fig. 1.1. A large number of researchers engaged in the field were energized by the thought of obtaining zero-resistance conductors cooled by relatively inexpensive liquid nitrogen. This also raised the expectations of HTSC applications in various fields from a commercial point of view.

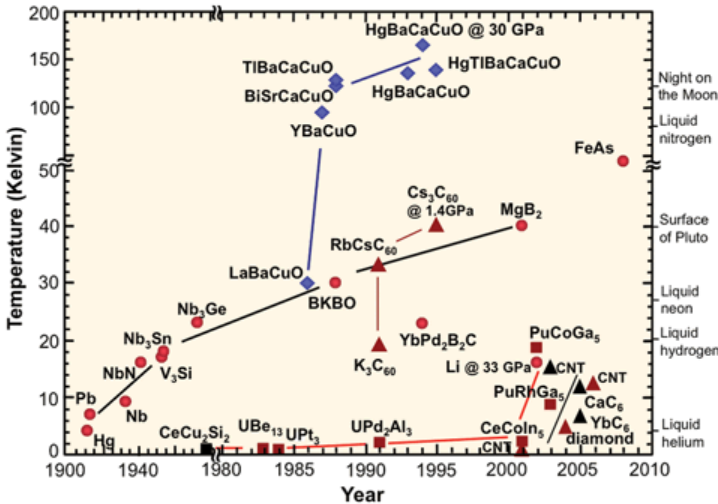


Fig.1.1. History of superconducting critical temperatures in metals, non-oxide ceramics, alloys, oxide ceramics (Ref. Wikipedia)

1.2 Properties of superconductors

1.2.1 Meissner Oshenfeld Effect

Apart from electrical properties, a superconductor also exhibits magnetic properties as amazing as its electrical properties. When a superconducting body of low demagnetisation factor is placed in a weak magnetic field, the field distribution around it always corresponds to a zero internal field, irrespective of its magnetic and thermal history. It is found that all the flux penetrating the superconductor is abruptly expelled (Fig.1.2) as the transition from normal to superconducting state takes place. Thus if a external field B_a is applied to a superconducting body, the field inside the superconductor B will be zero, hence

$$B = B_a + 4 \pi M = 0 \longrightarrow (i)$$

Which in turn gives susceptibility of a superconducting body

$$X = M/B_a = -1/4\pi \longrightarrow (ii)$$

Where M = magnetization

Thus superconductor shows perfect diamagnetism along with zero resistance property. This effect is known as Meissner Oshenfeld effect [3].

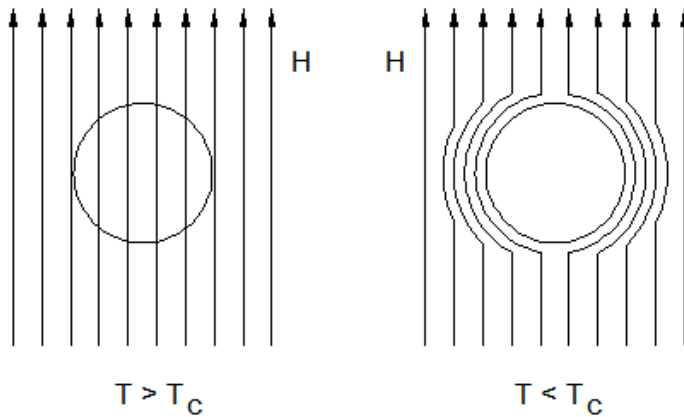


Fig.1.2 On passing below the transition temperature the magnetic lines of force are expelled, showing Meissner Oschenfeld effect

1.2.2 Penetration Depth

Though superconducting materials show perfect diamagnetism (Meissner Ochsenfeld Effect) but the variation of magnetic field at the normal-superconductor interface due to field exclusion is not abrupt. Certain amount of magnetic flux always penetrates into the superconducting body and the magnetic field inside it drops to a vanishingly small value over a characteristic distance. The field H at a depth x inside a superconductor whose surface field is H_0 is given by the expression:

$$H = H_0 e^{-x/\lambda} \longrightarrow \text{(iii)}$$

Where λ is known as penetration depth and it can be expressed as :

$$\lambda = (mc^2/4\pi n_s e^2)^{1/2} \longrightarrow \text{(iv)}$$

where m & e = mass & charge of electron respectively c = velocity of light; n_s = density of superconducting electrons.

The equation (iii) implies that the field should fall to zero inside a superconducting body in agreement with the Meissner Ochsensfeld effect, and that it should do so exponentially with a decrement x/λ .

Penetration depth is found to vary with temperature. It increases from a value $\lambda(O)$ at absolute zero to infinity at T_c . Experimentally the temperature dependence of λ can be represented as :

$$\lambda(T) / \lambda(O) = [1 - (T/T_c)^4]^{-1/2} \longrightarrow (v)$$

1.2.3 Coherence Length

The superconducting electrons behave differently as compared to the electrons in a normal conductor. The electrons in a superconductor responsible for supercurrent act coherently over a certain distance. The coherence length (ξ) is the distance in the superconductor over which the effects of perturbing force are appreciable and the range of propagation of a disturbance is of the magnitude of the superconducting order parameter n_s (the density of conducting electron pair) (T) and is expected to become large as T is raised towards T_c . Near T_c it follows the relation :

$$\xi(T) = \xi(O) / (1 - T/T_c)^{1/2} \longrightarrow (vi)$$

1.2.4 Type-I & Type-II Superconductors

In zero magnetic field all superconductors behave identically but in the presence of a magnetic field their behaviour is markedly different which can be placed in two different categories :

- (i) Type-I or soft superconductors
- (ii) Type-II or hard superconductors

1.2.4.1 Type-I or Soft Superconductors

A Type-I superconducting body below T_c , exhibits perfect diamagnetism and excludes a magnetic field upto a critical field H_c , where upon it reverts to the normal state as shown in H-M diagram (Fig. 1.3)

The presence of a normal – superconductor interface contributes an amount $H_c^2/8\pi$ to the surface energy, and hence the net surface energy becomes:

$$E_s - (\xi - \lambda) H_c^2/8 \pi \quad \longrightarrow \quad \text{vii)}$$

The ideal superconducting behaviour occurs only when the net surface energy is positive i.e., $(\xi - \lambda) > 0$, leading to an ideal Meissner effect. The very existence of this effect, requires the presence of a positive surface energy of the system.

Almost all the classic superconductors having $\xi(0)$ typically a few thousand Å show Type-I behaviour unless ξ is decreased by alloying or defects.

1.2.4.2 Type-II or Hard Superconductors

When a magnetic field is applied, Type-II superconductor passes from the perfect diamagnetic state to a mixed state at low magnetic fields and finally to the resistive state on further increase in magnetic field (Fig. 1.4). The material in the superconductive state

upto the magnetic field H_{c1} is perfectly diamagnetic. Between H_{c1} and H_{c2} a “vortex” state is found in which penetration of magnetic flux occurs into the bulk of the superconductor in the form of vortices that may pass completely through the superconducting slab. The fluxons (a minimal unit of magnetic flux) create regions of normal superconductor in a superconductive matrix. This is because of $(\xi - \lambda) < 0$ and therefore the material would tend to break into mixed state of normal and superconducting layers. The condition for the “vortex” state is that the coherence length should be smaller than the electromagnetic penetration depth or more precisely, the G-L parameter should be greater than $1/\sqrt{2}$.

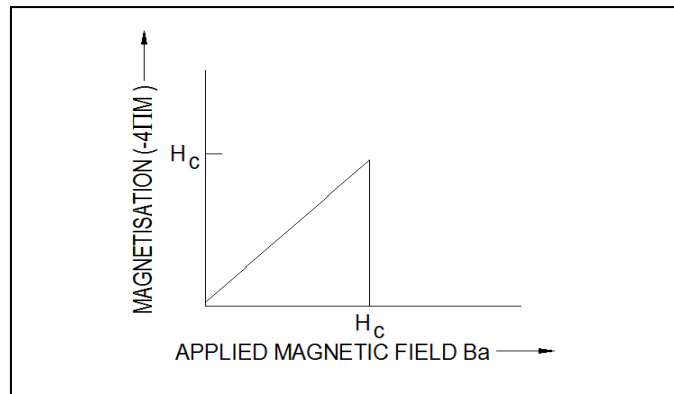


Fig.1.3 The behaviour of Type-I superconductor in an applied magnetic field

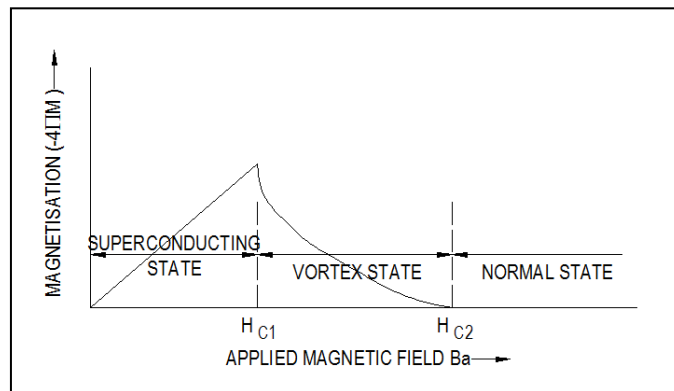


Fig.1.4 The superconducting magnetisation curve of Type-II superconductor

1.2.5 Isotope Effect

It has been observed [4,5] that the transition temperature of the superconducting state depends on the isotopic mass of atoms that make up the lattice of the material. Historically, isotope effect was an important indicator of the phononic origin of pairing mechanism in the superconductors [6]. It was expected in the phonon mechanism [7] that $z=0.5$ for all the elements in the relation showing dependence of T_c on an isotopic mass (M) :

$$T_c \propto M^{-z} \longrightarrow \text{(viii)}$$

This suggested that superconductivity involved an interaction between the conduction electrons and vibrational motion of the atoms in the lattice. Metals like Hg, Tl, Zn, Sn, Pb etc. all show an isotope effect [8] in accordance with the relation (viii). However, in the case of Os, a significant departure from $z = 0.5$ has been found [9]. Also Fowler et al., [10] measured the isotope effect in uranium isotopes and obtained a negative value for z ($z=-2.2$).

1.2.6 Specific Heat

There is a substantial change in specific heat of superconductor in normal and superconducting state. The specific heat decreases monotonically with temperature in the normal state and at the superconducting transition temperature there is a jump followed by rapid decrease in specific heat.

The specific heat C of a normal metal is usually regarded as composed additively of contributions from the lattice and from the conduction electrons and at very low temperature it may be expressed as :

$$C = T + \beta T^3 \longrightarrow \text{(ix)}$$

Where the first term on the right hand side is due to electrons and second term is due to the lattice contribution. The lattice contributions are unchanged between the normal and superconducting state and generally only electronic contribution to the specific heat is considered for the superconducting-normal transition.

In the absence of any magnetic field the transition occurs at the transition temperature and here critical magnetic field H_c becomes zero. This transition at zero magnetic field is a second order phase change and characterized by jump in the specific heat.

1.2.7 BCS Theory

The resistance of a metal is caused by the electron scattering primarily by lattice defects and by thermal lattice vibrations (phonons) which are present down to absolute zero temperature. It implies that obtaining a zero resistance in a material requires zero scattering of conduction electrons. At finite temperature, phonon scattering is possible if there are initial and final states available for scattering process. However, if a new electronic state could exist at temperatures upto a critical temperature, it could provide the impossibility of scattering by removing the final states of a scattering, then superconductivity could become possible.

BCS theory [11] proposes that in certain materials an unusual state of electrons near Fermi level is possible at low temperatures. This results from an attraction between two electrons through a phonon interaction by overcoming the coulomb repulsion between them. Two electrons are slightly excited from the ground state of Fermi

distribution at zero temperature, could form a real bound state in the presence of an attractive interaction. The bound state could be described by a single coherent wave function. It is envisaged that at low temperature, a free electron travelling through the crystal can attract neighbouring lattice ions, creating a region of excess positive charge that can in turn attract a second electron, thus forming a cooper pair of electrons [12]. This new state has an energy lower than that of the normal state of free electrons near Fermi level and separated from it by a superconducting energy gap (0.3 to 3 meV) that is larger than the energy of phonons available for scattering at the low temperature. Scattering, therefore, ceases since there is no energy conserving final state for the scattering transition, the scattering relation time becomes infinite, and the resistance goes to zero.

In order to minimize the energy of the new (superconducting) ground state, the electronic states from which the cooper pairs are to be formed must be chosen so as to maximize the binding energy of each pair and to obtain the greatest possible number of such pairs. Since in the scattering processes due to electron interactions the total momentum (or the total k-vector) is in general conserved, the maximum number of pairs that can be scattered coherently is obtained by pairing states such that all the cooper pairs have the same value of total momentum. In particular for the ground state, which carries no net current, the best possible pairing is between states of equal and opposite momentum. At the same time, since the exchange terms reduce the effective strength of interaction, the pairing of states with opposite spin, maximized the binding energy. In this way superconducting ground state may be formed by assuming that it can be expressed solely in terms of cooper pairs i.e., the pair of wave vectors $+k$ and $-k$ are

always occupied simultaneously. One cooper pair ($=k, -k$) can occupy another vacant position by exchanging an appropriate virtual phonon. Unpaired electrons can exist simultaneously with the cooper pairs in the superconducting state, but these are like ordinary electrons in the normal state and cannot take part in carrying super current. When an electric field is applied, the superconducting energy gap at the Fermi level moves along with the electric field and stabilized these pairs from the phonons available at the superconducting transition temperature or below it.

According to the BCS theory:

$$K T_c = 1.13 h w_D e^{-1/[N(E_F)V^*]} \longrightarrow (x)$$

Where K = Boltzman constant

w_D = characteristic Debye frequency

$N(E_F)$ = Density of states at the Fermi level

V^* = Electron Phonon Coupling constant

The BCS theory could provide a reasonably good explanation for the observed isotope effect, specific heat jump, microwave absorption etc. in the classic superconductors.

It says that electron pair formation occurs through the electron phonon interactions. Superconductor should show isotope effect because the vibrational motion of atoms depends upon the mass of the atoms in the lattice. Beside this, there does not seem to be any other reason for the superconducting transition temperature to depend on the number of neutrons in the nucleus.

According to BCS theory the superconductive state is more ordered state than the normal state as electrons remain as paired. The fact that just below the transition temperature the specific heat is much greater in the superconducting state than the normal state implies that, when a superconductor is cooled through this region, the entropy of its conduction electrons decreases more rapidly with temperature than the rate of decrease in the normal state as specific heat of a material is related to the rate of entropy change by the equation:

$$C = vT (\delta S/\delta T) \longrightarrow (xi)$$

Where v is volume per unit mass

Hence on cooling a superconductor some extra form of electron order (i.e., pairing of electrons) must begin to set in at the transition temperature in addition to the usual decrease in entropy of the conduction electrons which occurs when a normal metal is cooled. This additional ordering of electrons increases as the temperature is lowered and that contributes extra enhancement to $\delta S/\delta T$ and therefore the specific heat changes rapidly near transition temperature. As already mentioned, the transition in zero field is second order with no latent heat associated with the transition and no sudden change of entropy at the transition temperature, there is at the transition temperature only a change in the rate at which the entropy decreases as the temperature is reduced.

The BCS theory assumes that all the electrons in a superconducting body are paired into cooper pairs at zero Kelvin in the absence of an applied magnetic and electric field. The cooper pairs are broken up when energy is supplied to the body, for example by increasing the temperature or applying magnetic field. The population of unpaired

electrons is proportional to $\text{Exp}(-E/kT)$. This provides an explanation for the exponential dependence of specific heat below T_c .

1.3 High-Temperature oxide superconductors

1.3.1 Different systems of high temperature superconductors

Since the discovery of superconductivity by Bednorz & Müller at 30 K in La-Ba-Cu-O system, scientists have explored various other systems of high T_c superconducting materials. These have resulted in discovery of many other system with higher critical temperatures like $\text{YBa}_2\text{C}_3\text{O}_{7-\delta}$ (~90K)[9], $\text{Bi}_2\text{Sr}_2\text{Ca}_2\text{Cu}_3\text{O}_{10}$ (~110K) [10], $\text{Ta}_2\text{Sr}_2\text{Ca}_2\text{Cu}_3\text{O}_{10}$ (~120K) [11] and $\text{HgBa}_2\text{Ca-Cu}_2\text{O}_x$ (~130K) [12], at present, T_c attained is 164K, under high pressure. Most of these compounds have perovskite or oxygen-deficient perovskite structures.

The compounds in the above systems exhibit some common properties as given below

- (i) These compound shave a number of elements including copper
- (ii) Their structures contain CuO_2 layers
- (iii) They have large two dimensional anisotropy
- (iv) The coherence length (ξ) is very short ($<20\text{\AA}$ typically)

These characteristics are important inputs while deciding the synthesis protocol of HTSC materials.

Table 1.1 Depicts characteristics of HTSC materials and low- T_c materials (conventional metallic superconductors). The three factors described above must be considered when the superconducting materials are synthesised.

	Metals	Oxides
Dimensionality	Three dimensional	Two dimensional
Crystallinity	Not sensitive	Very sensitive
Coherence length	Long (greater than 100 Å)	Very short (less than 30Å)
Boundary effect	Small	Very large

Table 1.1 Characteristics of metallic and oxide superconductors

Largely, $\text{YBa}_2\text{Cu}_3\text{O}_{7-\delta}$ (YBCO) and Bi-Sr-Ca-Cu-O superconductors, have been explored as workhorses for the research and development of real applications due to following reasons:

- i) T_c being higher than 77 K;
- ii) High critical current densities have been obtained by using various processing techniques;
- iii) Appropriate phase diagrams, have been developed and these provide help in deciding the processing technique.

1.4 YBCO (Y-123) System

1.4.1 Crystal structure of Y-123 oxide

The crystal structure of YBCO material is a distorted oxygen-deficient perovskite structure of $\text{YBa}_2\text{Cu}_3\text{O}_{7-\delta}$ (Y-123), where $\delta = 0$ to 1. For values of $\delta=1$, Y-123 is tetragonal (Fig 1.5 (a)), but when $\delta=0$ it transforms orthorhombic structure (Fig.1.5 (b)), which was confirmed by several groups [13-15]. The tetragonal phase is not superconducting and shows a temperature dependence of the resistivity similar to that of semiconductors (insulator). Hence the orthorhombic phase is a superconductor (metallic resistivity trend) as shown in Fig.1.6 [16]. Since charge carriers are doped to the CuO_2 oxygen content, charge carriers are infused into the CuO_2 layer. Accordingly, T_c changes with δ , since the superconducting critical temperature (T_c) is thought to be significantly

dependent on the carrier concentration as shown in Fig.1.7 [17]. Y-123 shows two-dimensional anisotropy of the superconducting property due to the CuO_2 plane.

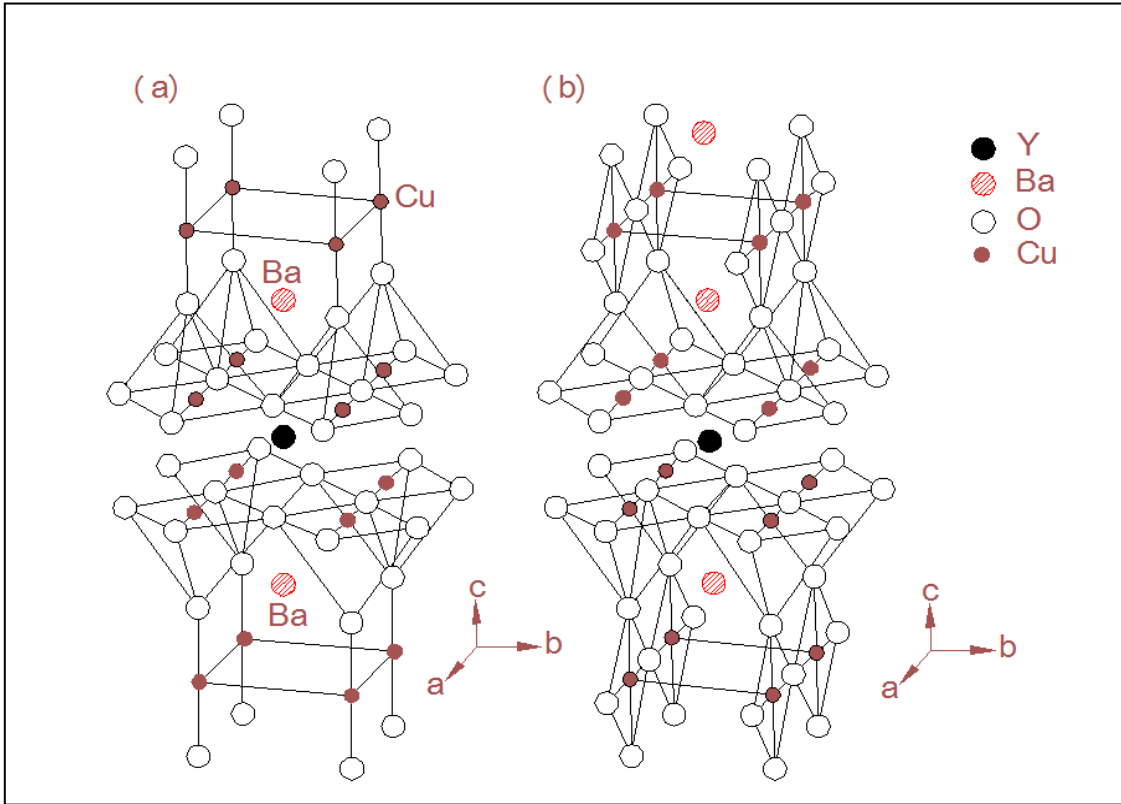


Fig.1.5 Crystal structure of YBCO (a) tetragonal phase ($\delta=1$) (b) Orthorhombic phase ($\delta=0$)

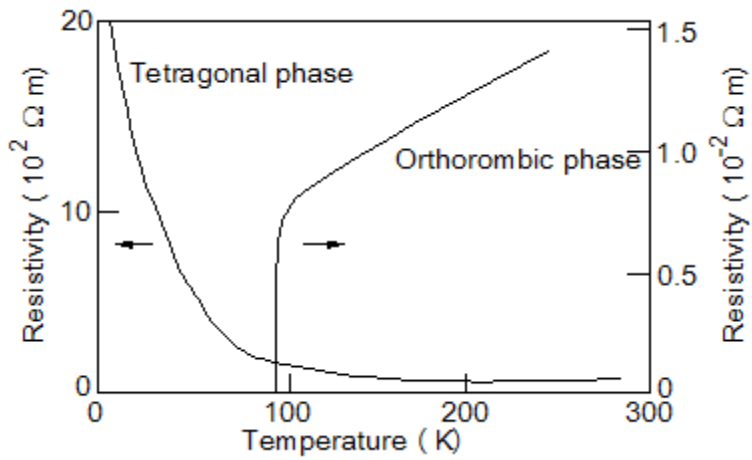


Fig.1.6 Temperature dependence of the resistivity for orthorhombic and tetragonal phase in YBCO [16]

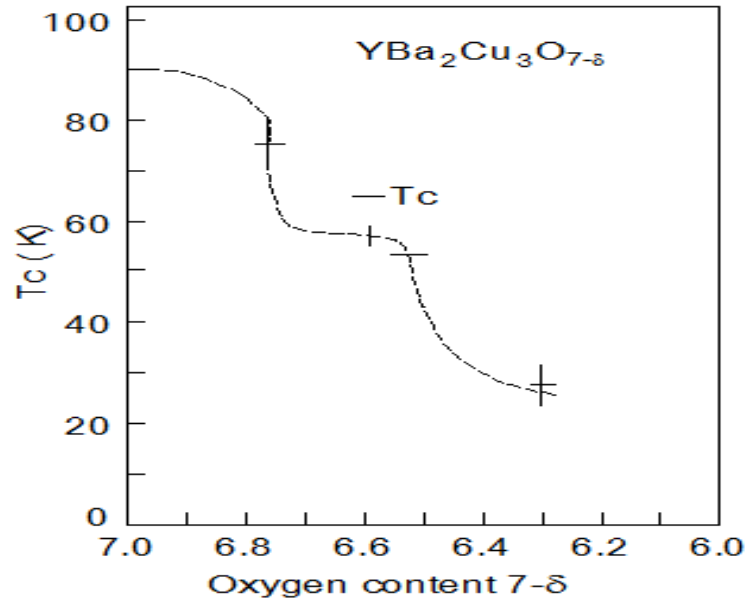


Fig.1.7 Dependence of T_c on oxygen content ($7-\delta$) in YBCO [17]

Fig.1.8 gives the oxygen stoichiometry in the Y-123 phase vs. the oxygen partial pressure (P_{O_2}) at different temperature [18,19]. The phase transition of tetragonal to orthorhombic depends on P_{O_2} and temperature. At higher temperatures beyond about 600°C in air ($P_{\text{O}_2} = 0.21$ atoms), the non-superconducting tetragonal phase is stable. The Y-123 materials produced by sintering or by melt growth generally have a tetragonal phase. Accordingly, the materials should be slowly cooled or post-annealed in an oxygen atmosphere for oxygenation to achieve high T_c . Dense ceramics and large single crystals require a longer time for oxygenation, but thin films, powders and porous ceramic samples can be easily oxygenated.

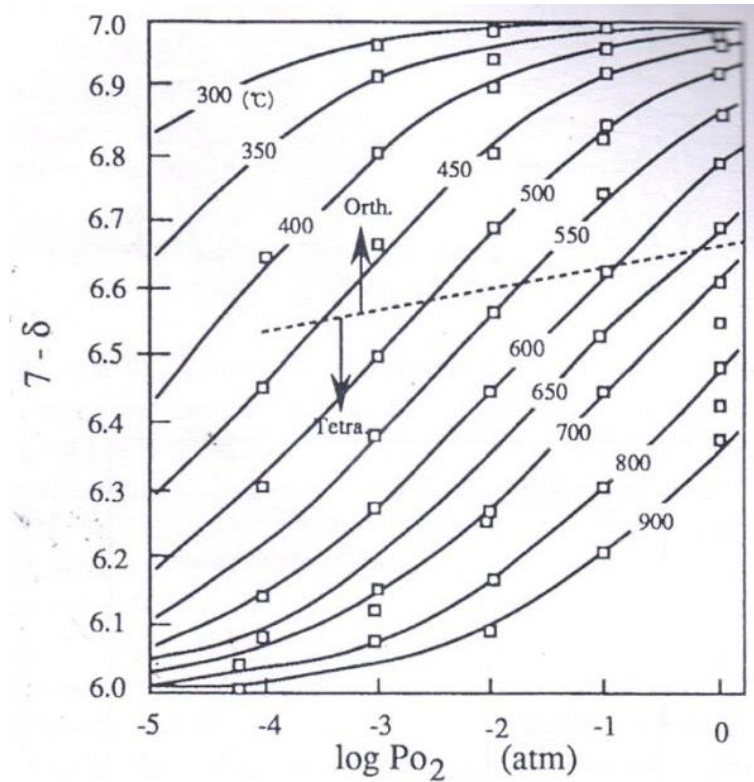


Fig.1.8 Calculated oxygen content in Y-123 compared with experimental data (open squares) [19] at various temperature and oxygen pressures [18]. Broken line indicates the solid phase orthorhombic to tetragonal phase transition

1.4.2 RE-123 system (RE=Rare earth)

All the rare earths (RE) except Ce and Pm can replace yttrium without any major effects on the superconducting characteristics. Fig.1.9 shows the relationship between the ionic radius of RE and T_c , the lattice parameters of the RE-123 structures and the peritectic temperatures (T) [23-26]. The T_c of Nd-123 was found to be 96K [32]. In general, T_c and phase transition temperature (T_p) increase with increasing ionic radius. Excellent J_c properties in a high magnetic field (several Tesla) have been reported in Sm-123 and Nd-123 systems [32-34].

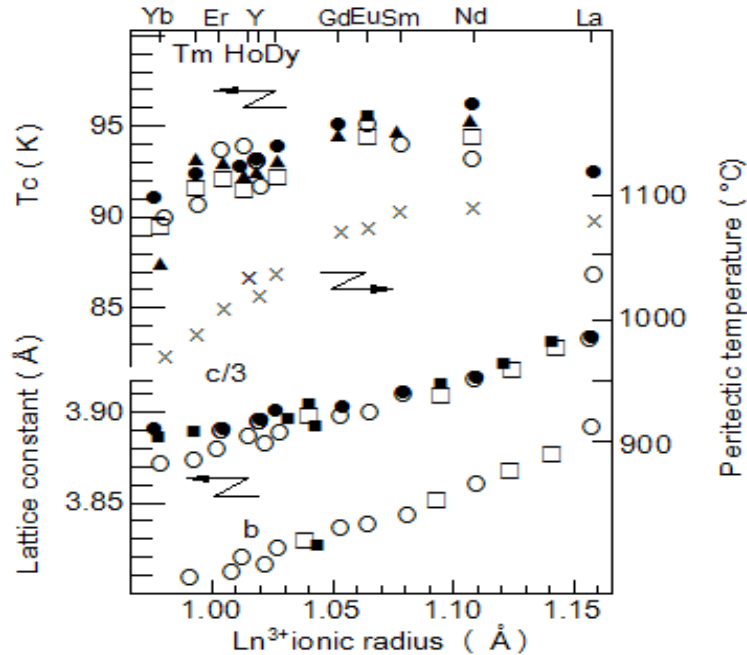


Fig.1.9 Dependence of RE (III) ionic radius on lattice constant and peritectic temperature in RE-123. The RE(III) ionic radii used for coordination number of eight [23-26]

1.4.3 Anisotropy in the Material

It has been shown that J_c in Y-123 is anisotropic, with the basal plane exhibiting J_c values (J_c^{ab}) higher by a factor of twenty than those along the c-axis (J_c^c) at 4K [65]. This is a result of the crystal structure of the compound and the intrinsic differences in the coherence lengths for different crystallographic directions in the orthorhombic structure. For Y-123, the coherence length is only 4 Å along the c direction and 32 Å in the a-b plane. These small coherence lengths (which are about two to three orders of magnitude smaller than those of conventional superconductors) necessitate that these bulk materials be prepared by special processing techniques to minimize the effect from a second concern, that of grain boundaries. Transport measurements have also been reported on melt-textured 123. Anisotropy ratios ($J_c^{ab} : J_c^c$) of approximately 20 have been

measured at 77 K. These values are somewhat lower than that have been measured in single crystals, a fact that many reflect improved pinning for transport parallel to the c-axis in textured specimens [66].

1.5 Applications of HTSC materials and property requirements

It is known that the superconductors exhibit characteristic properties like (zero electrical resistivity), Meissner effect (i.e. magnetic shielding) [35] and Josephson tunnelling (i.e. quantum effect) [36]), earlier investigations on metallic superconductors have been carried out only by limited researchers having a facility to handle liquid helium (4.2K). However, the discovery of HTSC materials above the boiling point of liquid nitrogen (77K) opened the way for a larger scientific community to participate in making possible the application of superconductivity in numerous fields. The typical superconductivity characteristics required strongly depend on the application. Table 1.2 gives a glimpse of required J_c values and relevant magnetic fields for several applications.

The applications of HTSC can be broadly divided into three categories

1. Wire and tape materials having high current carrying density for the transportation of large currents without power loss and for the generation of high magnetic fields.
2. Bulk materials with strong flux pinning for having applications in levitation and shielding.
3. Thin films for superconducting devices with quantum phenomena (i.e. Josephson tunnelling effect).

Form	Devices	Phenomena	Application	Required J_c (A/cm^2)	Operating field (T)
Wire	Wire Magnetic coils	Zero resistivity	Electrical energy transport	1×10^5	2
			NMR tomography	5×10^4	10
			Energy storage	1×10^5	11
			Generator Transformer Magnetic levitation (MAGLEV)	1×10^5	4
Bulk	Bulk	Levitation Attractive force	Bearing, flywheel	1×10^5	1
			Permanent magnet	1×10^5	1
Bulk Film	Wall, container	Meisner effect Flux pinning	Magnetic shielding	1×10^4 – 3×10^5	0.01 -6
Film	Strip line Patterned layer structures Joseph device	Zero resistivity Joseph tunneling	Passive microwave devices	1×10^5 2×10^5	0.06 0.04
			Interconnects in micro-electronics SQUID Computer Microwave detector and mixer		

Table 1.2 Application of HTSC materials [41-46]

As far as wires, tapes and bulk materials are concerned, the obtained critical current densities at 77K even in zero applied magnetic field have been very poor ($<1000 Acm^{-2}$). These are far less than the required J_c for applications. However, recent advances in the fabrication processes, together with a deeper understanding of the physical and chemical properties of HTSC materials, have raised the optimism for more applications. In the YBCO system, for example, J_c values of $\sim 10^5 A cm^{-2}$ at 77 K (0 Tesla) and $10^4 A cm^{-2}$ at 77 K (1 T) for bulk samples prepared by the quench and melt growth (QMG) and melt powder melt growth (MPMG) processes [3,4] have been reported. Similarly for rod-type samples prepared by the unidirectional solidification method [37-40] J_c values of $10^4 A cm^{-2}$ at 77 K (0 T) have been reported. Obviously these values are inadequate.

Therefore further improvement are needed for processing of bulk shapes, wires, tapes with better mechanical and chemical properties.

Bulk applications of superconductors are mostly based on zero resistance. The superconductors need to be fabricated in the form of long wires or tapes for such applications. This is not easy for brittle oxide superconductors. Also bending of HTSC wires for the fabrication of superconducting coils is difficult. Powder metallurgical methods, such as silver sheathed tapes in the Bi system and thin films deposited on a nickel-based alloy in the Y system [41], have achieved great progress, although the J_c values are still lower than those required at 77 K, especially with the applied magnetic field.

A few application fields have been proposed using the bulk form to avoid fabrication problems. The Meissner effect forces between a permanent magnet and a superconductor have been used to demonstrate magnetic bearings, fly-wheels [42,43], magnetically levitated transport systems [44] etc. It is notable that these applications are difficult in the case of metallic superconductor because a flux jump occurs due to the low specific heat, which drives the superconductor into the normal conducting state. This phenomenon is called quenching [45]. HTSC materials can be used at higher temperatures. Since the specific heat becomes high at higher temperature, even large bulk samples can be used at high temperatures [46]. This enables large HTSC materials to be used in the bulk form.

The Meissner effect means that superconductors can repel a magnetic field completely, [35]. The superconductor can be levitated above a magnet using this effect. In Type-II superconductors, the magnetic field above the lower critical field (H_{c1})

penetrates into the superconductors from the edge as shown in Fig.1.10 some part of the magnetic field is still repelled by the superconductor, resulting in the maintenance of the levitation force. If the magnetic flux is trapped by the strong pinning sites, a force to remove the magnetic flux from the pinning sites is required. This leads to attractive forces. In fact, melt-processed Y-123 superconductor with finely dispersed Y-211 particles, with strong pinning forces, can levitate a heavy object (for example, above 100 kg in weight) in a stable manner using the strong repulsive and attractive forces [46].

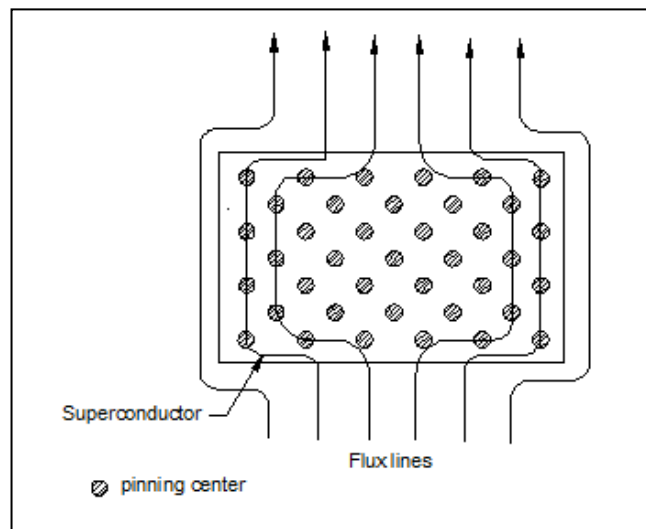


Fig.1.10 Schematic illustration of magnetic flux lines repelled by a superconductor with pinning centers [46]

In the case of thin films the applications requiring epitaxial growth and substrates are to be considered. The very short coherence length of HTSC materials poses specific problems, requiring atomically flat surfaces and sharp interfaces and patterning on the sub nanometer scale. A number of substrate materials have been used for the epitaxial deposition of HTSC materials. Fig.1.11 shows the lattice constants and thermal expansion of Y-123 and a few substrates used for Y-123 deposition. A substrate material has to satisfy the following requirements:

- i) In the temperature range between the substrate temperature (T_s) for growth and the applications temperature (T_a) the misfit between the expansion coefficients should be small ($\leq 0.2\%$)
- ii) In the temperature range between T_s and T_a ; There should be no phase transition and twinning.
- iii) The interface between the HTSC material and the substrate [47], should have good chemical and thermal stability.

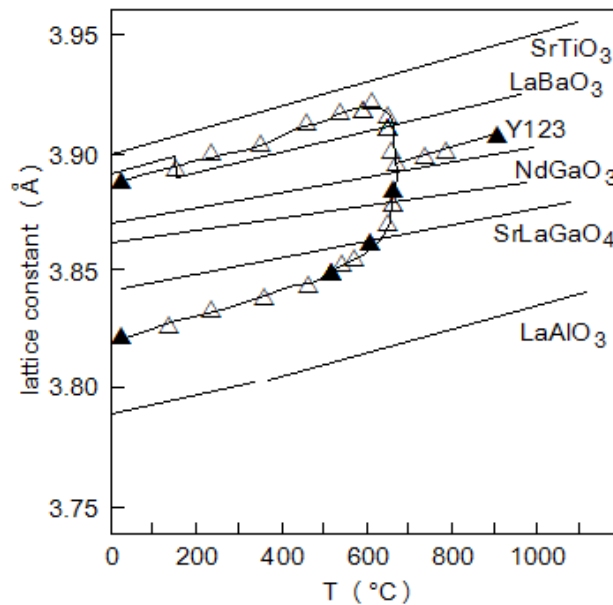


Fig.1.11 Lattice constant vs Temperature for Y-123 phase & for various substrates [47]

Considering the above requirements Y-123 or RE-123 single crystal substrates are considered to be the best. In fact, Y-123 films have been epitaxially grown on Y-123 single crystal substrates fabricated by the solute rich liquid crystal-pulling (SRL-CP) method [48]. Further efforts to solve these and twinning problems existing in RE-123 substrates are required.

1.5.1 Factors influencing critical current density

Critical current density is greatly influenced by microstructure which needs to be controlled rigorously in order to obtain higher J_c . A sintered sample has a much smaller J_c value than a melt-grown sample, even though the T_c values are the same. Therefore microstructural differences need to be explored. Sintering is commonly used in oxide materials, which are popular as 'ceramics', and has many advantages, i.e. precise shape formation required for practical applications and the relatively low temperature needed to produce compounds by solid state reaction. Some of the microstructural characteristics hindering high J_c in sintered samples are as follows:

- i. Relatively low apparent density.
- ii. A second phase maximum to be present at the grain boundary due to local non-uniformity of composition and low diffusivity in the solid.
- iii. Random orientation of grains.

The problems of low density and local non-uniformity in composition can be addressed by using well established ceramic processes such as co-precipitation and the sol-gel method for the preparation of fine, homogeneous starting powder [49-51]. Use of high pressure for compaction, cold isostatic pressing and liquid phase sintering can be employed for preparation of high-density samples and multi step sintering, with intermediate pulverisation. Optimization of the sintering temperature and time can result in the reduction of the secondary phase at the grain boundary. These processes have resulted in the improved J_c values to some extent.

However, even in the best prepared bulk sintered samples, the J_c values obtained are very low (of the order of 10^3 A cm^{-2} at 77 K) in zero field and decrease drastically when a

magnetic field is applied. This can be considered to be mainly due to the random orientation of grains, i.e. the existence of grain boundaries. This is supported by the fact that single crystals exhibit one or two orders of magnitude larger J_c values than polycrystalline sample [52]. The grain boundaries act as weak links' which decrease J_c .

Many researchers have investigated the types of grain boundaries which reduce super current flow. Dimos et al. [53] have shown the decrease in J_c in bicrystalline thin films with increasing misorientation angle between two grains, and such behaviour is independent of the preparation method or type of substrate. This result seems to suggest that high-angle grain boundaries are intrinsically weak links, because of the extremely small coherence length in oxide superconductors. After this famous experiment, it also has been reported that the high-angle grain boundaries in some films and bulk bicrystals of YBCO do not always behave as weak links, but the coupling between CuO_2 planes at grain boundaries affect the weak links rather than the angle itself [54]. This weak link problem takes place, especially in HTSC materials; is present due to the reason that the coherence length is much smaller than that of metal superconductors. It is therefore difficult to achieve high J_c values in sintered samples in which grain boundary structure cannot be controlled.

The randomly oriented samples also have a disadvantage because of the anisotropic superconducting property due to two dimensionality in the crystal structure of YBCO since the super current preferentially flows along CuO_2 planes.

One can also derive important information on high J_c values from conventional metallic superconducting materials as well as from sintered materials. In the case of NbTi, the first practical material for superconducting wire, the high J_c values are ascribed

to the introduction of finely dispersed α -Ti precipitates in the NbTi matrix because the precipitates act as effective magnetic pinning sites .

It is clear from the above discussion that some of the dominant factors for obtaining high- J_c materials are as follow:

- (i) Less weak links
- (ii) Highly oriented texture
- (iii) Presence of effective pinning centers
- (iv) Oxygen content which will determine T_c

In other words, the microstructure must be controlled to avoid grain boundaries (i.e. perfect matrix) and include pinning sites (i.e. defects) within the matrix not along the grain boundary. The necessary factors and the various sintering and melt processes for high J_c HTSC materials are summarized in Table 1.3.

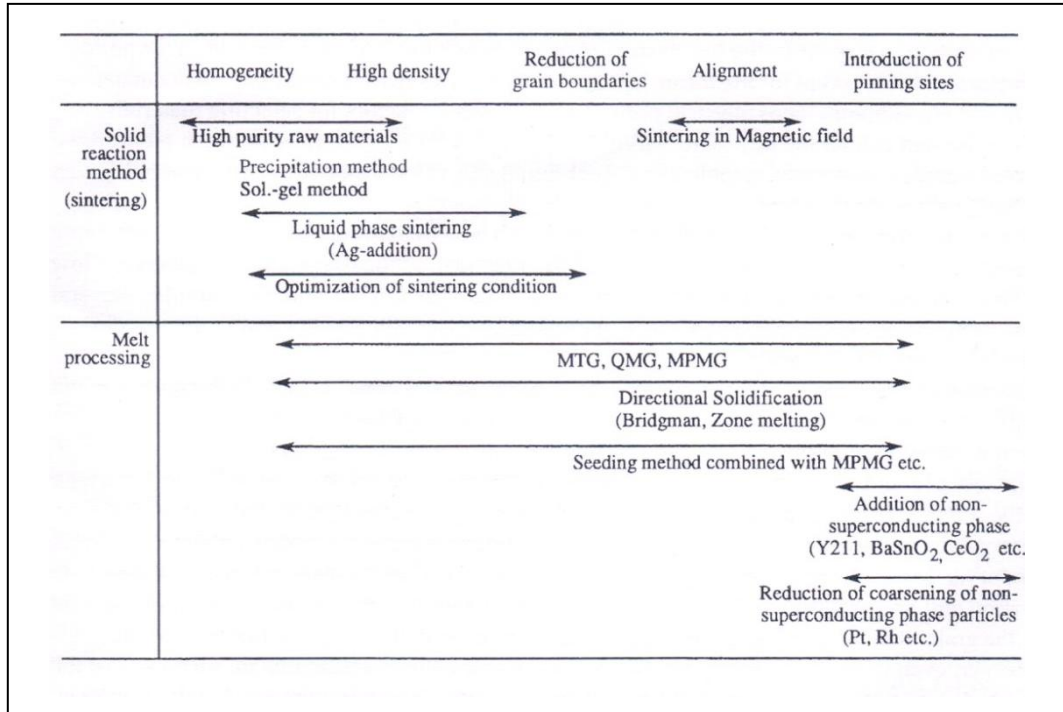


Table 1.3 Progress and necessary factors for high J_c HTSC materials

1.6 Sintering Method

Homogeneity and high density can be obtained using high purity raw materials, co-precipitation, sol gel, liquid phase sintering (Ag-addition) and optimisation of sintering conditions. Alignment of grains can be obtained using sintering in magnetic field.

1.6.1 Melt Processing

The MTG process first demonstrated the feasibility of using melt processing to align grains to overcome both the electrical anisotropy in Y-123 materials. With this technique, sintered Y-123 was partially melted at about 1100°C and then slowly cooled in a thermal gradient. The resulting microstructure showed preferred orientation for grain growth in the a-b plane and large, non uniformly distributed spherical Y-211 particles upto 40 microns in length. The connectivity of the 123 plates was not good and was attributed to nonuniform growth conditions associated with the 211 particle distribution. Although the properties were much improved over those of sintered materials, the J_c was found to drop precipitously in magnetic fields, indicating the absence of adequate flux-pinning sites in the Y-123 matrix.

After Jin's initial success with the MTG process [67-69], which enhanced J_c two or three orders of magnitude over that of sintered materials (with significantly less field dependence) a variety of melt-texturing methods were developed in an effort to further improve properties and / or facilitate processing. The most frequently applied methods include the modified MTG process, the quench-and-melt-growth (OMG) process, the melt powder-melt-growth (MPMG) process, the powder-melt process (PMP), the platinum-doped melt-growth (PDMG) process the Bridgman method and the floating-

zone-melt-process. All the above processes result in better homogeneity, high density, reduction of grain boundaries and grain alignment (discussed in later part of thesis). Pinning centres can be introduced by addition of non-superconducting phase (Y-211, Y_2O_3 , BaSrO₂, CeO₂ etc.)

Explanation of flux pinning mechanism, which should be understood with the guidance of how to control microstructures. Melt-processed YBCO with a high J_c value contains many defects which may act as pinning centres. These defects include twin planes, stacking faults, cracks, oxygen defects, dislocations and non-superconducting particles. Here, the focus was on the magnetic flux pinning mechanism of non-superconducting particles.

HTSC materials are Type-II superconductors in which external magnetic fields can penetrate below H_c . In other words, superconductivity and normal conductivity (or magnetic field) coexist. In such a `mixed state, the penetrating magnetic field is quantized and is called the fluxoid. The fluxoid has a normal conducting region at its centre and normal conductivity is transformed to superconductivity over the distance of the coherence length (ξ). The magnetic field is spread over the penetration length (λ).

In the case of the Y-123-Y-211 system, the coherence length of Y-123 is between several angstroms and several tens of angstroms [57]. Therefore Y-211 particles must be dispersed as finely as possible in Y-123 superconductors, if Y-211 particles are to be used as pinning centers. Indeed, finely dispersed Y-211 particles in Y-123 have been confirmed to contribute to increasing J_c values. However, it has not yet been clarified whether Y-211 particles act as flux pinning centers directly or indirectly because the Y-211 size is much larger than the coherence length. Several pinning mechanisms in

connection with Y-211 particles have been proposed, e.g. interfaces between Y-211 and Y-123 [58] and dislocation attacking faults around Y-211 particles [59] may be responsible for pinning sites.

At present, many applications using melt-textured YBCO are currently discussed [60]. The first demonstrators, e.g. motors, flywheels, and others, have already been built. The HTSC capability to transport electric current without any losses, together with low thermal conductivity, suggest the applications of HTSC for high current transport to low temperature SC devices such as magnets. The fault current limiter (FCL) seems to be the most promising superconducting power device that will be installed in the electric power networks. The higher levitation force of the YBCO bulk means that it can be used for various applications, such as non-contacted superconducting bearing [61], flywheel [62], magnetic levitation transport system and motors [63]. The application is mainly dependent on the physical properties of the YBCO bulk, such as levitation force and others. Although YBCO compound is one of the most widely studied superconducting materials, bulk YBCO superconductors are brittle and exhibit poor mechanical properties (strength and fracture toughness) [64]. Bulk textured Y-123 has to be considered as a brittle composite material due to the presence of micro-sized Y-211 inclusions in the Y-123 matrix. The most important problem of the superconductor materials is their poor mechanical properties. However, it can become as important if one takes into account the stresses appearing during practical service due to the mechanical action caused by magnetic and/or thermal cycling between room and liquid nitrogen temperatures [60]. These poor and unknown mechanical properties limit the performance of melt-textured YBCO in manufacture applications.

1.7 Objective of the present studies:

The objective of the present investigation is to develop viable technologies to process the brittle ceramic High temperature superconductors (HTSC) $\text{YBa}_2\text{Cu}_3\text{O}_{7-\delta}$ (**YBCO or Y-123**) into commercially exploitable forms. To achieve this objective, efforts were concentrated in areas such as synthesis of powders through different routes, detailed study of sintering and phase conversion process with time, optimizing the fabrication process to achieve highly oriented/textured poly-crystals materials to improve the critical current density (J_c) using various solidification and texturing employing Top Seeded Melt Texture Growth Technique (TSMTG).

The details of the above mentioned studies including general introduction and experimental techniques have been arranged in four different chapters of the thesis, in addition to Introduction, experimental and conclusion chapters.

1.8 Conclusion

During all these years a great advancement has been achieved in increasing the critical temperature of superconductors. Technologically these materials are very promising but problems related to its ceramics nature, suppression of critical current density (due to anisotropy, weak links, flux pinning etc.) chemical instability etc. have to be overcome for meaningful applications. However there is still a great progress about better understanding of these relationships. As fruitful as our empirical efforts to discover the ideal defect structure have been, one still has much to learn.

Chapter 2

Instrumentation and Experimental Techniques

All metals which display a resistive transition are not superconductors. Apart from zero resistance a superconductor must also display meissner effect i.e. flux exclusion. In both lossless condition and flux exclusion, charge carriers move with zero resistance by a mechanism that prevents energy absorption by scattering with normal electrons or with crystal lattice. Lossless transmission results from the pairing of superconducting charge carriers. In the following sections, the experimental set up for sample preparation, fabrication, characterization and also principles or salient features of different techniques which were utilized in the present study have been described.

As stated above, the two most characteristic properties displayed by superconductors are zero resistance and expulsion of applied magnetic field. Ambiguities and experimental artifacts can occur in each of these individuals measurements, therefore the identification of superconductivity in a new compound requires, not just careful experimentation, but also the measurement of both the phenomena. The most fundamental information required in understanding these transport and magnetic properties comes from crystal structure and chemical composition. The experimental techniques which have been used during this research work are described in this chapter. These include design and fabrication of a six side heating furnace (heating zone of 6 inch cube with an accuracy of $\pm 1^{\circ}\text{C}$ and cooling rate of $0.2\text{-}0.5^{\circ}\text{C/h}$). Low temperature (77K liquid nitrogen) critical transition temperature (T_c) measurement setup was designed and developed for multi-sample measurements in a single run. Silicon rubber molds were designed for compacting different shapes in cold isostatic press.

The iodometric titration technique used for the determination of oxygen stoichiometry has been elaborated. Critical current densities (J_c) of these samples were measured at Budapest University of Technology and Economics (BUTE), Budapest, Hungary. Other techniques such as X-ray diffraction, High temperature XRD for phase transition, phase purity and texturing, Laser particle size determination unit for particle size distribution, Orientation Imaging Microscope (OIM) for orientation mapping of the surface, Scanning Electron Microscope (SEM) for microstructural examination, Electron Probe Microscope Analyzer (EPMA) for micro structural, elemental analysis, Superconducting Quantum Interference Device (SQUID), High Resolution Transmission Electron Microscope (HRTEM) have also been discussed briefly.

2.1 Furnace fabrication

A six side furnace was designed and fabricated for processing. The melt texture growth technique, used to fabricate components of Y-123 requires a uniform hot zone of the accuracy of $\pm 1^\circ\text{C}$ and a very slow cooling rate of the order of $0.2 - 0.5^\circ\text{C}/\text{h}$. A three kilowatt box type muffle resistance furnace was designed and fabricated using kanthal wire as heating element, which can attain temperature upto 1100°C . This was connected with eurotherm programmable temperature controller model 2416, current meter and thyristor firing unit. For temperature sensing Chromel Alumel thermocouple was used. The special feature of this furnace is that it has six side heating facility, which maintains a large uniform hot zone.

2.2 Liquid nitrogen T_c measurement system

Low temperature (77K liquid nitrogen) critical transition temperature (T_c) measurement setup (Fig.2.1) was designed and developed for multi-sample measurements in a single run. For measuring T_c , standard four probe technique has been employed. A constant current is passed through the sample by Keithley make constant current source model 220, and the corresponding voltage drop was measured by Keithley make nanovoltmeter model 181. Oxford instruments temperature controller model ITC 503 was used to measure the temperature using a silicon diode sensor. A Keithley make switching device (scanner) was used to measure multiple samples which can connect one by one sample through current source, nanovoltmeter and temperature controller. All the units were connected through IEEE compatible card. The resistance Vs temperature graph was recorded on the PC. A room temperature setting silver paint was used to make the four ohmic contacts on the sample. The effect of thermal emfs nullified by reversing the current and taking the average voltage generated across the sample for the two directions of current flow. Four probe resistance Vs temperature measurements were carried out which shows enhancement of T_c for melt textured samples to 92K as compared to 90K for sintered samples.

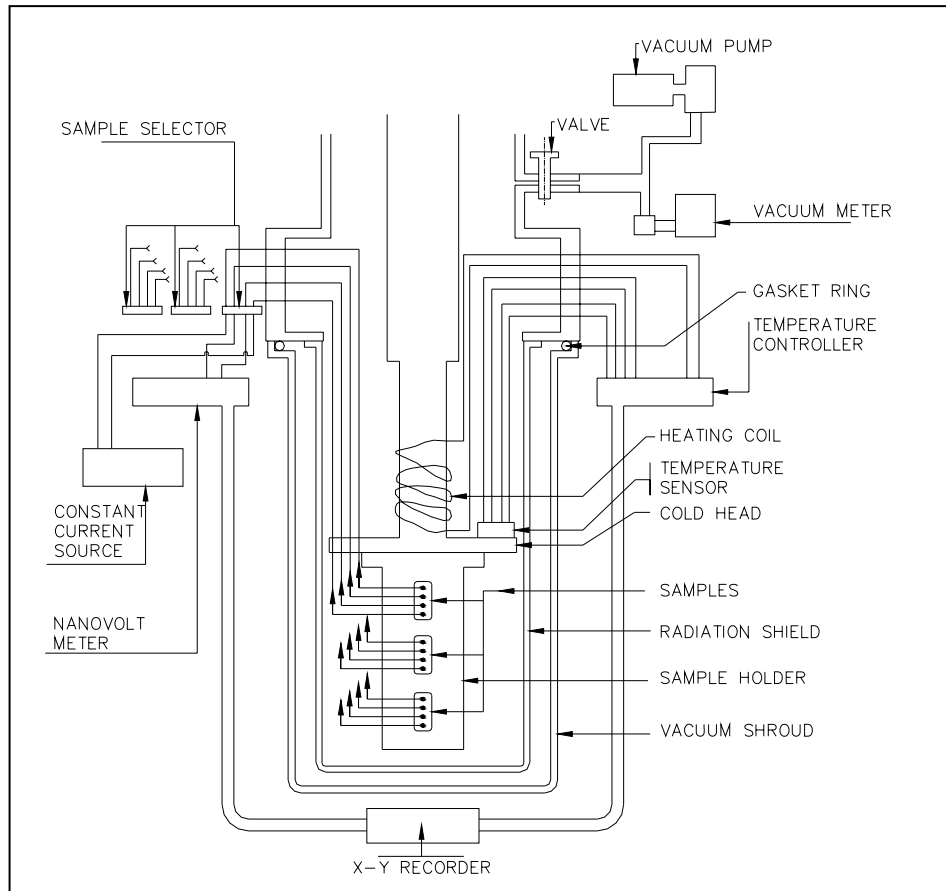


Fig.2.1 Schematic diagram of four- probe T_c measurement setup

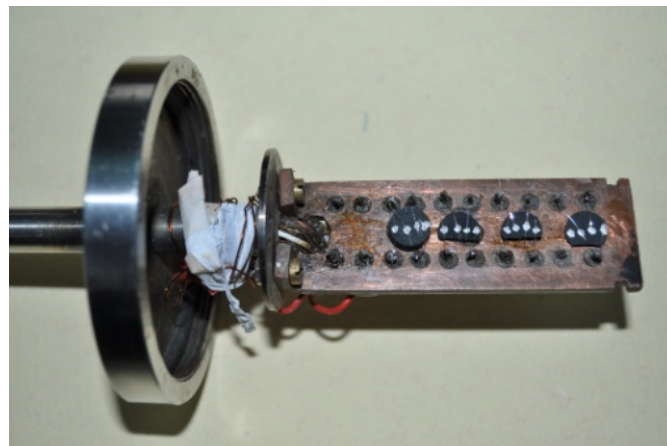


Fig.2.1a Sample holder with samples affixed for four probe T_c measurement

2.3 Compaction

Ceramics are generally characterized by a crystalline structure and an ionic bond of the atoms. The difference in the atomic bonding distinguishes them from metals, and their inorganicity from organic materials (plastics, rubbers and wood). Most ceramics are metal oxides. In general they are very stiff, hard but brittle, have low densities, high melting temperatures, high heat resistance, are electrical insulators, chemical and ageing resistant.

The following techniques are involved in forming ceramic powders into a desired shape:

- Uniaxial (Die) Pressing
- Isostatic Pressing
- Injection Molding
- Extrusion
- Slip Casting
- Gel Casting
- Tape Casting

2.3.1 Uniaxial pressing

This shaping method is inexpensive and suitable for high-volume production of simple shapes (limited geometrical possibilities) such as refractory, tiles, electronic ceramics, etc. The uniformity of compaction is not very high. Uniaxial pressing involves the compaction of powder into a rigid die by applying pressure in a single axial direction through a rigid punch or piston. The presses are usually mechanical or hydraulic. For complicated shapes, uniaxial pressing is not suitable, i.e. if the length and diameter of the

final product is more than one then the product will not have uniform density in the compact.

2.3.2 Isostatic Pressing

Isostatic pressing is a widely used process for forming and densifying powdered, cast and pre-formed materials using either high liquid pressure (Cold Isostatic Pressing), or high gas pressure at high temperature (Hot Isostatic Pressing). The resulting parts have excellent isotropic material properties and show the highest possible density of all available compaction methods.

Cold Isostatic Pressing is a process in which a powder material is filled into a flexible rubber mould having a scaled-up shape of the part (green body) to be produced. The powder is compacted in a pressure vessel under high liquid isostatic pressure (1380–4140 bar, 20,000-60,000 psi) at ambient or elevated temperature. After pressing, the resulting isotropic powder parts can normally be machined to final shape before firing, sintering, hot extrusion or hot isostatic pressing to final high density.

The cold isostatic pressing (CIP) method has the following advantages as compared to the die cold pressing method:

- Better uniformity of compaction;
- More complex forms (for example long thin-walled tubes) may be compacted.

For our material we have used CIP for pressing. A schematic drawing of CIP has been depicted in Fig 2.2. A silicon rubber material is used to fabricate the mould. Other techniques require surfactant, binders, in the form of liquid, which are suitable for pressing of our materials.

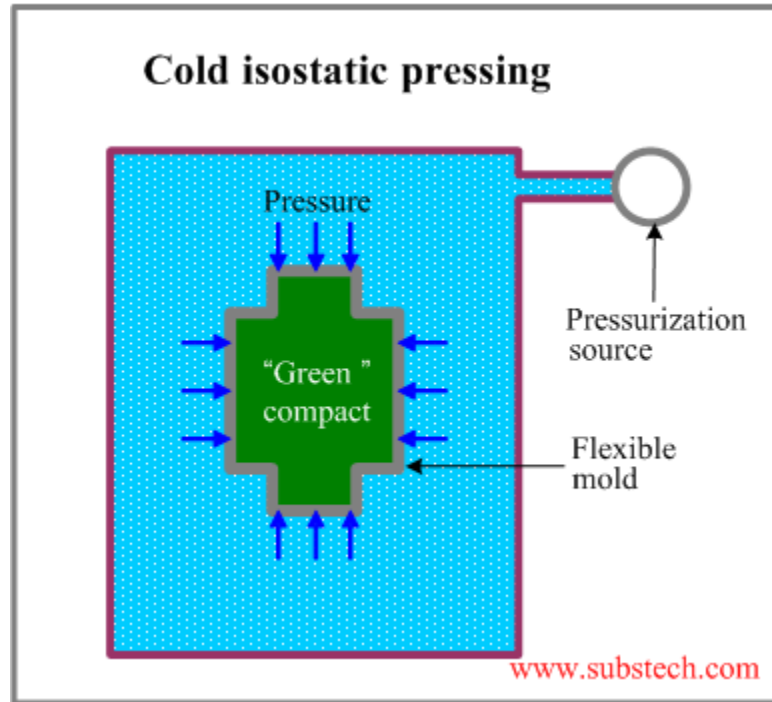


Fig.2.2 A schematic drawing of Cold isostatic press

2.3.2.1 Compaction studies

The aim of the current work has been to fabricate samples of large size with uniform density in the compact, and therefore the compaction was carried out using cold isostatic press. The composites (Y-123 + Y-211+ Ag, Y-123 + yttria + Pt, Y-123 + yttria + ceria) were mixed in zirconia pot, using zirconia balls and acetone as wet media in Fritsch make planetary ball mill. Before filling the mixed powder in rubber mould the powder was granulated i.e. they were first compacted at low pressure of 400 bar and then crushed and sieved. The mould was made of silicone rubber, The moulds were fabricated in a way so that they will result in the finished product or component of required dimensions accounting for shrinkage during the following three stage processing :-

i) During cold isotatic pressing, ii) while sintering and iii) finally shrinkage during MTG process. The granulated powder was filled in the rubber mould and placed inside the CIP vessel which contained water for isotatic pressing. The pressure applied was optimized to get dense and lamination free compacts and was in the range of 3000-3500 bar depending upon the shape and size of the specimen.

2.4 Particle size distribution

Particle size of the initial powder before mixing in the form of composite is very important, which plays a crucial role in the fabrication process. The effect of particle size on the superconducting properties like enhancing the critical current density (J_c) is discussed in detail in chapter 6. In general J_c increases with decrease in Y-211 particle size.

Particle size was measured by laser scattering method: Particle size analysis of the suspended powder sample was carried out in a MASTER SIZER-2000 (Malvern, UK) particle size distribution measurement unit. In this experiment, a dilute suspension (1 vol%) was prepared by ultrasonic agitation of the powder in aqueous medium. Calgon (sodium hexametaphosphate) was used as the dispersing agent during suspension preparation. The instrument works on the principle of general light scattering proposed by Mie [80]. According to this theory, for larger particles, the scattering is proportional to the square of the diameter and for small particles to the sixth power. Therefore, the scattering angle for small particles will be large. In order cover the measurement range of the particle size from 0.1 to 1000 μm , a helium-neon laser has been used as the monochromatic light to be scattered. The detectors are placed at different angles to record

the scattered light intensity. The particle size of the synthesized powders were found to be in the range of 4-15 microns.

2.5 X-ray diffraction

The X-ray diffractometer (XRD) (Diano USA Model 2000 series make) using Cu-K α radiation was used for XRD analysis. Analysis for crystallographic structure determination in principle is based on the Bragg's law of diffraction.

$$n \lambda = 2d \sin \theta \longrightarrow (2.1)$$

Eq. (2.1) relates to the 'd' spacing (Å) between the (hkl) planes of the lattice and the glancing angle 'θ' of the monochromatic beam of X-ray of wavelength (λ). The positions (2θ) of the diffraction peaks depend on the dimensions and geometry of the unit cell, while the relative intensities (I/I₀) depend on the way specific atoms are arranged at the lattice sites. The detection limit (for a phase) is normally 2-5 wt %. The intensity component due to the Cu-K β radiation was suppressed by using a graphite monochromator with the instrument. Standard silicon sample, supplied by the manufacturer was employed as a standard for calibration.

XRD of powder (sintered pellet) of Y-123 and Y-211 calcined powder reveals phase purity, XRD analysis of TSMTG sample reveals that the sample was highly textured in (001) planes.

High temperature XRD : A platinum strip was used as heating element and the sample was heated to 900°C and slowly cooled to room temperature, XRD data collection was carried out at intervals of 50 °C from 900 °C to 350 °C at a scanning speed of 1°C /min.

2.6 Morphology and compaction characterization

When a finely focused electron beam interacts with the matter mainly three phenomena occur, back scattering of electrons transmission of electrons, and emission of characteristic X-rays, Cathode luminescence and absorption of electrons also occur during the interaction of primary electrons with the matter. The various interactions of electron beam with the specimen is shown in Fig. 2.3 on which the various techniques like SEM, EPMA and TEM etc are based.

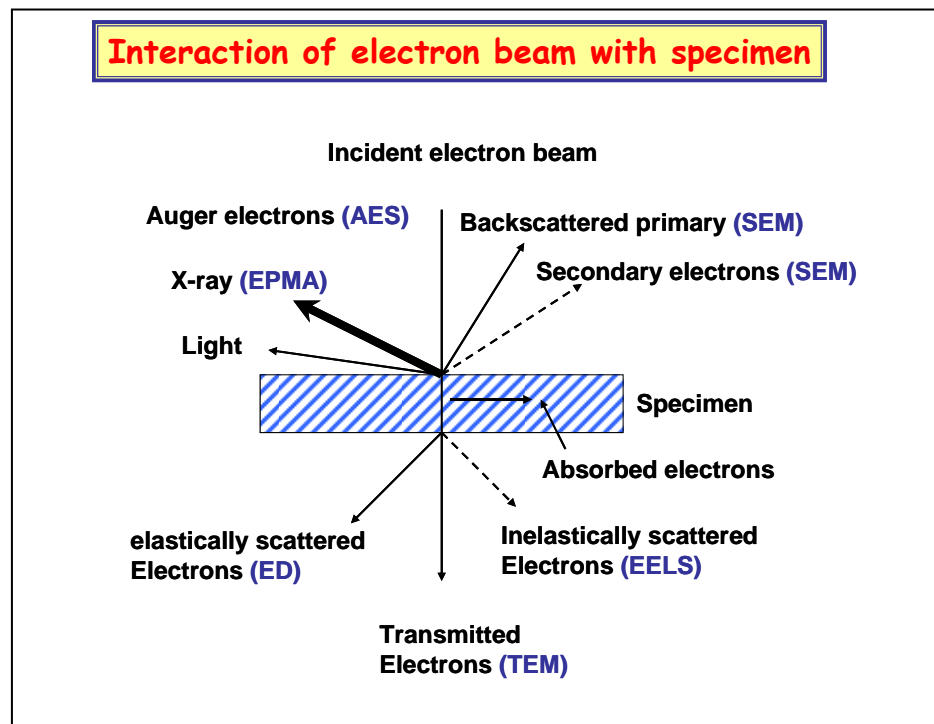


Fig.2.3 Schematic drawing of the various interactions of electron beam

2.6.1 Scanning electron microscope

A scanning electron microscope (SEM) is a type of electron microscope that images a sample by scanning it with a high-energy beam of electrons in a raster scan

pattern. The electrons interact with the atoms that make up the sample producing signals that contain information about the sample's surface topography, composition, and other properties such as electrical conductivity. The types of signals produced by an SEM include secondary electrons, back-scattered electrons (BSE), characteristic X-rays, light (cathodoluminescence), specimen current and transmitted electrons. Secondary electron detectors are common in all SEMs, but it is rare that a single machine would have detectors for all possible signals. The signals result from interactions of the electron beam with atoms at or near the surface of the sample. In the most common or standard detection mode, secondary electron imaging (SEI), the SEM can produce very high-resolution images of a sample surface, revealing details less than 1 nm in size. Due to the very narrow electron beam, SEM micrographs have a large depth of field yielding a characteristic three-dimensional appearance useful for understanding the surface structure of a sample. A wide range of magnifications is possible, from about 10 times (about equivalent to that of a powerful hand-lens) to more than 500,000 times, about 250 times the magnification limit of the best light microscopes. Back-scattered electrons (BSE) are beam electrons that are reflected from the sample by elastic scattering. BSE are often used in analytical SEM along with the spectra made from the characteristic X-rays. Because the intensity of the BSE signal is strongly related to the atomic number (Z) of the specimen, BSE images can provide information about the distribution of different elements in the sample. For the same reason, BSE imaging can image colloidal gold immune-labels of 5 or 10 nm diameter which would otherwise be difficult or impossible to detect in secondary electron images in biological specimens. Characteristic X-rays are emitted when the electron beam removes an inner shell electron from the sample, causing

a higher energy electron to fill the shell and release energy. These characteristic X-rays are used to identify the composition and measure the abundance of elements in the sample.

In a typical SEM an electron beam is thermoionically emitted from an electron gun fitted with a tungsten filament cathode. Tungsten is normally used in thermionic electron guns because it has the highest melting point and lowest vapor pressure of all metals, thereby allowing it to be heated for electron emission, and because of its low cost. Other types of electron emitters include lanthanum hexaboride (LaB₆) cathodes, which can be used in a standard tungsten filament SEM if the vacuum systems is upgraded and field emission guns (FEG), which may be of the cold-cathode type using tungsten single crystal emitters or the thermally-assisted Schottky type using emitters of zirconium oxide. The electron beam, which typically has an energy ranging from 0.5 keV to 40 keV is focused by one or two condenser lenses (as shown in Fig.2.4) to a spot about 0.4nm to 5 nm in diameter. The beam passes through pairs of scanning coils or pairs of deflector plates on the electron column, typically in the final lens, which deflect the beam in the x and y axes so that it scans in a raster fashion over a rectangular area of the sample surface.

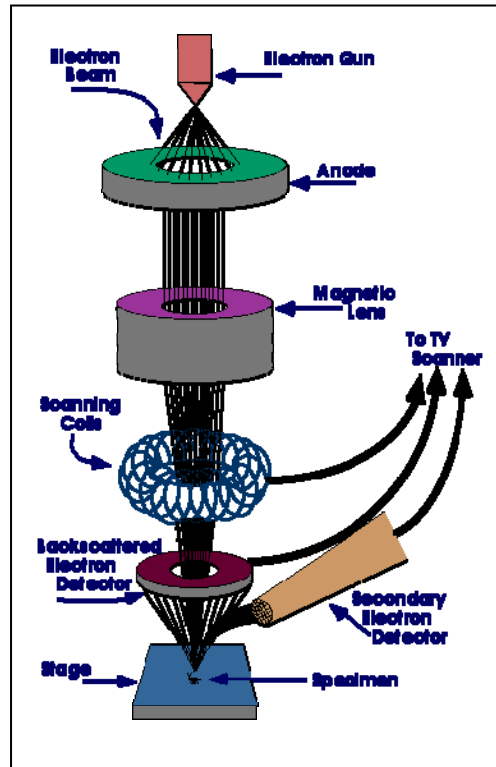


Fig.2.4 Schematic diagram of an SEM
 (source <http://www.purdue.edu/rem/rs/graphics/sem2.gif>)

When the primary electron beam interacts with the sample, the electrons lose energy by repeated random scattering and absorption within a teardrop-shaped volume of the specimen known as the interaction volume, which extends from less than 100nm to around 5nm into the surface. The size of the interaction volume depends on the electron's landing energy, the atomic number of the specimen and the specimen's density. The energy exchange between the electron beam and the sample results in the reflection of high energy electrons by elastic scattering, emission of secondary electrons by inelastic scattering and the emission of electromagnetic radiation, each of which can be detected by specialized detectors. The beam current absorbed by the specimen can also be detected and used to create images of the distribution of specimen current. Electronic

amplifiers of various types are used to amplify the signals which are displayed as variations in brightness on a cathode ray tube. The raster scanning of the CRT display is synchronized with that of the beam on the specimen in the microscope, and the resulting image is therefore a distribution map of the intensity of the signal being emitted from the scanned area of the specimen. The image may be captured by photography from a high resolution cathode ray tube, but in modern machines it is digitally captured and displayed on a computer monitor and saved to a computer's hard disk. Resolution is the ability to resolve two closely spaced points. Resolution is NOT the same as magnification. One way to improve resolution is by reducing the size of the electron beam that strikes the sample. Resolution can also be improved by

- Increasing the strength of the condenser lens
- decreasing the size of the objective aperture
- decreasing the working distance (WD = the distance of the sample from the objective lens).

Depending on the instrument, the resolution can fall somewhere between less than 1nm and 20nm. The world's highest SEM resolution at high beam energies (0.4nm at 30kV) is obtained with the Hitachi S-5500. At low beam energies, the best resolution (by 2009) is achieved by the Magellan XHR system from FEI Company (0.9nm at 1kV).

SEM gives information about

Topography: The surface features of an object on “how it looks”, its texture, direct relation between these features and materials properties.

Morphology: The shape and size of the particles making up the object direct relation between these structures and materials properties.

Composition: The elements and compounds that the object is composed of and the relative amounts of them; direct relationship between composition and materials properties.

Crystallographic Information: How the atoms are arranged in the object” direct relation between these arrangements and material projects.

2.6.2 Energy dispersive X-ray spectrometry

Energy-dispersive X-ray spectrometry (EDS or EDX) is an analytical technique used for the elemental analysis or chemical characterization of a sample. It is one of the variants of X-ray fluorescence spectroscopy which relies on the investigation of a sample through interactions between electromagnetic radiation and matter, analyzing X-rays emitted by the matter in response to being hit with charged particles. Its characterization capabilities are due to large part of the fundamental principle that each element has a unique atomic structure allowing X-rays that are characteristic of an element’s atomic structure to be identified uniquely from one another.

To stimulate the emission of characteristic X-rays from a specimen, a high-energy beam of charged particles such as electrons or protons, or a beam of X-rays, is focused into the sample being studied. At rest, an atom within the sample contains ground state (or unexcited electrons in discrete energy levels or electron shells bound to the nucleus). The incident beam may excite an electron to an inner shell, ejecting it from the shell while creating an electron hole where the electron was. An electron from an outer, higher-energy shell then fills the hole, and the difference in energy between the higher-energy shell and the lower energy shell may be released in the form of X-ray. The

number and energy of the X-rays emitted from a specimen can be measured by an energy-dispersive spectrometer. As the energy of the X-rays are characteristic of the difference in energy between the two shells, and of the atomic structure of the element from which they were emitted, this allows the elemental composition of the specimen to be measured. There are four primary components of the EDS setup the beam source, the X-ray detector, the pulse processor and the analyzer. A number of free-standing EDS systems exist. However, EDS systems are most commonly found on scanning electron microscopes (SEM-EDS) and electron microprobes. Scanning electron microscopes are equipped with a cathode and magnetic lenses to create and focus a beam of electrons, and since the 1960s they have been equipped with elemental analysis capabilities. A detector is used to convert X-ray energy into voltage signals, this information is sent to a pulse processor, which measures the signals and passes them onto an analyzer for data display and analysis.

SEM (SERON Inc, Korea, Model: AIS2100) was used to examine the morphology of the porous samples at different magnifications. The microstructure was revealed in the samples. For chemical composition determination the EDS (Oxford Instruments, UK Model No: INCA E350) was used in the present studies. As the carbon samples are conducting there was no specific requirement of giving any conductive coating to the samples.

As the samples were conducting in nature there was no specific requirement of giving any conductive coating to the samples. The SEM analysis was carried out on sintered samples and MTG samples. The Scanning Electron Microscope (SEM) images of TSMTG fabricated sample using initial precursor of solid state route (initial powder

average particle size 10-15 microns) show Y-211 particles of 15-20 microns range. The SEM image of TSMTG fabricated sample using nitrate decomposition powder (initial powder average particle size microns) show Y-211 particles of 3-5 microns range dispersed in the matrix of YBCO.

2.6.3 Electron Probe Micro-Analyzer (EPMA)

The electron microprobe analyzer uses a focused beam of electrons to locally excite X-rays from a region as small as a few micrometers or less on a specimen. The schematic of the instrument is shown in Fig 2.5. The heated tungsten filament of an electron gun serves as a source of electrons. They are given energy of 5-30 keV by applying a potential difference between the filament (cathode) and the anode which is grounded. The grid cap of the electron gun is connected to the filament by means of a variable-bias resistor. The probe size is in the range of 0.1-1.0 μm with corresponding currents in the range of about 10 -1000 nA.

When the electron beam strikes the sample the vast majority of the energy is dissipated thermally. In an incident beam of energy E_0 on interacting with solid specimen produces a wide variety of emissions. It can be in the form of characteristic X-ray emission or ejection of an Auger electron or back scattered electrons or secondary electrons.

X-ray photons are produced following the ejection of an inner orbital electron from an excited atom and subsequent transition of atomic orbital electron from states of high to low energy. The beam of radiation emerging from the absorber has an intensity

distribution across the irradiation area of the specimen, which is related to the average atomic number distribution across the same area.

Characteristic radiation: When a high energy electron beam is incident upon a specimen, X-ray photons are emitted which have energy proportional to the difference in energy states of atomic electrons. Thus the spectral lines from a given element will be characteristic of that element. This can be illustrated through Moseley's law which uniquely relates the wavelength of each observed spectral line to a specific element through the relationship:

$$1/\lambda = k (Z-\sigma)^{1/2}$$

where λ is the X-ray wavelength, k is a constant for each spectral line series, Z is the atomic number of the element from which the X-rays originate and σ is a constant associated with the atomic screening effects. Isolation of individual characteristic line allows the unique identification of an element to be made and elemental concentration can be estimated from characteristic line intensities. Thus it is possible to can obtain both qualitative and quantitative analysis.

Electron Probe Micro-Analyzer

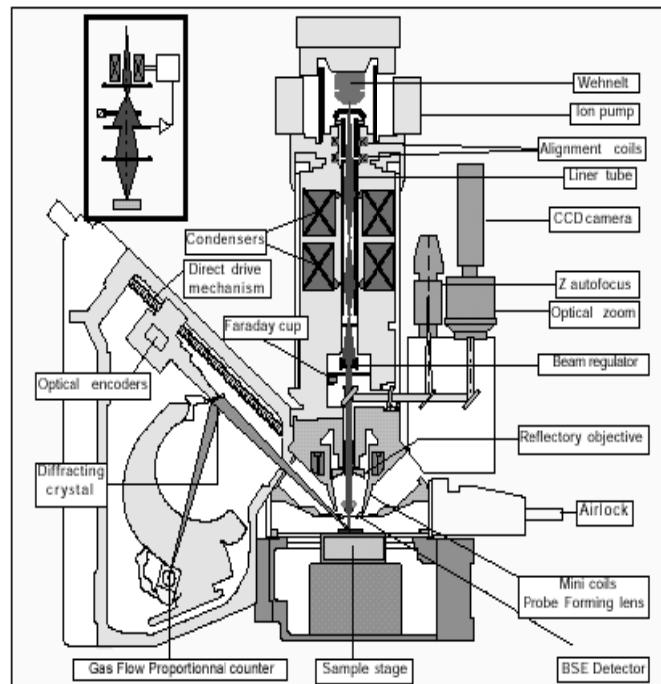


Fig.2.5 Schematic of EPMA system

Continuous radiation: When a high energy electron beam is incident upon a specimen, in addition to characteristic lines, an emission of a broad wavelength band of radiation called continuum or continuous radiation or white radiation also occurs. These are the principal source of back ground radiation

Back-scattered electrons: These are incident electrons that have been scattered through such large angles within the sample that they emerge traveling in the opposite direction to the one from which they arrived. The average energy of the back-scattered electrons are 0.5 to 0.6 E_0 .

Secondary electrons: These are electrons produced by a variety of inelastic scattering processes within the sample. The average energy of the secondary electrons is

0 to 50 eV. They are very surface specific as they can travel only a few nanometers. Thus they are the most popular choice of interaction with which to form image.

X-ray analysis: In the EPMA X-ray spectral measurements are principally performed using the crystal-diffraction spectrometers (CDS). Energy dispersive spectrometers are also used. The basic components of CDS include an analyzing crystal, a detector and read out electronics. Different crystals can be used in the CDS to detect almost all the elements from Beryllium onwards. The following table gives the composition, the inter-planar spacing and the elements, which can be detected using the different crystals.

The X-ray detector most commonly used on the CDS is a proportional counter as illustrated in the Fig.2.6. The detector is filled with a mixture of an inert gas and a small percentage of methane. X-rays from the analyzing crystal enter through a thin window mounted on the side or end of the metal tube. For soft x-rays argon is the most commonly used inert gas fill with a thin-film polymer window. A sealed beryllium window proportional counter containing either krypton or xenon is used for detection of harder x-rays.

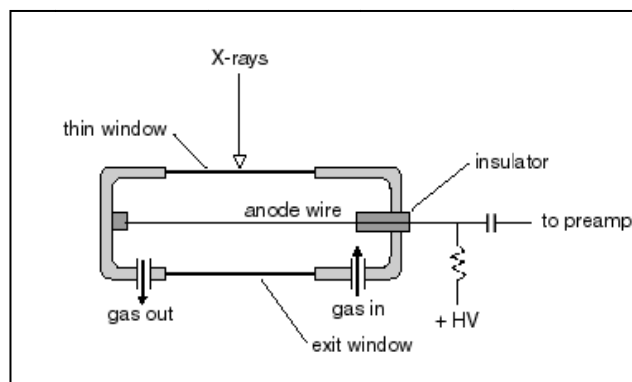


Fig.2.6 Schematic of proportional counter detector of EPMA system

By biasing the detector to a modest positive potential it can attract these electrons to itself even though they are low in energy. The detector is based on a disc of scintillator which emits light under the impact of electrons. The light travels along a light pipe, through a vacuum window and into a photomultiplier.

Imaging:

Topographic contrast: Increase in θ , the angle of incidence between the beam and surface normal will lead to an increase in the yield of secondary electrons. If an electron beam moves over a surface, which has topography then the local angle of incidence and surface normal will change and produce a corresponding change in the secondary signal. When the sample has a rough surface or significant surface topography, then it results in an image containing pronounced light and shadow effects. Faces at a high angle of inclination to the beam will be darker whereas those that are facing the light will be brighter.

Voltage contrast: Surfaces at different potentials produce images of different brightness. The collection field from the detector to the negatively charged area is increased while the corresponding field to the positively charged area is reduced. The region that has a negative potential will repel the secondary electrons emitted from it but the positively charged area will attract and recollect some of the secondary electrons emitted from it. Thus, positively biased strip will appear dark while the negatively biased strip will be bright. EPMA images and corresponding elemental mapping show particle size distribution of Y-211 phase in the matrix of YBCO. These experiments also reveal the line profile of the variation of individual elements from matrix of Y-123

(superconducting) and Y-211 (non-superconducting) phases. The line profile shows the sudden discrete variation in the atomic percentage corresponding to Y, Cu and Ba.

2.6.4 Transmission electron microscope (TEM)

The Transmission Electron Microscope (TEM) is used to study samples at extremely high magnifications. It probes the internal structure of solids and gives us access to microstructure. This allows for a more detailed study of samples that are at or beyond the resolution of the light microscope or SEM. The TEM provides both morphological information through imaging and structural information through electron diffraction.

In TEM the sample is placed on grid. The grid is then placed into the TEM through an airlock and bombarded with a focused electron beam. The instrument of transmission electron microscope is shown in Fig. 2.7. As may be noticed, a typical TEM has three sections.

1. Illumination system. It takes the electrons from the gun and transfers them to the specimen giving either a broad beam or a focused beam. In Fig. 2.7, the parts above the specimen belong to illumination system.
2. The objective lens and stage.
3. The TEM imaging system. It includes the intermediate lens and projector lens.

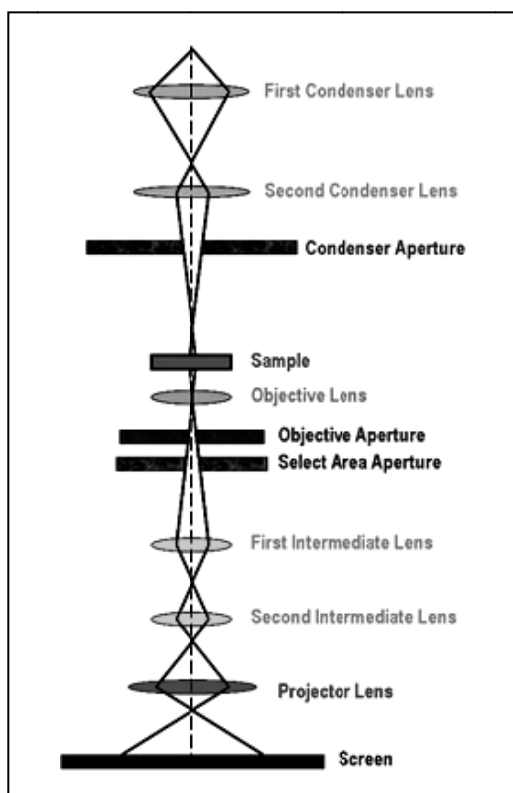


Fig. 2.7 The schematic diagram of a transmission electron microscope

The diffraction pattern and image of the object are formed at back focus plane and image plane of the objective lens respectively. By focusing the intermediate lens and projector lens on the back focus plane of the objective lens, a diffraction pattern is obtained on the screen. It is known as the diffraction mode. By focusing the intermediate lens and projector lens on the image plane of the objective lens, image is obtained on the screen. It is the image mode. These operations in a modern TEM are carried out by pressing a single button, as computer attached has pre-recorded values of current, which changes the focal length of these lenses suitably to toggle between these two modes.

A TEM (JEOL 2000 FX TEM located at BARC) operated at 160 KV was used to study the microstructure. Selected area electron diffraction patterns (SAEDP) were

analyzed for phase identification. Bright field (BF) and dark field (DF) images were obtained to understand the morphology of phases.

Sample preparation: Powder of samples were suspended in high purity methanol. 15 minutes of sonication was carried out to produce a uniform suspension and few drops from this suspended medium were put on carbon 3 mm carbon coated copper grid with 200 mesh size. Samples were dried under a vacuum chamber and subsequently examined under electron microscope Techani F-30.

2.6.5 Orientation Imaging Microscope (OIM)

1. Electron Diffraction in an SEM
2. System Configuration and Operation
3. Visualization of the Microstructure

2.6.5.1 Electron Diffraction in an SEM

When the beam of a Scanning Electron Microscope (SEM) strikes a crystalline material mounted at an incline around 70° , the electrons disperse beneath the surface, subsequently diffracting among the crystallographic planes. The diffracted beam produces a pattern composed of intersecting bands, termed electron backscatter patterns, or EBSPs. The patterns can be imaged by placing a suitable film or phosphor screen in close proximity to the sample in the SEM sample chamber.

An example of such a pattern is shown here (Fig. 2.9). The bands in the pattern are referred to as Kikuchi bands and are directly related to the crystal lattice structure in the sampled region.

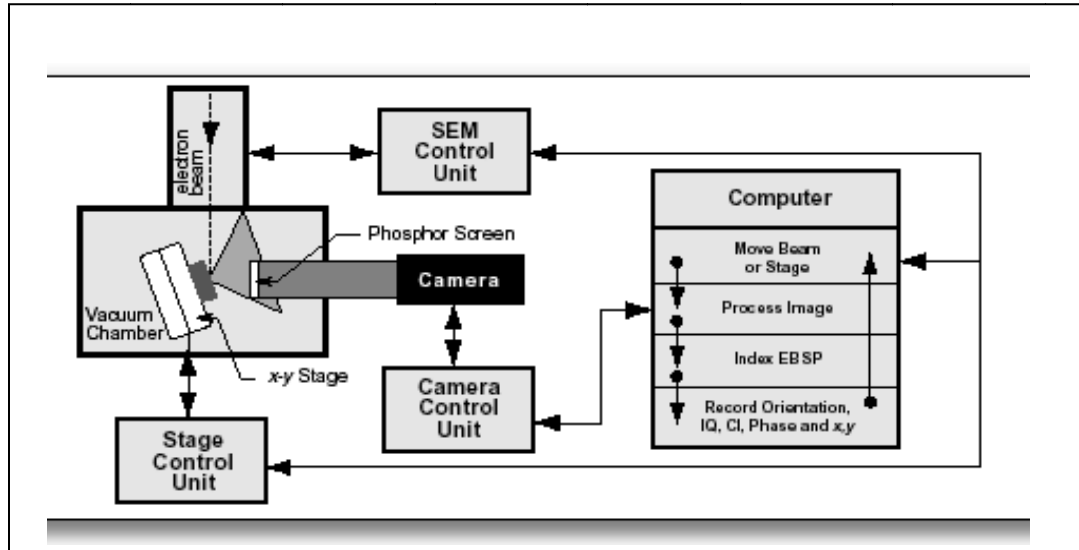


Fig.2.8 Schematic of OIM

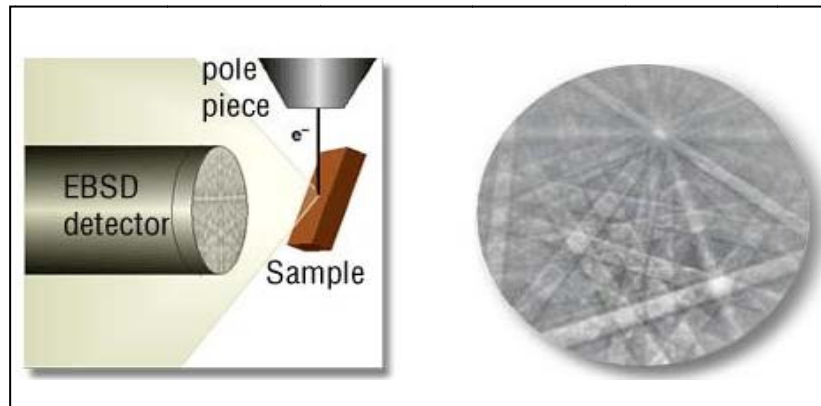


Fig. 2.9 Typical setup of EBSD with Kikuchi bands

The core that goes on in EBSD is "indexing" the pattern. If the sample produces good diffraction patterns, getting the proper indexing is a process of:

1. Locating the bands
2. Determining the angles between the bands
3. Comparing the angles to theoretical values
4. Determining the phase

This technique allows microstructural phase and crystal orientation information to be determined at very specific points in a sample. The spatial resolution varies with the accelerating voltage, beam current, and spot size of the SEM along with the atomic number of the sample material. Indexable patterns can be obtained from about 0.05 microns with a field emission source.

The most difficult part of indexing was the identification of Kikuchi bands. Their locations were usually determined by an operator tediously locating and drawing the lines on an image. Variations in image intensity, background, pattern quality, etc., frustrated most attempts to automate band identification with image-analysis techniques until the Hough transform was applied to the process.

Basically, the Hough transform converts bands in an image to points in Hough space, which are subsequently easier to identify and localize in an image using software. In the images below (Fig.2.10), the color-coded Kikuchi bands in the right image have been identified from the same colored peaks in the Hough space image shown to the left.

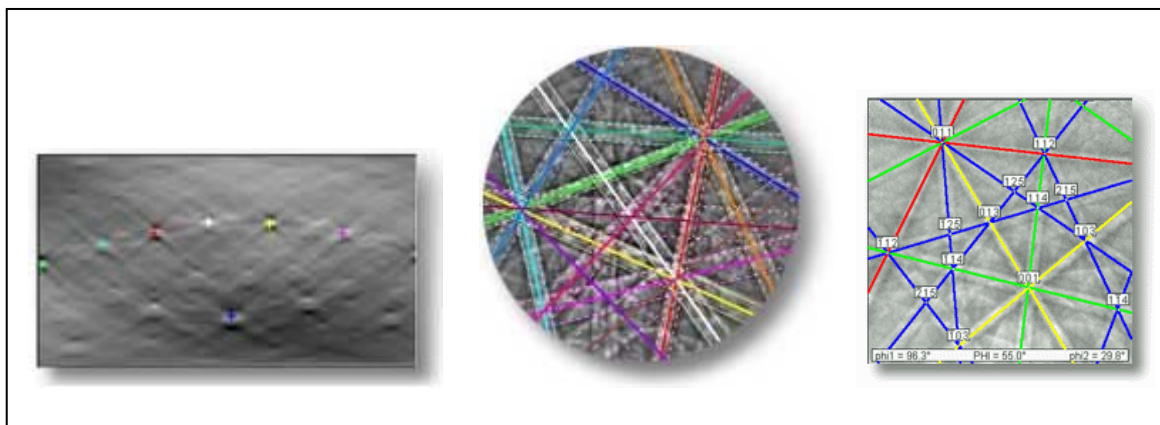


Fig.2.10 Kikuchi bands and corresponding indexing patterns

Once the bands have been identified, the next step, determining the angles between the bands, is pretty much straight math. The subsequent process, which determines the actual indexing, involves comparing the information derived from the Kikuchi bands to the theoretical values for reflectors in known phase reference tables.

2.6.5.2 System Configuration and Operation

For modern, automated EBSD mapping and phase identification applications, the (Fig. 2.8) majority of commercial systems place a specially coated phosphor screen inside the specimen chamber, in close proximity to the sample.

A camera is mounted on the SEM and images the phosphor screen. The electron beam is focused on a particular point of interest in the sample. The interaction of the beam and the microstructure results in an EBSD image forming on the phosphor screen, which is captured by the camera and then further processed. Depending on the system, the image is typically adjusted for background effects using either a dedicated signal processor or PC software. Ultimately, a digital image of the Kikuchi bands is present in the computer for indexing.

In OIM mapping, a variety of data and parameters are calculated and recorded, including the orientation of the crystal, a quality factor defining the sharpness of the diffraction pattern (IQ), the "confidence index" (CI – patented by TSL) indicating the degree of confidence that the orientation calculation is correct, rough data, the phase of the material, and the location (in x,y coordinates) where the data was obtained on the specimen, etc.

2.6.5.3 Visualization of the Microstructure

The stored data (location, orientation, image quality, confidence index, and phase) can be processed to create Orientation Imaging Micrographs, enabling a visual representation of the crystallographic microstructure. Each point can be assigned a color or gray scale value based on a variety of parameters such as orientation, image quality, confidence index, phase, etc.

For example, an orientation map is generated by shading each point in the OIM scan according to some parameter reflecting the crystallographic rotation. The map below and left is an Inverse Pole Figure (IPF) map (Fig.2.11) in which the colors correspond to the crystal orientations as shown in the projection. Crystals with their 111 axis normal to the surface of the sample will be blue, and so on.



Fig. 2.11. Inverse pole figure mapping

A grain boundary map can be generated by comparing the orientation between each pair of neighboring points in an OIM scan. A line is drawn separating a pair of points if the difference in orientation between the points exceeds a given tolerance angle. The map below shows grain boundaries color coded according to the ranges given in the key to the right.

The OIM micrograph is based upon 30,000 local orientation measurements. The underlying determinant of resolution of the crack in the OIM micrograph is the spatial scale of the OIM data. The OIM micrograph accurately reproduces the features visible in the optical micrograph, but contains inherently greater crystallographic detail. The OIM micrograph is based upon quantitative and spatially specific crystallographic data, which can be manipulated and displayed according to the research interests of the scientist.

Images of OIM that have been captured have been shown in chapter 6 shows Y-211 particle distributed in the matrix of YBCO and the color coding shows that all red color in the matrix are 001 oriented YBCO and the green color corresponds to Y-211 phase, which is randomly oriented. This OIM orientation is in corroboration with XRD analysis where the pattern shows all the peaks corresponds to 001 oriented plane.

2.7 Magnetic measurements

2.7.1 SQUID magnetometer

Magnetization measurements presented in this thesis were carried out on Superconducting Quantum Interference Device (SQUID) magnetometer (Quantum Design's (QD) Magnetic Property Measurement System (MPMS) equipped with a superconducting magnet capable of generating a magnetic field upto 5.5 Tesla. The superconducting magnet is a high homogeneity notch solenoid made of NbTi superconducting wire with a field uniformity of 1 in 10000 in a 1 cm diameter spherical volume (dsv). Processes like charging the magnet to desired value without overshoot (especially important for measurements on superconductors), persistent switch for better temporal stability of the magnetic field and SQUID noise reduction are incorporated in

the system [84]. Measurement scan be carried out from room temperature down to 2.25 K and the temperature control system of MPMS is a excellent integration of Sample chamber heater, Gas heater, Helium reservoir, two thermometers (Germanium for 2-40 K, Platinum for above 40 K) and the pumping system giving on overall accuracy of 0.5% of the set target temperature.

A magnetic moment measurement in an MPMS SQUID magnetometer involves scanning a sample through a second order gradiometer pick up coil over few centimetres distance called scan length, in uniform applied field. A schematic of this is shown in Fig. 2.13. The pickup coil coupled to a SQUID sensor through a step down transformer is shown in Fig. 2.13. A current proportional to the magnetic flux (due to the magnetic moment) linked to the pickup coil is induced in the loop which is detected by the SQUID sensor by an RF biased tank circuit. The magnetic flux linked to the pickup coil as a function of the position of a unit magnetic dipole moment is given by [85].

Superconducting Quantum Interference Device (SQUID) :- A superconducting loop with single Josephson junction generally referred as RF SQUID is used in the MPMS magnetometers. It is able to resolve a flux change of the order $\sim 10^{-10}$ G.

The pickup coil is placed symmetrically with respect to the magnet. Ideally, the SQUID response of a dipole moment is given by

$$V(z) = c\phi(z) \longrightarrow (1.21)$$

Where the c is the calibration factor of the instrument. However, a constant offset a and a linear drift bz are usually present, which modify the SQUID response into the form

$$V^{\text{modified}}(z) = a + bz + mV(z-z_0) \longrightarrow (1.22)$$

here z_0 is correction for off centring of the sample. The measured SQUID response (output of the tank circuit) is fitted to the above expression by the MPMS software to obtain the magnetic moment.

The pickup coil, positioned symmetrically with respect to the superconducting magnet, is coupled to the SQUID through a superconducting isolation transformer with a heater to drive the superconducting primary and secondary loops of the transformer normal thereby destroying the memory of previous measurements. This heater is switched on during the charging of the superconducting magnet preceding each measurement scan to eliminate the persistent currents induced in the circuit. The heater is switched off during the measurement. The inset of Fig. 2.13 shows a typical SQUID voltage response as a function of the sample position.

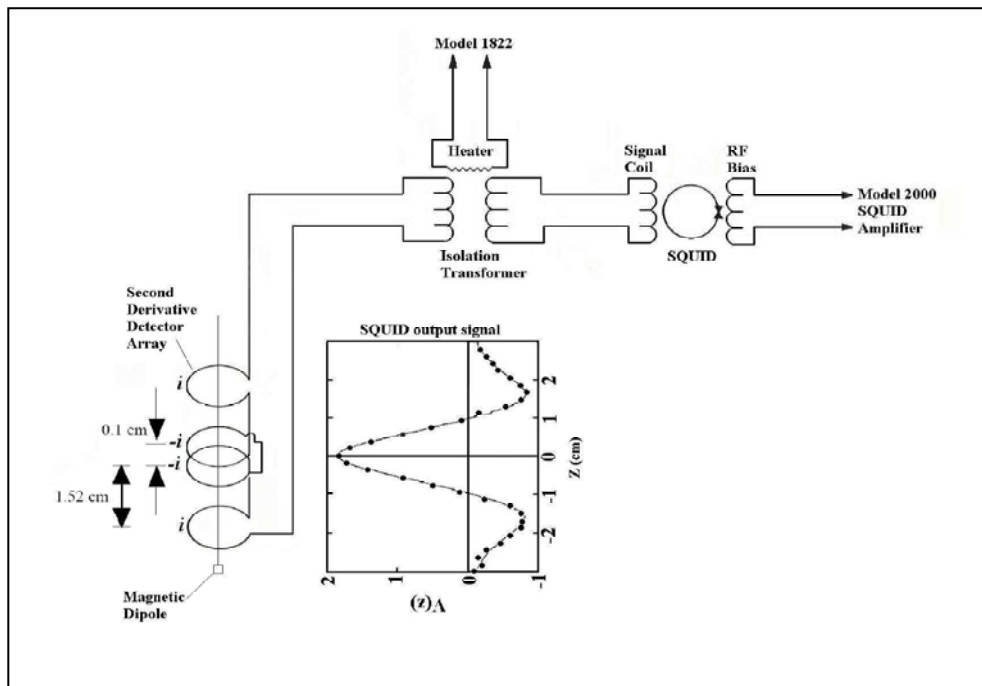


Fig.2.13 Magnetic measurement in SQUID

2.7.2 Trapped magnetic field and Levitation force measurement system

It is not easy to characterize these relatively large superconductors by conventional methods such as transport current density measurement. These methods are not only destructive but also applicable only to small samples. In this thesis, an automatic system was developed to characterize the levitation force and trapped magnetic field of large samples in a relatively short period. Fig. 2.14 shows the combined unit of trapped magnetic field and levitation force measurement system.

The setup for mapping trapped magnetic field in bulk MTG samples is depicted schematically in Fig. 2.16. The setup consists of a cryogenic Hall probe connected to a Gauss meter (FW Bell make model 7010, with magnetic field sensitivity of 0.1 G) with a spot of area 0.2 mm^2 and a motorized X-Y stage. Gauss meter and XY stepper motors are automated through PC. A magnetizing system (Fig. 2.15) which has permanent magnet of opposite field, has a capacity of 1T in a gap of 2 inch, the components are kept in the gap for magnetization. Once the sample is field cooled to 77 K in a magnetic field of 1 T, it is quickly placed inside the liquid nitrogen bath mounted on the X-Y automated stage. The probe is then positioned on top of the sample with a gap of less than 0.5 mm. During the measurement, the sample on the XY stage is moved step by step and the hall probe generates a signal which is proportional to the trapped magnetic field and detected by gauss meter. An automated data acquisition system continuously measures the signal from the gauss meter and simultaneously measures the XY parameter from the XY motorized stage. The XY parameter is plotted in X and Y axis and the field is plotted on the Z axis. All the data is stored and displayed online on the computer at a regular intervals of 3 seconds. The resolution of the X-Y stepper motor is 0.005mm. The user

has options to change the sample name, step size, and scanning range. A typical scanning route is depicted in Fig.2.17. For a sample size of 25 x 25 mm rectangular, the whole scanning process takes 90-120 min depending upon the step size used. Usually a step size of 0.5 mm is adequate to generate an accurate profile.

2.7.3 The levitation force measurement system

In this case, a highly sensitive force gauge (Mecmesin model AFG50N) with Nd-B-Fe permanent magnet 25 mm dia x 12 mm thick, surface field 0.4 T is attached to a Z-motor. The whole attachment moves along vertical axis with fine resolution. Before the measurement begins, the MTG sample is clamped inside the liquid nitrogen bath and cooled down to 77K in the absence of magnetic field. The permanent magnet is then moved down at a step size of 0.2 mm from a distance of about 30 mm from the sample to a distance very close to sample surface. At each point, the force vs distance data is recorded and displayed online on the computer. The whole process has a duration of 5 minutes for a typical 30 mm travel distance. The plates were cooled down to liquid nitrogen temperature 77K and using a highly sensitive strain gauge connected to a SmCo magnet which was used for measurement. The magnet was moved downwards and away from the superconductor zero field cooled condition and since the sample is perfect diamagnetic it repels the magnet. This force is measured against the distance from the magnet. The distance Vs force was plotted. The maximum force achieved in MTG sample was found to be 25 N.



Fig.2.14 Trapped magnetic field and levitation force measurement system



Fig.2.15 Magnetizing system

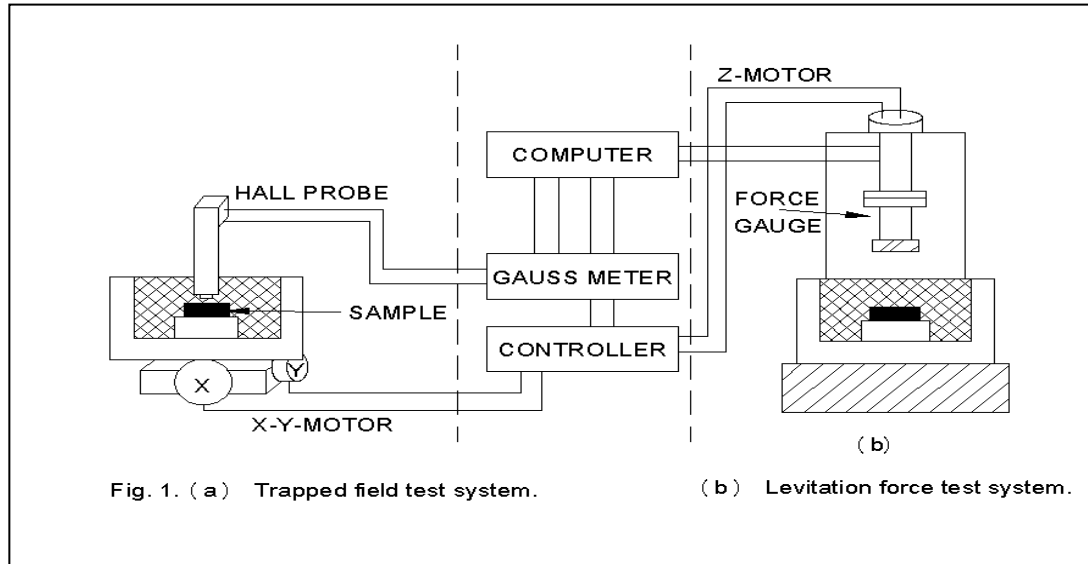


Fig.2.16 Schematic of trapped magnetic and levitation force measurement system

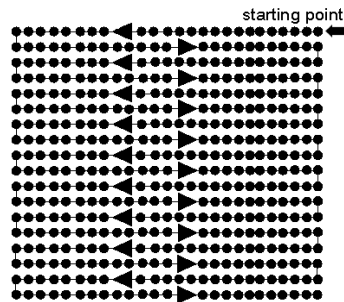


Fig.2.17 Data collection mapping of trapped magnetic field of MTG samples

2.8 Critical Current Density Measurements

Many of the envisioned bulk applications for Y-123 generally involve either monolithic structures such as flywheels or bearings, or wire applications such as magnets or other long-length conductors. In both of these areas, among the most important characteristics of the superconductors are their critical current density and their ability to pin magnetic flux. Thus, much of the characterization of the superconductors is aimed at assessing these properties. Fig.2.18 shows magnetic hysteresis loops at 77K for a zone-melt-textured Y-123 wire and a sintered Y-123 pellets acquired with a vibrating sample

magnetometer (VSM). The great difference in the magnetic properties is illustrated here where the hysteresis loop for the sintered sample is so small. One of the most useful aspects of the hysteresis curve is that it can be used to approximately determine the critical current density by applying Bean's model, where the critical current density is described by $J_c = C \Delta M/d$, where C is a geometric constant that depends on the sample shape, M is the width of the hysteresis loop, and d is the diameter of the super current loop. Modifications to the model are necessary for various sample geometries, but it allows the J_c to be characterized in a contactless fashion with a VSM.

Measuring J_c , by a four-point electrical measurement requires the application of low-resistance electrical contacts, usually formed by firing silver paint at 500°C, followed by soldering with a low-melting-point solder. Poor contacts will inhibit the ability to fully characterize the material, because at high currents the contacts will lead to sample heating, thereby yielding results that are too low. One way to avoid this difficulty is to characterize the sample in high magnetic fields, where the J_c , will be lower, so the applied currents will be reduced. Otherwise, the sample cross section must be reduced in order to lower the current necessary to achieve a certain current density level. A recent review discusses in great detail the preparation of contacts to high-temperature superconductors [83].

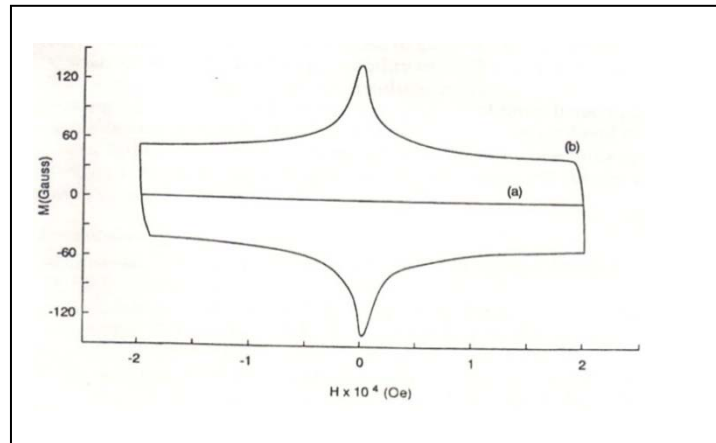


Fig.2.18 Hysteresis loops at 77K for (a) a sintered Y-123 and (b) a zone melt textured Y-123 showing the increase in magnetization due to texturing

One of the precautions that must be considered while using the magnetic J_c measurements is that they are relatively insensitive to the effect of cracks and insulating layers at grain boundaries. Thus, a sample that might carry zero transport current because of a crack may still exhibit very good magnetic properties and pin flux extremely well. This is not a problem in considering materials for flux-trapping applications such as frictionless bearings or flywheels, but it is a consideration in characterizing wires.

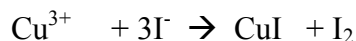
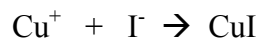
J_c of these samples were measured at Budapest University of Technology and Economics (BUTE), Budapest, Hungary. The calculation of the J_c was based on the measurement of the inductive type superconducting fault current limiter (iFCL) with SC ring. The activation current of the iFCL refers to the AC critical current of the superconducting ring. Assuming that the magnetic coupling between the two sides of the FCL is full; the AC critical current of the SC ring is calculated from the activation current and the number of turns of the iFCL [70].

2.9 Determination of oxygen content

For Y-123 system, the strong dependence of T_c on oxygen content is well known [71-74]. Shafer et al. [75] have shown that the principal variable, controlling T_c , to be the average charge 'P' on the species $[\text{Cu-O}]P^+$. The oxygen content of Y-123 compound has been determined by H_2 or CO reduction and obtaining the change in mass by thermogravimetry [72]. It can also be determined by Photometric method (oxidation of Fe^{2+} , Fe^{3+}) [76], volumetric method (evolution of oxygen) [74-75] or mass spectrometric method [77]. Nazzal et al. [79] have described the degree of oxidation in terms of the $[\text{Cu-O}]P^+$ charge, rather than the formal copper valence $(2+p)$ or the concentration of Cu^{3+} or O^- in Y-123 system by iodometric titration technique.

The general method of iodometric titration for the determination of the degree of oxidation of copper oxide compound involves dissolving the compound under inert atmosphere in an acidic solution in presence of excess KI.

The following reactions occur :



or more generally,

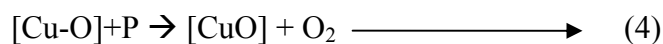
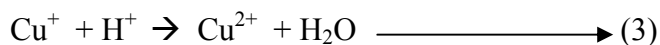


Any Cu^+ in the sample could precipitate out as CuI without generating any neutral iodine. All species in the sample oxidised beyond Cu^+ will react to yield a quantity of free iodine directly proportional to the degree of oxidation greater than Cu^+

i.e., proportional to (p+1). The quantity of neutral iodine thus produced can be accurately determined by titrating against sodium thiosulphate solution and using starch as an indicator, assuming the stoichiometry of the sample is known accurately (and there are no second phases, or other complications).

To determine the copper concentration independently an additional titration is carried out. For this titration the sample of copper oxide is dissolved in an acidic solution (in air, but without KI) to convert all the copper to Cu^{2+} state.

Following reactions occur:



If V_1 and V_2 are the volumes of the $\text{Na}_2\text{S}_2\text{O}_3$ required to titrate W_1 and W_2 g of sample of 1st and 2nd titration, respectively, then the degree of oxidation or average charge of $[\text{Cu-O}]_p$ is given by the simple expression :

$$P = (V_1/W_1) / (V_2/W_2) - 1 \longrightarrow (5)$$

The formal copper valence is (2+p). The oxygen content therefore can be calculated if the stoichiometry is known, using charge neutrality. In $\text{YBa}_2\text{Cu}_3\text{O}_{7-\delta}$, the oxygen content 'y' is obtained from the relation :

$$2y = 3(2+p) + 7 \longrightarrow (6)$$

In the second titration 30 - 40mg (W_2) of the sample weighed to the nearest 0.1mg was placed in 100 ml and dissolved in 10ml of 6N HCl. It is subsequently diluted to 40ml with water and heated in a steam bath for 10 min, 10ml of 6N NH_4OH was added drop wise while stirring till a persistent blue colour was formed followed by 2ml of 85% H_3PO_4 . The solution was then cooled to room temperature and blanketed with N_2 . 1 g of

sold KI is added and the solution is titrated with a 0.01 N [V_2 (ml)] solution of $\text{Na}_2\text{S}_2\text{O}_3$ to a starch end point.

First titration 30-40m (W1) of the sample weighed to the nearest 0.1mg is taken in a 100ml three neck flask under nitrogen atmosphere. 1 g powdered KI is added so as to cover the sample and 10ml of 6 N HCl is slowly added in such a way so that the sample is always in contact with the large excess of iodide. When the entire sample was dissolved, it was diluted to 40ml and cooled in an ice bath. Approximately 10ml of 6N NH_4OH was added drop wise till a persistent greenish blue colour appeared, followed by 2ml of 85% H_3PO_4 . The solution was cooled to room temperature and titrated with 0.01 (N) [V_1 (ml)] solution of $\text{Na}_2\text{S}_2\text{O}_3$ to a starch end point.

Chapter 3

Bulk powder processing, densification and characterization of Y-123 and Y-211 powders

The chemical reactions occurring during the preparation of ceramic compounds depend critically on the properties of precursor powders. The nature of precursor constitutes an important parameter along with temperature and duration, in the preparation of homogeneous final product. Powder processing involves the control of both particle size and mixing of powders, whether starting reactants are partially reacted intermediates. Generally the chemical reactions are diffusion controlled, and they can be accelerated by prior production of fine precursors, to get uniform mixture of fine particles. These particles subsequently react and are transformed into products before final sintering. Each of these methods commonly used in preparation of ceramics have typical characteristics, which are described in the latter part of the chapter.

For this study, $\text{YBa}_2\text{Cu}_3\text{O}_{7-\delta}$ (YBCO or Y-123) superconductor, has been chosen as the main focus for the research and development of real applications, due to the following reasons:

- (a) Its critical temperature (T_c) is above liquid nitrogen temperature (77 K)
- (b) Several processing techniques have been developed to achieve high J_c for practical uses.
- (c) The intrinsic properties and phase diagrams, which guide the appropriate direction for materials processing, are well documented.

Since Y-123 oxide is a multi-component system, precautions have to be taken to produce phase pure powder while synthesizing it on a large scale. The initial particle size plays an important role in achieving superconducting properties like critical current density (J_c) and critical magnetic field (H_c). This chapter describes the bulk powder synthesis of phase pure Y-123 and Y_2BaCuO_5 (Y-211) powder by different routes. These powders were characterized by X-ray diffraction and particle size distribution. Oxygen estimation (iodimetric titration) was performed by quenching the Y-123 pellet from different temperatures and was correlated with critical temperature (T_c). The changes in crystal structure at various temperatures were studied by high temperature X-ray diffraction.

3.1. Synthesis

Several methods have been employed for preparing Y-123 compound, with good superconducting characteristics. Process parameters such as reaction temperature, pH, milling, calcinations, etc. are specified in the discussion.

3.1.1 Ceramic method

The most common means of preparing Y-123 powder is through the so-called ceramic method, or what is sometimes euphemistically referred to as “shake and bake”. In this process all the precursors are in powder form, generally being metal oxides or carbonates. As typically practiced, the precursor powders are mixed, often being ball milled to enhance mixing and to reduce powder particle sizes. The mixed powders are

then heated at high temperature to allow inter diffusion of the cations. The main disadvantages of the ceramic method are as follows :

1. The starting mixture is inhomogeneous at the atomic level.
2. The reaction process is very slow because it relies on solid-state diffusion. Multiple cycles of grindings and heatings are required, often totalling 48 hours or even more. In cases where a liquid phase is present, diffusion through the liquid helps to accelerate inter diffusion. In the case of Y-123, however, the presence of a liquid phase during processing is undesirable because it limits the critical current density (as will be discussed latter.)
3. Even with multiple intermittent grinding steps, a compositionally homogeneous product is difficult to obtain.

Despite these shortcomings, the ceramic method is by far the most widely used process because it is facile easy to practice. The only equipment required for the most basic processing is a mortar and pestle and a furnace. Typically, after mixing and grinding, the powders are calcined at 900-950°C for 8-24 hours and then pulverized, and the process is repeated one or more times. The success of this process depends to some extent on the precursor chosen, and subsequent modifications to the process to enhance decomposition of some of the precursors. The most widely used set of precursors for Y-123 are Y_2O_3 , CuO and $BaCO_3$.

$BaCO_3$ is used because it is stable in air and does not tend to pick up moisture (unlike BaO_2). The problem with using $BaCO_3$, however, is that CO_2 released during decomposition can lower the melting point of the low melting point liquid (a eutectic of $BaCuO_2$ and CuO). As a result, to avoid the formation of any liquid phase during

calcining or sintering, one is restricted to temperatures below 890°C. By lowering the permissible reaction temperature, the diffusion kinetics are slowed, thereby increasing the total reaction time required to achieve satisfactory homogeneity. Otherwise if higher temperatures are used a liquid phase is present, which leads to rapid grain growth and the presence of frozen liquid at three particle junctions in the final microstructure. However, presence of a liquid phase does offer two advantages, increases reaction rate and greater density is achieved in the final product.

One way of avoiding the deleterious effects of CO₂ evolution is to use BaO₂ as the barium precursor [86]. Another way is to use vacuum calcination, a novel technique developed by Balachandran and co-workers [87]. The technique involve using a so-called dynamic vacuum to maintain a reduced CO₂ partial pressure. In this process flowing oxygen is introduced into one end of a tubular furnace while a vacuum pump at the other end maintains a pressure of 2 mm Hg. The CO₂ partial pressure is continuously monitored to maintain it below a level of 2% of the total O₂ pressure. This process permits the use of BaCO₃ as the barium precursor without the formation of a liquid phase. In addition, because cation diffusion is faster in a reduced partial pressure of oxygen environment [88], the reaction duration for powder production is reduced with this process. As a result, 1000 g of phase-pure Y-123 can be produced in one thermal cycle of 8h duration.

An alternative means of avoiding liquid phase formation and also in some cases to decrease the reaction time, is to use intermediate precursors. Ruckenstein and his co-workers [89] explored the rates of reaction and the purity of the final product by using a number of different precursors. Their work showed that decomposition of BaCO₃ was

the limiting factor in the reaction rate to form Y-123. Their technique changes the slow reaction into a first step, allowing the superconducting compound to be obtained in a second, more rapid step. For example, one can prepare BaCuO_2 by reacting CuO and BaCO_3 in the first step, and then reacting BaCuO_2 , CuO , and Y_2O_3 in the second step. In this way, the CO_2 evolution is confined to one step, and the second reaction to form the superconducting compound can occur without the presence of CO_2 . The BaCuO_2 reacts rapidly with the other two precursor materials, therefore rapid grain growth in the presence of a liquid phase with extended reaction times is not a problem.

3.1.2 Co-precipitation technique

Another method for preparing superconducting powders is co-precipitation. This process involves a solid containing various ionic species in stoichiometric quantities precipitating out of a solution. The resulting precipitates are heated to appropriate temperatures in a suitable atmosphere to produce the desired compound. The precipitated product is uniform with respect to stoichiometry compared with ceramic oxide processing, resulting in shorter reaction times and more homogeneous reaction products. In addition, finer powder particles sizes can result from the co-precipitation process.

As applied for preparing Y-123, co-precipitation of the component metals from a nitrate solution as formate, acetate, and oxalate has been investigated [90]. Oxalate co-precipitation in particular has been widely reported. In this process an oxalic acid solution is added to an aqueous solution of Y, Ba, and Cu nitrates, and the pH of the solution is adjusted. The resulting oxalate is then heated in air and converted to Y-123.

The major drawback of this process is that control of the final product stoichiometry can be difficult owing to the difference in stability of different oxalates.

3.1.3 Aerosol techniques

Fine, homogenous mixed particles can be formed from the nitrate solutions by atomization in a jet of gas such as O₂. The aerosol formed can be either frozen and dried in a freeze drier, or alternatively, dried and reacted by passing in a flow of O₂ gas through a furnace. The latter process is known as spray drying, or as spray calcination if the furnace temperature is sufficiently high to promote chemical reaction. An aerosol is formed by an atomizer, sometimes adapted from commercial humidifiers. If, for example, an aerosol flow rate of 3 standard litres per minute is passed, with a residence time of 25 seconds, through a furnace raised to 950°C, powders formed from the nitrates of Y, Ba and Cu decompose and react. Dried, calcined powder is collected on a warmed filter at the end of the furnace. Typical particle sizes obtained are in the range of 2-10 micrometer.

3.1.4 Sol-Gel processing

Sol-gel processing allows one to achieve homogeneous mixing of cations on an atomic scale. Originally developed by Pechini [91], this process permits rapid formation of the final product at reduced temperature during the solid state reaction. Sol-gel processing is so named because a concentrated sol (a suspension of colloidal particles) is converted to a semi-rigid gel. The gel is subsequently heated at an appropriate temperature to obtain the final product. Although this technique allows one to produce

high quality powder [92], the resulting bulk solids fabricated from such powder show no appreciable increase in J_c over solids prepared from ceramic-processed powder due to the inherent limitations of polycrystalline sintered Y-123.

3.1.5 Other processing methods

Many other processing techniques have been employed to produce Y-123 or other rare-earth powders. Noteworthy among these are combustion synthesis, spray drying, freeze drying, and metal precursor routes.

Combustion synthesis, reviewed recently [93], is based on using the heat liberated by a highly exothermic reaction to propagate the reaction-front through a sample. Specifically, an energy source (e.g., a pulse from a laser or some external heat) triggers a reaction at one end of a powder compact, and the heat given off by the reaction allows the reaction-front to proceed along the length of the compact in a relatively short time (of the order of seconds). It thus offers a fast, low-energy approach to prepare many inorganic compounds. In the case of Y-123, the oxidation of copper metal can act as the fuel, BaO_2 as an oxygen source, when combined with Y_2O_3 and ignited; these allow rapid formation of Y-123. Nevertheless, achieving phase-pure multi-component material by this technique remains a problem [94].

In spray drying, a solution (frequently a nitrate solution) containing the metal cations is sprayed into a hot chamber. The solvent evaporates, leaving behind a powder that, when heated in an oxidizing environment, decomposes to form the desired compound (Y-123). A variation of this technique uses an ultrasonic device to atomize very fine liquid droplets. After evaporation, very uniform and chemically homogeneous

submicron size powder particles can be produced [95]. To date, however, powder production by this process is somewhat limited.

Freeze drying also starts with the reactants in solution. In this case, however, the solution is sprayed into cold environment (e.g. liquid nitrogen) in order to freeze the droplets. The solvent is removed at low pressure in a vacuum chamber to yield the reactants as a fine powder. This powder is then heated to an elevated temperature to permit solid state reaction. As in the case of spray drying, the advantage of this route is that diffusion distances required during the solid-state reaction are lower compared with ceramic processing [96].

Finally the metallic precursor method has also been successfully employed to produce Y-123 powder. In this case metal powders are intimately mixed in an inert atmosphere. A high energy mill is effective for this type of mixing. After mixing, controlled oxidation is used to form the super conducting oxide [97]. The advantage of this process is that the metal mixture can be formed into useful shapes (such as wire through drawing or rolling) prior to oxidation, bypassing some of the limitations of working with brittle fired ceramic shapes.

3.2 Experimental

3.2.1 Synthesis of Bulk Y-123 and Y-211 powder by solid state route

Stoichiometric amounts of AR grade Y_2O_3 , CuO and $BaCO_3$ were weighed and mixed in planetary ball mill in acetone media using zirconia bowls and balls for 15-20 min. The powder mixture was calcined in an alumina boat at $880^\circ C$ for 10 h and then

again mixed ground and calcined at 900°C for 10 h. A flow sheet of synthesis is shown in Fig.3.1.

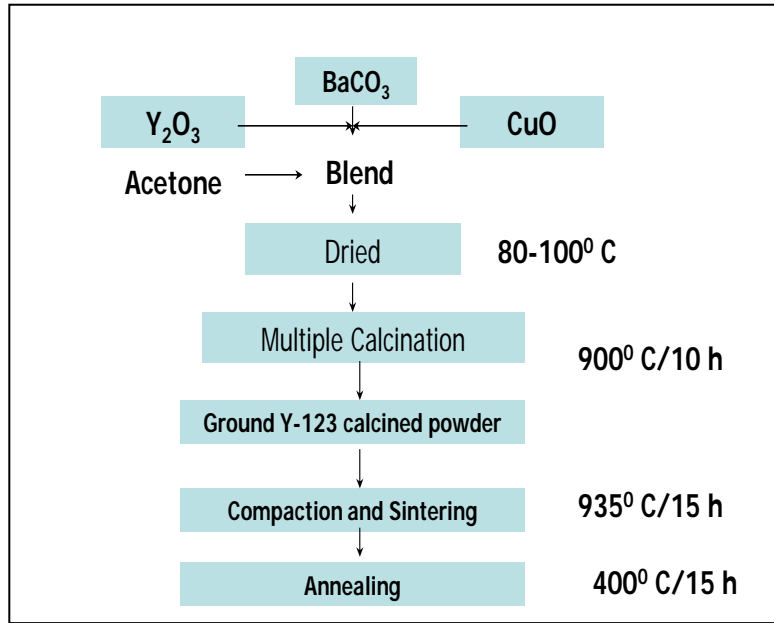


Fig.3.1 Flow sheet of synthesis (solid state route) Y-211 & Y-123

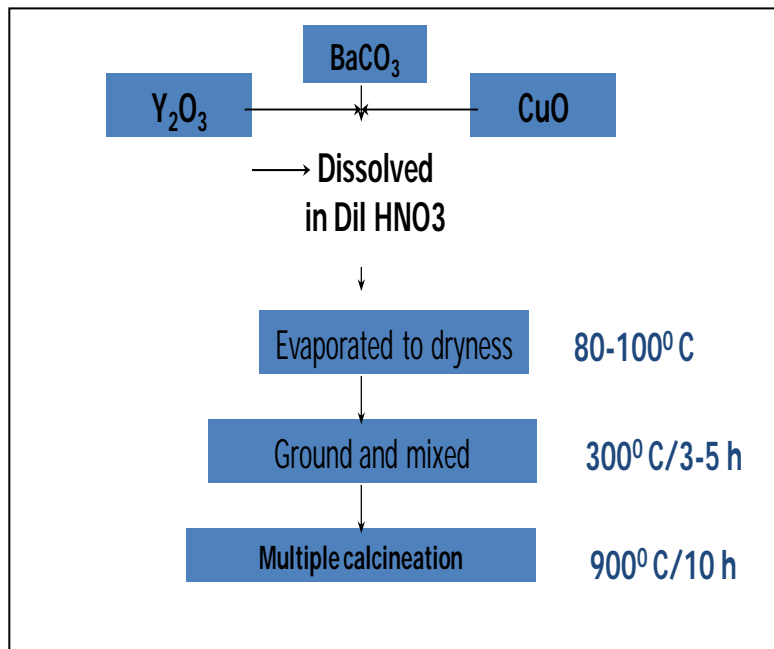


Fig.3.2 Flow sheet of synthesis (nitrate decomposition route) of Y-211

3.2.2 Synthesis of Y-211 by nitrate decomposition route

Stoichiometric amounts of AR grade Y_2O_3 , CuO and $BaCO_3$ were weighed and dissolved in dilute 1:1 nitric acid and evaporated to dryness along with stirring. The nitrate slurry was then subjected to heat treatment at 300 °C for 1h. The nitrate mixture was then decomposed at 600 °C for 6 h in an alumina boat and then resulting oxide powder was ground mixed and calcined at 900 °C for 10 h. A flow sheet of synthesis is shown in Fig.3.2.

The calcined Y-211 powders obtained by both solid state route as well as by nitrate decomposition route powders were characterized for X-Ray diffraction that showed the formation of phase pure material. The particle size of powder was studied by laser particle size measurement unit. The average particle size distribution of powder synthesized by nitrate decomposition was 3-5 microns whereas powder synthesized by solid state route was 15-20 microns. Large scale of nearly one kg of phase pure powder of Y-123 (Fig.3.3) and Y-211 (Fig 3.4) powders were synthesized in a single batch.



Fig.3.3 Y-123 powder (approx one kg) in an alumina boat



Fig. 3.4 Y-211 powder (approx 0.5 kg) in an alumina boat

3.3 Characterization of powder

The calcined powders were characterised by following methods:

3.3.1 Particle size distribution

Particle size analysis was conducted by laser particle size analyser. Particle size of Y-123 & Y-211 synthesised by solid state route was found to be 15-20 micrometer and Y-211 prepared by nitrate decomposition route was found to be 3-4 micrometer (Fig.3.5).

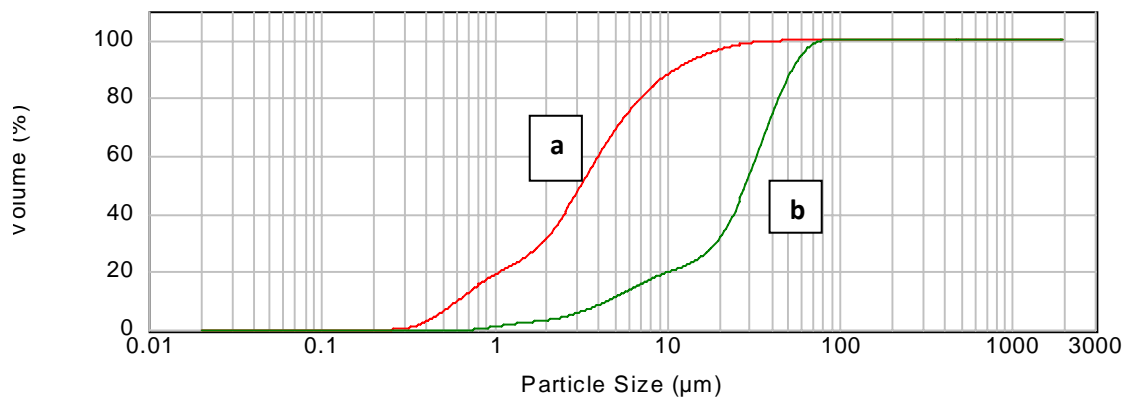


Fig.3.5 Particle size distribution of Y-211 powder (a) Synthesised by solid state route (SSR) (b) Synthesised by nitrate decomposition route (NDR)

3.3.2 XRD studies

X-ray powder diffraction patterns were recorded for calcined Y-211 synthesized by solid state route (Fig. 3.6), by nitrate decomposition route (Fig 3.7) and Y-123 by solid state route (Fig.3.8) all the XRD patterns show phase pure calcined powder.

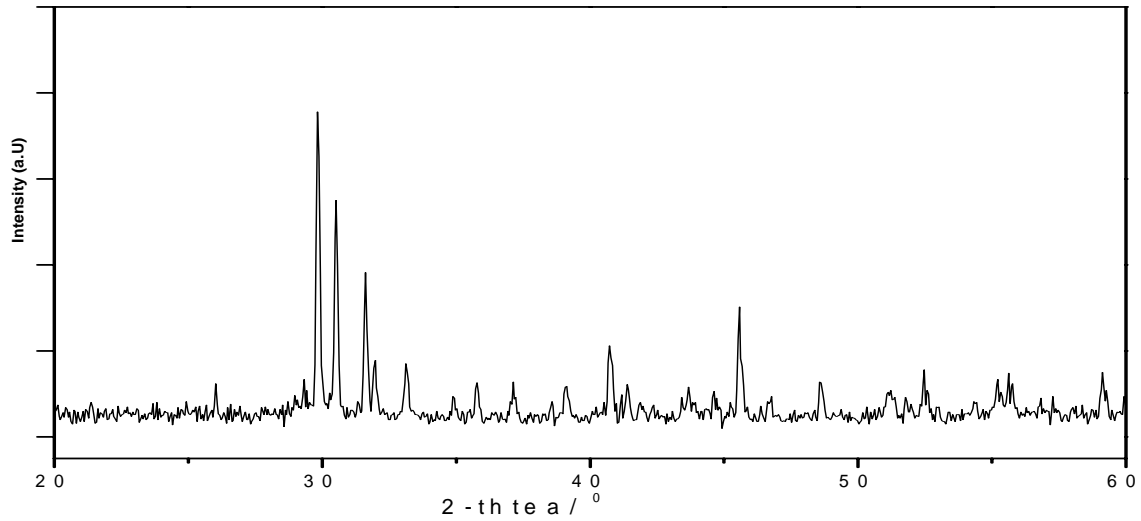


Fig.3.6 XRD pattern of Y-211 powder synthesized by solid state route (SSR)

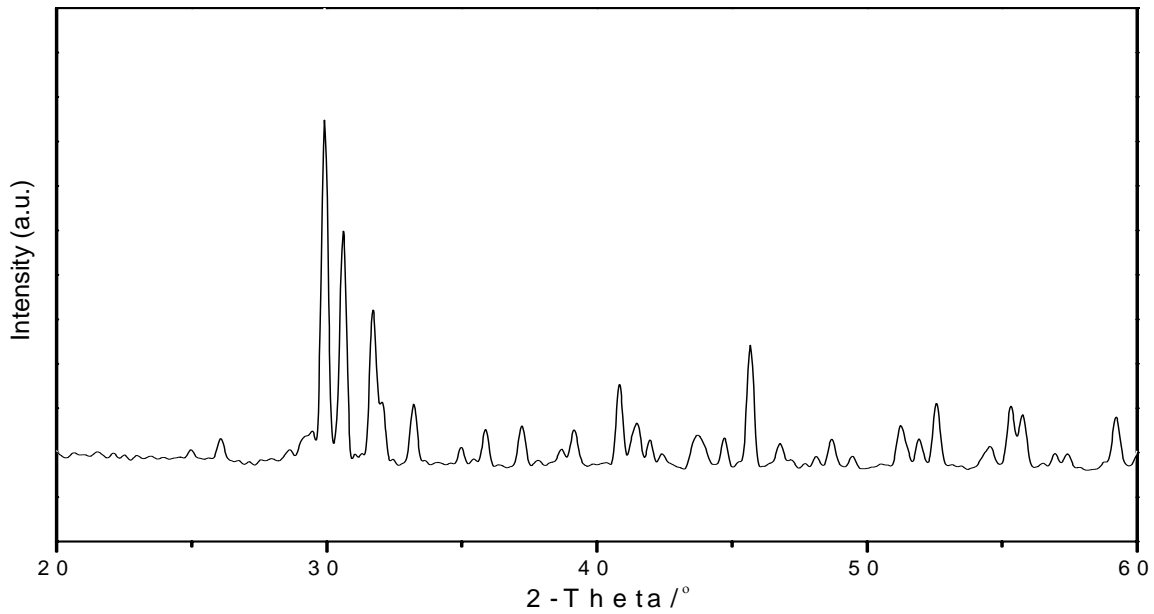


Fig.3.7 XRD pattern of Y-211 synthesized by nitrate decomposition route (NDR)

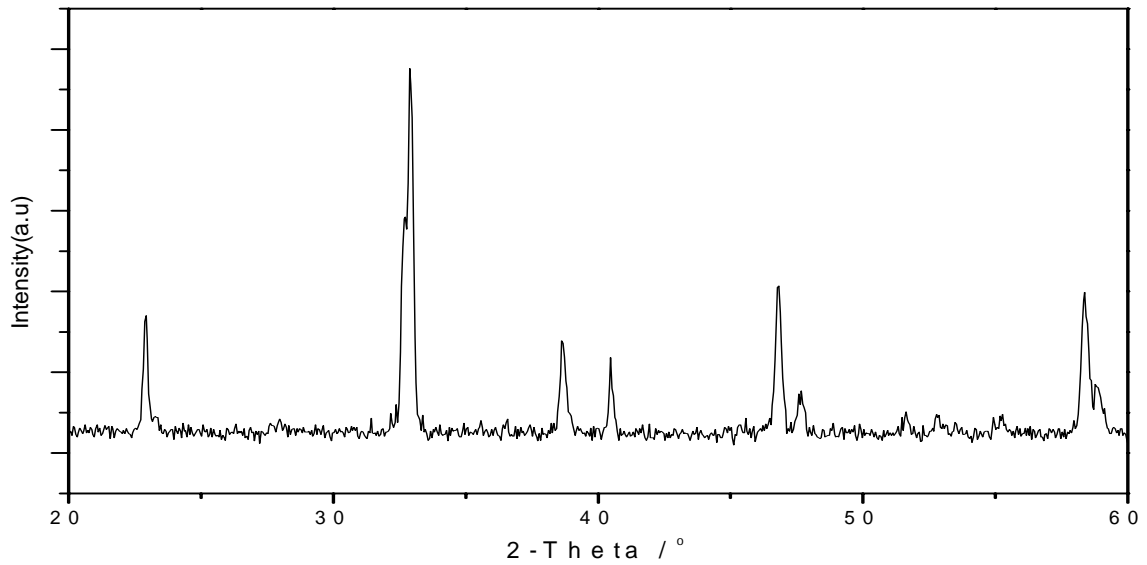


Fig.3.8 XRD pattern of Y-123 powder synthesized by solid state route

3.4 Sintering and its characterization of sintered Y-123 oxide

3.4.1 Sintering

The Y-123 powder was compacted in the form of pellet of 10 mm diameter and 1 mm thickness by uniaxial pressing and the pellet was sintered at 935°C for 15h and annealed in oxygen at 400°C for 15h.

3.4.2 Critical transition temperature

Critical transition temperature was carried out on the indigenously designed, developed and fabricated “Liquid nitrogen T_c measurement system” as mentioned in Chapter-2 section 2.2 (see Fig. 2.1). The sintered pellet was attached on the sample holder, current of 10ma was passed and the corresponding voltage drop and temperature was measured. Resistance was calculated by ohms law and plotted against temperature. The R vs T plot (Fig.3.9) of sintered pellet reveals critical transition temperature (T_c) 90K.

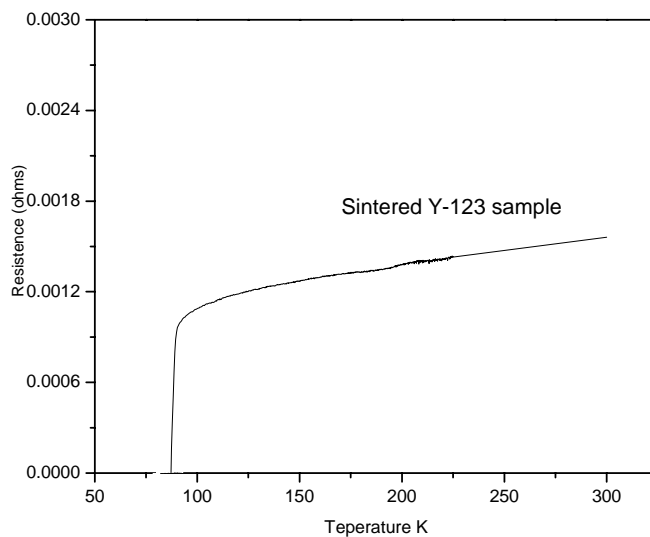


Fig.3.9 R vs T of sintered Y-123 pellet

3.4.3 SEM characterization

SEM image (Fig.3.10) of fractured sample shows porous body structure.

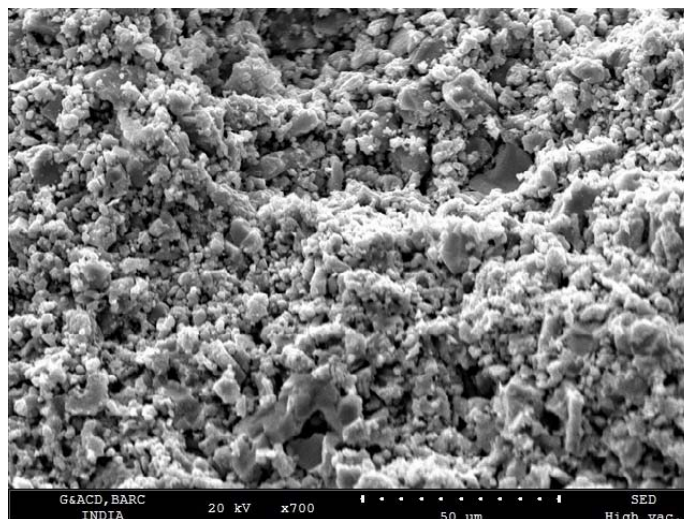


Fig.3.10 SEM image of fractured surface sintered Y-123 pellet

The electrical and structural changes have been studied for sintered samples of different oxygen content by quenching (details of the study is described in next section) at different temperatures in liquid nitrogen. It has been found that the T_c and the unit cell lattice parameters change smoothly with oxygen content. Oxygen rich samples are found to have better superconducting properties and are orthorhombically distorted. As they become oxygen deficient, superconducting properties get suppressed and unit cell changes to tetragonal symmetry. A series of compounds have been synthesized with oxygen content between two extremes i.e. $O_{7.0}$ to $O_{6.4}$ and they were characterized by X-ray diffraction, T_c and oxygen stoichiometry measurements. The superconducting samples transformed to semiconductors below the oxygen stoichiometry $O_{6.4}$. The occupation of oxygen vacancies create holes in the structure and with increase in hole concentration by oxygen pick up, T_c increases up to the upper limit 90K. At this stage oxygen content is found to be ≈ 6.9 . Prolonged annealing in oxygen atmosphere at low temperature where rate of oxygen pick up is maximum does not yield higher T_c . This suggests that the saturation point for oxygen content in Y-123 compound is ≈ 7.0

3.5 Quenching study of Y-123

The changes in lattice parameters and T_c of samples quenched (¥) from different temperature to liquid nitrogen, have been shown in Table 3.1. The zero resistance temperature and the oxygen content of the samples reduced as the quenching temperature was increased.

Sample code	Quenching Temperature °C	Oxygen Content 7- δ	T _c (K)	Lattice Parameters		
				a (Å)	b (Å)	c (Å)
¥1	500	6.93	89	3.815	3.890	11.69
¥2	550	6.76	75	3.819	3.896	11.69
¥3	600	6.67	60	3.826	3.884	11.71
¥4	650	6.59	50	3.835	3.882	11.73
¥5	700	6.53	40	3.865	3.865	11.73
¥6	750	6.53	<30	3.862	3.862	11.75

Table 3.1 Oxygen content, T_c and lattice parameters of Y-123, quenched from various temperature to liquid nitrogen

3.5.1 High Temperature X-ray diffraction studies

It was also observed from the High temperature X-ray diffraction studies (Fig.3.11) that with increase in quenching temperature a and b lattice parameters gradually became equal which is clearly observed from the reverse split in 2-theta peak between 32 & 33° and 58.5 & 59 ° which depicts the transformation of high temperature tetragonal phase above 750 °C to mixed phase at around 600 °C and then orthorhombic phase below 500°C.

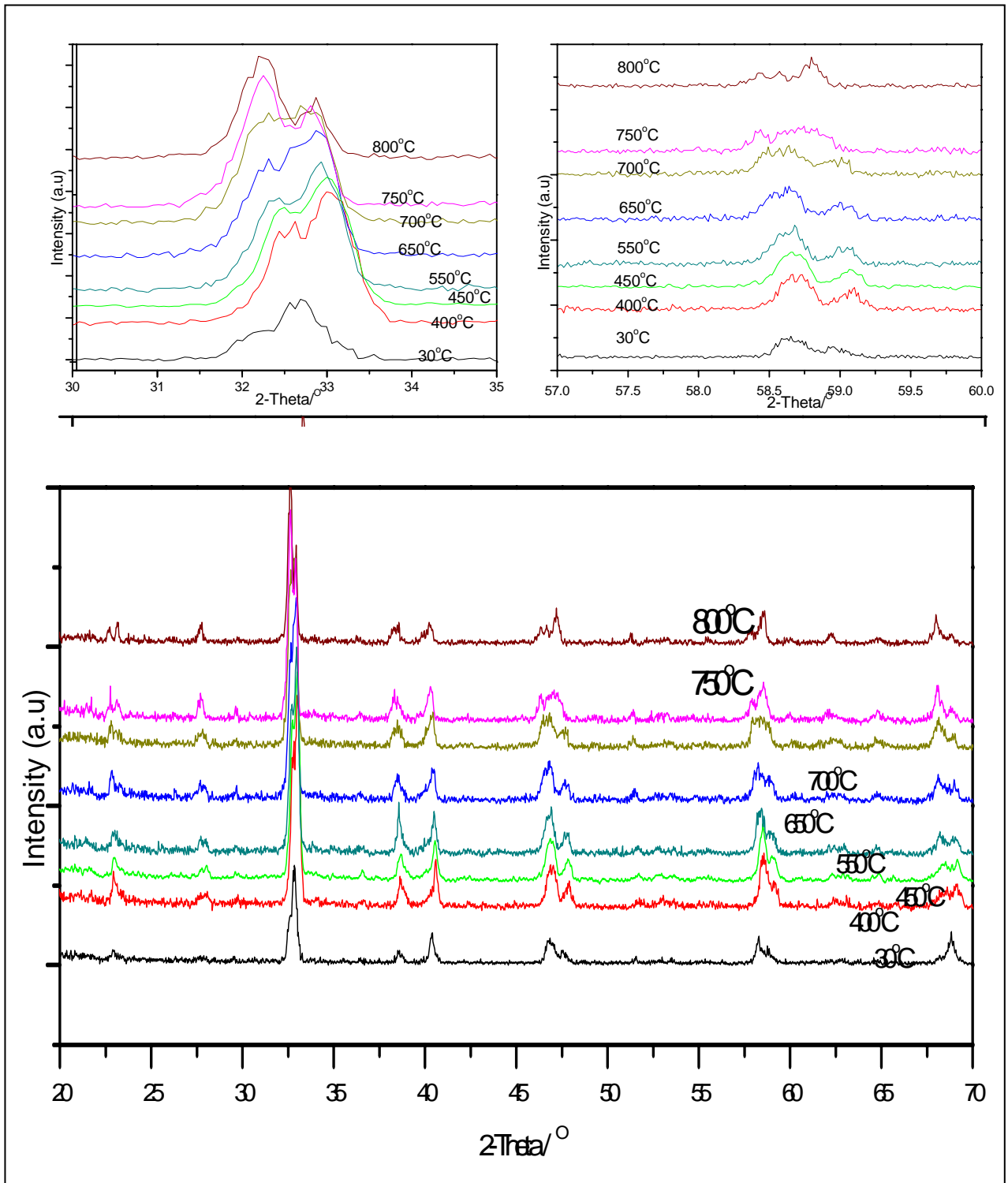


Fig.3.11 High temperature XRD patterns of sintered Y-123 powder

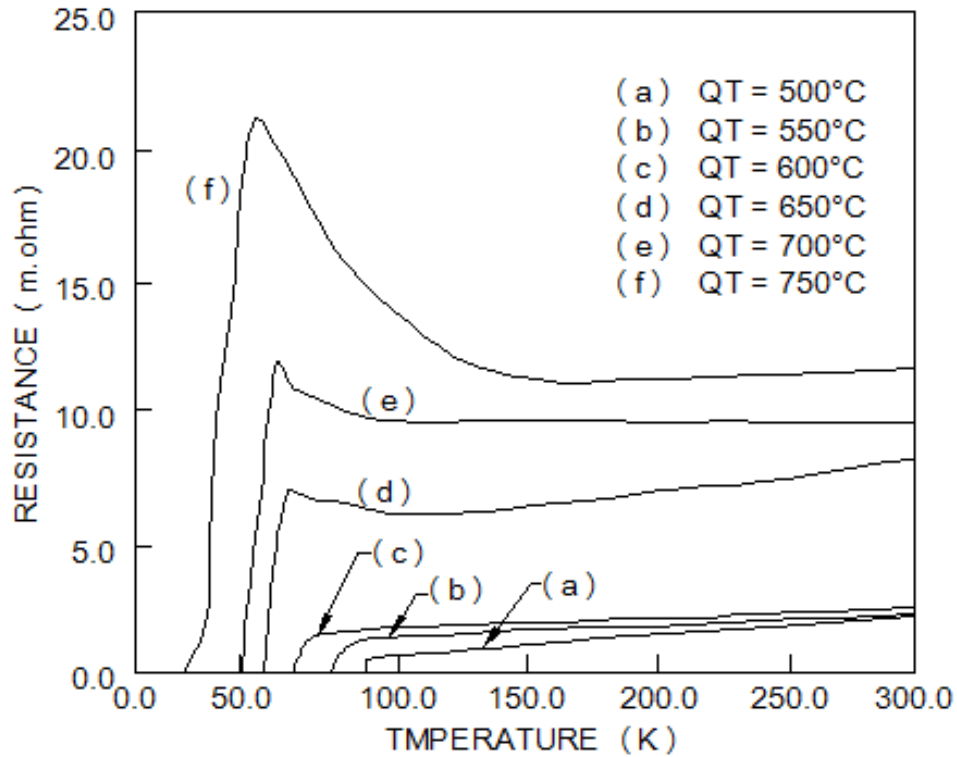


Fig.3.12 R Vs T plot of Y-123 samples quenched from different temperatures to liquid nitrogen.

The changes in lattice parameters with temperature are given in Table 3.1. As the quenching temperature (Q_T) was increased from 500°C to higher temperature, the zero resistance temperature was found to decrease monotonically from 89K to 32K for 750°C. In the R Vs T plots (Fig.3.12) it can be seen the transitions have started at 90K and become broader with the increase of Q_T . Up to $Q_T=600^\circ\text{C}$, the samples showed metallic resistivity behaviour but further increase in Q_T turned the material semiconducting in nature before the transition temperature was reached, where upon the resistance of the samples decreased rapidly. This can be explained as follows. As the Q_T increases the superconducting phase content gradually decreases, and the amount of semiconducting phase increases. When the quenching temperature was increased to 800°C the samples

became purely semiconducting down to 10K. The oxygen content which has been determined iodometrically was found to decrease from ~6.93 for 500°C to ~6.52 for $Q_T = 750$ °C. It has been also found that when the sample was kept for long time at 400°C in oxygenatmosphere, oxygen content became ~6.99 as shown in Table 3.1.

The T_c was measured in indigenously designed, developed and fabricated set up. A constant current is passed through the sample by Keithley make constant current source model 220, and corresponding voltage drop was measured by Keithley make nanovoltmeter model 181. Oxford instruments temperature controller model ITC 503 was used to measure the temperature using a silicon diode sensor. A Keithley make switching device (scanner) was used to measure multiple samples which can connect one by one sample through current source, nanovoltmeter and temperature controller. All the units were connected through IEEE compatible card. The resistance Vs temperature graph was recorded on the PC. A room temperature setting silver paint was used to make the four ohmic contacts on the sample. The effect of thermal emfs nullified by reversing the current and taking the average voltage generated across the sample for the two directions of current flow.

The variation in T_c and oxygen content can be seen in from the Fig.3.13 The sample having Oxygen content 6.9 shows $T_c = 90$ K as the oxygen content is near 6.5 the sample shows T_c less than 30K.

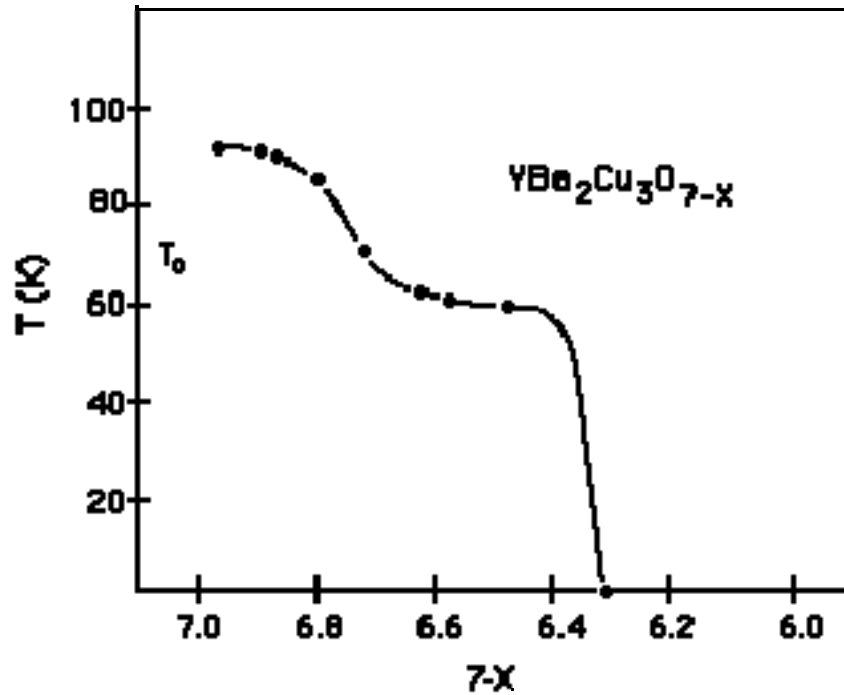


Fig.3.13 T_c as a function of oxygen content in Y-123

3.6 Conclusion

An economical process was developed for a large scale (Kg level) synthesis of Y-123 oxide. The final products were characterized for their particle size distribution, phase purity and oxygen content etc. The effect of quenching temperature on the oxygen stoichiometry and crystal structure has been examined. Sintered samples have been characterized by their resistivity vs temperature behavior. It was found by taking appropriate precautions, it is possible to prepare high quality Y-123 oxide at large scale without any deterioration in superconducting properties.

Chapter 4

Preparation and characterization of different composites for MTG components

Most of the potential applications of bulk YBCO require high critical currents in applied magnetic fields. There are two factors limiting the increase in critical current densities (J_c): existence of weak-links at large angle grain boundaries and lack of effective flux pinning centers. Since the concept of the melt-texturing growth (MTG) technology invented by Jin et al. [102], highly textured large YBCO single domains can be prepared and weak-links at large angle grain boundaries have been overcome to a great extent. Various modified editions of MTG, such as the liquid phase processing (LPP) method by Salama et al. [103], the Quenching Melting Growth method (QMG) by Murakami et al. [104] and the powder melting process (PMP/PMG) by Zhou et al. [105], have been developed and substantial increase in high critical current densities has been obtained. On the basis of the elimination of weak-links by these melt growth techniques, further increase in critical current density (J_c) needs forceful pinning centers like Y_2BaCuO_5 (Y-211) has been reported [103] to enhance the flux pinning ability of YBCO dramatically. It is believed [106] that the reduction in Y-211 size will increase Y-123/Y-211 interfacial area and induce many micro-defects around Y-211 particles, which enhance the flux pinning ability and result in a high J_c value. In fact, introducing ultrafine Y-211 ($<1\mu\text{m}$) into YBCO is one of the most effective approaches to increase J_c value for every melting growth technology by now, due to different thermal schedules and starting precursors, morphologies and distribution of Y-211 are different for various melting growth technologies. As far as the MTG technology is concerned, Y-211 in a

product of the peritectic decomposition of Y-123 phase at high temperature (usually 1050°C). The phase Y-211 nucleates and grows up during the peritectic decomposition. Owing to the high decomposition temperature, Y-211 particles are very easy to grow up to several tens of microns. In order to suppress the growth of Y-211, several techniques such as optimizing thermal schedules (to lower the decomposition temperature), using additives (Pt, CeO₂) to promote [107] nucleation and restrain the coarsening of Y-211, have been attempted. Although substantial increase in growth has been made, still it is a problem to introduce ultrafine Y-211 into YBCO for practical applications. Different from other melt growth techniques, PMP uses Y₂BaCuO₅, BaCuO₂ and CuO as precursors. The size, morphology and distribution of Y-211 can be conveniently controlled before melting process. During melt growth, if proper processing parameters are employed, the coarsening of Y-211 particles can be suppressed or minimized. Therefore, if the size of Y-211 precursors is fine enough, it is possible to incorporate ultrafine or even nanometer sized Y-211 particles into YBCO. The incorporation of sub-micron Y-211 phase dispersed in YBCO matrix is the objective of this study. Detailed discussion of above processing technique are described in chapter 5.

4.1 Preparation of composite powders for fabrication of components

This chapter describes the preparation and characterization of selected composites for fabrication of components of different shapes by using melt textured growth technique (MTG). The relative stability of solidification growth fronts has been examined by using different varieties of composites given as follows :

Sr. No	Sample composites	Composite Name
1	Y-123 + 25 wt % Y-211 (solid state route) + 5 Wt % Ag	A
2	Y-123 + 25 wt % Y-211 (nitrate decomposition route) + 5 Wt % Ag	B
3	Y-123 +25 wt % yttria + 1 wt % Pt	C
4	Y-123 +25 wt % yttria + 1 w % ceria	D

4.2 Addition of Y-211 phase

The inclusion of Y-211 particles has several advantages to the growth and properties of bulk Y-123 components, such as :

- a) It prevents the liquid flow so as to decrease the amount of pores.
- b) It shortens the space between the Y-211 particles to help growth of the Y-123 crystal as well as creating the Y-123/Y-211 boundaries which are effective flux pinning sites [108].
- c) Volume fraction of Y-211 particles is approximately constant: the current density (J_c), value is an inverse measure of the mean size of Y-211 phase. The high critical density values could be achieved by controlling the volume fraction and particle size of the Y-211 phase [109].

Y-211 is believed to act as reinforcement to the melt due to which the shape of the component is retained.

4.2.1 Addition of silver

In order to improve the mechanical and fracture properties of the Y-123 superconductors, different types of superconducting composites have been investigated [110-112]. Among these, the Y-123/Ag composites [113-119] appear to be one of the

most promising choices. Silver has been observed to be one of the few materials that does not degrade the superconducting properties of the Y-123 [113] material. In addition, the presence of Ag lowers the normal-state resistivity and the contact resistance of the composite [114], and facilitates oxygen diffusion into the bulk material [115]. The degree of sintering in Y-123 is also enhanced by the Ag addition, resulting in decreased porosity as the Ag content is increased. Consequently, mechanical properties like Young's modulus and fracture strength increase with the Ag addition [115-116].

4.2.2 Addition of platinum and ceria

Platinum and cerium oxide powders have been reported to be added for suppressing the coarsening of Y-211 particles during melt texture processing.[120-121].

4.2.3 Preparation of composites

To avoid shrinkage during fabrication using melt texture growth technique, Y-123 powder was first calcined at higher temperature i.e. below sintering temperature at about 900°C, the chunks were then crushed in vibratory mill and passed through 70 # sieve. The high temperature calcined powder was used for fabrication of components.

4.2.3.1 Preparation of sample composite A

400 g of pre-calcined Y-123 powder and 125 g of Y-211 powder (synthesized by solid state route) and 25 g of silver powder (99%) were mixed in a nylon bowl using zirconia balls in a planetary ball mill for 30 min in acetone media. The powders were dried in an oven at 100 °C.

4.2.3.2 Preparation of sample composite B

400 g of pre-calcined Y-123 powder and 125 g of Y-211 powder (synthesized by nitrate decomposition route) and 25 g of silver powder (99%) were mixed in a nylon bowl using zirconia in a planetary ball mill for 30 min in acetone media. The powders were dried in an oven at 100 °C.

4.2.3.3 Preparation of sample composite C

400 g of pre-calcined Y-123 powder, 125 g of yttria (99.9 %) and 4g platinum (99%) powder were mixed in a nylon bowl using zirconia balls in a planetary ball mill for 30 min in acetone media. The powders were dried in an oven at 100 °C.

4.2.3.4 Preparation of sample composite D

400 g of pre calcined Y-123 powder, 125 g of yttria (99.9 % , -325 mesh size) and 4g ceria (99.9%) powder were mixed in a nylon bowl using zirconia balls in a planetary ball mill for 30 min in acetone media. The powders were dried in an oven at 100 °C.

4.3 Granulation of composite powders

High density can be obtained if free flowing powder is available. To obtain free flowing powder it is necessary to granulate the composite powders. The mixed powders were filled in flexible latex bag, vacuum sealed and pressed in cold isostatic press at

1000-1200 bar pressure. These compacts were then crushed in vibratory mill and sieved to obtain -70 # powder.

4.4 Sintering of composites

Composite A , B, C, D and pure Y-123 powders were pelletized using 10 mm dia SS die and sintered in tubular kanthal furnace at 930°C at a heating rate of 3°C /min. for about 10 h and then cooled at the rate of 3°C/min to 400 °C and held for 15 h in a flowing oxygen atmosphere.

Composites B,C and D were pelletized, heated to 1010°C and then quenched in liquid nitrogen.

4.5 Characterization of sintered and quenched composites

4.5.1 X-ray diffraction studies

4.5.1.1 XRD of sintered Y-123

X-ray diffraction pattern of sintered Y-123 is depicted in Fig.4.1. Orthorhombic splitting was observed at 32.8° and 58.6° which clearly indicates the single phase orthorhombic structure. No other phase was detected in the X-ray diffraction pattern.

4.5.1.2 XRD of composite B

Fig.4.2 shows the X-ray diffraction pattern of composite B. XRD pattern of the as mixed powder (B1) showed the presence of Y-123 and Y-211 phases as expected. XRD pattern of sintered powder (B2) showed peaks of orthorhombic Y-123 phase along with small peaks of Y-211. XRD pattern of quenched composite (B3) showed mixed phase of

tetragonal Y-123 and Y-211. The Y-211 peaks observed in the (B3), is due to the decomposition of Y-123 at this temperature to form Y-211.

4.5.1.3 XRD of composite C

Fig.4.3 shows the X-ray diffraction pattern of Composite C. XRD pattern of the as mixed powder (C1) shows mixed Y-123 and yttria phases. The sintered (C2) powder showed presence of orthorhombic Y-123 phase along with small quantity of yttria and Y-211 phase. Y-211 phase observed is due to the reaction between Y-123 and excess yttria added in the composite. XRD pattern of quenched composite (C3) showed mixed phase of tetragonal Y-123 phase along with Y-211 and yttria phase. The Y-123 starts to decompose above 960°C and converts partially to Y-211 phase, hence Y-211 phase is seen in (C3). No platinum peaks were observed due to the presence of low amounts.

4.5.1.4 XRD of composite D

XRD pattern of composite D are shown in Fig 4.4. XRD pattern of the as mixed powder (D1) shows mixed phase of Y-123 and yttria phase and the sintered powder showed (D2) mixed phase of orthorhombic Y-123 phase along with small phase of yttria and Y-211 phase. The Y-211 phase observed in the XRD pattern is due to the reaction of Y-123 with excess yttria in the composite. XRD of quenched material (D3) shows mixed phase of tetragonal Y-123, yttria and secondary phase of Y-211. The Y-211 phase observed in (D3) is due to decomposition of Y-123 above 960°C.

The XRD patterns of quenched samples of all the composites indicate the presence of the tetragonal Y-123 phase. Retention of the high temperature ($>1010^{\circ}\text{C}$) tetragonal phase at room temperature is feasible only due to the high quenching rates in all the samples.

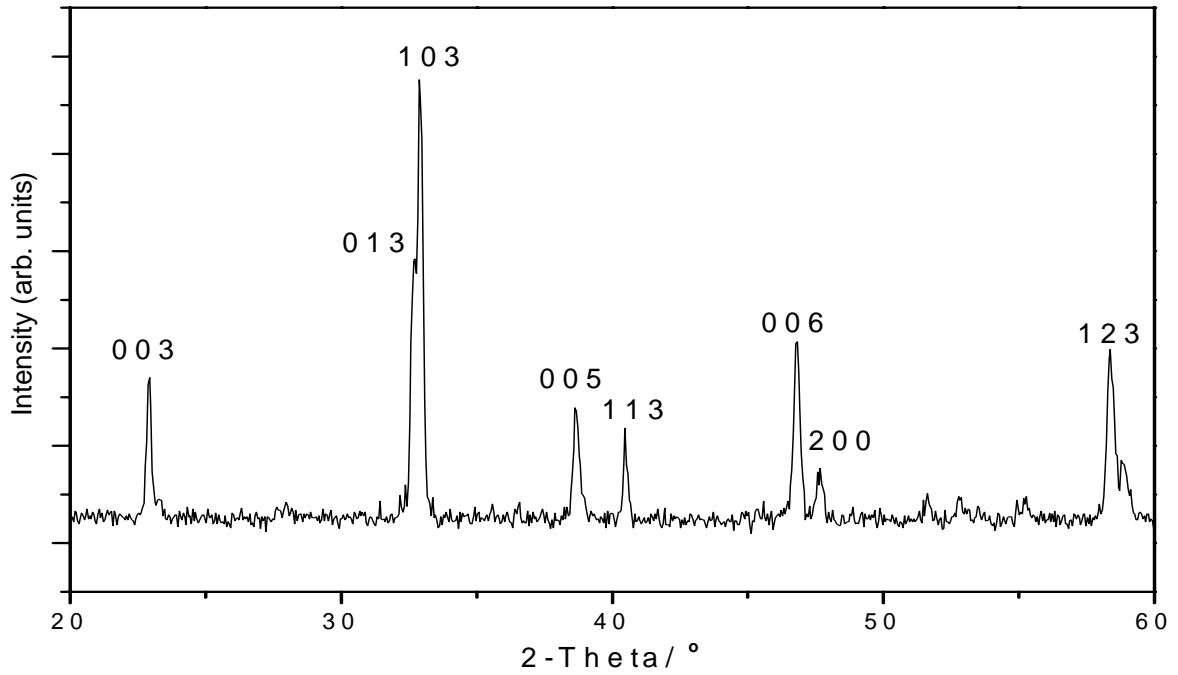


Fig.4.1 XRD pattern of sintered Y-123 powder

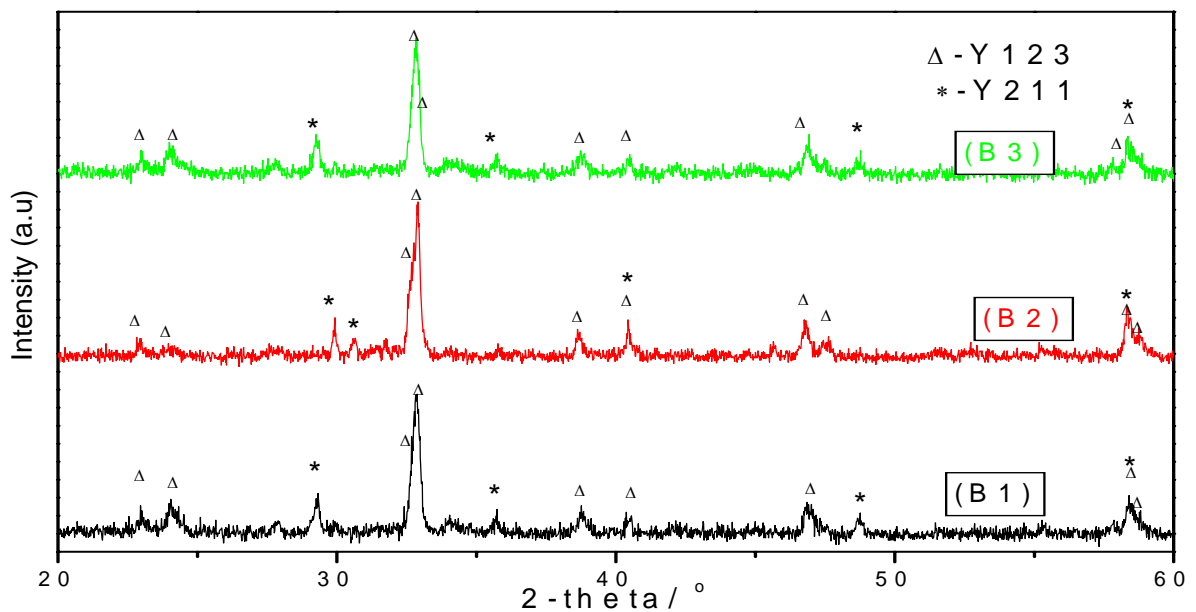


Fig.4.2 XRD patterns of composite B, (B1)-as mixed powder, (B2)- sintered powder, (B3)-Quenched powder

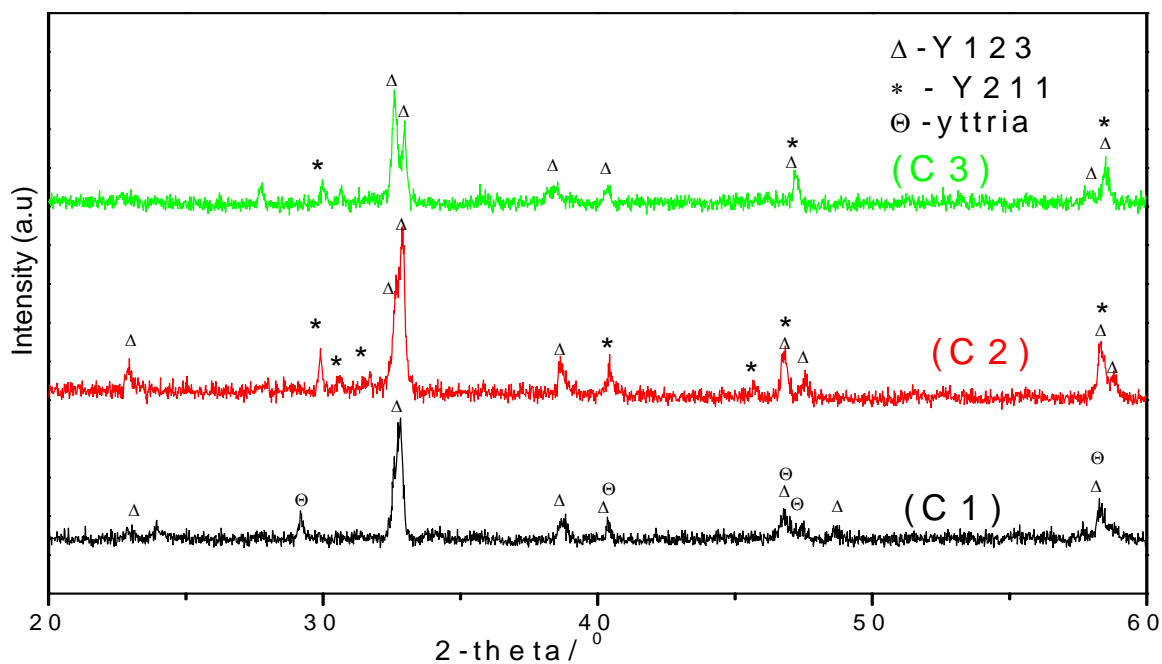


Fig.4.3 XRD patterns of composite C. (C1)-as mixed powder, (C2)-sintered powder, (C3)-Quenched powder

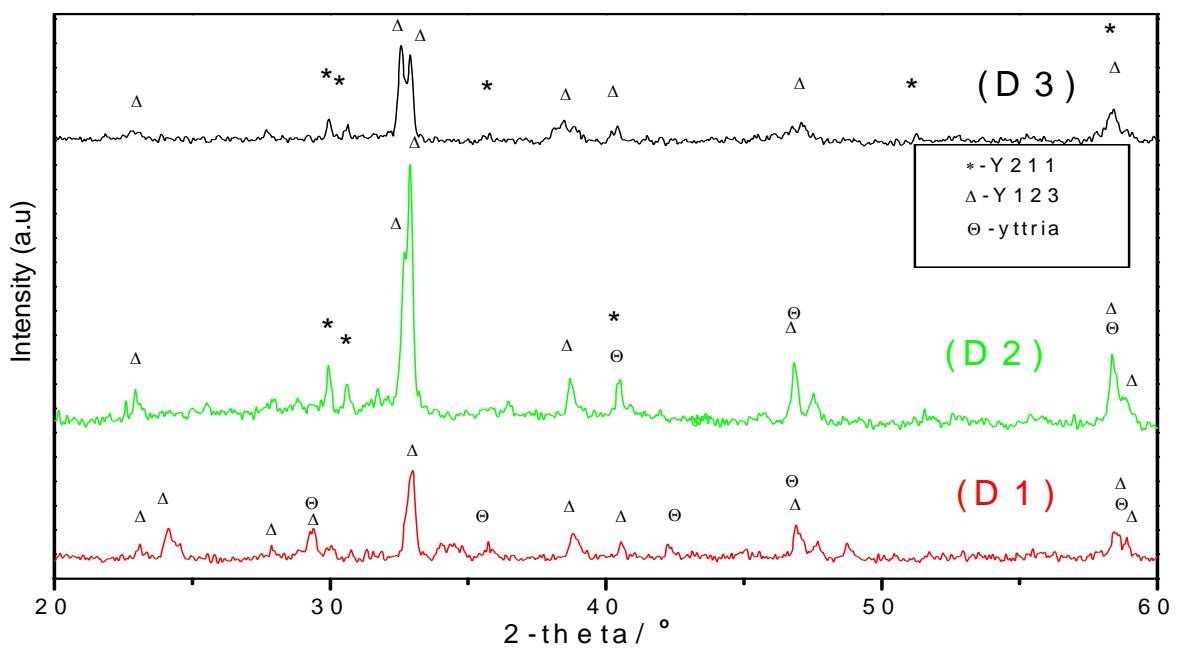


Fig.4.4 XRD patterns of composite D. (D1)-as mixed powder, (D2)-sintered powder, (D3)-Quenched powder

4.5.2. Scanning electron microscopy

The fractured surface, as investigated by SEM, of Y-123 sintered at 930°C for 10h followed by an annealing at 400°C for 10 h in oxygen atmosphere is shown in Fig.4.5. The fractograph revealed presence of a highly porous structure. The grain size distribution was fairly broad and mostly towards a multimodal distribution. The fracture mode is found to be inter-granular in nature.

The fractograph of sintered composite A (Y-123 + 25 wt % Y-211 + 5 wt % Ag) is shown in Fig.4.6a. Like Y-123 sample, this sample was also subjected to sintering at 930°C for 10h followed by an annealing at 400°C for 10 h in an oxygen atmosphere. The composite material attained a relatively higher density as compared to pure Y-123, although the sample was porous in nature. The micrograph reveals the presence of intra-granular fracture.

The fractograph of sintered composite B (Y-123 + 25 wt % Y-211 + 5 wt % Ag) is shown in Fig.4.6b. Like Y-123 sample, this sample was also subjected to sintering 930°C for 10h followed by an annealing at 400°C for 10 h in oxygen atmosphere. The composite material attended a relatively higher density as compared to pure Y-123, although the sample was porous in nature. The micrograph reveals the presence of intra-granular fracture with smaller grain size particles as compared to composite A.

The SEM micrograph of composite C and D, which were subjected to similar heat treatment as mentioned above for pure Y-123 and composite B, is shown in Fig.4.7 and Fig. 4.8, respectively. The microscopic feature of these samples were similar to that of composite B. Like composite B, composite C and D also showed presence of predominantly intra-granular fracture mode.

All the samples composite B (Fig.4.9), composite C (Fig. 4.10 and composite D (Fig.4.11) were heated to 1010°C, soaked for one hour and quenched into the liquid nitrogen bath, have shown open pore free highly dense structure. Predominantly, intragranular fracture mode was observed in the samples. The evidence of randomly distributed elongated grain can be seen in the micrograph. The structure was monotonous and it is difficult to conclude from the micrographs whether there was any secondary phase present along the grain boundary or within the matrix.

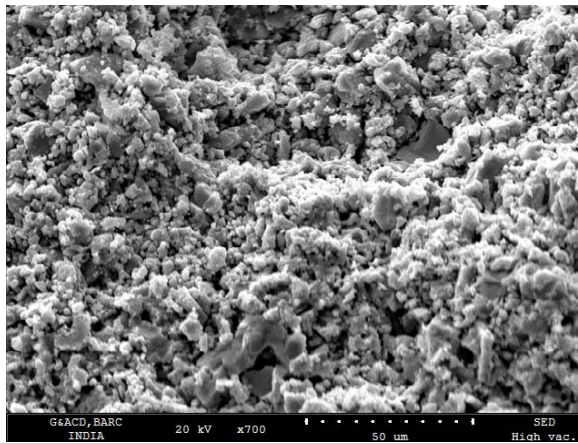


Fig.4.5 SEM micrograph of fractured surface of sintered pure Y-123 pellet

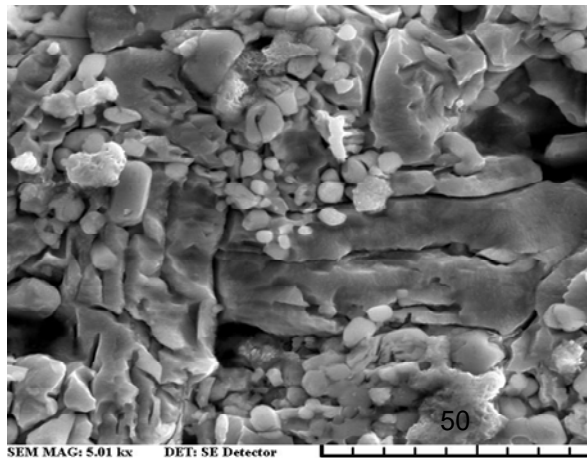


Fig.4.6a SEM micrograph of fractured surface of sintered pellet of composite A

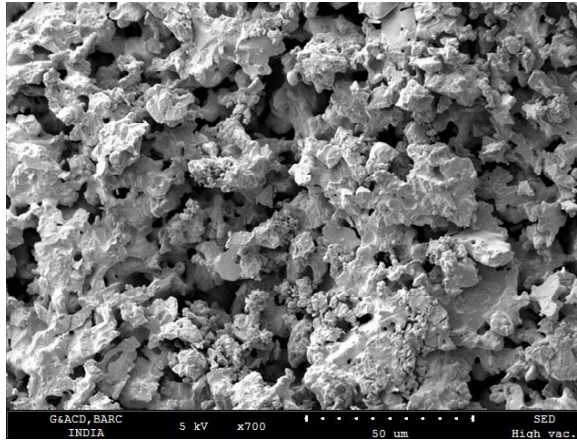


Fig.4.6b SEM micrograph of fractured surface of sintered pellet of composite B

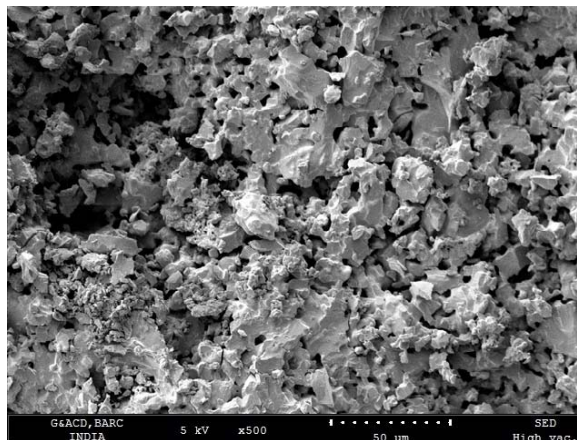


Fig.4.7 SEM micrograph of fractured surface of sintered pellet of composite C

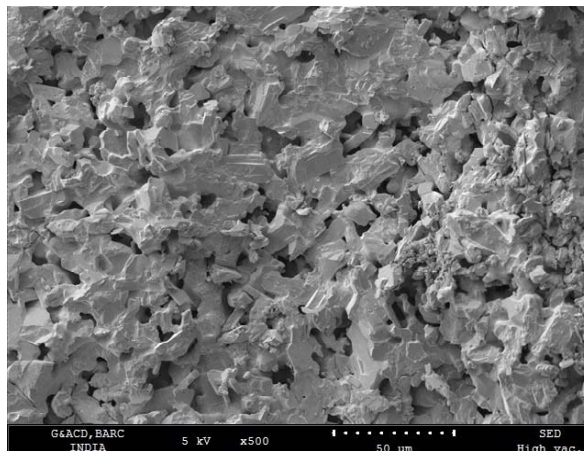


Fig.4.8 SEM micrograph of fractured surface of sintered pellet of composite D

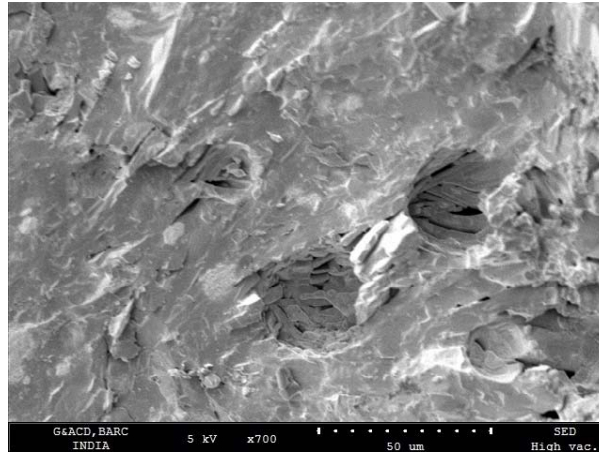


Fig.4.9 SEM micrograph of fractured surface of quenched pellet of composite B

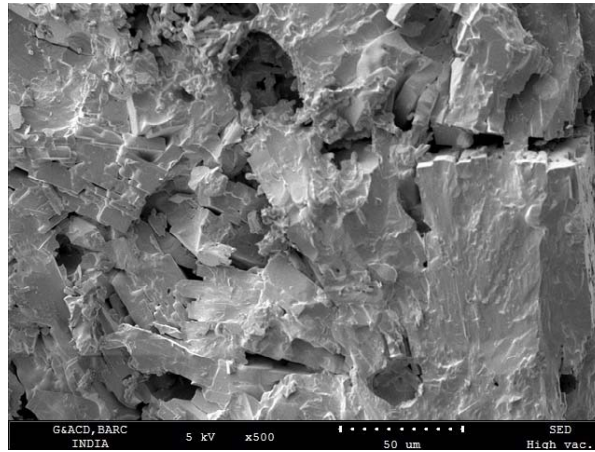


Fig.4.10 SEM micrograph of fractured surface of quenched pellet of composite C

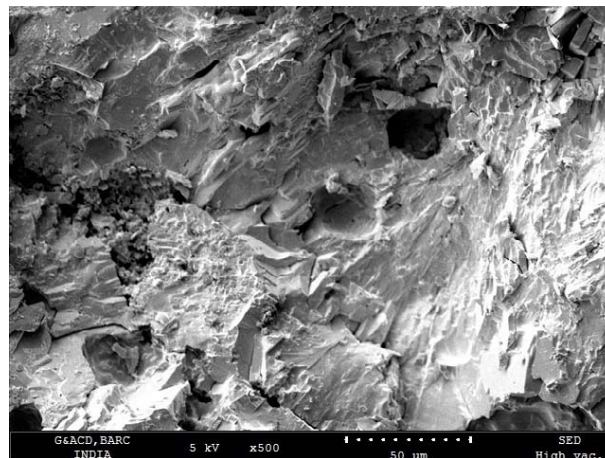


Fig.4.11 SEM micrograph of fractured surface of quenched pellet of composite D

4.5.3 EPMA analysis

Sintered samples of the composites B, C and D were subjected to electron probe micro analysis (EPMA). The back scattered electron images and corresponding X-ray mapping for the elements are recorded.

It is observed from the Fig.4.12 that the BSE image has the dark region due to the presence of porosity in the sintered pellet of composite B. The X-ray mapping of Y clearly shows presence of larger concentration of Y (green colour) in Y-211 phase and relatively smaller concentration of Y in Y-123 phase. The concentration of Cu is more in Y-123 therefore the reddish regions are more and at the same time it can be seen that Y is less at reddish regions. The regions where Y is more, but the Cu concentration is less represents Y-211. The X-ray mapping of Ag shows homogeneous distribution of silver in the matrix. This shows the evidence that Y-123, Y-211 and Ag are uniformly distributed.

It is observed from the Fig.4.13 that the BSE image has also dark region due to the presence of porosity in sintered pellet of composite B. The X-ray mapping of Y shows presence of larger concentration of Y, this is due to addition of excess amount of yttria in the composite. The x-ray mapping of Ba and Cu shows the uniform distribution of Ba and Cu. The X-ray mapping of Pt shows uniform distribution. Thus it is concluded that Y-123, yttria and Pt are uniformly distributed in the composite.

It is observed from the Fig.4.14 that the BSE image has the dark region due presence of porosity in sintered pellet of composite D. The X-ray mapping of Y shows presence of larger concentration of Y, which is due to addition of excess amount of yttria in the composite. The X-ray mapping of Ba and Cu shows the uniform distribution

of Ba and Cu. The X-ray mapping of Ce shows uniform distribution of Ce. This concludes that uniform distribution of Y-123, yttria and CeO₂.

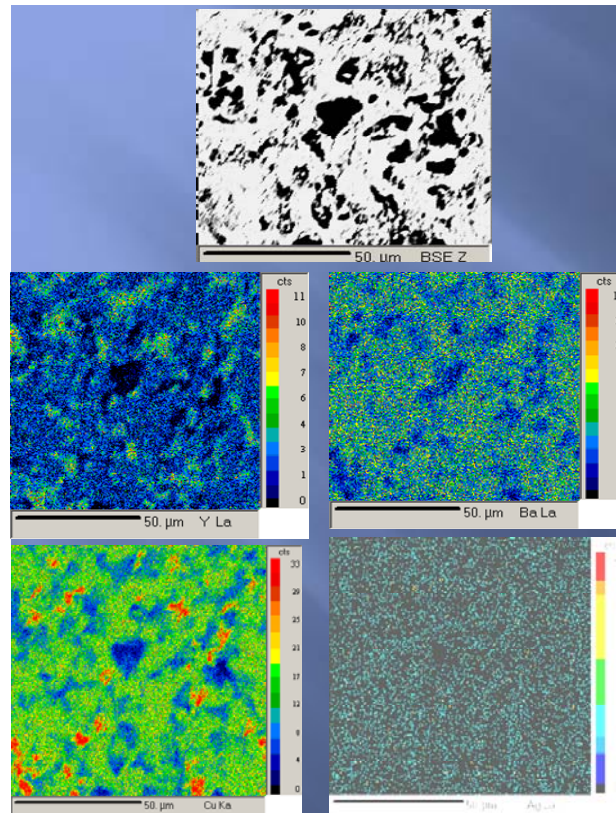


Fig.4.12 BSE image and corresponding X-ray mapping of sintered composite B

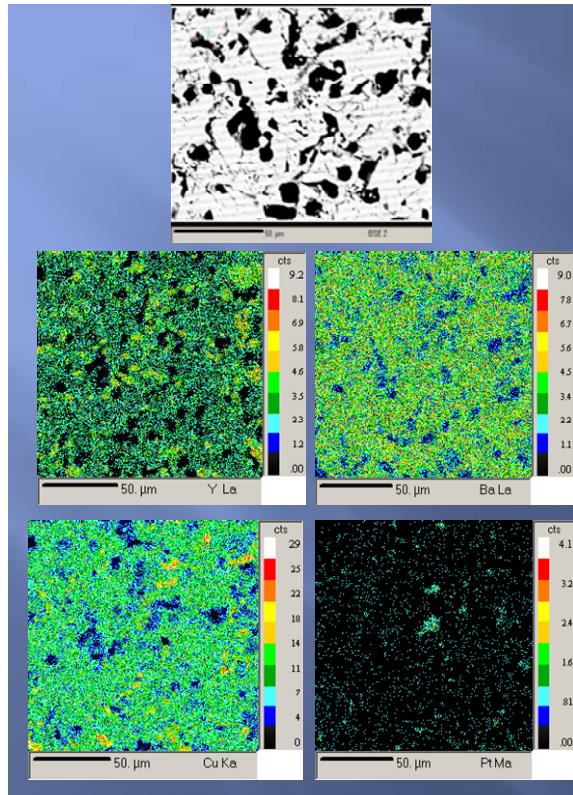


Fig.4.13 BSE image and corresponding X-ray mapping of sintered composite C

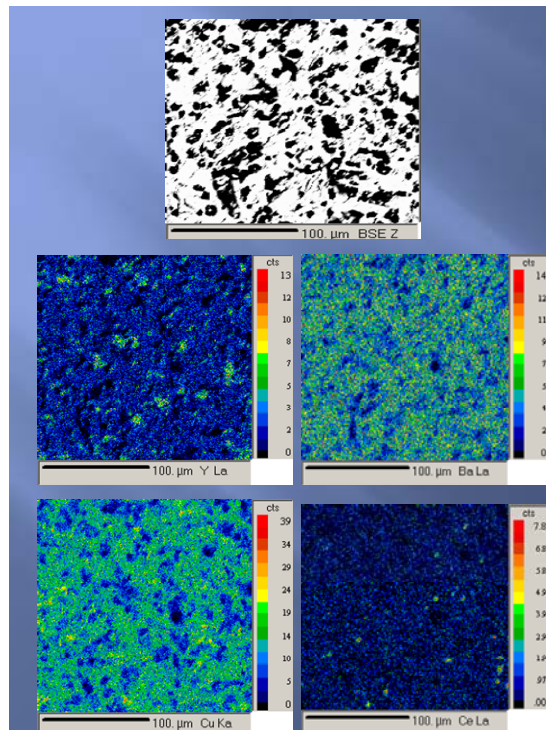


Fig.4.14 BSE image and corresponding X-ray mapping of sintered composite D

4.5.4 Critical transition temperature measurement

All the samples (B2, C2 and D2) were sintered at 930°C for 10 h followed by an annealing at 400°C for 10 h in oxygen atmosphere. Critical temperature measurements on the different types of sintered samples were carried out using the equipment specially designed for this purpose and described earlier in Chapter 2. Resistance vs Temperature (R vs T) plot of B2, C2 and D2 showed onset drop at 94 K, there was no superconducting behavior till 77K liquid nitrogen temperature. The R Vs T data of all the quenched samples B3, C3 and D3 showed semiconducting behavior.

4.6 Conclusion

Four types of composites were prepared i.e. (i) Y-123 + Y-211 + Ag (solid state route), (ii) Y-123 + Y 211 + Ag (Nitrate Decomposition Route) (iii) Y-123 + Y₂O₃ + Pt and (iv) Y-123 + Y₂O₃ + CeO₂. The samples from pure Y-123 and these composites were (a) sintered at 930°C/10 hours and annealed at 400°C for 15 hours in oxygen atmosphere and (b) Quenched from 1010°C into liquid nitrogen bath. The samples have been characterised by X-ray diffraction, scanning electron microscopy, Electron Probe Micro Analysis (EPMA) and critical temperature measurements (T_c). XRD patterns reveal the phase composition while SEM shows the microstructural features. EPMA revealed homogenous elemental distribution confirming uniform mixing during preparation of samples. T_c measurement of pure samples showed a drop at 94 K and there was no superconducting behaviour upto liquid nitrogen temperature, this is because of 25 wt % addition of non-superconducting phase like yttria and Y-211 phase

which destroys the superconducting properties and all quenched samples showed semiconducting behaviour.

The compacts using all the above four composites were fabricated in hollow cylindrical and plate shapes. These compacts were then subjected to MTG, followed by prolonged annealing in oxygen atmosphere. Their detailed characterization is discussed in the next chapter.

CHAPTER-5

Fabrication of components using MTG technique

The stimulus for the development of melt processing techniques has been the demand for high-quality HTSC materials, i.e. materials combining high current density (J_c) and large magnetization with high mechanical strength. In recent years it was realized that the attainment of high J_c and strong magnetization (e.g. for levitation purpose) requires materials in which weak links, involving features such as cracks, voids, high-angle grain boundaries, and insulating phases at grain boundaries, are eliminated. At the same time, a sufficiently high concentration of flux pinning sites (certain defects, impurities or secondary phases) need to be present. The conventional solid state sintering, which was extensively employed during the early development of HTSC materials, yields materials with low J_c values due to the presence of an excessive number of weak links. These materials also tend to have low density and poor mechanical strength. On the other hand, large, pure and stress-free single crystals of Y-123 cannot be expected to contain enough flux pinning centres. Accordingly, the most promising materials for HTSC applications are polycrystalline materials which can provide, on one hand, high density and a high degree of grain alignment to minimize the number of weak links, and on the other hand, a sufficient number of defects to serve as flux pinning centres. As described subsequently, melt-based techniques can be controlled to produce second phases such as Y-211, which provide effective flux pinning sites.

There are many different types of melt processing techniques such as Mixed-Powder-Partial-Melting (MPPM), Melt-Powder-Melt-Growth (MPMG), Powder Melting Process (PMP), Quench-and-Melt-Growth(QMG), Melt-Texture Growth (MTG) and Top

seed melt texture growth technique (TSMTG) which are described as follows. This chapter describes the design of mould for different shapes, filling the moulds with composites, compaction at varying pressure, temperature, subjecting to TSMTG and prolonged annealing in oxygen atmosphere. Further characterizations of the MTG compacts have also been carried out and will be discussed in the next chapter.

5.1 Melt Processing of YBCO

5.1.1 Melt-Texture Processing

Texture processing was developed as a means to avoid or minimize the effects of many of the weak-link limitations to J_c in polycrystalline Y-123. By having a microstructure where the current flow can be directed primarily in the basal plane, and by minimizing the occurrence of high-angle grain boundaries, some of the primary causes of weak link behaviour can be considerably minimized, if not eliminated. Formation of texture in bulk Y-123 has been achieved by a number of different techniques, including compaction processes, magnetic alignment of particles and directional solidification.

Numerous groups have shown that compaction, both with and without the use of elevated temperatures, can help develop texture in Y-123. Although textured microstructures have been produced, however, transport properties comparable to those produced by directional solidification processes have not been achieved [122-123].

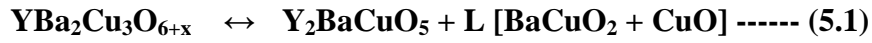
Magnetic alignment has also been successful for developing texture. Particles of Y-123 have been aligned in epoxy [124] to simulate single crystal-like behaviour and also in organic solvents [125-126]. After the solvent evaporates, the aligned particles can be sintered, resulting in well-textured bulk samples. Transport properties achieved by

this technique, however, are not comparable with those produced through directional solidification (see below) because the alignment produced by the applied field allows for rotation in the nonaligned directions (e.g. a and b directions), producing high-angle twist boundaries between aligned grains. A more effective use of magnetic alignment involves solidification in an applied magnetic field. In this case the Y-123 crystals tend to rotate and become aligned while remaining in the liquid phase. As a result, growth under the influence of the field results in a well-textured sample with excellent grain-to-grain alignment [127].

Texturing by directional solidification from the melt has proven much more successful as a means to achieve texturing from the melt. By this route a microstructure is produced that consists of large grains that are well aligned with respect to each other. Grain boundaries in the direction of current flow can be eliminated by these melt-texturing techniques, so that transport J_c values exceeding 10^4 A/cm^2 in applied fields of several Tesla can now be achieved. Since these melt-processing techniques have proven to be so successful, they are the only practical means to achieve high J_c in Y-123, they will be discussed in more details in the following section.

Jin et al. used the term ‘melt texturing’ to describe their pioneering work in this area [128-130]. In the case of Y-123, melt texturing describes directional solidification from the melt or partially melted state. While there are a number of variations of the texturing techniques, as described below, they all involve heating Y-123 above its peritectic decomposition temperature (1015°C in air) and slow cooling to form aligned generally large grains of Y-123. This can be understood upon examination of the section of the ternary phase diagram shown in Fig. 5.1. It can be seen that upon heating above

approximately 1015°C, $\text{YBa}_2\text{Cu}_3\text{O}_{6+x}$ will decompose to yttrium-rich Y_2BaCuO_5 (Y-211) and a yttrium-deficient liquid phase consisting of $\text{BaCuO}_2 + \text{CuO}$. Upon slow cooling (e.g., less than 1°C/h) from 1015°C to approximately 900°C, the Y-123 will nucleate and grow.



5.1.2 Techniques used for melt processing

5.1.2.1 Mixed-Powder-Partial-Melting (MPPM)

In the MPPM process, Y-211 phase pure powder is mixed with a Y-123 pre-calcined powder. The yttrium content of the YBCO precursor can vary from the stoichiometric Y-123 ratio [131] to about zero [132]. The resulting mixture is first heated above the peritectic reaction temperature and then slowly cooled through the peritectic range to react the Y-211 phase with the liquid phase present to form Y-123 with residual Y-211 providing pinning centers. This method was also studied extensively with varying target concentrations of yttrium in the final product in the present investigation. Again, this method, like all other partial melting techniques, suffers from extensive loss of the liquid phase at high temperatures while fabricating large specimens.

The main advantage of various partial melting techniques is that they do not require complete melting, which is normally done in a crucible. Molten Y-123 is very reactive and dissolves almost any crucible materials with which it comes in contact, even noble metals such as platinum and rhodium. Accordingly, the use of partial melting procedures, with the liquid largely confined within the solid structure of the Y-123 material,

minimizes the problem of attack by the reactive melt on the crucible and the resulting contamination of the melt by dissolved crucible material.

5.1.2.2 Melt-Powder-Melt-Growth (MPMG) Process

The MPMG process is similar to the QMG process described latter, being usually practiced with a starting powder stoichiometry that is Y-211 rich [133-134]. The key to this variation on QMG is that the quenched material is powdered before further processing to ensure a homogeneous distribution of Y_2O_3 (which then converts to Y-211) in both the melt and the final melt textured microstructure. The resulting acicular Y-211 particles are less than $1\mu\text{m}$ in length. Murakami [134] has reported that the properties of MPMG processed material improve with increasing Y-211 content and has suggested that Y-211 acts directly as flux pinning site.

5.1.2.3 Powder Melting Process (PMP)

The PMP process was developed by Lian and his coworkers [135]. This method uses a starting mixture of Y-211/ $BaCuO_2$ /CuO powders to secure a uniform distribution of fine Y-211 in the melt without having to employ a melt-quenching process. The pressed samples are processed either by the MTG or modified MTG thermal profile, which yield microstructures identical to those obtained when comparable premixed YBCO stoichiometries are similarly processed. The advantage of this process is that the initial particles size of the Y-211 can be controlled, for example, by milling or using a sol-gel route to produce the Y-211. In MTG by comparison, there is less well defined control over the Y-211 size. Although not mentioned explicitly temperatures because of

the precursors used, since the liquid phase melts below this temperature and begin reacting with the Y-211.

5.1.2.4 Quench and Melt-Growth (QMG) Process

The QMG process was first reported by Murakami and his coworkers [136-138]. This method involves using the Y-211 peritectic reaction to refine the size of the starting Y-211 particles. First, a sintered sample (or a mixture of calcined powders of the required stoichiometry) is quickly heated above the Y-211 decomposition temperature (1270°C) in a platinum crucible. The material is held at 1400°C for 20 minutes and then quenched using cold copper plates. The quenched sample consists of Y₂O₃ particles and an amorphous liquid phase. The quenched material is then processed by the modified MTG process described earlier. When heated above 1015°C, the Y₂O₃ reacts with the liquid to form Y-211, which in turn reacts with the liquid melt on cooling to form Y-123. The distribution of Y-211 in the melt is controlled by the distribution of Y₂O₃ in the quenched material. For stoichiometric Y-123, the QMG process results in a textured material that has little residual Y-211 phase and J_c values on the order of 2 x 10⁴ A/cm² in zero applied field. The Y-211 refinement which leads to near complete reaction with the applied field. The Y-211 refinement which leads to near complete reaction with the liquid to form Y-123 has subsequently been attributed to the presence of platinum in the melt (dissolved from the sample crucible).

5.1.2.5 Melt-Texture Growth (MTG) technique

The MTG process first demonstrated the feasibility of using melt processing to align grains to overcome the electrical anisotropy in Y-123 materials. With this technique, sintered Y-123 was partially melted at about 1150°C and then slowly cooled in a thermal gradient. The resulting microstructure showed preferred orientation for grain growth in the a-b plane and large, non uniformly distributed spherical Y-211 particles upto 40 microns in length. The connectivity of the Y-123 plates was not good and was attributed to non-uniform growth conditions associated with the Y-211 particle distribution. Although the properties were much improved over those of sintered materials, the J_c was found to drop precipitously in magnetic fields, indicating the absence of adequate flux-pinning sites in the Y-123 matrix. Jin's initial success with the MTG process [139-141], which enhanced J_c two or three orders of magnitude over that of sintered materials (with significantly less field dependence) led to a variety of melt-texturing methods which were developed in an effort to further improve properties and facilitate processing.

5.1.2.6 MTG Process

The modified MTG process was developed to homogenize the Y-211 distribution and minimize the Y-211 coarsening observed during the MTG process [142]. Here, samples are again quickly heated to approximately 1100°C, but rather than being slow cooled, they are held for only 20 minute at the maximum temperature before being quickly cooled to the peritectic temperature. The samples are then slow cooled from the peritectic temperature to about 950°C. The initial heating and thermal hold at 1100°C is

designed to ensure adequate sample melting (required to minimize pore formation), while the quick cooling to the peritectic temperature minimized Y-211 coarsening. The final microstructure shows improved Y-123 connectivity and a more uniform distribution of fine Y-211 particles ranging from 1 to 5 μ m size. The bulk textured material can be produced using the Melt-textured growth (MTG) technique.

5.1.2.7 Modified MTG Process

Top-seeded melt texture growth (TSMTG) is known as the most effective process to fabricate block-type samples used for example in energy storage applications, such as superconducting flywheel system and others. In this technique, too long isothermal step and large processing times is regarded as one of the most significant weak points. In the case of melt texturing with a temperature gradient, processing time is shorter, but the sample shape and size are restricted.

The TSMTG technique has been widely used to grow $\text{YBa}_2\text{Cu}_3\text{O}_x$ crystals as large as several centimetres [143], but these crystals were intended for application like magnetic levitation. The size of single-domain is generally about several centimetres in diameter and limited to about 10 cm for high quality YBCO bulk up to now, because of the grains mis-orientation during the melt growth process [144]. The resulting cubic centimetre-size YBCO crystals are further annealed to obtain the oxygen-ordered orthorhombic phase ($x=6.5$).

Uniquely, the TSMTG process yields large, single grains of approximately the dimensions of the green body [145-147]. The TSMTG technique has become the preferred method for the fabrication of bulk Rare earth (RE)-123 superconductors and is

used routinely in the processing of single-grain cylindrical/square shape samples of up to 50 mm in diameter [148].

TSMTG processing is classified into two types by seeding method; cold seeding and hot seeding. Cold and hot seeding are named for the moment when the seed crystal is placed on the powder compact. In case of sample handling, the cold seeding method is easier than hot seeding, because the seeding is performed at room temperature [149]. In this study the seeding method used is cold seeding has been employed for TSMTG.

In order to obtain large-domain-sized YBCO and to control the growth orientation, seeding affects should be taken into consideration sufficiently [150]. The seed should not only have a similar structure and lattice constant of similar order to those of as-grown YBCO bulks, but also control the orientation and ensure single-domain growth [151]. The seed crystal initiates the nucleation and growth of the Y-123 phase in the incongruent melt, which subsequently solidifies into single large grain during controlled cooling.

A variety of seeds have so far been applied for the melt-textured (MT) growth of YBCO bulks [150], can be classified into three major categories :

- i. Non-superconductors, such as MgO.
- ii. Bulk superconductors, such as RE-123 Melt texture bulks or single crystal, such as Nd-123, Sm-123, and others.
- iii. RE-123 thin films (RE-Rare-earths) [152].

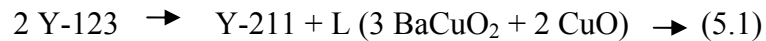
In principle, the seed material should not melt during the texture process, because the maximum process temperature should be below their melting points. However, the seed crystals were observed to dissolve frequently when they were in contact with the Ba-Cu-

O liquid that was formed as a result of the incongruent melting of Y-123 compact during a high temperature holding period [153]. As the seed dissolves during processing, it no longer acts as a seed for growth of textured Y-123 crystal. In the case of dissolution formed, decreasing the levitation force and trapped magnetic field by reducing the size of the shield current loop has been observed. For this reason, the growth mode of Y-123 grains is critically dependent on seed thickness [154].

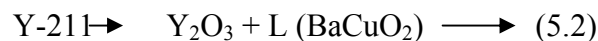
This chapter describes, in details, the TSMTG process and fabrication of bulk textured components using cold isostatic pressing (CIP) for preparing green compacts.

5.2 The Y-123 Pseudo-Binary Phase Diagram

The Y_2O_3 -CuO-BaO phase diagram has been the subject of many investigations. Recently a summary of existing phase diagrams for all high-temperature superconductors has been published [155]. Aselage and Keefer [156] identified eleven invariant points on the Y_2O_3 -CuO-BaO phase diagram, including the incongruent melting temperature of Y-123 and Y-211. They found that Y-123 decomposed in air at 1015°C and resulted in the formation of Y-211 and a barium-rich liquid according to the following relation:



On further heating the decomposition of the Y-211 phase was found to occur at 1270°C and produced Y_2O_3 and a liquid as follows:



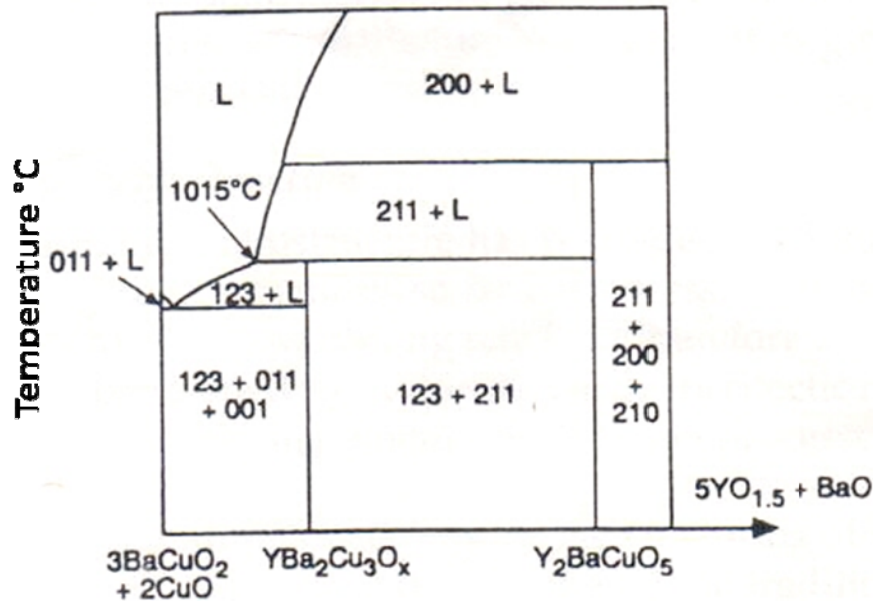
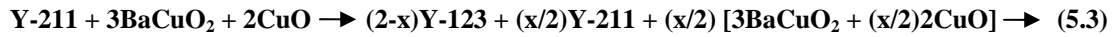


Fig.5.1 Section of the Y-123 ternary phase diagram [139-140]

Subsequently, these two sets of peritectic reactions have formed the basis for all YBCO melt-texturing techniques aimed at eliminating the problems associated with both the weak-link character and the poor pinning properties of sintered YBCO. All the significant melt-processing strategies to date ultimately involve slow cooling from the partial melt (above 1015°C) to below 960°C (either isothermally or in a temperature gradient) to form Y-123. As with other (metallic) peritectic systems, the reaction of the primary phase (Y-211) with the liquid to form the peritectic product (Y-123) is extremely slow and rarely proceeds to completion to yield phase-pure Y-123 under normal melt-processing thermal cycles.

For stoichiometric Y-123 samples, this incomplete reaction can be exacerbated by a combination of inadequately slow cooling rates and / or liquid phase segregation (i.e., to the sample surface or grain boundaries), which results in a shift in composition to a more 211-rich stoichiometry. Even under optimal conditions, however, the reaction

usually will not go to completion because growing Y-123 will trap unreacted Y-211, eliminating its further reaction, as the growing Y-123 traps unreacted Y-211, eliminating its further reaction with the liquid. Consequently, on cooling the reaction is more accurately represented as



If the growth of Y-123 were to proceed by the conventional peritectic mechanism, the primary solid (which would be Y-211 in this case) would react with the liquid to form a shell of peritectic product (Y-123) around itself. The reaction would proceed by the diffusion of species through this shell and would result in a microstructure containing randomly oriented (Y-123) grains which could have undissolved primary solid (Y-211) cores. The fact that melt-processed YBCO does not result in this cored microstructure indicates that its growth from the melt is not by the conventional peritectic mechanism.

5.2.1 The Y-123 peritectic reaction

Although a desirable microstructure has been identified that yields high J_c values, generating such structures so far has necessitated extremely slow cooling rates (0.1-0.3°C/h). The slow cooling rate (and therefore the long processing time), which is necessitated by the kinetics of the peritectic reaction, is the greatest disadvantage of the directional solidification processes as currently practiced.

Much of the early literature concerning the melt texturing of Y-123 assumed that the formation of Y-123 from the melt occurs by the traditional peritectic reaction in which the Y-123 forms a shell around a Y-211 particle and thus separates the Y-211 from

direct contact with the Ba- and Cu- rich liquid. This Y-123 envelope would then slow down any further growth of Y-123, since it would depend on the solid-state diffusion of the reactants through the Y-123 layer. The existence of such a shell is, however, not seen in melt-textured Y-123.

It has been postulated that in most peritectic systems, the peritectic reaction does not occur because crystallization of the peritectic phase occurs directly from the liquid. In peritectic systems in which the liquidus lines of the properitectic and peritectic phases coincide, however, a peritectic reaction can occur at some temperature below the peritectic temperature. St. John has examined the peritectic reaction [157]. In this work he distinguishes between the peritectic transformation and the peritectic reaction. The peritectic reaction is the formation of the peritectic or secondary phase (Y-123, in this case) by reaction of the primary phase (Y-211 in this case) with the liquid at the peritectic temperature. This is the reaction between Y-211 and liquid Y-123. The peritectic transformation, distinct from this, is the growth of the secondary phase (Y-123), which occurs by diffusion through the already-formed secondary phase coating the primary phase. The work by St. John and a number of other groups has shown that a competition exists between the peritectic transformation, which occurs relatively slowly because of the rate limiting solid-state diffusion, and nucleation of the secondary phase directly from the melt. The extent to which the peritectic product grows by the peritectic transformation as opposed to nucleation from the melt will depend on the rate of solid-state diffusion step, and nucleation of the secondary phase directly from the melt. The extent to which the peritectic product grows by the peritectic transformation as opposed to nucleation from the melt will depend on the rate of solid-state diffusion through the

peritectic product. In all of the systems in which secondary-phase nucleation from the melt have been reported the secondary phase is not a line compound, as is the case for Y-123. In other work [158] St. John has classified peritectic systems into three types depending on the slopes of the α solidus and the solvus line between the α and $\alpha+\beta$ regions. In Type C systems, in which line compounds form, the extent of the peritectic transformation is only marginally observed. This suggests that during the formation of Y-123, the main mode of formation can be expected to be a growth directly from the melt.

5.2.2 Mechanism of Y diffusion growth model

In 1992, Izumi [159], Cima [160] and Mori [161] reported a Y-123 growth model based on yttrium diffusion. They assumed that the Y-123 crystal growth rate is limited by the yttrium diffusion. In a classical peritectic reaction, once the Y-123 formation occurred, the Y-211 particles would be wrapped by Y-123 phase and yttrium would have to diffuse through the Y-123 solid towards the liquid phase. As the Y-123 becomes larger, it would become more difficult for yttrium to reach the Y-123 solid–liquid interface. The resulting microstructure would be an assembly of Y-123 grains with a Y-211 core. This is not what is experimentally observed. On the contrary large Y-123 grains are obtained trapping many Y-211 particles.

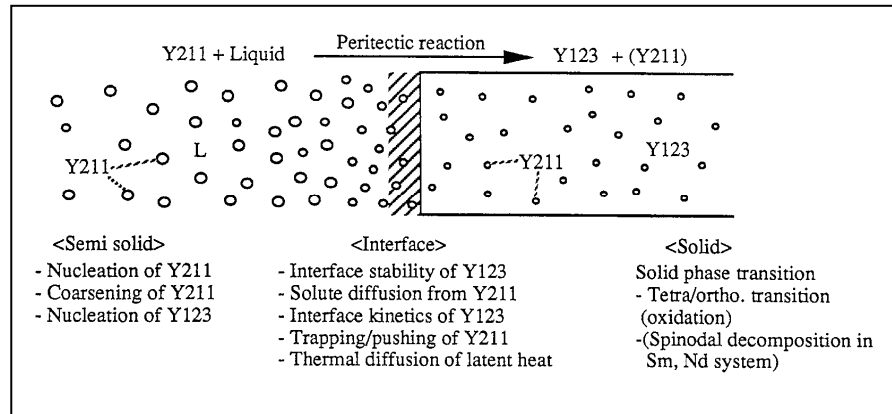


Fig.5.2. Mechanism of Y-211 diffusion to solid Y-123 front growth in MTG technology [161]

To solve this inconsistency, a new mechanism has been proposed which is illustrated in Fig. 5.2. In this model, the Y-211 particle dissolves partially in the melt and the yttrium is transported to the growing Y-123 interface by diffusion in melt. Once the Y-123 nucleation occurs, the required amount of yttrium necessary for the Y-123 growth front is provided by the neighboring Y-211 particles. As the liquid phase is depleted in yttrium by the growth front, these particles partially melt to compensate the yttrium depletion. The dissolved yttrium ions travel across the liquid to the Y-123 growth interface front- driven by the yttrium gradient for feeding the Y-123 crystal continuous growth. Thus, the growth rate is controlled by the yttrium diffusion rate.

5.3 Compaction of composites

Unlike metals, ceramics are generally shaped using different techniques like cold isostatic pressing, hot isostatic pressing etc. Prior to heating, it is essential to have a preform with shape and dimensions close to the final geometry. This is not only due to

their brittle nature which makes them difficult to machine, but also because pressure is normally required before subjecting them to thermal cycle so as to ensure large areas of surface contact between the grains. Such large areas of surface contact not only increase reaction rates, but also tend to increase the density and strength of the components.

The fabrication of components of different shapes follow various steps sequential such as :

- i. Densification by using Cold Isostatic Press (CIP)
- ii. Sintering
- iii. Subjecting to thermal cycle through melt texture growth (MTG) technique

Compaction study has been carried out to achieve maximum green density by varying the pressure in CIP. The effects of pressure are :

- (i) To reduce pore size
- (ii) To break up particles at surfaces in contact
- (iii) To introduce strain and plastic flow to achieve maximum green density.

5.3.1 Preparation of preform and densification

Since the components are of larger size, uniaxial pressing is not possible, where L/D ratio cannot be maintained. This leads to variation in density in the entire sample and also complex shapes cannot be pressed using uni-axial pressing. Therefore, for higher L/D ratio and to achieve uniform density throughout the sample, cold isostatic pressing (CIP) was used. The compacts using CIP are generally more homogeneous i.e. a uniform density is maintained in the entire compact shape and it is free of microcracks compared

to the axially pressed counterparts. During cold isostatic pressing, the pressure is applied hydrostatically, resulting in a uniform pressure on all points of the mould.

5.3.1.1 Designing of rubber mould for fabricating different shapes

The required final dimensions to be used in various application are mentioned in Table 5.1. The components as mentioned in Table, at Sr. nos. 1, 2 and 3 have been used to fabricate HTSC prototype motors and fault current limiters and component 4 have been used to study the effect of ceria and Pt on superconducting properties. The fabricated component sr. no 5 was cut in to two halves horizontally and their critical density has been measured. The result of both halves will ensure that the J_c value is uniform in both halves. These results will be discussed in subsequent sections.

Sr. No	Shapes of the components	Final size of MTG components required for applications
1	Hollow cylinder	36mm ID x 46mm ODmm x 50 mm height
2	Plates	25mm width x 50mm height x 3.5mm thick
3	Pins	8 mm OD x 25 mm height
4	Hollow cylinders for studying the effect of additives like ceria and Pt on HTSC properties.	~29 mm OD x ~19mm ID x ~32mm
5	Hollow cylinders for studying transport property in top and bottom portion.	—

Table 5.1 Required final dimensions of MTG components

To obtain the required final dimensions in MTG components, silicon rubber moulds were designed. Some of the moulds along with corresponding dimensions are shown in Fig.5.3 and the corresponding dimensions in Table 5.2. Moulds were designed in order to account for the shrinkage during compaction and sintering as well as before subjecting to melt texture growth technique (MTG). The anticipated reduction in dimension at all the three stages has to be computed for design of the moulds. Hardness of mould was optimized, so that the pressed compact is easily removed from the mould after releasing the pressure. The optimized hardness of the silicone rubber mould was optimized at 55-60, and pressure varies from shape and size of the component to be pressed.

5.3.2 Densification of composites using CIP

The granulated composites prepared as the procedure described in the previous chapter were filled in the respective moulds as shown in Table 5.2. Filling and vibrating of moulds on a vibrating mill is done simultaneously as shown in Fig.5.4. Vibration is carried out to ensure that the powder is uniformly filled in the mould to ensure pore free, and to achieve compact with maximum packing green density. The type of the composite, size of the mould used to fill and corresponding name of the component are mentioned in Table 5.3 along with the applied pressures which were optimized for different size to achieve maximum green density without lamellar cracks in the compacts. Maximum shrinkage is observed during compaction in CIP (see Table 5.4).



Fig.5.3 Picture of moulds for fabricating components :- (1)-Mould for hollow cylinder 1, (2)- Mould for Plates, (3)-Moulds for PINS, (4)-Moulds for hollow cylinder 2, (5)-Mould for hollow cylinder 3

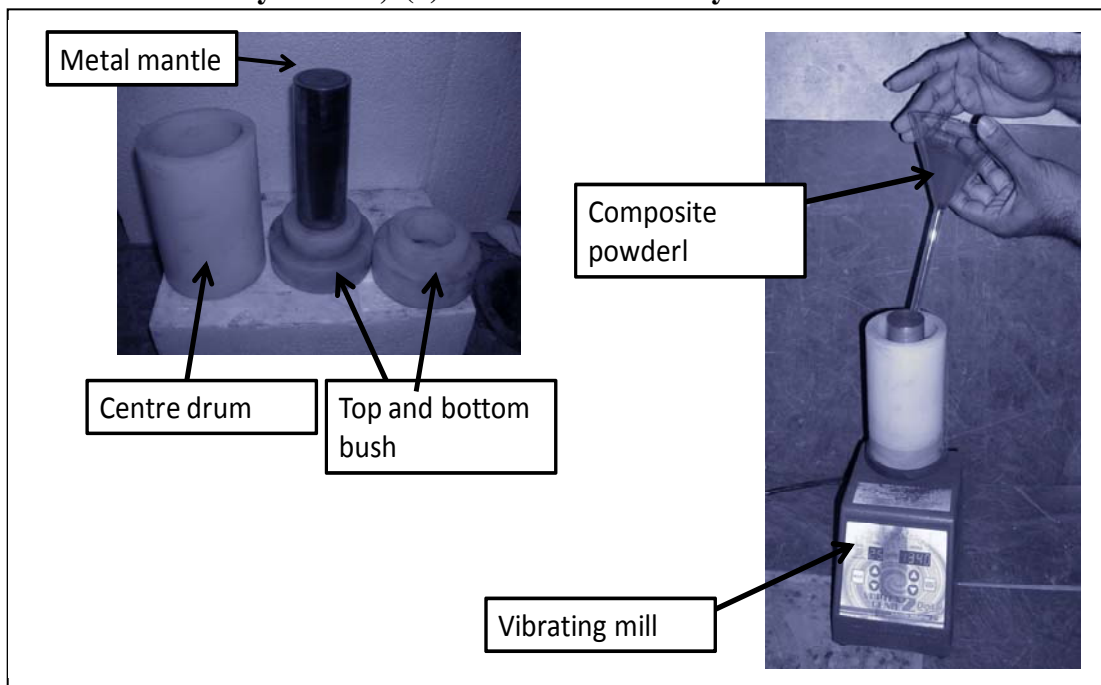


Fig.5.4 Typical picture of mould and filling composite powder in mould with vibrating

Sr. No (photograph)	Mould shape	OD (mm)	ID (mm)	Height (mm)
1.	Hollow cylinder 1	75	56	70
2.	Plate 1	45 width (W)	6 thick (T)	70
3	Pins 1	20	13	35
4	Hollow cylinder 2	35	23	38
5	Hollow cylinder 3	75	24	25

Table 5.2 Various moulds with shapes and sizes designed for fabricating components with corresponding photographs

Name of the composite used	Shape of the rubber mould used as mentioned in Table 5.2	Component name	Pressure applied (bar)
Composite A	Hollow cylinder (1)	SSR-CY-1	3000
Composite A	Plate 1	SSR-PL-1	3000
Composite B	Hollow cylinder (1)	NDR-CY-2	3000
Composite B	Hollow cylinder (3)	NDR-CY-3	3000
Composite B	Plate 1	NDR-PL-2	2500
Composite B	Pin 1	NDR-PI-1	2000
Composite C	Hollow cylinder (2)	Pt-CY-5	2500
Composite D	Hollow cylinder (2)	Ce-CY-6	2500

Table 5.3 Components fabricated using composites in rubber moulds

(Abbreviations used are as follows: NDR- nitrate decomposition route, SSR- solid state route, CY- cylinder shape, PI- pins shape, PI-plate shape)

5.4 Solidification of compacts using MTG and TSMTG technique:

In bulk material, weak links that affect current transport arise from a combination of several features, including

- a) High angle grain boundaries.
- b) Anisotropic current flow resulting in circuitous paths.
- c) Chemical or structural variations at grain boundaries.
- d) Insulating intergranular phases, and
- e) Microcracking due to thermal stresses arising partly from phase transformations and partly from anisotropic expansion coefficients.

A major goal in processing HTSC material for applications requiring high currents lies in texturing the grains. The procedure for obtaining textured Y-123 grains using MTG technique is described as follows. The texturing occurs as a result of growth of new Y-123 grains from the slowly cooled Y-211 and yttrium deficient liquid below the peritectic temperature. A typical schedule employed by the MTG is indicated in Fig. 5.4. If the temperature of the materials is kept within a few degrees of the melting temperature, the pre-sintered material remains rigid during processing, though densification and shrinkage occur. The grain growth is slow as this diffusion controls texturing, so the process is time consuming.

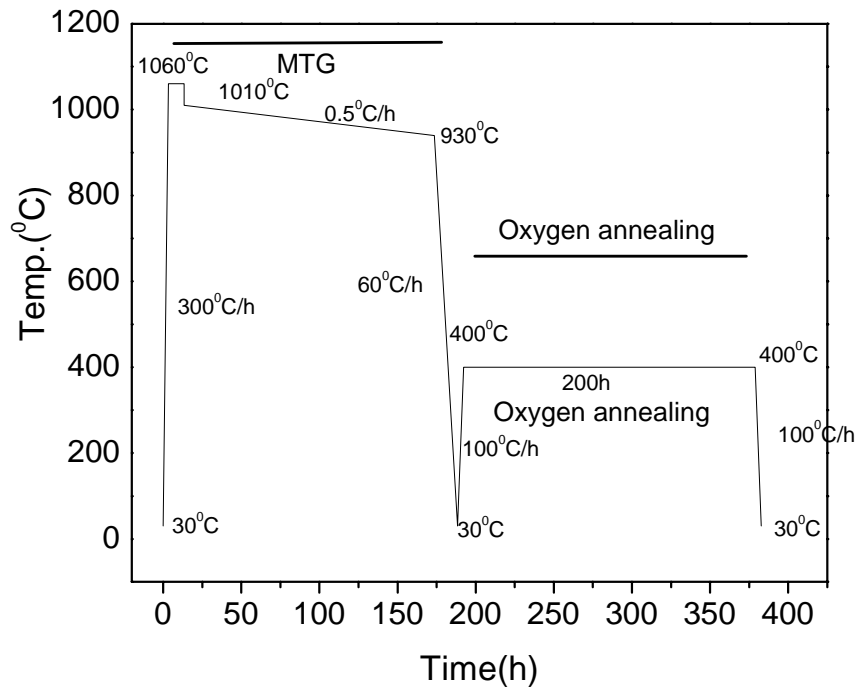


Fig.5.5 Typical thermal schedule for fabricating MTG components

5.4.1 Sintering of compacts

During MTG process the compact attains higher temperature than the peritectic temperature 1010°C, the upper portion partially melts and shrinks. The lower portion of the compact also partially melts, reacts with the container/base support due to which the shape is distorted at the bottom where the sample is in contact with base material. The lower part of the compact has to be cut and discarded. Therefore in order to decrease the loss of material and to retain optimum shape of the compact, a pre-sintering step is introduced to all the green compacts before it is subjected to MTG in which the compact is slowly heated to 930 °C at rate of 2°C /min and soaked for 5-10 h depending on the size, shape of samples and cooled to room temperature at the rate of 6°C/min to avoid

thermal shock due to which cracks may be generated in the sample to near melting point. It ensures the maximum shrinkage in the components while sintering.

5.4.2 Melt texture growth technique (MTG) of compacts

The typical flow chart of heat treatment pattern followed in this study is shown in Fig. 5.6. The optimization of the temperature profile is crucial for the production of large YBCO components. Depending upon the shape and size of the compacts the temperature varies. The cylindrical and pins shape compacts were heated up to 1060°C at a rate of 300 °C/h, and held for 6-10 h for homogenous melting. The hold time varies depending upon the shape and size of the samples. At this temperature Y-123 dissociates into solid Y-211 and liquid of Ba and Cu oxides. After that, the samples were cooled to about 1010°C at a rate of 180°C/h, and further cooled to 960°C at a rate of about 0.3-0.5°C/h. During slow cooling from 1010-940 °C (peritectic temperature) the Y-123 nucleates from undercooled mixture of Y-211 particles and melt consisting of BaCuO₂ and CuO. Thus to facilitate the growth of Y-123, the dissolution of Y-211/yttria is essential so that additional Y³⁺ ions are supplied to Y-123 solidification front. The solidification front will engulf Y-211/yttria particles, this depends upon the particle size of Y-211, velocity of the growth front and interface energies between Y-123, Y-211 and the melt. Therefore it was decided to add 25 wt % of Y-211 in all NDR-X-X and SSR-X-X samples, and 25 wt% yttria to Y-123 in Pt-Cy-4 and Ce-Cy-5 samples before melt processing [samples decoding given in Table 5.3]. This ensures the formation of defects, which are necessary for pinning, as well as enough supply of Y³⁺ so that loss of liquid during melting is minimized. Y-211 recombines with BaCuO₂ liquid to form Y-123. Then the samples

were cooled to room temperature at a rate of 300°C/h. All the TSMTG was performed in the indigenously fabricated furnace, the compacts were kept on an alumina crucible, since the sample reacts and sticks with the alumina base after MTG process, it becomes difficult to remove from the alumina crucible, to avoid this, 1-2 mm bed of Y-211 coarse powder was spread in between compact and the alumina crucible, which helps in easily removing the sample from the crucible. To maintain the circularity of the hollow cylinders and pins, the compacts were kept in alumina cylinder. A gap between the compact OD and the ID of alumina cylinder is 5-7 mm. This arrangement helps in maintaining the constant temperature of the compacts.

The thermal schedule for SSR-CY-1, NDR-CY-1 and NDR-CY-3 is as shown in Fig.5.5. The temperature was raised to 1060°C at the rate of 300 °C/h and held for 10 h where partial melting takes place. Further the sample was cooled to 1010°C at the rate of 600 °C/h. From 1010 °C to 940°C where the nucleation starts, the compacts were slow cooled at the rate of 0.3-5 °C/h. The furnace was cooled to room temperature from 940°C.

In the thermal schedule for SSR-PL-1, NDR-PL-2, NDR-PI-1 and Pt-Cy-5 and Ce-CY-6 temperature was raised to 1060°C at the rate of 300 °C/h and held for 6 h where partial melting takes place, further cooled to 1010°C at the rate of 600 °C/h, and then cooled to 940°C at the rate of 0.3 °C/h. Finally, the compacts were furnace is cooled to room temperature.

The soaking temperature for plates and pins were slightly less i.e. 3-4 h, and for cylinders the soaking time was 10 h at 1060°C. Rest of the thermal schedule remains

same as that for cylinders. Since the wall thickness is around 20mm, to partially melt the whole component, The soaking time higher than pins and plates was required.

Finally, the as-grown MTG specimens were annealed at 400- 450 °C in flowing oxygen for 150-300 h (In this step phase transformation from tetragonal to orthorhombic phase occurs as a result of oxygenation).

Top seeded melt texture growth were carried out in Pins and plates samples. A MgO seed crystal of preferred orientation (00l) with a size 1mm x 1 mm was placed on the top portion before commencing MTG process.

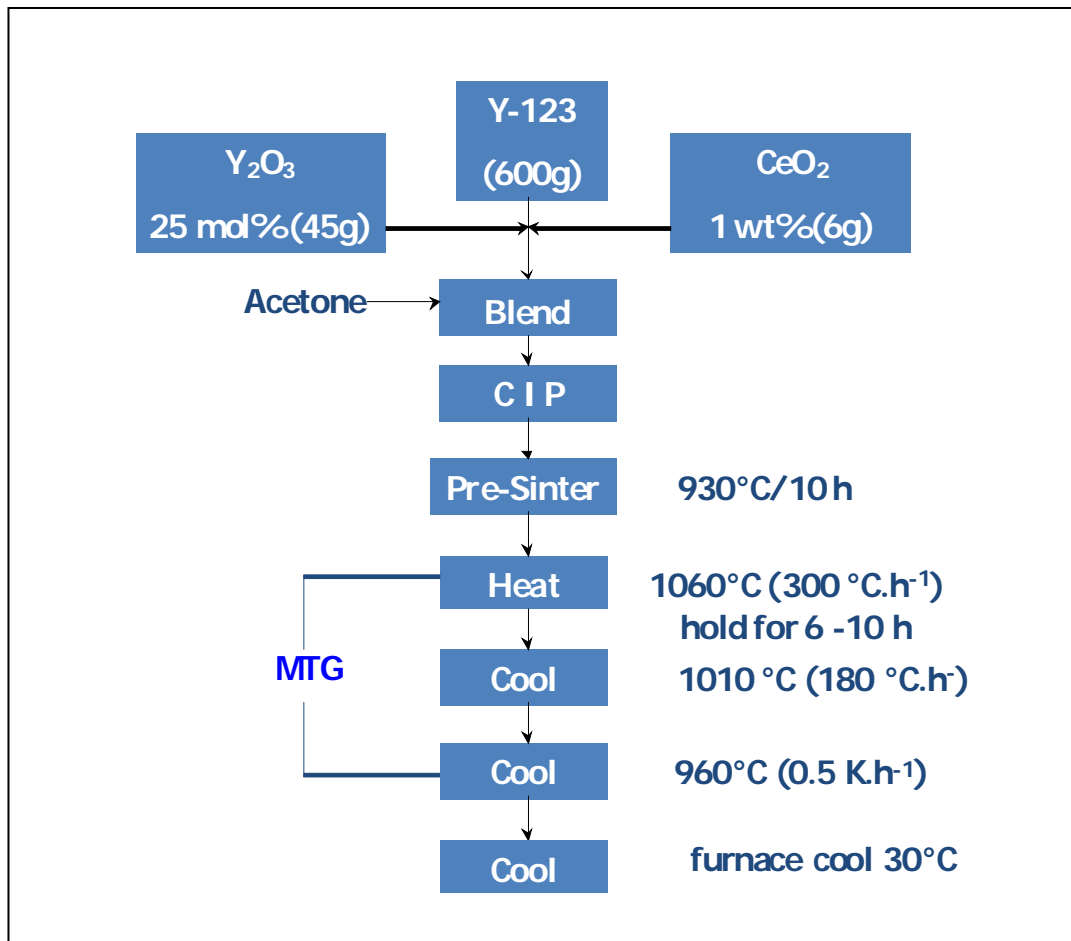


Fig.5.6 Flow chart of typical MTG technique

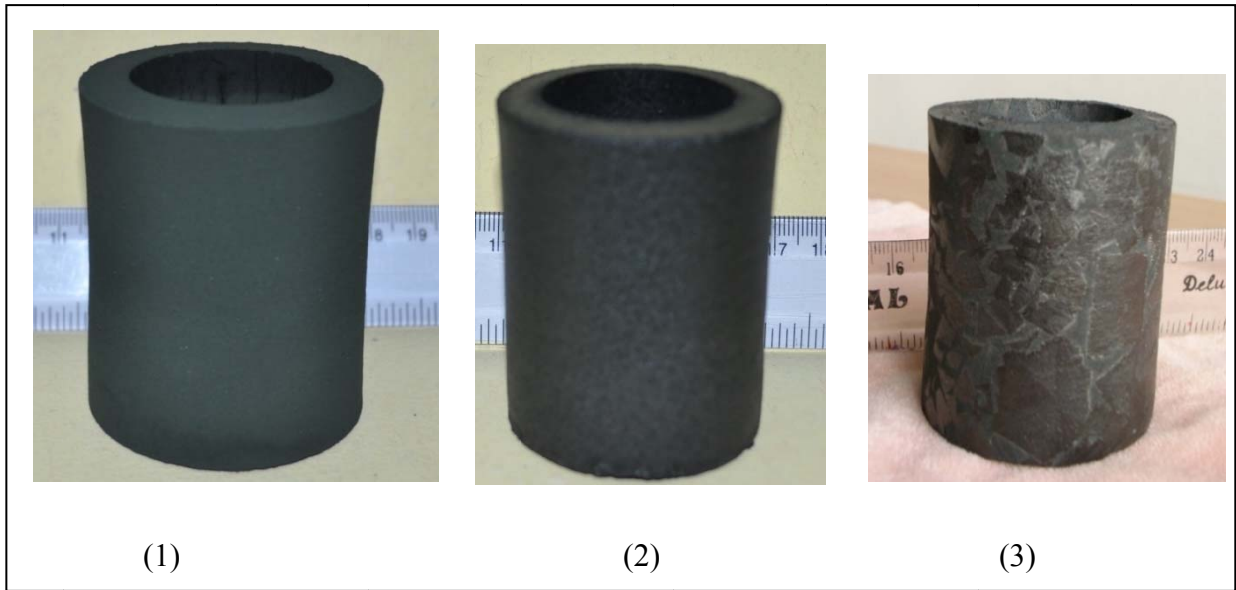


Fig.5.7 Picture of cylinder during stages of fabrication using mould size hollow cylinder size as mentioned in Table 5.1 Sr. No. 1 : (1) Compacted cylinder, (2) Sintered cylinder, and (3) MTG cylinder

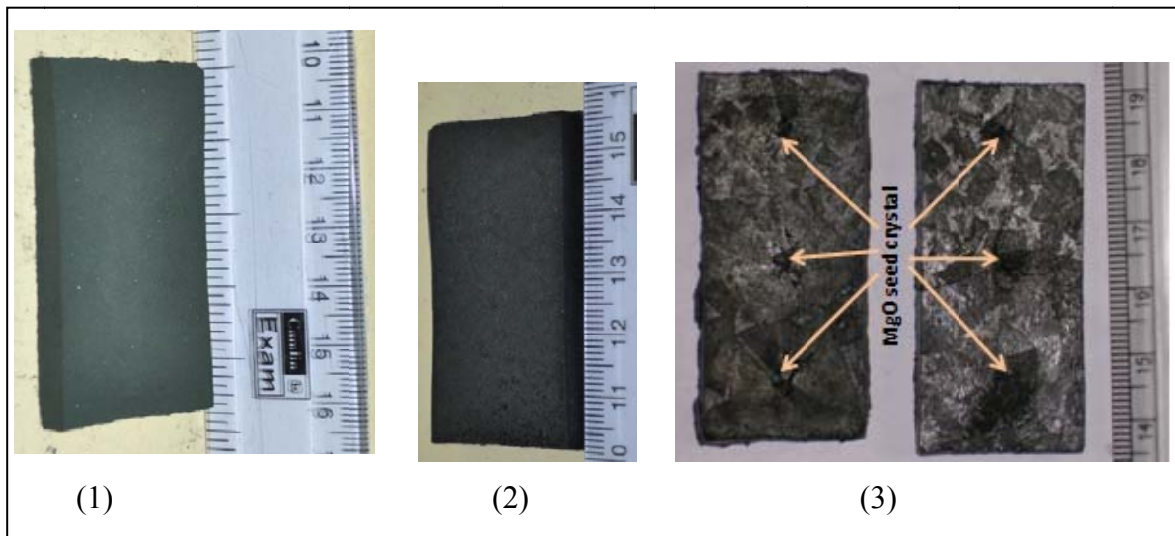


Fig.5.8 Pictures of plate during various stages of fabrication using mould size plate as mentioned in table 5.1 Sr. No.2.: (1) Compacted plates, (2) Sintered plates and (3) TSMTG plates



Fig.5.9 Pictures of pin during various stages of fabrication using mould size pin as mentioned in Table 5.1 Sr. No. 3 : (1) Compacted pin, (2) Sintered pin, and (2) TSMTG pin

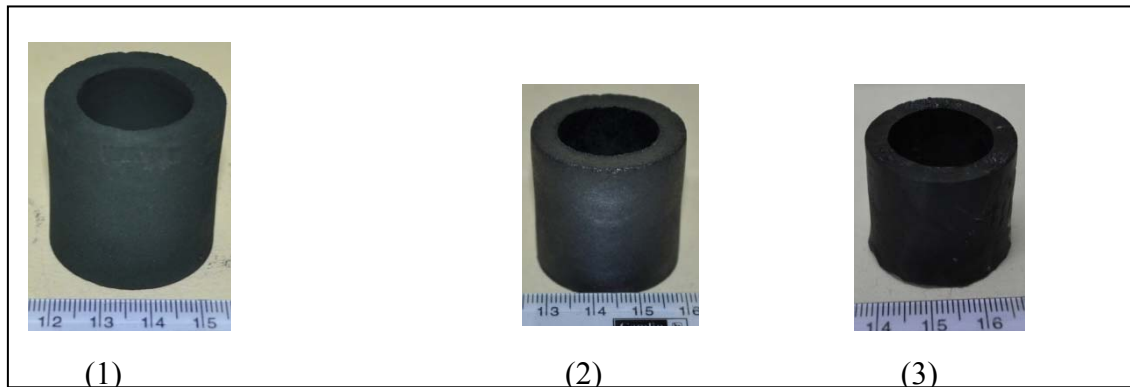


Fig.5.10 Pictures of cylinder during various stages of fabrication using mould size hollow cylinder as mentioned in Table 5.1, Sr.No.4. : (1) Compacted cylinder, (2) Sintered cylinder, and (3) TSMTG cylinder.

The shrinkage behavior of composites at various stages like pressing, sintering and while subjecting to MTG is shown in Table 5.4 and Figures 5.7, 5.8, 5.9 and 5.10. Here it can be seen that maximum shrinkage occurs while compaction in CIP, but the shrinkage while CIP is maximum in height of the sample i.e. around 10-15 %. Then during sintering the compacts shrink about 2-4 % of CIP pressed compacts and after subjecting to MTG the pre-sintered compacts shrinkage is around 1-2%.

5.5 Machining of MTG compacts

During MTG process the compacts partially melt and the shape gets distorted from the original shape. To apply the compacts in Fault current limiter (FCL) and motors, the compacts have to be machined. Since the compacts are brittle in nature, while machining considerable care is necessary. The lower 5-7 % part of the compacts reacts with base material and therefore the lower portion was sliced in high speed cutting machine using diamond cutting wheel. Machining was done in CMC milling machine to the accuracy of $\pm 0.2\text{mm}$ using oil as cooling fluid.

SSR-CY-1 and NDR-CY-2 samples were machined to dimensions 36mm OD x 46 mm ID and 50mm H respectively and oxygenated at 400 °C for 200h. The cylinders were surface protected with paraffin wax (as mentioned in section 5.7) and studies on microstructural features and other superconducting properties were carried out. The J_c values were measured at Budapest University Technology and Economics (BUTE), Hungary.

SSR-PL-1 and NDR-PL-2 samples were machined to dimensions 25mm width x 50mm height x 3.5mm thick and oxygenated at 400 °C for 150h. The plates were then surface protected with paraffin wax (as mentioned in section 5.7) and then measurements for trapped magnetic field and levitation force were carried out.

30 Nos Pins were fabricated using composite B (NDR-PI-1) compacted in mould size Sr. no. 3 as mentioned in Table 5.2. Pins were then sintered and subjected to TSMTG and further machined to size 8mm OD x 25 mm H. The pins were then oxygenated at 400 °C for 150h further surface protected with paraffin wax (as mentioned in section 5.7) and then measured for levitation force.

NDR-CY-3 cylinder was fabricated using composite B. The compact was pressed in mould size Sr. no. 5 as mentioned in Table 5.2. The green compact was sintered and subjected to TSMTG and further oxygenated and surface protected by applying paraffin wax. This hollow cylinder was cut into two halves horizontally. These two hollow cylinders were oxygenated and further surface protected by applying paraffin wax. Both the halves were sent to Budapest University of Hungary, Hungary for measuring J_c .

Likewise Pt-CY-5 and Ce-CY-6 hollow cylinders were also fabricated using composite C and D respectively in mould size Sr. no.4 as mentioned in Table 5.2., compacted, sintered and subjected to TSMTG, oxygenated and further surface protected. Both the cylinders were also sent to BUTE, Hungary for measuring J_c . Followed by characterisation of microstructure and other HTSC properties.

5.5.1 Machined MTG components

Some of the HTSC MTG machined products (Fig.5.11, Fig.5.12, and Fig.5.13) which are shown below were applied in HTSC prototype motor used to rotate HTSC motor as rotor (details are given in chapter 8).

Compact name	SSR-CY-1			NDR-PL-1			NDR-CY-2			NDR-CY-3			NDR-PL-2			NDR-PIN-1			Pt-CY-4			Ce-CY-5		
	Cylinder (mm)			Plate (mm)			Cylinder (mm)			Cylinder (mm)			Plate (mm)			Pin (mm)			Cylinder (mm)			Cylinder (mm)		
dimensions	OD	ID	H	W	T	L	OD	ID	H	OD	ID	H	W	T	L	OD		H	OD	ID	H	OD	ID	H
Inner size of mould	56	35	70	45	6	70	56	35	70	75	24	28	45	6	70	13	-	35	35	23	38	35	23	38
Size after CIP	52	35	64	41	4.8	65	52	35	64	62	24	26	42	4.7	65.5	12.5		32	32	23	35	32	23	35
Size after sintering	51	32	62	38	4.4	64	51	32	62	58	23	24	38	4.5	64	12		31	31	21.5	33	31	21.5	33
Shape after MTG	49	34	60	36	4	60	49	34	60	54.8	20.8	21	36	4.1	61	11		29	~29	~20.5	~28	~28.5	~20	~27
Final size after Machining	46	36	50	25	3.5	50	46	36	50				25	3.5	50	8		25						

Table 5.4 Shrinkage in size of the compacts while pressing, after sintering and after subjected to MTG



Fig.5.11 Machined TSMTG cylinders



Fig.5.12 Machined TSMTG plates



Fig.5.13 Machined TSMTG pins using composite B (NDR-PI-1)

5.7 Surface protection

The application of bulk YBCO TSMTG compacts requires on the environmental compatibility and long term stability of the bulk material. The protection against degradation has become a major issue. Humidity, aggressive ambient and thermal cycling can slowly degrade the superconducting properties of the YBCO bulk material. Under environmental conditions, it is mainly the carbonic acid from dissolved atmospheric CO₂ which leads to the long term degradation of YBCO. In order to provide an effective surface protection layer, the sample has to inhibit the contact of water or CO₂ or both. Considering the requirements for the cryogenic use the most important ones are chemical compatibility with the delicate superconducting material, curing, adhesion, thermal expansion mismatch, water absorption and diffusion, dielectric losses, and good insulation. Considering the degradation of the MTG components, all the MTG components were dipped in a molten liquid containing paraffin wax and paraffin liquid in a weight ratio 2:1 respectively for about 15-20 min on a heating mantle whose temperature maintained at 150 °C. Here the liquid enters the open pores and forms a layer of coating on them which protects the samples from environmental attack.



Fig.5.14 Picture of rubber mould used to fabricate MTG components

5.8 Conclusion

Taking into consideration the shrinkage behaviour at various stages of fabrication i.e. during compaction using CIP, sintering and while subjecting to MTG, rubber moulds were designed and fabricated as per the final required dimensions. The hardness of the moulds was optimised so that the green compact is released from the mould after CIP. The corresponding composites were filled along with in situ vibration in the moulds to achieve maximum green density with minimum pores. The MTG thermal schedules and oxygen annealing time were optimised for various shapes and subjected to MTG schedule. Before subjecting to MTG all the green compacts were sintered.

Various components were fabricated using different composites. In the next chapter the superconducting properties of MTG samples are given. The samples were

studied for T_c , microstructure (SEM), composition (EPMA), Texture (OIM), transport properties, trapped magnetic field, levitation force and critical current density. The superconducting properties like J_c , levitation force as well as trapped magnetic field of components TSMTG SSR-CY-1, TSMTG SSR-PL-1 were compared with TSMTG NDR-CY-2, TSMTG NDR-PL-2, respectively.

CHAPTER 6

Characterization of fabricated MTG components

Not all metals which display a resistive transition are superconductors. A superconductor must also display the Meissner effect. In both the processes i.e. lossless conduction and flux exclusion, charge carriers move with zero resistance by a mechanism that prevents energy absorption by scattering with normal electrons or with the crystal lattice. Lossless transmission results from the pairing of superconducting charge carriers. In the following sections, several important parameters used to establish superconductivity in materials are described. The two most characteristic properties displayed by superconductors are zero resistance and expulsion of applied magnetic field. Ambiguities and experimental artifacts can occur in each of these individual measurements, so the identification of superconductivity in a new compound requires, not just careful experimentation, but also the measurement of both transport and magnetic phenomena. The most fundamental information required in understanding these charge transport and magnetic properties comes from crystal and chemical compound. Standard methods by diffraction of radioactive and particle beams and microstructural characterization by SEM, HRTEM, EPMA, and OIM, transport, critical current density and magnetic properties measurement techniques are usually employed, for characterisation of fabricated products in order to assess their suitability for practical applications.

6.1 Characterisation of TSMTG samples

Characterisation of TSMTG samples prepared using composite A and comparison of the same with TSMTG samples prepared by composite B.

6.1.1 Critical transition temperature

Critical transition temperature (T_c) has been determined by Four Probe Resistivity method (Resistance Vs temperature {R vs T}). T_c depends on both applied field and on current. Typical curves (shown in Fig.6.1) of R vs T measured by four-probe technique with smallest supply of currents needed to detect the transitional voltage drop. The typical current is 10 mA. At temperature below T_c , the resistance of the superconductor becomes very small of the order of $10^{-9} \Omega$. T_c measurement was carried out on sintered pellet as well as TSMTG which was cut in rectangular shape of 10 mm x 5 x mm x 5 mm dimension.

The R Vs T curves of sintered sample and that of TSMTG sample SSR-PL-1 plate cut into 10 mm length x 5 mm width and 2 mm thick are shown in Fig.6.1. The sintered sample showed an onset of 89K and T_c of 85K. The melt textured samples show onset of 93K and T_c of 91K, having ΔT_c of $\approx 2K$. The width of transition (ΔT_c) in the sintered sample is more because they have large number of grain boundaries which act as weak links for flow of current where as in melt textured sample, the number of grain boundary weak links are reduced due to which current flows with less resistance.

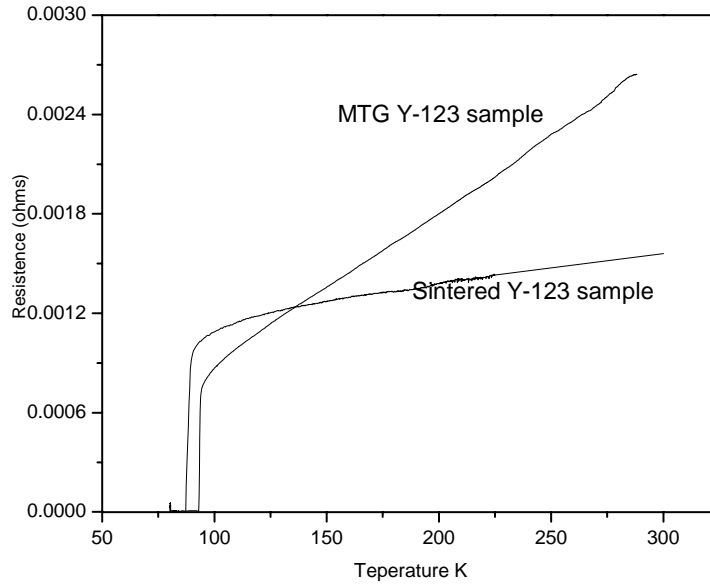


Fig.6.1 Critical transition temperature R Vs T plot of sintered Y-123 & TSMTG SSR-PL-1 plate

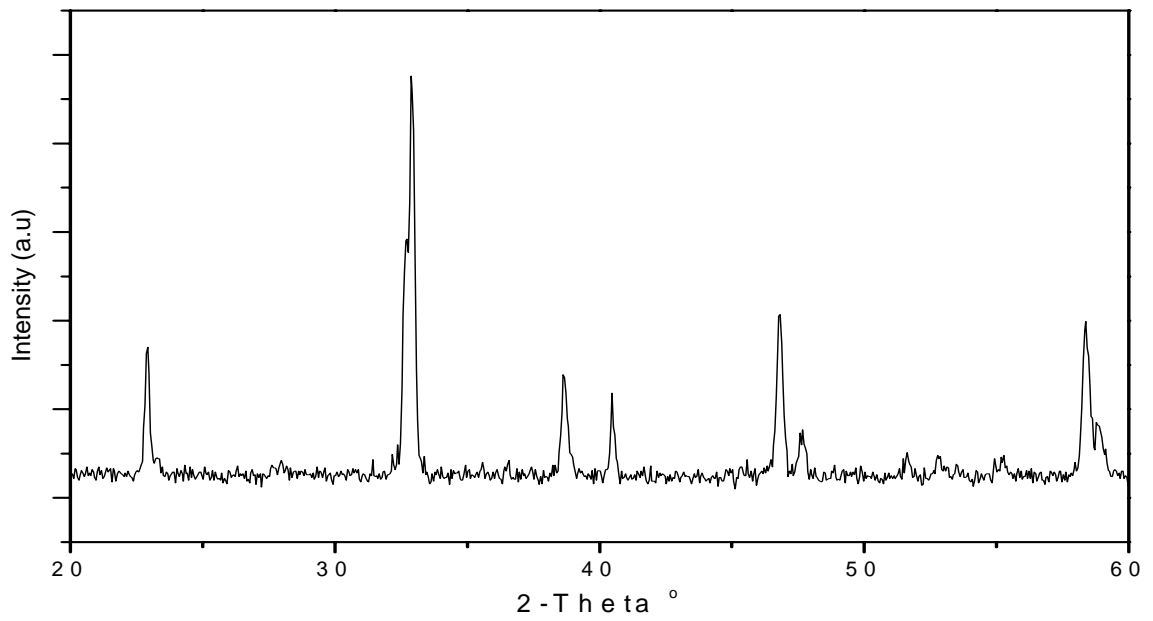


Fig.6.2 XRD pattern of sintered Y-123 pellet

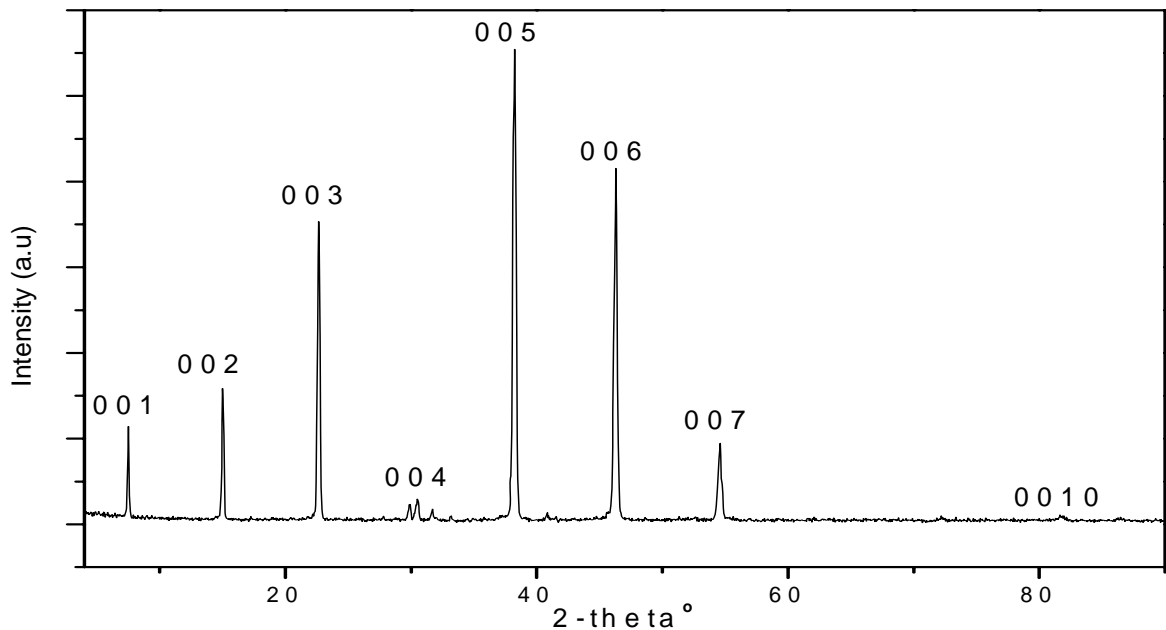


Fig.6.3 XRD pattern of TSMTG SSR-PL-1 plate

6.1.2 XRD studies of sintered and TSMTG SSR-PL-1 plate

XRD pattern of sintered pellet (Fig. 6.2) showed peaks due to phase pure sample without any orientation. The top portion of the MTG plate, (where the MgO seed has been placed) the seed was removed and plate was subjected to XRD. The MTG plate sample SSR-PL-2 (Fig. 6.3), showed highly c-axis oriented 001 peaks.

6.1.3 Microstructure analysis

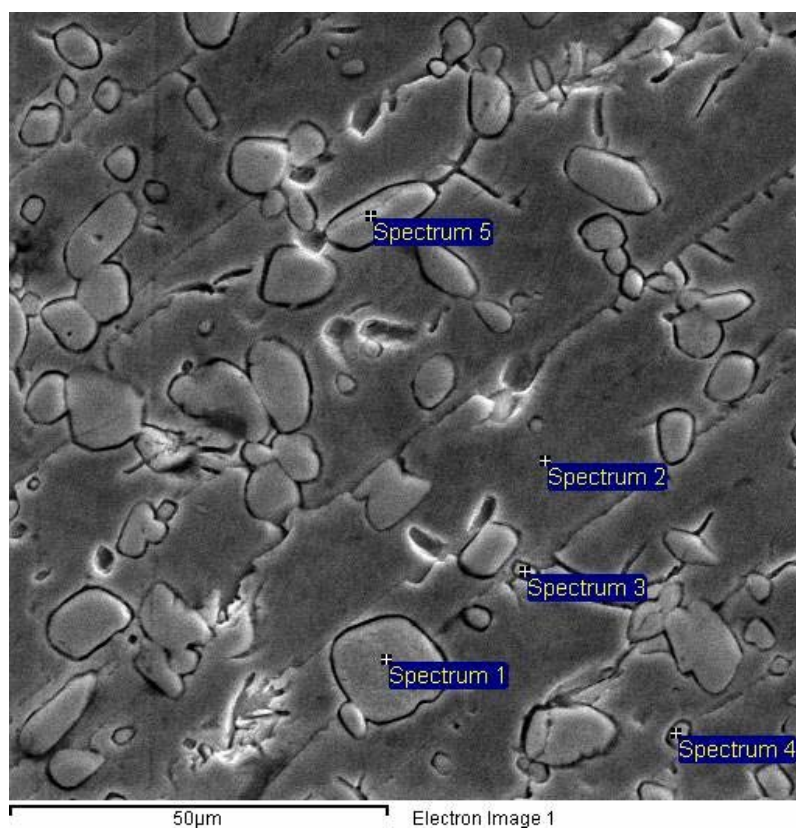
6.1.3.1 Etching of TSMTG for microstructure analysis

Etchant solution was prepared by adding 1 ml of conc. HCl to 99 ml of pure AR grade ethanol. TSMTG samples were dipped in solution for 1-3 seconds and then cleaned thoroughly 2- 3 times in pure ethanol solution. This assures removal of acid from the samples, which were then dried in oven for 1 h at temperature of 120 °C.

6.1.3.2 Scanning electron microscope analysis of TSMTG grown SSR-PL-1

TSMTG SSR-PL-1 plate was prepared for microstructural studies. The plate was first polished using starting paper size of 400 emery paper, slowly to finer emery paper from 600-800 and then 1000. The plate was then subjected to etching. Etching was done as described above.

TSMTG SSR-PL-1 plate was fabricated using composite A, containing Y-211 of initial average particle size 15 microns synthesized by solid state route. The SEM showed (Fig.6.4) dense structure with average particle size of Y-211 as 15-20 microns evenly distributed in the matrix of textured Y-123. Corresponding EDS studies on the particle and the matrix show atom percentage of Y, Ba and Cu elements in the ratio of Y-211 and Y-123 respectively. EDS results are the evidence of Y-211 particles being distributed uniformly in the matrix of Y-123.



Spectrum	Y	Ba	Cu
1 (atom %)	22.46	10.94	11.11
2 (atom %)	8.82	16.81	22.04

Fig.6.4 SEM and EDS of TSMTG SSR-PL-1 plate

6.1.3.3 EPMA studies

The Back Scattered Electron (BSE) image of sintered SSR-PL-1 plate is shown in Fig.6.5. where the dark region was due to presence of porosity. The X-ray mapping of Y clearly shows the presence of larger concentration of Y (green colour) in Y-211 phase and relatively smaller concentration of Y in Y-123 phase. The concentration of Cu is

found to be less in Y-211 phase (bluish) as compared to Y-123 phase (greenish). As expected, it is also observed that the phase containing less amount of Y, also contains more amount of both barium and copper (Y-123) and vice - a - versa (Y-211). Apart from that, a copper rich phase is found to be present in the sintered sample (reddish). The X-ray mapping of Ag shows homogeneous distribution of silver. This shows the evidence that Y-123, Y-211 and Ag are uniformly distributed in the matrix.

Secondary Electron (SE) image (Fig. 6.5) of TSMTG SSR-PL-1 plate reveals dense and textured microstructure of Y-123. Randomly oriented Y-211 particles are found to be distributed uniformly in the matrix of Y-123. As described earlier the X-ray mapping of Y clearly shows the presence of larger concentration of Y (shown as reddish green) in Y-211 and relatively smaller concentration Y in Y-123 phase in the matrix, correspondingly while Y-rich portion shows lower concentration of Ba and Cu and vice versa i.e. the area where Y content is low there the concentration of Ba and Cu is found to be high.

SE image (Fig.6.6) and the corresponding line profile reveals the variation of individual elements in the matrix [Y-123 (superconducting) phase] and dispersed phase [Y-211 (non-superconducting) phase]. The line profile shows the sudden discrete variation in the atomic percentage corresponding to Y, Cu and Ba in between matrix and dispersed phases. As usual it is observed that the Y-123 phase is rich with Cu and Ba, as compared to Y-211 phase. On the other hand Y concentration is found to be more in Y-211. The boundary between Y-211 and Y-123 is found to be very sharp as revealed from the sudden change in elemental concentration across the boundary.

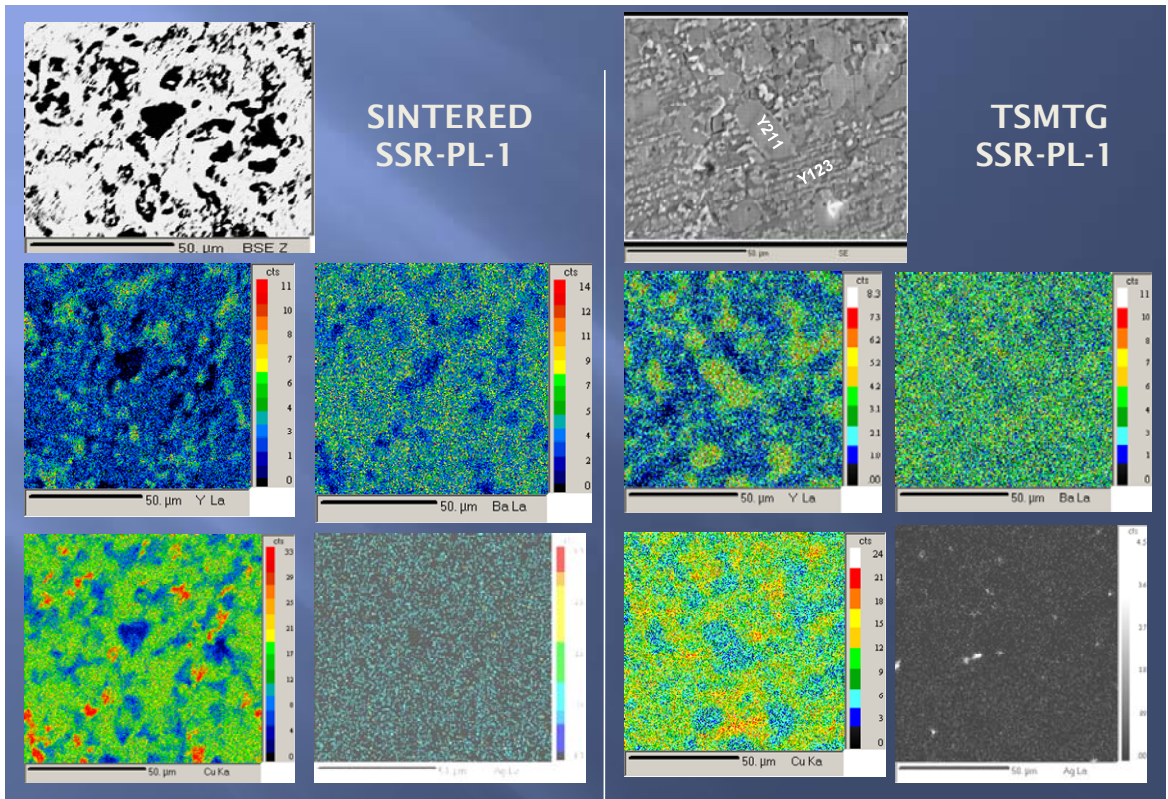


Fig.6.5 BSE image and corresponding X-ray mapping of sintered & TSMTG SSR-PL-1 plate

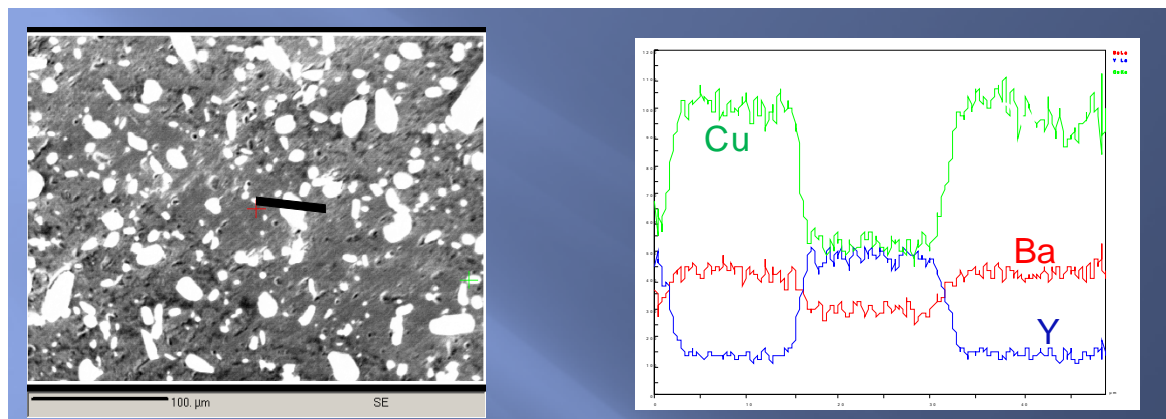


Fig 6.6 SEM image of TSMTG SSR-PL-1 and corresponding elemental line profile

6.1.3.4 Orientation Imaging Microscope (OIM) study of TSMTG SSR-PL-1 plate:

Two different top portions near the MgO seed crystal of SSR-PL-1 plate (Fig 6.7) show Y-211 particle (green color) distributed in the matrix of Y-123 and the color coding shows that maximum area (70-72%) covered with red color in the matrix. The corresponding pole figure shows 001 oriented Y-123 and the green color corresponds to Y-211 phase (30-33%) and its corresponding pole figure shows randomly oriented Y-211 phase. This OIM orientation is in corroboration with XRD analysis where the pattern shows all the peaks are of 00l oriented.

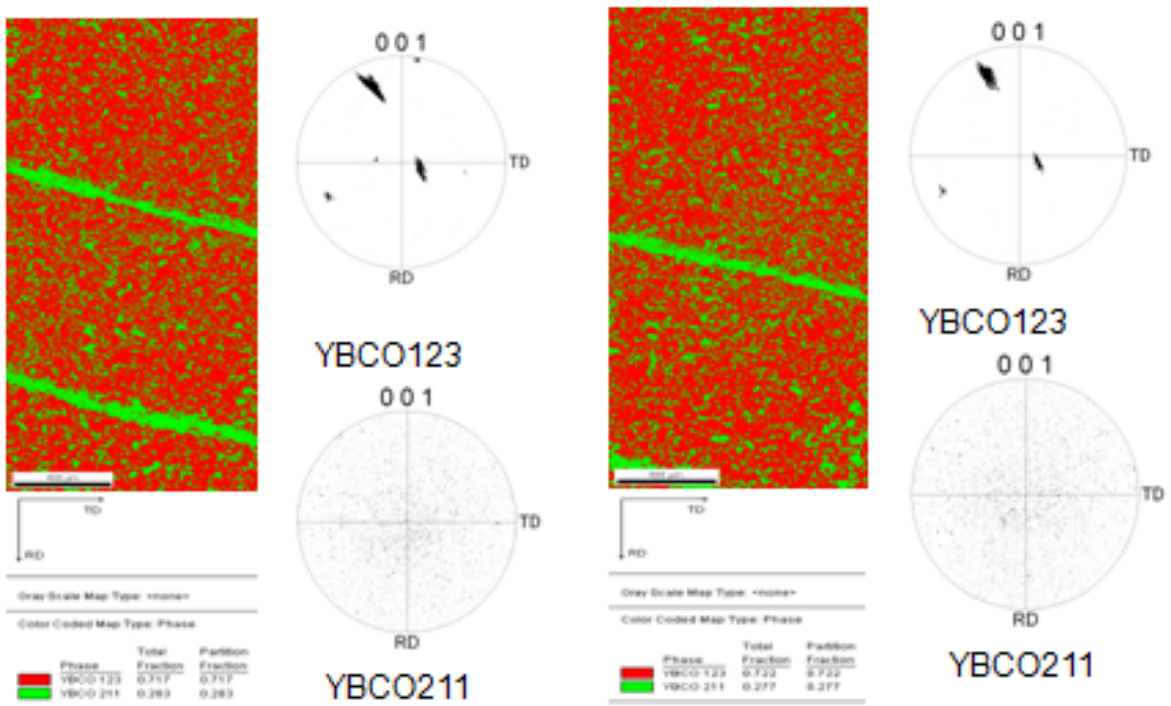
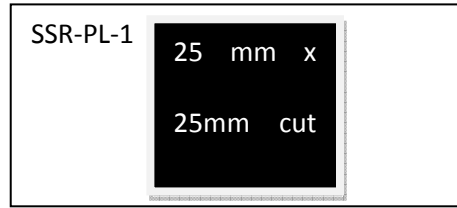


Fig.6.7 OIM images of two different top portions of TSMTG SSR-PL-1 plate

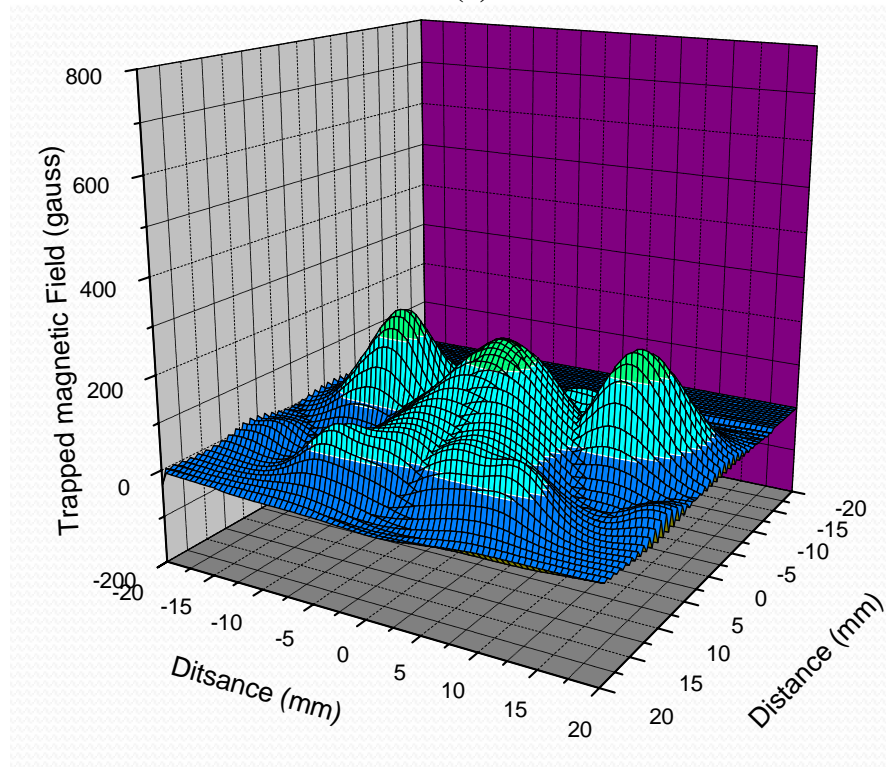
6.1.4 Magnetic measurements of TSMTG samples

6.1.4.1 Trapped magnetic field measurements

Trapped magnetic field was measured using indigenously designed, developed and fabricated unit as described earlier (Chapter 2). TSMTG plate SSR-PL-1 was cut in to 25 mm x 25 mm size from the center as shown in Fig.6.8. The black portion of the plate was used for measuring trapped magnetic field and levitation force measurement. The plate was kept in a thermocole container and placed in between two opposite permanent magnets having a constant field of 6000 gauss. The plate was cooled to liquid nitrogen temperature by pouring liquid nitrogen in the container. The plate was kept in the field for 5-6 minutes. The temperature of liquid nitrogen bath was maintained by pouring the liquid nitrogen in the bath. Field was trapped in the plate. The whole container along with plate was lifted and kept on the X-Y automated stage. The Hall probe was then positioned on top of the sample with a gap of less than 0.5 mm. During the measurement, the sample on the XY stage is moved step by step and the Hall probe generates a signal which is proportional to the trapped magnetic field and detected by gauss meter. An automated data acquisition system continuously measures the signal from the gauss meter and simultaneously measures the XY parameter from the XY motorized stage. The XY parameter was plotted in X and Y axis and the field is plotted on the Z axis as shown in Fig. 6.8. The field trapped inside the plate was found to be 0-200 gauss.



(a)



(b)

**Fig.6.8 (a) TSMTG SSR-PL-1 plate was cut as shown in figure.
(b) The cut black portion was used for measuring the trapped magnetic field and graph shows plot for TSMTG SSR-PL-1 plate**

6.1.4.2 Levitation force measurement

A system has been developed, designed, and fabricated for the measurement of levitation force. The details of this unit are mentioned in Chapter-2. The same SSR-PL-1 plate which was used for measurement of the trapped magnetic field was immersed in liquid nitrogen in a thermocole container at zero field. A samarium cobalt permanent

magnet fitted vertically in line with a load cell is gradually approached to the plate from the top at distance of 1 mm gap between plate and magnet and then reversed back. The HTSC plate is diamagnetic below T_c i.e. 90K as it repels the field. The repelled field is plotted against the distance from the plate and the magnet. The maximum force at a distance of 1mm was found to be 8 Newton (Fig.6.9).

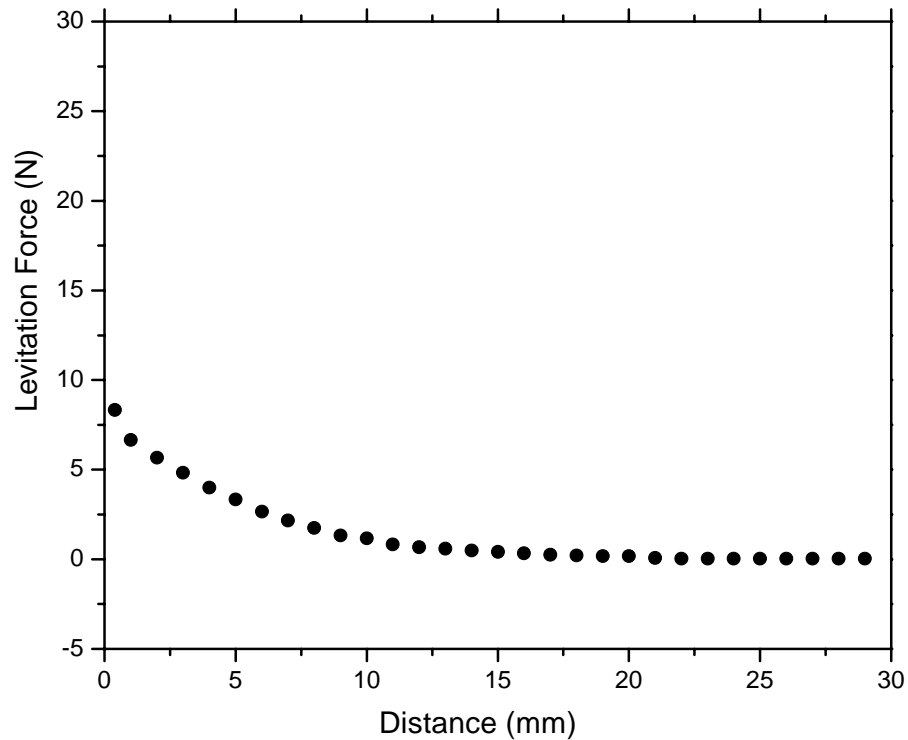


Fig.6.9 Levitation force measurement of TSMTG SSR-PL-1 plate

6.1.5 Critical current density measurement:

Critical current densities (J_c) of TSMTG in the form of hollow cylindrical shaped samples were measured at Budapest University of Technology and Economics (BUTE), Budapest, Hungary [160-161]. The calculation of the J_c was based on the measurement of the inductive type superconducting fault current limiter (iFCL) with SC ring. The

activation current of the iFCL refers to the AC critical current of the superconducting ring. It was assumed that the magnetic coupling between the two sides of the FCL is full. The AC critical current of the SC ring was calculated from the activation current and the number of turns of the iFCL. The current was slowly increased, till the MTG cylinder is in superconducting stage, the current and voltage drop increases linearly, as and when the MTG cylinder loses the superconducting property there was a sudden change in voltage drop, and corresponding current is the excitation current. J_c was calculated by dividing the product of the number of turns used in primary coil with the excitation current, with the cross section area of the cylinder.

From the current Vs voltage plot (Fig. 6.10) of SSR-CY-1 cylinder excitation current was found to be 16.8A. The number of turns in the primary coil was 100 therefore multiplying the number of turns (100) in the primary coil with excitation current (16.8A) and dividing the product with the area of cross section of the cylinder the J_c was calculated and found to be 838 A/cm^2 .

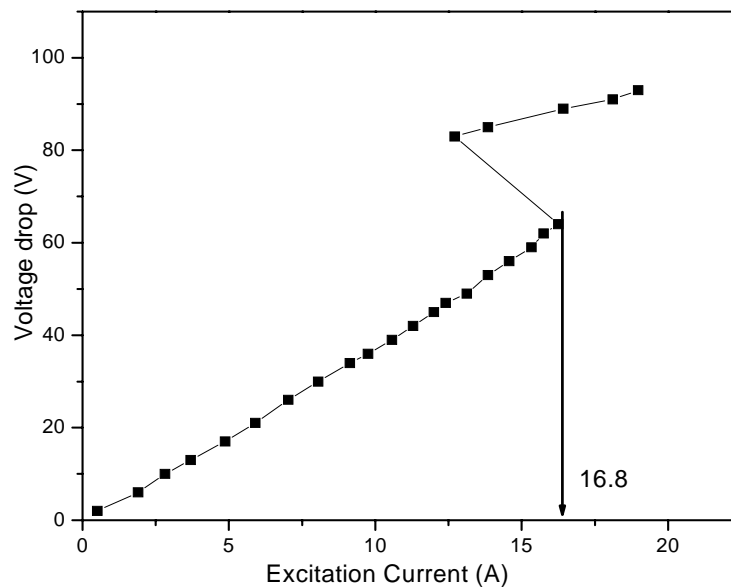


Fig.6.10 Critical current density of TSMTG SSR-CY-1 hollow cylinder

6.2 Characterisation of superconducting properties TSMTG components fabricated using composite B :- (1) NDR-PL-2, (2) NDR-CY-2, (3) NDR-PI-1 & (4) NDR-CY-3

Decoding of these compositions :

NDR-CY-2 represents: NDR-synthesis of Y-211 powder using nitrate decomposition route, CY- hollow cylinder shape, 2 – No. of cylinder.

NDR-PL-2 represents: NDR-synthesis of Y-211 powder using nitrate decomposition route, PL-plate shape, 2 – No. of plate.

NDR-PI-1: NDR-represents synthesis of Y-211 powder using nitrate decomposition route, PI-pin shape, 1 – No. of pin.

NDR-CY-3 represents : NDR-represents synthesis of Y-211 powder using nitrate decomposition route, CY- hollow cylinder, 3- No. of cylinder.

The top portion of the MTG plate, (where the MgO seed has been placed) the seed was removed and plate was subjected to XRD. The MTG plate sample NDR-PL-2 (Fig. 6.10a), showed highly c-axis oriented 001 peaks.

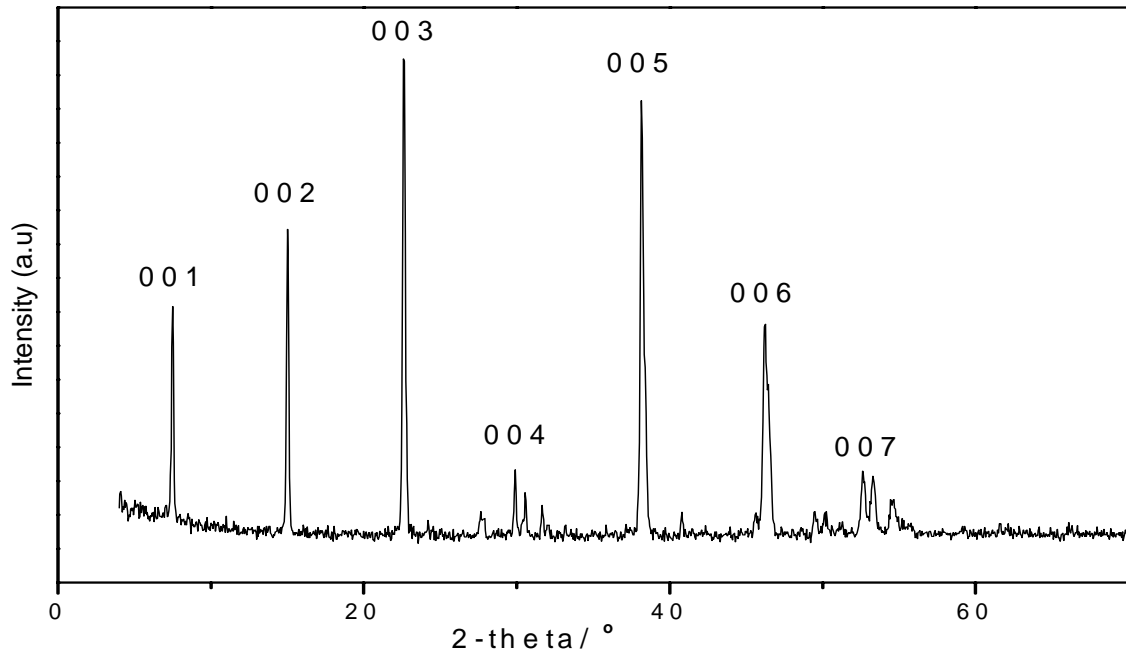


Fig.6.10a XRD pattern of TSMTG NDR-PL-2 plate

6.2.1 Microstructure analysis of TSMTG NDR-PL-2 plate

6.2.1.1 Scanning electron microscope analysis of TSMTG NDR-PL-2

TSMTG NDR-PL-2 plate was prepared for microstructure studies. The plate was first polished starting with 400 silicon carbide emery paper, slowly switching over to finer emery paper from 600, 800 and 1000. The plate was then subjected to etching. Etching was done as described in section 6.3.1.

TSMTG NDR-PL-2 plate was fabricated using composite B, containing Y-211 of initial average particle size of 3-5 μ m synthesized by solid state route. The SEM (Fig.6.11) showed dense structure with average particle size of Y-211 in the range of 5-6 μ m uniformly distributed in the matrix of textured Y-123.

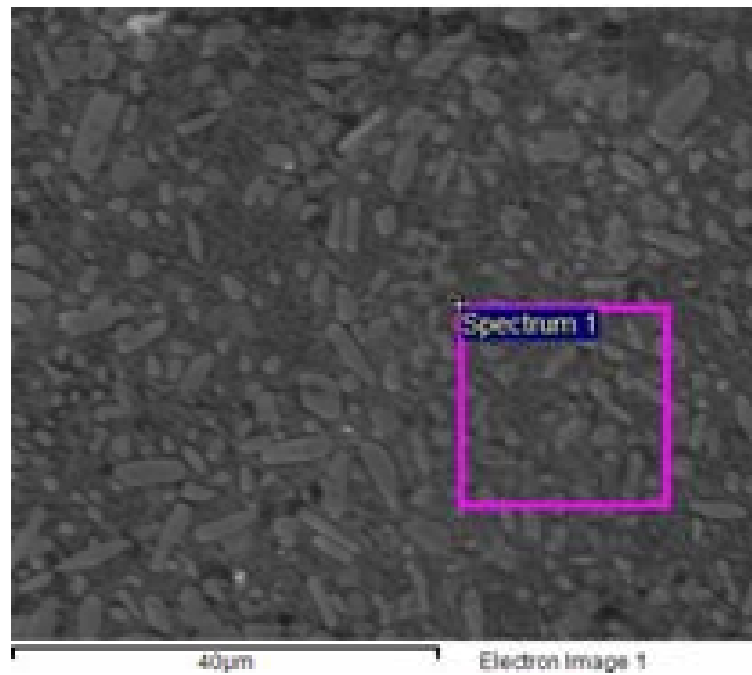


Fig.6.11 SEM micrograph of TSMTG NDR-PL-2 plate

6.2.1.2 OIM study of TSMTG NDR-PL-2 plate

Fig.6.12 shows the Orientation Imaging Microscope (OIM) image of two different top portions of NDR-PL-2 plate near the MgO seed crystal. The images show Y-211 particles (green color) distributed in the matrix of Y-123. The color coding shows that maximum area (65-70%) is covered with red color (in the matrix). The corresponding pole figure shows 001 oriented Y-123. The green color corresponds to Y-211 phase (30-35%) and its corresponding pole figure shows randomly oriented Y-211 phase. This OIM orientation is in corroboration with XRD analysis where the pattern shows all the peaks are 00l oriented.

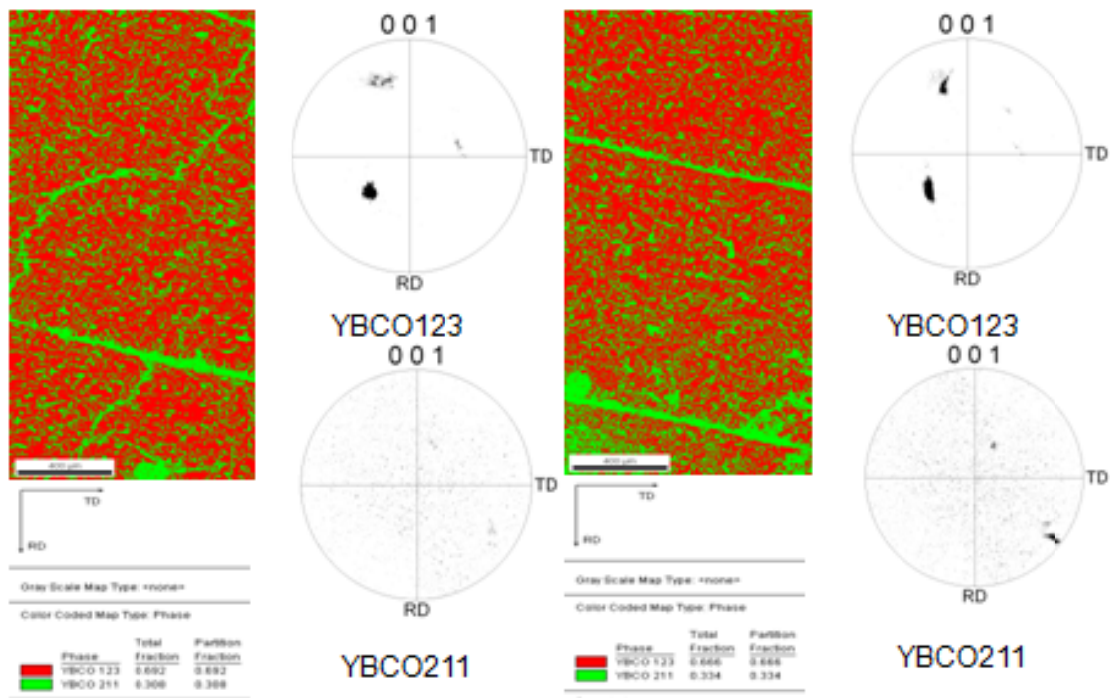


Fig.6.12 OIM image of two different portions of TSMTG NDR-PL-2 plate

6.2.1.3 HRTEM study

TEM sample preparation: Samples in the form of powder were suspended in high purity methanol. 15 minutes of sonication was carried out to produce a uniform suspension and few drops from this suspension were put on carbon coated copper grid of 200 mesh size. Sample were dried under a vacuum chamber and subsequently examined under electron microscope Techani F-30.

A sintered pellet of Y-123 was crushed in agate pestle mortar and the powder was prepared for HRTEM study as mentioned above. For TSMTG NDR-PL-2 plate, a small flake was plucked and crushed in pestle mortar and the powder was subsequently prepared for HRTEM study.

High resolution images of Y-123 sintered powder were compared with TSMTG powder. The high resolution image of the Y-123 sintered powder is shown Fig.6.13. Interplanar spacing between planes pertaining to different grains could be observed from the micrograph. No specific low angle relationship among plans could be observed from the figure. After examining many such regions, it was concluded that the grains of sintered powder were randomly oriented.

The powder from TSMTG NDR-PL-2 plate on the other hand, showed several grains with strong texture and alignment. HRTEM images of two typical grains is shown in Fig.6.14. The image shows the $\langle 100 \rangle$ oriented grains. Angular relationship and interspacing among the spots confirmed their orientations. Respective unit cells with proper orientations are presented along with HREM in Fig.6.13 and 6.14. A line vector along $[001]$ direction of each grain is drawn to measure their orientations. It may be noticed from this figure that the angle of separation between the two grains is of the order of few degrees which is far lower than the value of a typical random boundary ($\sim 60^\circ$). This shows that crystals of Y-123 grains are textured and aligned.

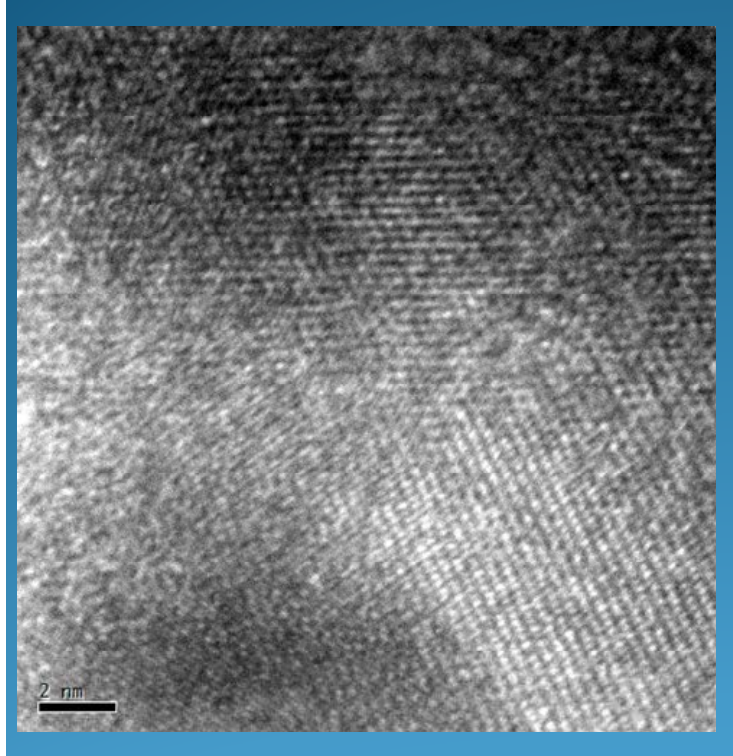


Fig.6.13 HRTEM image of sintered Y-123 powder

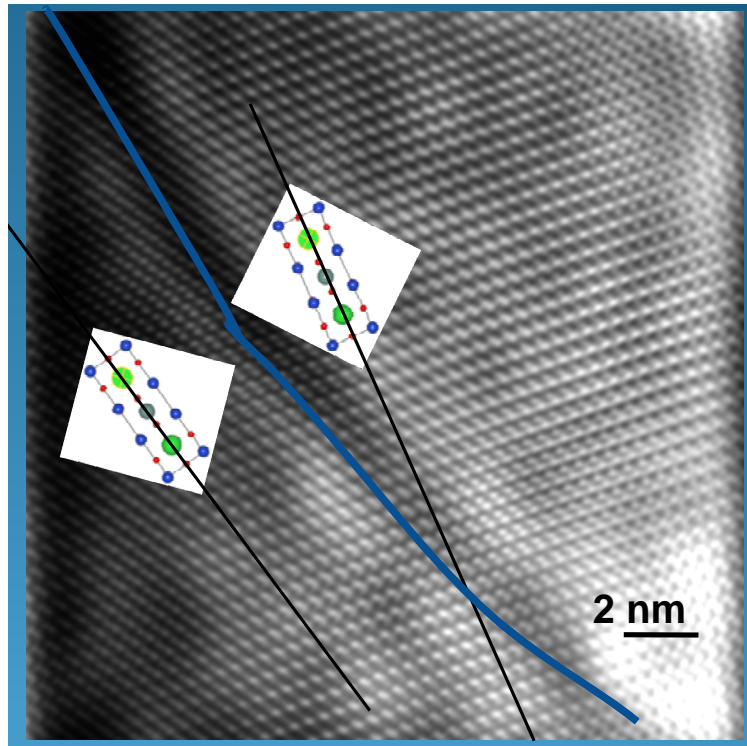
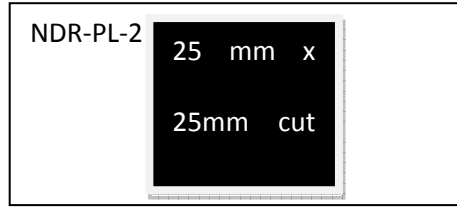


Fig 6.14 HRTEM image of TSMTG NDR-PL-2 powder

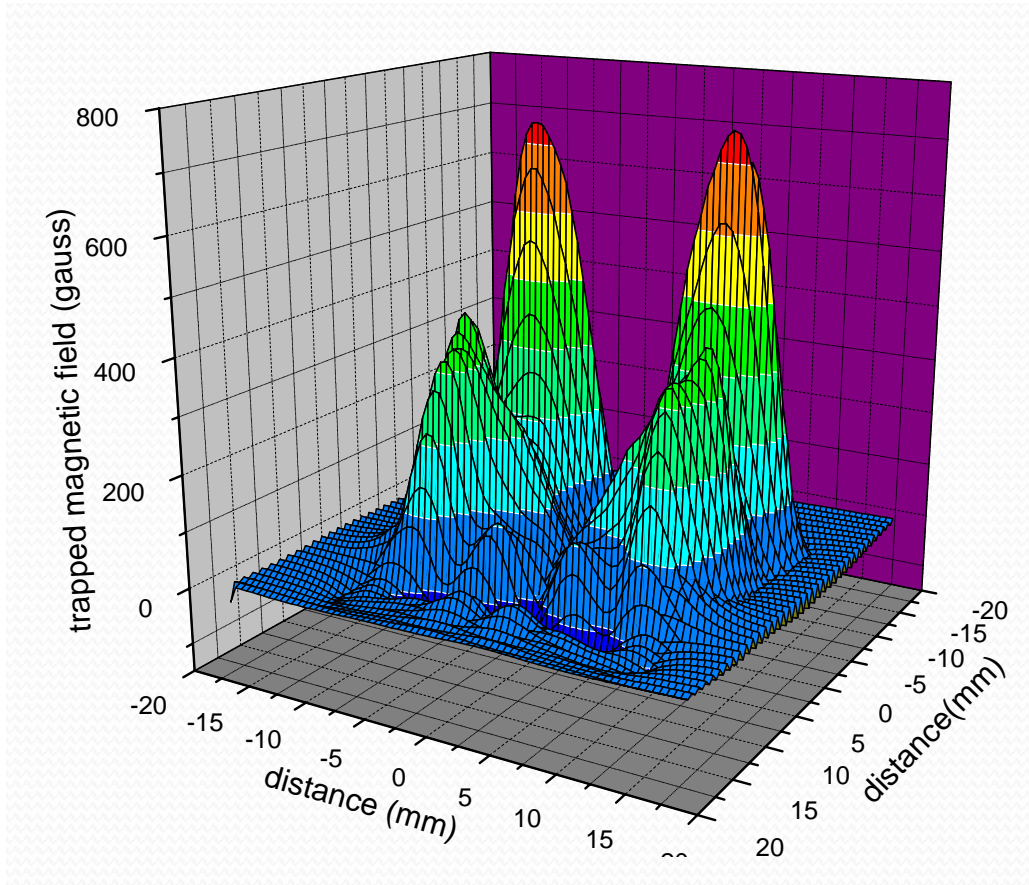
6.2.2 Magnetic measurements of TSMTG NDR-PL-2 plate

6.2.2.1 Trapped magnetic field measurement

TSMTG NDR-PL-1 plate was cut in to 25 mm x 25 mm sample (Fig. 6.15) was used to measure the trapped magnetic field and levitation force measurement. The plate was kept in a thermocole container and placed in between two opposite permanent magnets having a constant field of field 6000 gauss, the plate was cooled to liquid nitrogen temperature by pouring liquid nitrogen in the container. The plate was kept in the field for 5-6 minutes. Liquid nitrogen temperature is maintained by pouring the liquid nitrogen in the bath. Field is trapped in the plate. The whole container along with the plate is lifted and kept on the X-Y automated stage. The Hall probe is then positioned on top of the sample with a gap of less than 0.5 mm. During the measurement, the sample on the XY stage is moved step by step and the Hall probe generates a signal which is proportional to the trapped magnetic field and detected by gauss meter. An automated data acquisition system continuously measures the signal from the gauss meter and simultaneously measures the XY parameter from the XY motorized stage. The XY parameter is plotted in X and Y axis and the field is plotted on the Z axis as shown in Fig.6.15. The field trapped inside the plate was found to be 0-800 gauss.



(a)



(b)

**Fig.6.15 (a) TSMTG NDR-PL-2 plate was cut as shown in figure.
 (b)The cut black portion as used for measuring the trapped magnetic field and graph shows plot for TSMTG NDR-PL-2 plate**

6.2.2.2 Levitation force measurement

The levitation force is measured using the unit designed, developed and fabricated, details are mentioned in Chapter-2. The same plate which was used for measurement of trapped magnetic field NDR-PL-1 was immersed in liquid nitrogen in a

thermocole container at zero field. A Samarium Cobalt permanent magnet fitted vertically in line with a load cell is gradually approached towards the plate from the top at distance of 1 mm gap between plate and magnet and then reversed back. The HTSC plate is diamagnetic below T_c i.e. 90K, it repels the field. The repelled field is plotted against the distance from the plate and the magnet. The maximum force at a distance of 1mm was found to be 28 Newton (Fig.6.16).

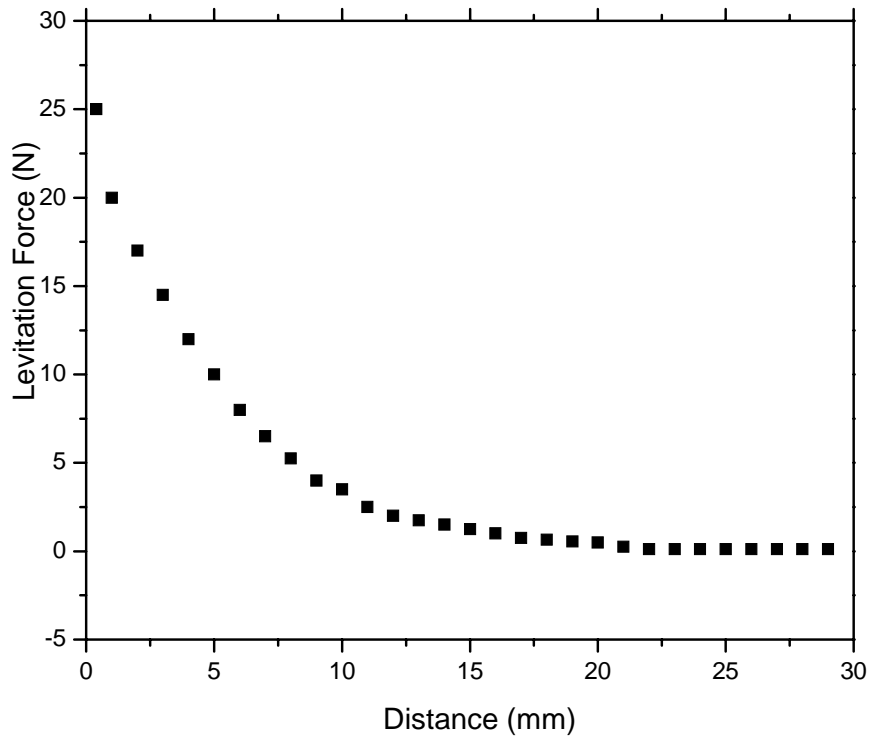


Fig.6.16 Levitation force of TSMTG NDR-PL-1 plate

6.2.2.3 SQUID measurement of TSMTG NDR-PL-2 plate

The SQUID magnetometer was used to test the magnetic property of sample. Samples of 1mm x 1mm size were cut from the large single domain plate. The starting transition temperature of sample was 89K, and the transition width was about 1K.

Furthermore, a modified Bean critical state model was used to determine the magnetic critical current density J_c from the hysteresis loop (Fig.6.17). The J_c reaches a maximum value of 6000 A/cm^2 at 20K.

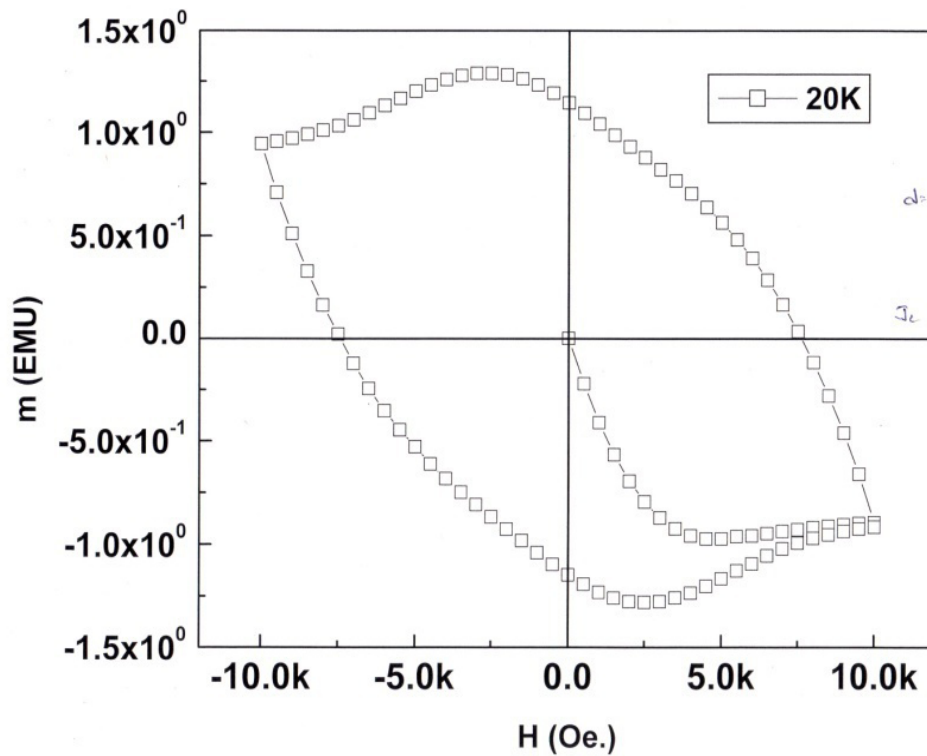


Fig.6.17 SQUID plot of TSMTG NDR-PL-2

6.2.3 Critical current density measurement

Critical current densities (J_c) of TSMTG in the form of hollow cylindrical shapes samples were measured at BUTE, Budapest, Hungary. The calculation of the J_c was based on the measurement of the inductive type superconducting fault current limiter (iFCL) with SC ring. The activation current of the iFCL refers to the AC critical current of the superconducting ring. It was assumed that the magnetic coupling between the two sides of the FCL is full; such AC critical current of the SC ring was calculated from the

activation current and the number of turns of the iFCL. Current is slowly increased, till the MTG cylinder was in superconducting state, the current and voltage drop increases linearly. As and when the MTG cylinder loses the superconducting property, there was a sudden change in voltage drop, and the corresponding current was the excitation current. From the excitation current J_c was calculated by dividing the value of excitation current from the plot with the cross section area of the rings.

From the current vs voltage plot (Fig.6.18) of NDR-CY-2 cylinder excitation current was found to be 14A, multiplying the number of turns in the primary and dividing the area of cross section of the cylinder, calculated J_c was found to be 4032 A/cm^2 .

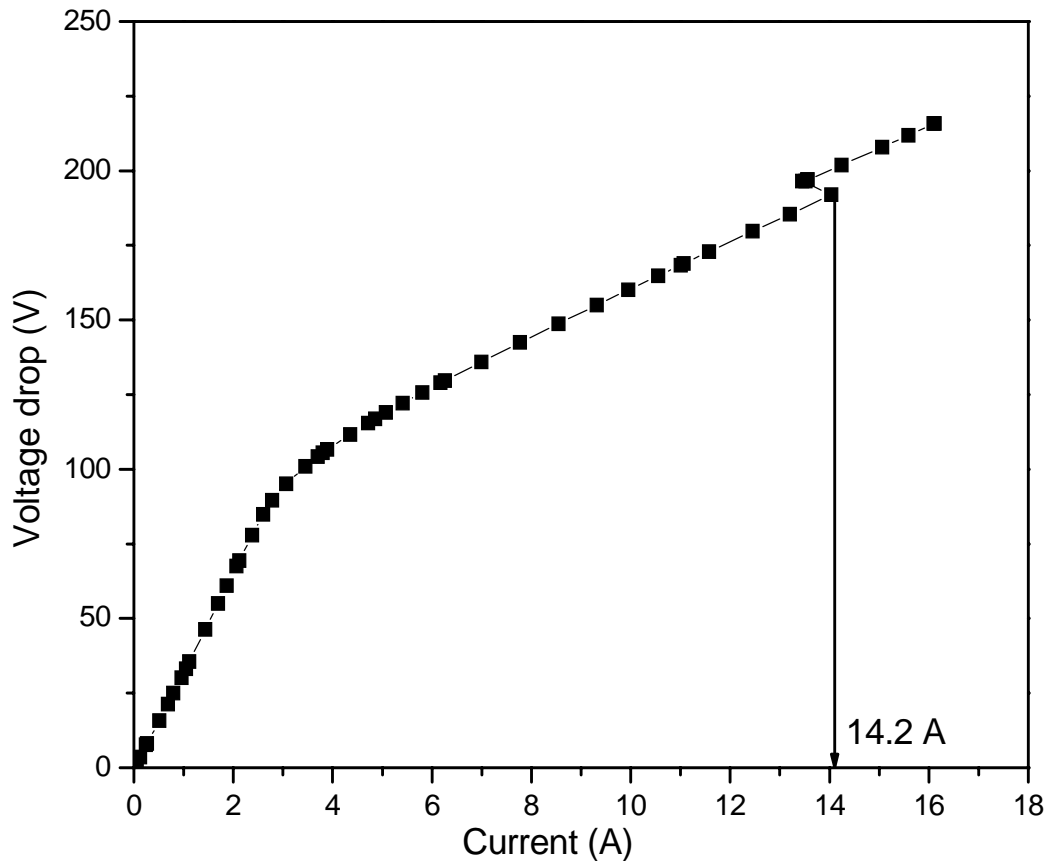


Fig.6.18 J_c measurement of TSMTG NDR-CY-2 cylinder

For studying the reproducibility of the processing technique, one more hollow cylinder was fabricated with composite-B, Similar pressure, sintering temperature, thermal schedule and oxygen annealing were used. The hollow cylinder was sent to BUTE, Hungary for measuring J_c . The J_c of the cylinder was calculated and found to be 3780 A/cm^2 (Fig.6.18a).

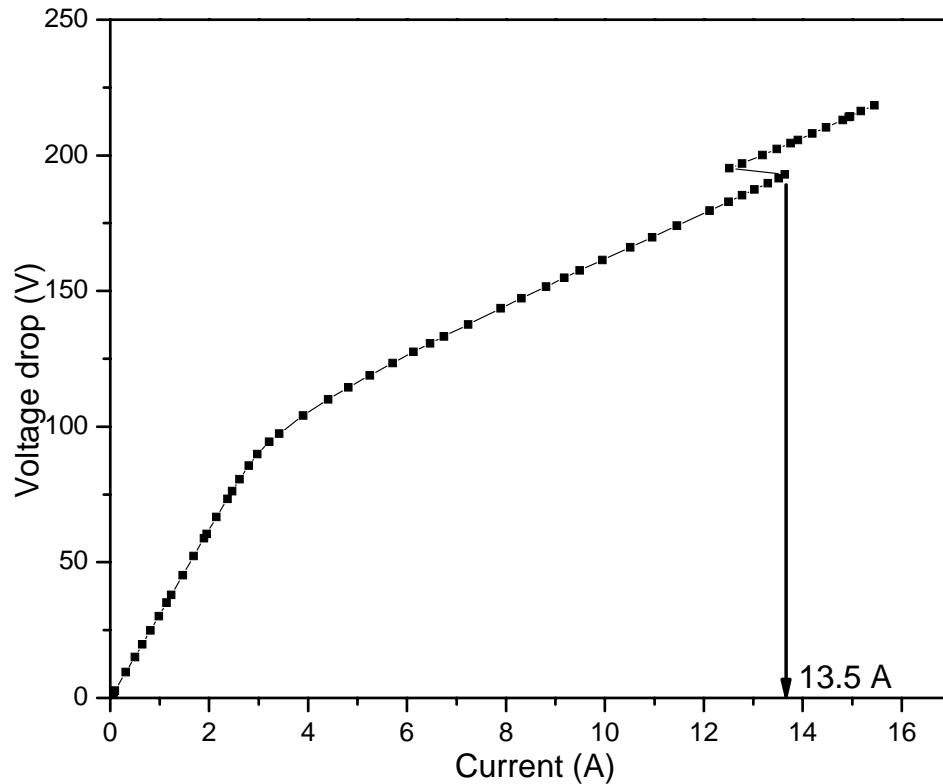


Fig.6.18a J_c measurement of TSMTG hollow cylinder NDR-CY-2a fabricated using composite –B with similar process used as in NDR-CY-2 cylinder

6.2.4 Characterisation of TSMTG NDR-CY-3 cylinder

In order to confirm the uniformity of critical current density J_c in the TSMTG samples, Cylinder NDR-CY-3 was fabricated using composite B. This was pressed by CIP at a pressure of 3000 bar in rubber mould (Table 5.2, Sr. No.5, chapter 5) sintered and subjected to TSMTG. The thermal schedule was same as given in Fig. 5.4 in Chapter

5, except that the hold time was increased to 10 h, because the wall thickness of the cylinder is large compared to the wall thickness of other hollow cylinders (approximately 20 mm). More holding time was required for partial melting of the cylinder.

Further to confirm the J_c in the cylinder, the cylinder was cut in to two halves horizontally. The bottom portion which reacts with the base material was sliced and removed. The measurement was carried out on both the halves.

Bottom half of the cylinder was of the size 5.6 mm H x 21.9 mm ID x 51.3 mm OD. The upper half of the portion cylinder was of the size 5.6 mm H x 20.7 mm ID x 53.4 mm OD. The cross section area was calculated to be 0.915 cm² and 0.825 cm² respectively.

Critical current density of top portion (Fig.6.19) : The number of turns in the primary coil were 100 and the excitation current was found to be 20A. Therefore estimated current in whole cylinder was 2000A. The calculated critical current density was 2185A/cm² (see Table 6.1)

Critical current density of bottom portion (Fig.6.20) : The number of turns in the primary coil were 100 and the excitation current was found to be 20 A. Therefore estimated current in whole cylinder was 2000A. The calculated critical current density was 2424A/cm² (see Table 6.1). Therefore it is concluded from the J_c that the whole cylinder fabricated using TSMTG was having uniform J_c values.

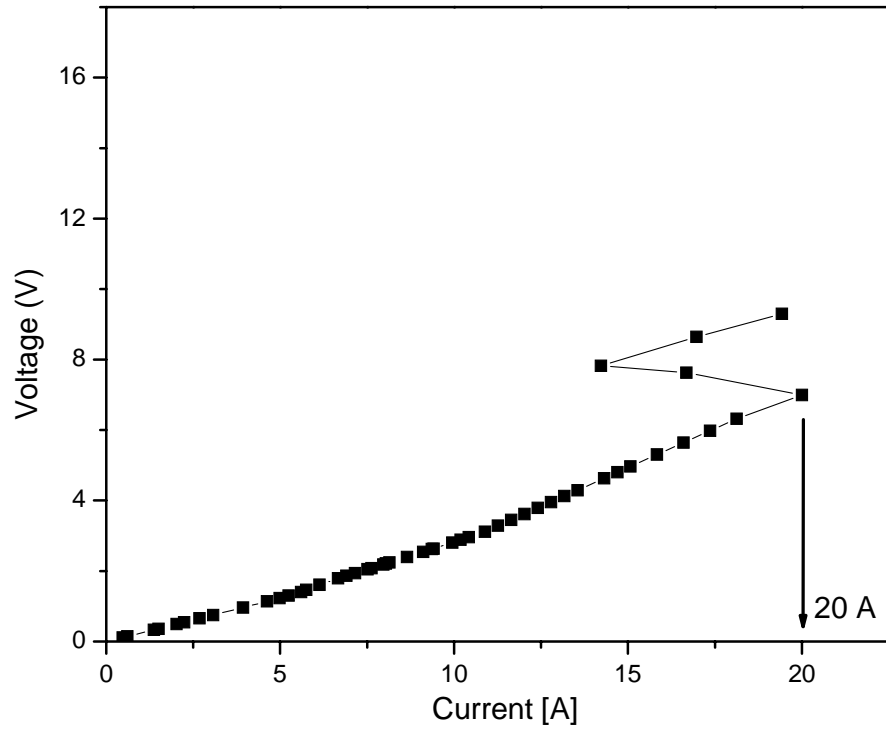


Fig.6.19 J_c of top portion of TSMTG NDR-CY-3 cylinder

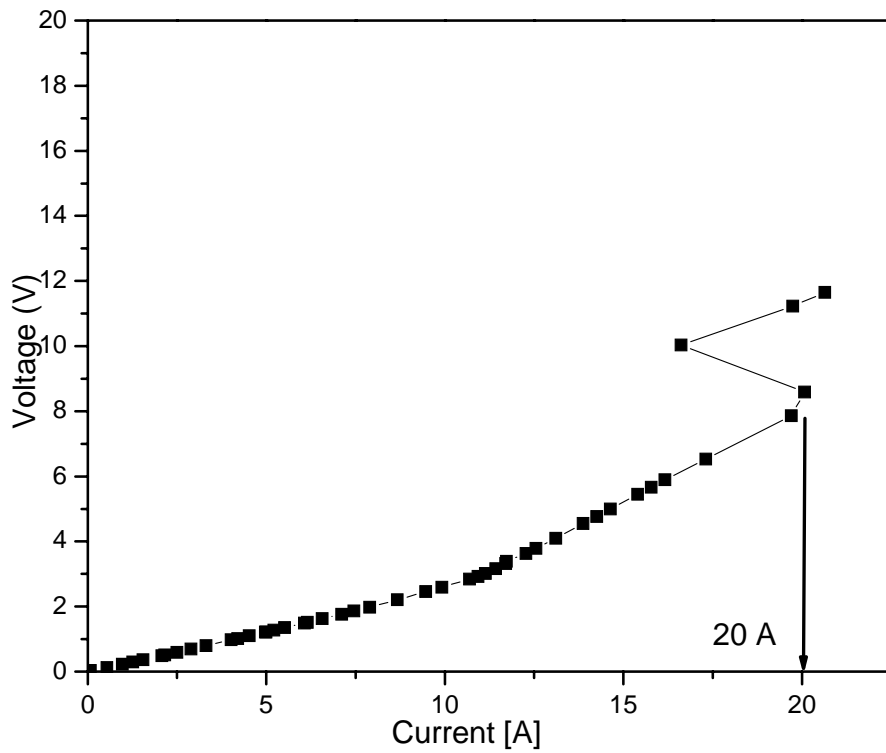


Fig.6.20 J_c of bottom portion of TSMTG NDR-CY-3 cylinder

6.3 Effect of Pt and Ceria additions in Y-123 on TSMTG superconducting properties

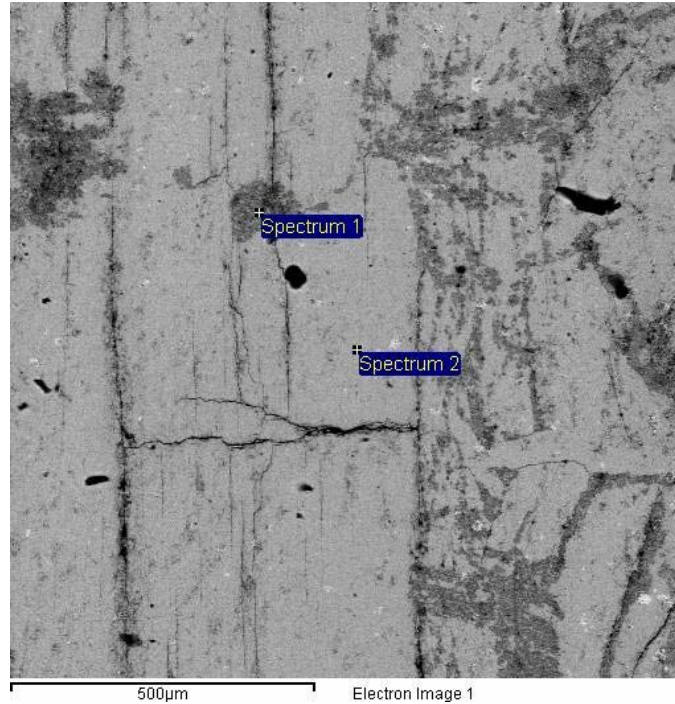
In order to study the effect of additives like Pt and ceria on the superconducting properties, TSMTG hollow cylinders Pt-Cy-5 and Ce-Cy-6 were fabricated using composite C and Composite D respectively. These composites were pressed by CIP at a pressure of 2500 bar in the rubber mould (Table 5.2, Sr. No. 2), sintered and subjected to TSMTG. The thermal schedule was same as given in Fig. 5.4 in chapter 5, except that the hold time at 1060°C was 6 h, because of the wall thickness of the cylinder is approximately 5 mm.

6.3.1 Characterisation of TSMTG Pt-CY-5 samples

6.3.1.1 Microstructure study of TSMTG Pt-CY-5

6.3.1.1.1 SEM of TSMTG Pt-CY-5 sample

The cylinder was cut vertically and polished, etched as mentioned in section 6.3.1. SEM shows (Fig.6.21) the presence of a dense structure. The EDS spectrum 1 shows the presence of cerium in the matrix of Y-123 and spectrum 2 shows Y, Ba and Cu in the ratio approximately 1:2:3, therefore it confirms that Ce is distributed in the matrix of Y-123.



Spectrum	Y	Ba	Cu	Pt
Atom %				
Spectrum 1	5.33	7.41	8.00	0.04
Spectrum 2	12.86	23.48	38.79	0.00

Fig.6.21 SEM and corresponding EDS of TSMTG Pt-CY-5

6.3.1.1.2 EPMA of TSMTG Pt-CY-5 sample

For preparation of the sample for EPMA study, the cylinder was cut vertically, polished and etched following the procedure mentioned in Section 6.3.1. The BSE image of Pt-CY-5 of sintered plate is shown in Fig.6.22. In the micrograph the dark region was due to the presence of porosity. The X-ray mapping of Y clearly shows presence of larger concentration of Y (greenish red color) which is homogeneously distributed, the greenish red colour is due to excess Y in the composite C. It is observed from the X-ray mapping

that distribution of both Ba and Cu is uniform in Y-123 matrix. Pt is also found to be uniformly distributed within the matrix.

SE image of TSMTG grown Pt-CY-5 shows dense, textured structure of Y-123. The X-ray mapping reveals that the white portion in SE image contains Y-rich phase (greenish red), where the concentration of Cu was found to be low (blue). Apart from this region Cu is found to be uniformly distributed throughout the matrix. The X-ray mapping also reveals that Pt is uniformly distributed within the matrix.

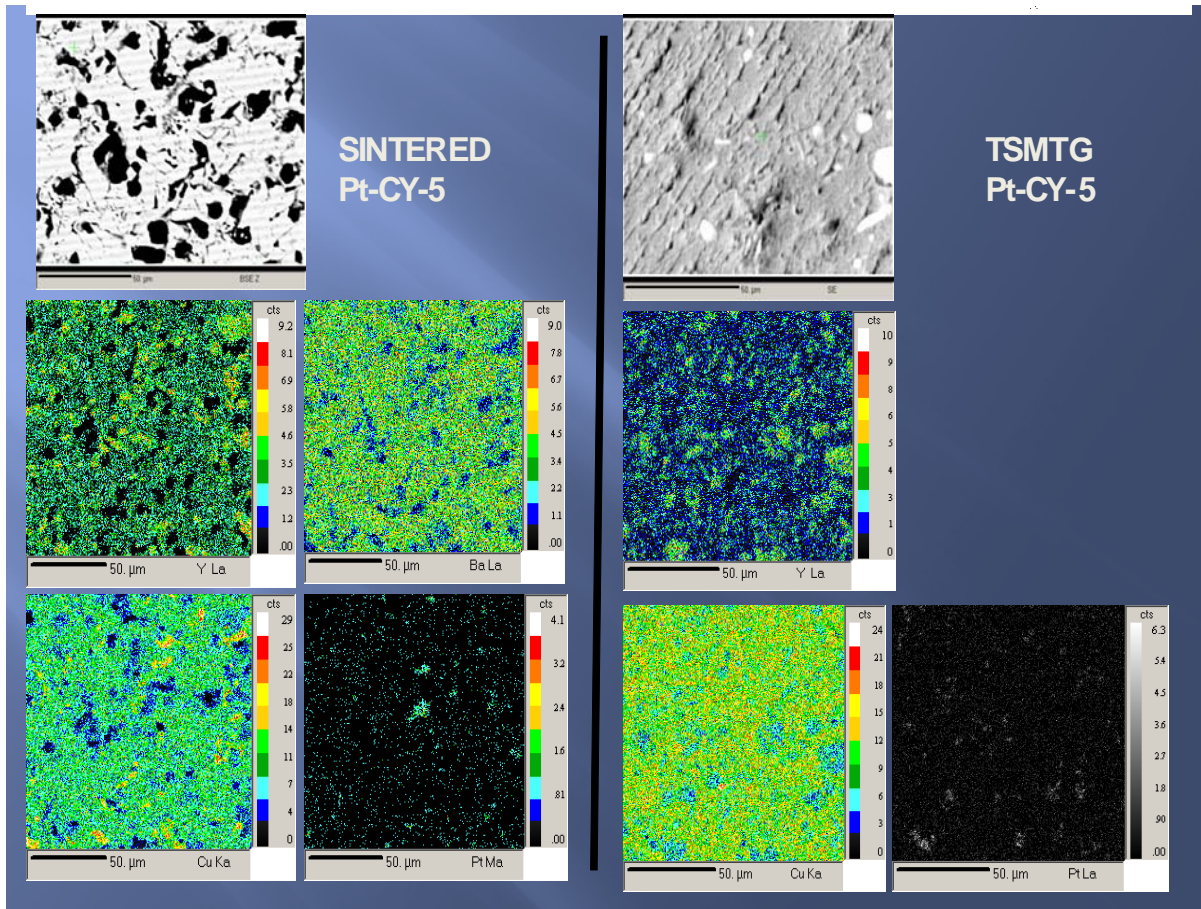


Fig.6.22 BSE and corresponding X-ray mapping of sintered Y-123 and TSMTG SSR-PL-1 plate

6.3.2 J_c measurement of TSMTG Pt-CY-5 cylinder

The critical current density of Pt-CY-5 hollow cylinder is shown in Fig.6.23. The number of turns in the primary coil were 100 and the excitation current was found to be 13.4A, therefore the estimated current in whole cylinder was 1340A (excitation current multiplied by number of turns in the coil i.e. $13.4 \times 100 = 1340A$). Critical current density is calculated by dividing the current by area of cross section, which was 0.595 cm^2 (15.7 mm H, 21.1 mm ID, and 28.7 mm OD). The critical current density is calculated by product of primary coil and excitation with cross section area of cylinder. The J_c calculated was found to be 2246 A/cm^2 .

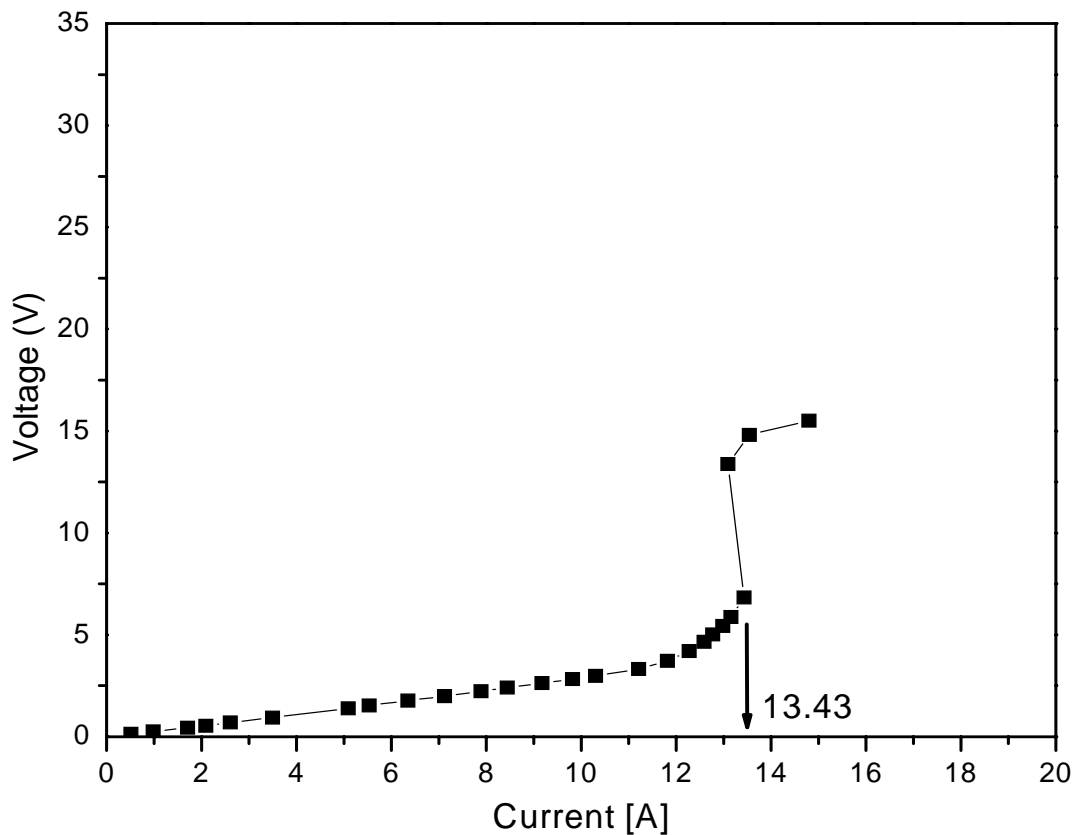


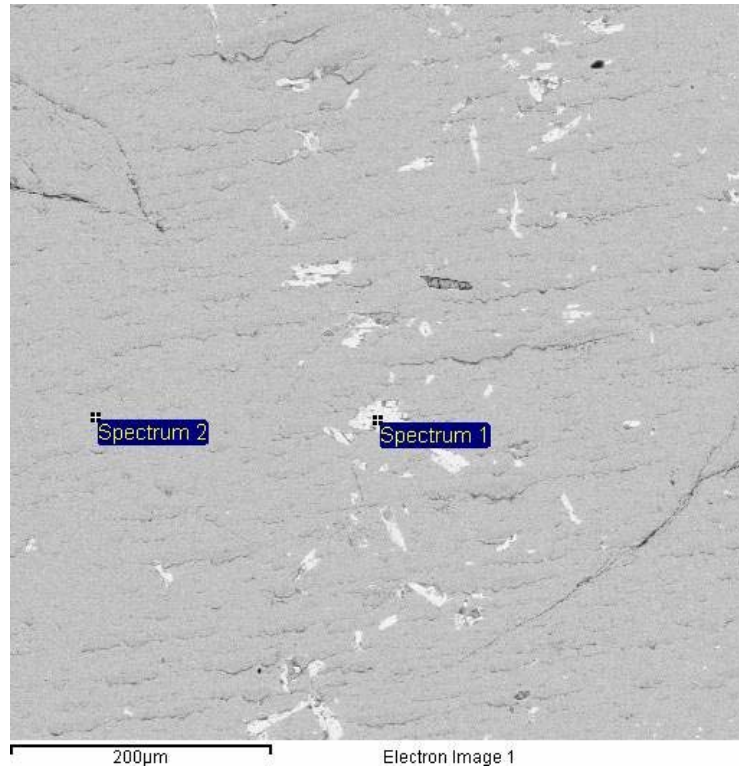
Fig.6.23 J_c measurement of TSMTG Pt-CY-5 cylinder

6.4 Characterisation of TSMTG Ce-CY-6 sample

The cylinder was cut vertically and polished, etched as mentioned in section 6.3.1.

6.4.1 SEM of TSMTG Ce-CY-6 cylinder

SEM image of TSMTG Ce-CY-6 plate shows (Fig.6.24) dense structure. From EDS spectrum 1 the white portion in the graph shows presence of cerium and spectrum 2 shows Y, Ba and Cu in the ratio approximately 1:2:3 which gives the evidence that Ce is homogeneously distributed in the matrix of Y-123.



Spectrum atom %	Y	Ba	Cu	Ce
Spectrum 1	5.45	6.32	10.8	0.04
Spectrum 2	12.36	23.56	38.35	0.00

Fig.6.24 SEM and EDS spectrum of TSMTG Ce-CY-6 plate

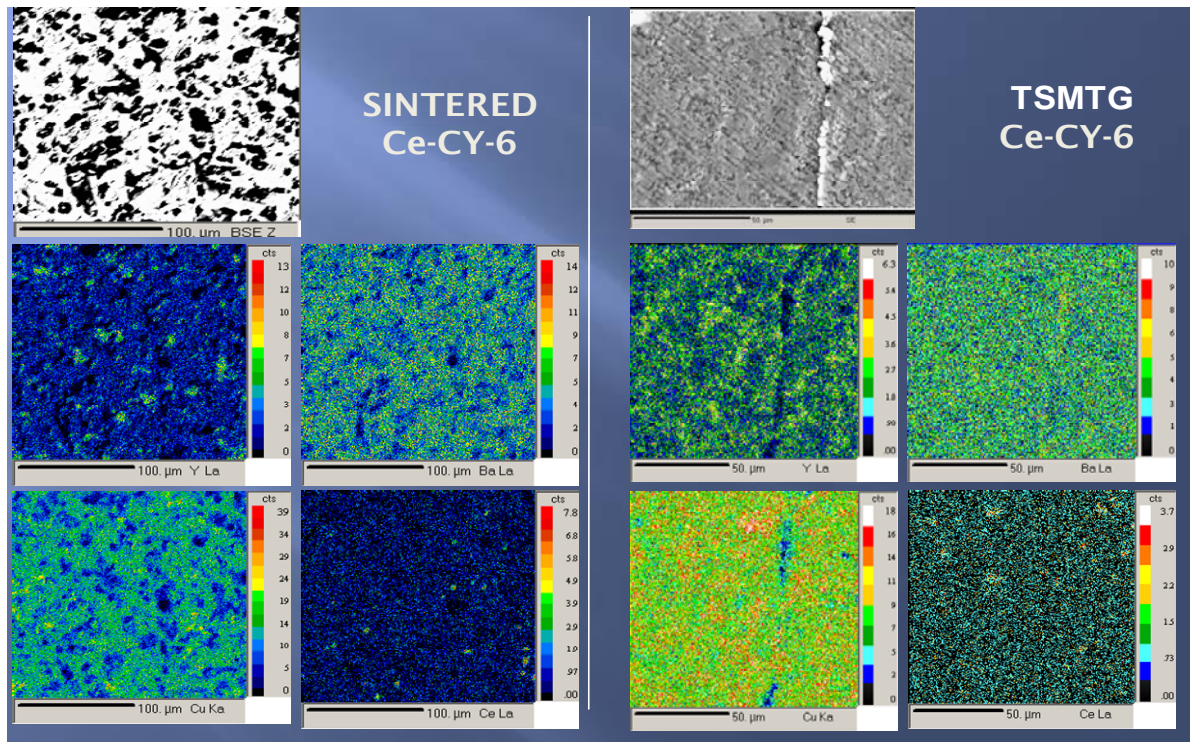


Fig.6.25 EPMA sintered Y-123 pellet and TSMTG of Ce-CY-6 plate

6.4.2 EPMA of TSMTG Ce-CY-6 plate

The cylinder was cut vertically polished and etched as mentioned in para 6.3.1. and subjected to EPMA analysis. Fig.6.25 shows the BSE image of Pt-CY-5. The dark region was due to the presence of porosity. The X-ray mapping of Y clearly shows presence of larger concentration of Y (green color) which is homogeneously distributed, the green colour is due to excess 25 wt % Y added in the composite C. X-ray mapping of Ba (greenish yellow) shows homogenous distribution. X-ray mapping of Cu (yellowish green color) shows the concentration of Cu is higher. At the same time less amount of Cu is seen, where the Y concentration is more. X-ray mapping of Pt shows homogeneous distributed Pt. This confirms that Y, Y-123 and Pt are uniformly distributed.

The microstructural observation made here for Back Scattered Electron (BSE) Images corroborates with the finding for Secondary Electron (SE) Images. The X-ray mapping of Y clearly shows presence of larger concentration of Y (green colour) in Y-rich phase and relatively smaller concentration of Y (blue colour) in Y-deficient phase in both sintered and MTG samples.

In the sintered sample, Y-rich phase is due to the addition of excess Y whereas in MTG sample it is most probably due to the formation of Y-211. The figure clearly indicates a better homogeneous distribution of both Y-rich and Y-deficient phase in MTG sample as compared to the sintered sample. The concentration of both Ba and Cu was higher in Y-deficient phase as compared to Y-rich phase. For both Ba and Cu, the green to yellowish colour represents Y-deficient phase (most probably due to Y-123 phase) and the bluish colour was for Y-rich phase (In sintered sample it is most probably due to addition of Y)

Similar observation was also made in MTG sample except for Cu. The Y-rich phase was shown by greenish colour whereas Y-deficient phase was represented by red colour. From the figure, it was evident that the distributions of both Ba and Cu in the respective phases were more uniform in MTG sample. The amount of Y-rich phase is found to be more in MTG sample as compared to sintered sample. It may be due to part of Y-123 transforming to Y-211 by reacting with Y_2O_3 during melt texturing process. Cerium was distributed uniformly both in sintered and MTG samples. However, due to its low concentration, it was difficult to conclude, whether Ce remained as a separate phase or it formed a solid solution.

6.4.3 J_c measurement of TSMTG Ce-CY-6 hollow cylinder

Fig.6.26 shows critical current density of Pt-CY-5 hollow cylinder. The number of turns in the primary coil were 100 and the excitation current was found to be 10.2A, therefore the estimated current in whole cylinder was 1020A (excitation current multiplied by No. Turns in the coil i.e. $10.2 \times 100 = 1020A$). Critical current density is calculated by dividing the current by area of cross section which was 0.42 cm^2 (9.8 mm H, 20.4 mm ID, and 29 mm OD). The critical current density is calculated by dividing the overall current divided by area of cross section that was found to be 2240 A/cm^2 .

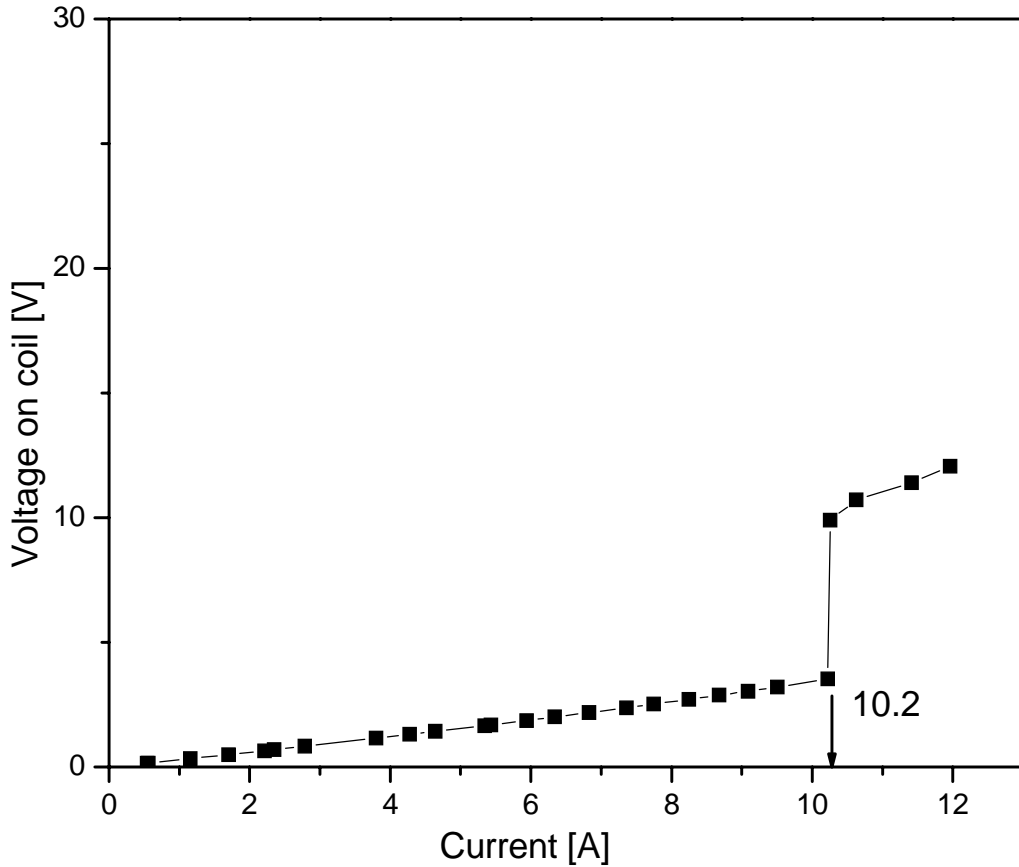


Fig.6.26 J_c measurement of TSMTG Ce-CY-6 cylinder

6.5 Conclusion

Characterisation of TSMTG components by various techniques was carried out. X-ray diffraction was used for phase purity and to determine orientation. Critical transition temperature (T_c) was measured by four probe method. Microstructural studies were carried out using SEM, EPMA, HRTEM and OIM. Magnetic properties were determined by using trapped magnetic field system, levitation force system and SQUID. Critical current density (J_c) was measured by inductive fault current limiting device (iFCL) at Budapest University of Technology and Economics (BUTE), Budapest, Hungary.

XRD of sintered samples shows phase pure Y-123 structure and XRD of typical TSMTG plate shows highly oriented Y-123 structure in 00l direction.

Critical transition temperature (T_c) of sintered and TSMTG sample was found to be 88K and 92K respectively.

TSMTG SSR-PL-1 plates were fabricated using composite A, containing Y-211 of initial average particle size of 15 microns synthesized by solid state route. The SEM showed average particle size of Y-211 as 15-20 microns, evenly distributed in the matrix of Y-123. EDS shows the atom % of Y, Ba, and Cu in matrix of Y-123 and Y-211 particles.

TSMTG NDR-PL-1 plates were fabricated using composite B, containing Y-211 of initial average particle size of 3-5 microns synthesized by nitrate decomposition route. The SEM showed average particle size of Y-211 as 5-6 microns, uniformly distributed in the matrix of Y-123.

EPMA image of TSMTG NDR-PL-2 and TSMTG SSR-PL-1 plate shows particle size of Y-211 and their distribution in the matrix of Y-123 and line profile shows the

discrete variation in Y, Ba, and Cu, which is evidence of distribution of Y-211 and Y-123 in the sample.

OIM images show the uniform distribution of Y-211 in the matrix of Y-123 and also show the texturing of Y-123 in 001 planes and randomly oriented Y-211 phase in MTG samples.

The comparison of magnetic properties is given in Table 6.1. The J_c value for various samples in different geometries were also measured and the results are summarised in Table 6.2.

The TSMTG NDR-CY-2 has shown maximum J_c compared to SSR-CY-1. From TSMTG NDR-PL-2 shows maximum trapped field and levitation force (Table 6.2) compared to SSR-PL-1. The four fold increase in J_c values, the increase in trapped magnetic field and levitation force is due to the smaller particle size of Y-211. Y is transported during melt texturing across the Y deficient liquid phase to the growing Y-123 nuclei. Y-211 particles act as the source for Y. It is understood that finer the particle size of Y-211 for a given volume fraction of the Y-211 phase, the more uniform will be the distribution and hence shorter the diffusion path length for Y. In such a case, the Y-123 nuclei grow larger resulting in improvement in critical current density (J_c).

It is clear from the above results that the melt textured samples show considerable improvement in all the properties like T_c , J_c , levitation force and trapped magnetic field. The uniformity of J_c values in the entire cylinder is clearly demonstrated by the similar value of J_c in the two halves of the same cylinder. Addition of Pt and ceria does not show any additional benefit in J_c values.

Nitrate decomposition route results in finer Y-211 grains which is more uniformly distributed and hence these samples show considerable improvement in properties. Thus use of fine uniformly distributed Y-211 to provide adequate pinning center and heat treatment by melt texturing technique to obtain grain orientation to reduce weak links has been clearly demonstrated to obtain usable shape with improved properties in MTG components of Y-123.

TSMTG components name	Levitation Force (N)	Trapped magnetic field (G)
SSR-PL-1 SSR- synthesis of Y-211 powder using solid state route, PL-plate shape and plate No.1. [plate fabricated using composite A, i.e.Y-123+Y-211(SSR)+Ag]	8	0-200
NDR-PL-2 NDR- synthesis of Y-211 powder using nitrate decomposition route, PL-plate shape and plate No.2 [plate fabricated using composite B, i.e.Y-123+Y-211(NDR)+Ag]	28	0-800

Table 6.1 Comparison of magnetic properties of TSMTG plates at a glance

Sr. No.	Cylinder name	ID (cm)	OD (cm)	Height (cm)	Cross section area Cm^2	Primary coil No. of turns	Excitation current (A)	HTSC cylinder current (A)	Critical current density (J_c) (A/cm^2)	
1	SSR-CY-1 SSR- synthesis of Y-211 powder using solid state route, CY- cylinder shape and Cylinder No.1. [cylinder fabricated using composite A, i.e.Y-123+Y-211(SSR)+Ag]	36	46	40	2	100	16.76	1676	838	
2	NDR-CY-2 NDR- synthesis of Y-211 powder using nitrate decomposition route, CY- cylinder shape and cylinder No.2 [cylinder fabricated using composite B, i.e.Y-123+Y-211(NDR)+Ag]	36	46	50	2.5	713	14	10082	4032	
3	NDR-CY-2a NDR- synthesis of Y-211 powder using nitrate decomposition route, CY- cylinder shape, cylinder No. 2a. [cylinder fabricated using composite B, i.e.Y-123+Y-211(NDR)+Ag]	36	46	50	2.5	713	13.5	9625	3850	
3	NDR-CY-3 NDR- synthesis of Y-211 powder using nitrate decomposition route, CY- cylinder shape and cylinder No. 2a. [cylinder fabricated using composite B, i.e.Y-123+Y-211(NDR)+Ag was cut horizontally in to two halves- top and bottom]	top	20.7	53.4	5.6	0.915	100	20	2000	2185
4		bottom	21.9	51.3	5.6	0.825	100	20.07	2007	2424
5	Pt-CY-5 Pt- platinum, CY-cylinder shape, cylinder No. 5. (cylinder fabricated using composite C, i.e. Y-123+yttria+Pt)	21.1	28.7	15.7	0.595	100	13.4	1340	2246	
6	Ce-CY-6 Ce- cerium oxide, Cy-cylinder shape and cylinder No. 6 (cylinder fabricated using composite D, i.e. Y-123+yttria+Ceria)	20.4	29	9.8	0.42	100	10.2	1020	2240	

Table 6.2 Critical current density of TSMTG hollow cylinders

CHAPTER 7

Conclusions and future scope

7.1 Conclusions

Fabrication of large usable shapes of high temperature superconductors having a T_c of above liquid nitrogen temperature oxide superconductors and high critical current densities for particle applications was a challenging task. This required a rigorous control at every step starting from synthesis of powders. This work addressed several key issues associated with the fabrication process. The salient features of this work are as follows:

i) A six sided heating 3 KW kanthal furnace capable of operating upto 1150°C was designed, developed and fabricated for processing the HTSC components using melt texture growth technique (MTG). MTG requires uniform temperature inside the hot zone of the order of $\pm 1^\circ\text{C}$ and very slow cooling rates of 0.2 to 0.4°C/h . This was connected with eurotherm programmable temperature controller model 2416, current meter and thyristor firing unit. Chromel Alumel thermocouple was used for temperature measurement. The special feature of this furnace is that it has six side heating facility, which provides a uniform hot zone of $\pm 1^\circ\text{C}$ and a ramp rate of $0.2\text{-}0.5^\circ\text{C/h}$ can be maintained.

ii) Low temperature (77K liquid nitrogen) critical transition temperature (T_c) measurement setup (Fig.2.1) was designed and developed for multi-samples measurements (five samples) in a single run. For measuring T_c , standard four probe technique has been employed. A constant current source, nano-voltmeter, temperature controller and a multichannel scanner was connected. In a sequential manner the data of

all the samples were recorded using a PC controlled set up. The resistivity was plotted as a function of temperature to obtain T_c .

iii) A combined unit for measurement of trapped magnetic field and levitation force of large MTG samples was designed, developed and fabricated. The unit has an advantage of generating data relatively in very short period and the results reveal about the quality of the MTG sample. The technique developed is used for measuring large sample with size of 25 x 25 mm in 90-120 min without destroying the shape. From the data, it could be concluded whether the sample quality is good or not.

iv) An economical process was developed for synthesis of bulk Y-123 and graded Y-211 phase pure powders in one Kg size batch. The powders were characterized for their particle size distribution, phase purity, oxygen content and critical current density. The effect of quenching on T_c , oxygen content and crystal structure was studied. By taking appropriate precautions it was possible to prepare high quality Y-123 oxide and Y-211 oxide powders without any deterioration of their properties. The final products were well characterised for their microstructure, T_c , J_c , and magnetic properties.

v) Four types of composites were prepared i.e. (i) Y-123 + Y-211 + Ag (composite A) (ii) Y-123 + Y-211 + Ag (composite B) (iii) Y-123 + Y_2O_3 + Pt (composite C) and (iv) Y-123 + Y_2O_3 + CeO_2 (composite D). Pure Y-123 and all the above composites (A,B,C and D) were pelletised. Further the pellets of each composites were (a) sintered at 30°C/10 hours and annealed at 400°C for 15 h in oxygen atmosphere and (b) Quenched from 1010°C into liquid nitrogen bath. Both sintered and quenched samples have been

characterised by X-ray diffraction, scanning electron microscopy, Electron probe micro analysis (EPMA) and critical temperature measurements (T_c). XRD patterns reveal the phase composition while SEM shows the microstructural features. EPMA revealed homogenous elemental distribution confirming uniform mixing during preparation of samples. T_c measurement of pure Y-123 showed that it superconducts at 88K. Sintered composite samples were found to be non-superconducting upto liquid nitrogen temperature, this is because addition of 25 wt % non-superconducting phase like yttria and Y-211 phase in Y-123 superconducting phase kills the superconducting properties. All sintered and quenched composite samples showed semiconducting behaviour above 77K. The BSE images of sintered composite A and B showed multi granular porous structure, whereas quenched samples of composite A and B showed dense structure. The elemental X-ray mapping of sintered sample of composite B shows Y-211 and Ag are homogeneously distributed in the matrix of Y-123. The X-ray mapping of sintered sample of composite C shows uniform distribution of Y and Pt in the matrix of Y-123. In the same way sintered sample of composite D shows Y and Ce are uniformly distributed in the matrix of Y-123.

vi) The compacts using all the above four composites were fabricated in hollow cylindrical, pin shape and plate shapes. Rubber moulds were designed for carrying out cold isostatic pressing, taking into account the shrinkage during different processing steps. The pressure and the thermal schedule for different shape of MTG samples were optimized. These compacts were then subjected to MTG, followed by prolonged annealing in oxygen atmosphere. They were characterized for critical transition temperature (T_c) measurement, microstructure by SEM, OIM, EPMA etc., Critical

current density (J_c) was measured at Budapest University of Technology and Economics, Hungary. Trapped magnetic field and levitation force were measured using the in-house developed unit. The critical transition temperature of MTG samples show sharp drop at 92 K and T_c was found to be 91K.

vii) The Scanning Electron Microscope (SEM) images of TSMTG fabricated sample using initial precursor of solid state route (initial powder average particle size 10-15 microns) show 15-20 microns of Y-211 particles. The SEM image of TSMTG fabricated sample using nitrate decomposition powder (initial powder average particle size 3-5 microns) show 3-5 micron size of Y-211 particles along with their distribution in the matrix of YBCO.

viii) Electron Probe Micro-Analyzer (EPMA) image and corresponding elemental mapping show particle size distribution of Y-211 phase in the matrix of YBCO. These experiments also reveal the line profile of the variation of individual elements from matrix of Y-123 (superconducting) and Y-211 (non-superconducting) phases. The line profile shows the sudden discrete variation in the atomic percentage corresponding to Y, Cu and Ba.

ix) Orientation Imaging Microscope (OIM) images shows Y-211 particle to be distributed in the matrix of YBCO and the color coding shows that all red color in the matrix are 001 oriented YBCO and the green color corresponds to Y-211 phase, which is randomly oriented. This OIM orientation is in corroboration with XRD analysis where the XRD patterns show all the peaks correspond to 00l oriented plane.

x) TEM of Y-123 sintered powder is compared with TSMTG powder. The TEM of sintered powder showed that the grains are not aligned. The MTG powder shows two types of grains which are aligned with an angle of approximate 3-4 degree. This shows that crystals of Y-123 grains are textured and aligned.

xi) The J_c of sintered Y-123 compact was only 600 mA/cm². The critical current density (J_c) was found to be 838 A.cm⁻² for Y-123 samples containing Y-211 prepared by solid state route. However, TSMTG Y-123 samples containing Y-211 prepared by nitrate decomposition route showed a remarkably high J_c value of 4032 A.cm⁻². The five-time increase in current density is mainly attributed to the finer size of the Y-211 phase obtained by the nitrate decomposition route. The J_c values measured for other TSMTG samples generated using Pt, ceria added additives were found to be lower as compared to Y-211 addition.

xii) The maximum trapped field values for TSMTG plate prepared by solid state route and for TSMTG sample prepared from nitrate decomposition route were 0-200 gauss and 0-800 gauss, respectively. Levitation force measured at 1 mm distance from magnet of TSMTG plate prepared by solid state route show force of 8 N and whereas in TSMTG sample prepared by Y-211 synthesized by nitrate decomposition route show remarkably high force of 28 N.

xiii) Melt-texture growth of polycrystalline YBa₂Cu₃O_{7-δ} superconductor using MgO as seed crystal created an essentially highly dense structure, preferably aligned parallel to the ab-plane. The new microstructure, which completely replaces the previous granular

and random structure in the sintered bodies, exhibits improved transport J_c values at 77 K of 4032 A/cm^2 in zero field (compared to 600 mA/cm^2 in sintered bodies). The remarkable improvement in J_c is attributed to the combined effects of graded Y-211 particles, compaction, appropriate thermal cycle, alignment of crystals, formation of cleaner grain boundaries.

xiv) Melt textured samples of specified dimensions for construction of a superconductors based motor were fabricated and supplied to the motor designer. The motor was tested in collaboration with Control Instrumentation Division, BARC and report is attached in Appendix.

7.2 Future scope of this work

Fabrication process for large HTSC MTG components will be optimized for enhanced superconducting properties. Since from the present study, it is established that the particle size of Y-211 plays an important role in enhancing the superconducting properties, synthesis of nano Y-211 powders which will act as pinning centres will be carried out choosing proper variation in process parameters. Using the above synthesized nano Y-211 MTG components will be fabricated by optimizing the pressure for CIP, thermal schedule etc. The components will be characterized for microstructure, J_c and other HTSC properties. However, this engineering work is out of scope of the present thesis and hence it will be taken up subsequently. Also to apply the fabricated components it is required to study the mechanical properties at room temperature as well at liquid nitrogen temperature.

Other HTSC material like $\text{Bi}_{1.7}\text{Pb}_{0.3}\text{Sr}_2\text{Ca}_2\text{Cu}_3\text{O}_{10}$ (BSCCO) powder will be synthesized. Attempts will also be made to fabricate similar components from the above

powder. The powder will also be used to fabricate long length tapes using powder in tube technique. These tapes will be used in winding the HTSC motors.

Appendix

Control Instrumentation Division (CnID) BARC had been assigned the task of designing a prototype HTSC motor. As per the design requirement, a consignment of MTG components of hollow cylinder, plates and pins, was prepared by the top seeded melt texture growth (TSMTG) technique described in this thesis. The details of the supply are :

A.1 Supply of MTG components of different shapes:

A set of 30 pins of Y-123 oxide were fabricated using methods discussed in present thesis. Composite B powder was filled in mould size pins 1, compacted in CIP. All the 30 pins were sintered and subjected to TSMTG thermal schedule. After MTG, they were machined to 8 mm OD x 25 mm height and further subjected to annealing in oxygen atmosphere at 425°C for 150 h.

A set of 2 plates were fabricated. The composite B powder was filled in mould size Plate 1, compacted in CIP. Both the plates were sintered and subjected to MTG in identical condition of thermal schedule. The plates were machined to 3.5 mm thick x 25 mm length x 50 mm and further subjected to annealing in oxygen atmosphere at 425°C for 150 h.

A hollow cylinder was fabricated using composite B. The composite B powder was filled in the mould, compacted in CIP. The cylinder was then sintered and subjected to MTG thermal schedule. The cylinder was machined to 46 mm ID x 36 mm OD x 50 mm height and further subjected to annealing in oxygen at 425°C for 200 h.

A.2 Characterisation of MTG components

A.2.1 Levitation Force Measurement of YBCO Pins

TSMTG Pins were tested for levitation force before using in motor. The 8mm-dia x 25mm-long pins were bunched in 7 nos and 19 nos and immersed in liquid nitrogen in a thermocole container at zero field. A samarium cobalt permanent magnet fitted vertically in line with a loadcell was gradually approached to YBCO pins from the top. A fibre glass distance piece between magnet and loadcell isolates the load cell from thermal and magnetic field of superconductor. A 3-dimensional micrometer helps in positioning the magnet centrally over the pins and measuring the varied vertical distance of magnet from the pins. The levitation force measured at a distance of 1mm from magnet and pins for 7 pins bunched was found to be 16 N (Fig. A.1) and levitation force of 19 pins was found to be 34 N (Fig. A.2).

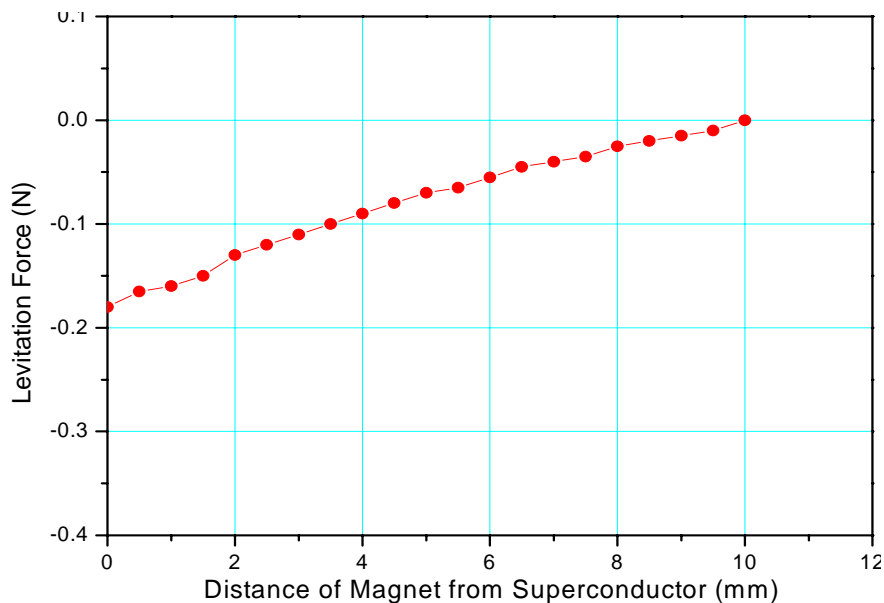


Fig. A.1 Levitation force measured at a distance of 1mm from magnet and pins for 7 pins bunched was found to be 17 N

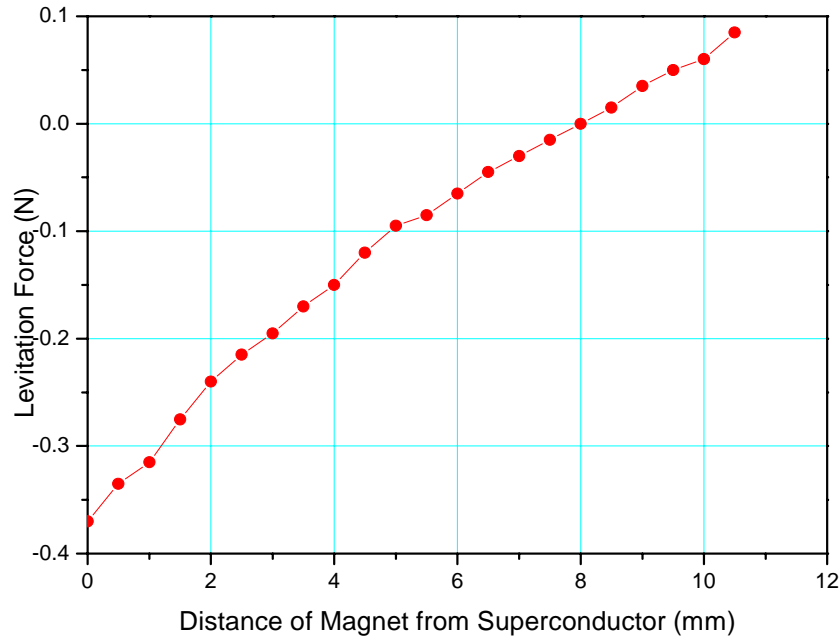


Fig. A.2 Levitation force measured at a distance of 1mm from magnet and pins for 19 pins bunched was found to be 34 N

A.3 Application of MTG components as rotor in prototype HTSC motor

The MTG plates, pins and hollow cylinders were used in HTSC motor. Fig A.3, shows the schematic drawing of HTSC rotor, assembly of parts of rotor with HTSC plates and assembled rotor.

The schematic drawing of HTSC rotor, assembly of parts of rotor with HTSC pins and assembled rotor is shown in Fig. A.4.

The HTSC hollow cylinder fixed inside the rotor is shown in Fig.A.5. The assembled rotor fixed with HTSC cylinder is also shown in Fig.A.5

The picture of HTSC motor assembly is shown in Fig. A.6.

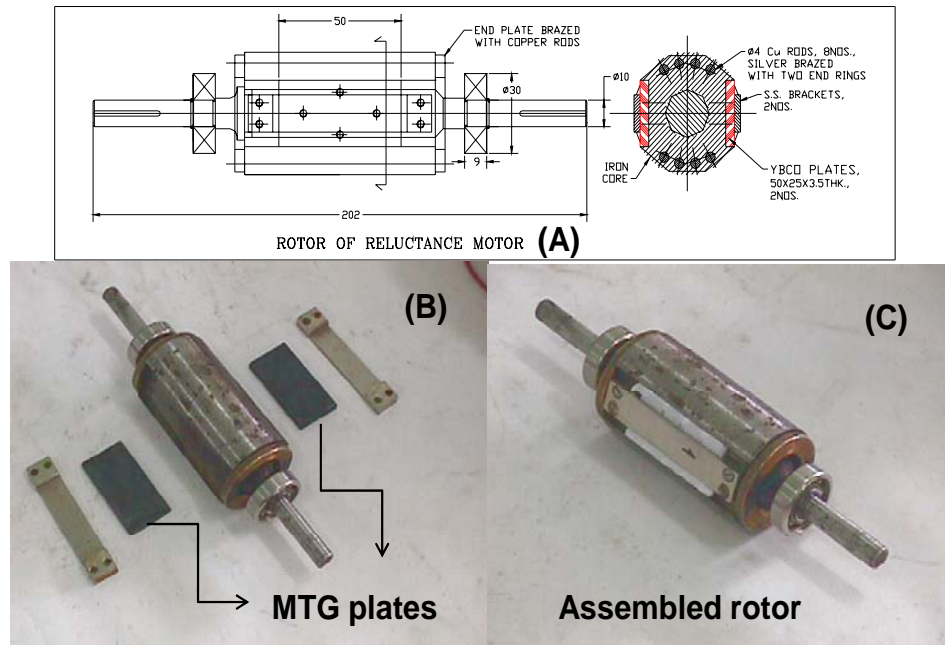


Fig.A.3 (A) Schematic drawing of rotor, (B) parts of rotor with HTSC plates, (C) assembled plate type rotor

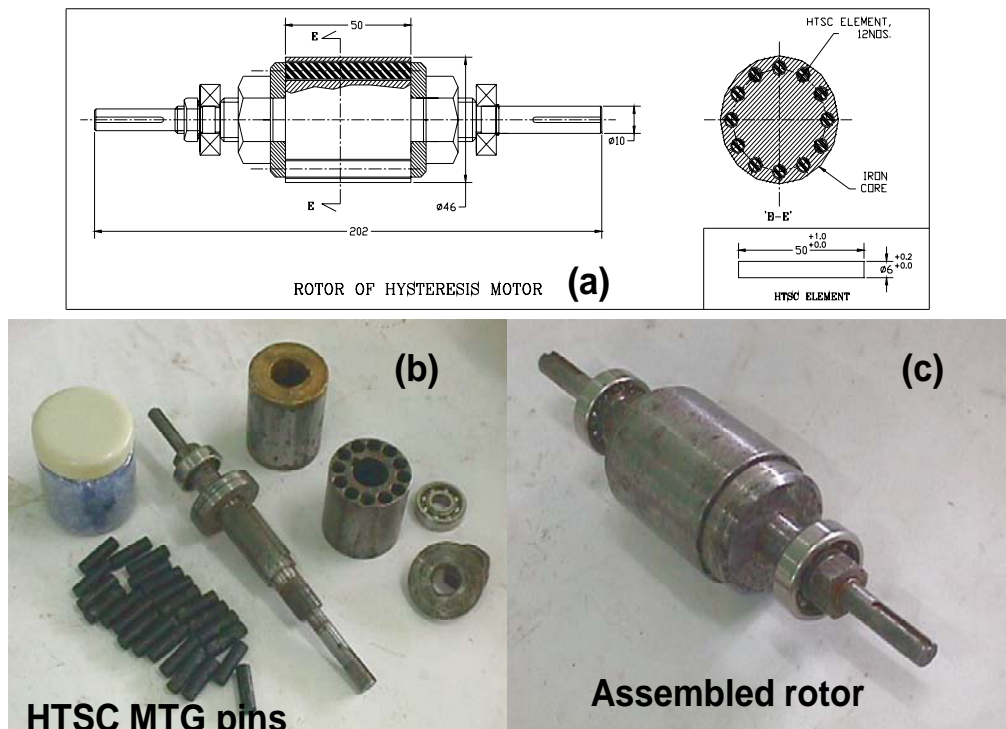


Fig.A.4 (a) Schematic drawing of rotor, (b) parts of rotor with HTSC pins, (c) assembled pin type rotor



HTSC MTG hollow cylinder

Fig. A.5 HTSC hollow cylinder fixed inside the rotor and assembly of hollow



Fig.A.6 HTSC motor assembly

A.4 Test report

Test Report of Motor with YBCO pins: From the testing report of Y-123 MTG 24 Nos. pins supplied to Control instrumentation Division, BARC, it was established that the motor was working and exhibited flat torque characteristics up to synchronous speed of 2900 rpm without load.

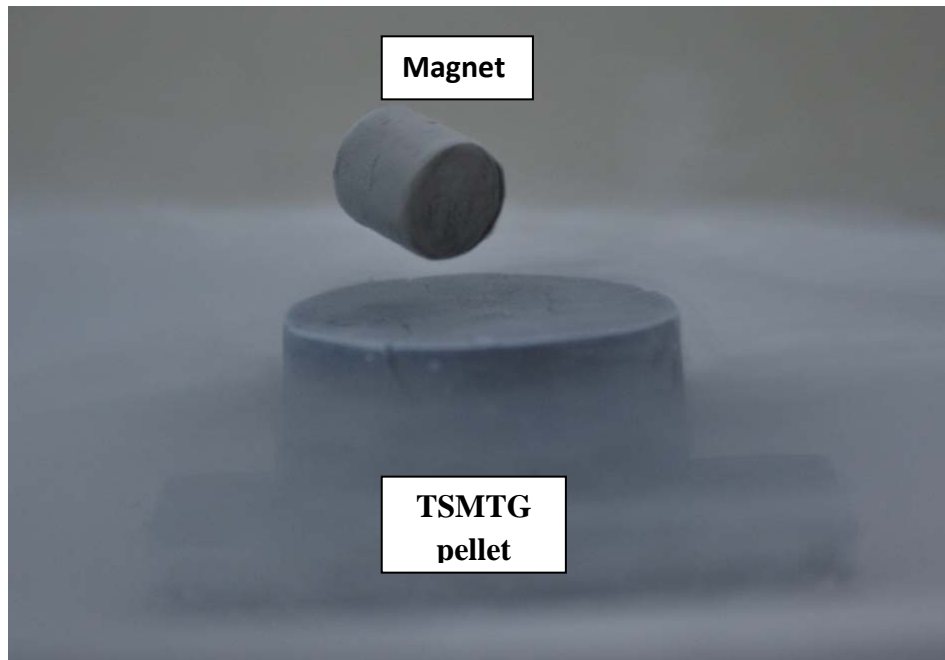


Fig.A-7 Levitating magnet on TSMTG pellet

References

1. J.G. Bednorz and K.A. Muller, *Z. Phys. B*, 64 (1986) 189.
2. D. Larbalestier, A.Gurevich, D. Feldmann, *Nature* (2001) 414.
3. W.Meissner and R.Oschenfeld, *Naturwissenschaften*, 21 (1993) 287.
4. E.Maxwell, *Phys. Rev.* 78 (1950) 477.
5. C.Reynolds, B.Serin, W.Wright and L.Nesbitt, *Phys. Rev.*78 (1950) 487.
6. J.Bardeen, *Phy.Rev.*79 (1950) 167.
7. H. Frohlick, *Phy. Rev.*79 (1950)845.
8. R.D. Parks, *Superconductivity*, Marcel Dekker, New York (1968).
9. T.Geballe, T.Maahias, G.W.Hull and E.Corenzwit, *Phy. Rev. Lett.* 6 (1961) 275.
10. R.D.Flower, J.D.G.Lindsey, R.W.White, A.H.Hill and B.T.matthias, *Phys. Rev.* (1967) 892.
11. J.Bardeen, L.N.Cooper and J.R.Schrieffer, *Phy. Rv.*, 106 (1957) 162: 108 (1957) 1175.
12. L.N. Cooper, *Phys. Rev.* 104 (1956) 892.
13. M.A. Beno, L. Soderholm, D.W. Capone II, D.G. Hinks, J.D. Jorgensen, J.D. Grace, I.K. Schuller, C.U. Segre and K. Zhang, *Appl. Phys. Lett.* 51 (1987) 57.
14. F. Izumi, H. Asano, T. Ishigaki, A. One and F.P. Okamura, *Jpn. J. Appl. Phys.*, 26 (1987) L611.
15. J.J. Capponi, C. Chaillout, A.W. Hewat, P. Lejay, M. Marezio, N. Nguyen, B. Reveau, J.L. Soubeyroux, J.L. Tholence and R. Tournier, *Europhys, Lett.*, 3 (1987) 1301.
16. T. Hatano, A. Mastsushita, K. Nakamura, Y. Sakka, T. Matsumoto and K. Ogawa, *Jpn. J. Appl. Phys.*, 26 (1987) 721.

17. R.J. Cava, B. Batlogg, C.H. Chen, E.A. Rietman, S.M. Zahurak and D. Werder, *Nature*, 329 (1987) 423.
18. B.J. lee and D.N. Lee, *J. Am. Ceram. Soc.*, 74 (1991) 78.
19. T.B. Lindemer, J.F. Hunley, J.E. Gates, Jr. A.L. Sutton, J. Brynestad, C.R. Hubbard and P.K. Gallagher, *J. Am. Ceram. Soc.*, 72 (1989) 1775.
20. S. Hosoya, S. Shamoto, M. Onoda dn M. Sato, *Jpn. J. Appl. Phys.* 26 (1987) L325.
21. S. Kanbe, T. Hasegawa, M. Aoki, T. Nakamura, H. Koinuma, K. Kishio, K. Kitazawa, H. Takagi, S. Uchida, S. Tanaka and K. Fueki, *Jpn. J. Appl. Phys.*, 26 (1987) L613.
22. S. Hikami, S. Kagoshima, S. Kamiyama, T. Hirai, H. Minami and T. Masumi, *Jpn. J. Appl. Phys.*, 26 (1987) L 347.
23. T. Tamegai, A. Watanabe, I. Oguro and Y. Iye, *Jpn. J. Appl. Phys.*, 26 (1987) 1987.
24. J.M. Tarascon, W.R. McKinnon, L.H. Greene, G.W. Hull and E.M. Vogel, *Phys. Rev. B*, 36 (1987) 326.
25. K. Takita, H. Akinaga, H. Kato, T. Ipposhi and K. Masuda, *Jpn. J. Appl. Phys.* 26 (1987) L854.
26. T. Iwata, M. Hikita and S. Tsurumi, *Adv. Supercond. I* (1989) 197.
27. S.I. Yoo and R.W. McCallum, *Physica C*, 210 (1993) 147.
28. T. Wada, N. Suzuki, T. Maeda, A. Maeda, S. Uchida, K. Uchinokura and S. Tanaka, *Appl. Phys. Lett.* 52 (1988) 1989.
29. M. Daeumling, J.M. Seunjens and D.C. Larbalestier, *Nature*, 346 (1990) 332.
30. J. Bardeen, L.N. Cooper and J.R. Schrieffer, *Phys. Rev.* 108 (1957) 1175.

31. M. Morita, S. Takebayashi, M. Tanaka and K. Kimura,
Adv. Supercond., 3 (1991) 733.
32. S.I. Yoo, M. Murakami, N. Sakai, T. Higuchi and S. Tanaka,
Jpn. J. Appl. Phys.,33 (1994) L1000.
33. S.I. Yoo, N. Sakai, H. Takaichi, T. Higuchi and M. Murakami,
J. Appl. Phys. 65 (1994) 633.
34. M. Murakami, S.I. Yoo, T. Higuchi, N. Sakai, J. Weltz, N Koshizukza
and S. Tanaka, Jpn. J. Appl. Phys. 33 (1994) L715.
35. W. Meissner and R. Ochsenfeld, Naturwissenschaften, 21 (1933) 787.
36. B.D. Josphson, Phys. Lett., I (1962) 251.
37. P. McGinn, W. Chen, N. Zhu, M. Lanagan and U. Balachandran, Appl. Phys.
Lett.57 (1990) 1455.
38. R.L. Meng, C. Kinalidis, Y.Y. Sun, K. Gao, Y.K. Tao, P.H. Hor and C.W. Chu,
Nature, 345 (1990) 326.
39. T. Izumi and Y. Shiohara, J. Mater. Res. 7 (1992) 16.
40. A.M. Figueredo, M.J. Cima, M.C. Flemings, J.S. Haggerty, T. Hara, H. Ishii, T.
Ohkuma and S. Hirano, Physica C, 241 (1995) 92.
41. Y. Iijima, N. Tanabe, O. Kohno and Y. Ikeno, Appl. Phys. Lett., 60 (1992) 769.
42. F.C. Moon, M.M. Yanoviak and R. Ware, Appl. Phys. Lett., 52 (1988) 1534.
43. H. Fukuyama, K. Seki, T. Takizawa, S. Aihara, M. Murakami, H. Takaichi and
S. Tanaka, Adv. Supercond. 4 (1992) 1093.
44. H. Ogiwara, T. Azukizawa and M. Morihita, Appl. Supercond. 3-6 (1993) 1185.
45. S.L. Wipf and H.L. Laquer, IEEE Trans. Magn., 25 (1989) 1877.
46. M. Murakami, Melt Processed High-Temperature Superconductors, World
Scientific, Singapore, 1992.

47. H.J. Scheel, M. Berkowski and B. Chabot, *J. Cryst. Growth*, 115 (1991) 19.
48. H. Sakai, Y. Yamada, Y. Shiohara and S. Tanaka, *Physica C*, 241 (1994) 292.
49. H. Hojaji, A. Barkatt, K.A. Michael, S. Hu, A.N. Thorpe, M.F. Ware, I.G. Talmy, D.A. Haught and S. Alterescu, *J. Mater. Res.*, 5 (1990) 721.
50. M. Miyajima, S. Nagaya, I. Hirabayashi, Y. Ogawa, Y. Mitsune, Y. Ishikawa and S. Yoshizawa, *Adv. Supercond.*, 2 (1990) 427.
51. T. Kumagai, W. Kondo, H. Yokota, H. Minamiue and S. Mizuta, *Chem. Lett.* (1988) 551.
52. T.K. Worthington, W.J. Gallagher, D.L. Kaiser, F.H. Holtzberg and T.R. Dinger, *Physica C*, 153-155 (1988) 32.
53. D. Dimos, P. Chaudhari and J. Mannhart, *Phys. Rev. B*, 41 (1990) 4038.
54. S.E. Babcock, X.Y. Cai, D.L. Kaiser and D.C. Larbalestier, *Nature*, 347 (1990) 167.
55. M. Temkin, *Introduction to Superconductivity*, McGraw-Hill, New York, 1975.
56. A.M. Campbell and J.E. Evetts, *Adv. Phys.*, 21 (1992) 199.
57. Y. Matsuda, Y. Hirai, S. Komiyama, T. Terashima, Y. Bando, K. Iijima, K. Yamamoto and K. Hirata, *Phys. Rev. B*, 40 (1989) 1989.
58. M. Murakami, *Progr. Mater. Sci.*, 38 (1994) 311.
59. K. Yamaguchi, M. Murakami, H. Fujimoto, S. Gotoh, N. Koshizuka and S. Tanaka, *Jpn. J. Appl. Phys.* 29 (1990) L 1428.
60. M. Ullrich, A. Leenders, J. Krelaus, L. Schidt, *Mat. Sci. Eng. B* 53 (1998) 148.
61. J. Hull, F.E. Hilton, T.M. Mulchay, Z.J. Yang, A. Lockwood, *Appl. Phys.* 78 (1995) 6833.
62. Hull, J., Mulcacy, K.L. Uhreka, R.A. Erck, R.G. Abboud, *Appl. Supercond.* 2 (1994) 449.

63. B.Oswald, Krone, K.J.Beast, W. Gawalek, H.C.freyhardt.
Physica C, 372 (2002) 1513
64. J.P.Singh,J.Joo,D.Singh,R.B.Poeppel, J.Mater. Res. 8, (1993) 1226
65. T. Dinger.T.Worthington,W.gallagher, and R.Sandstrom,
Phy. Rev. Lett. 58, (1987) 152.
66. V.Sevamanickam and K.Salam, Appl. Phys. Lett 57,(1990) 1575.
67. Jin, T. Tiefel, R. Sherwood, R. van Dover, M. Davis, G. Kammlott, and R.
Fastnacht, Phys.Rev. B 37, 7850 (1988) 7850.
68. S. Jin, T. Tiefel, R. Sherwood, M. Davis, R. Van Dover G. Kammlott, R.
Fastnacht, and H. Keith, Appl. Phys. Lett. 52 (1988) 2074.
69. S. Jin, R. Sherwood, E. Gyorgy, T. Tiefel, R. Van Dover, S. Nakahara, L.
Schneemeyer, R. Fastnacht, and M. Davis, Appl. Phys. Lett. 54(1989) 584.

Chapter 2

70. Gyore, I. Vajda, M.R. Gonal, D K Pandya, IEEE transaction on applied
superconductivity, 17, 2, (2007) 1899.
71. M.K. Wu, J.R. Ashburn, C.J. Torng, P.H. Hor, R.L. Meng, L. Gao, Z.J. Huang,
Y.Q. Wang and C.W. Chu, Phys. Rev. Lett. 58 (1987) 908.
72. C.N.R. Rao, P. Ganguly, A.K. Ray Chaudhuri, R.A. Mohan Ram, and K.
Sreedhar, Nature 326 (1987) 856.
73. R.J. Cava, B. Batlogg, R.V. vanDover, D.W. Murphy, S. Sunshine, T. Siegrist,
J.P. Remeika, E.A. Rietman, S. Zahurak and
G.P. Espinosa, Phys. Rev. Lett. 58 (1987) 1676.
74. J.D. Jorgensen, M.A. Beno, D.G. Hinks, L. Soderholm, K.J. Volin, R.L.
Hitterman, J.D. Grace, I.K. Schuller, C.U. Segre, K. Zhang and M.S. Kleefisch,
Phys. Rev., B36 (1987) 3608.

75. J.S. Swinnea and J. Steinfink, *J. Mater. Res.*, 2 (1987) 442.
76. P.K. Gallagher, H.M. O'Bryan, S.A. Sunshine and D.W. Murphy, *Mat. Res. Bull.* 22 (1987) 995.
77. M.A. Beno, L. Soderholm, D.W. Capone II, D.G. Hinks, J.D. Jorgensen, I.K. Schuller, C.U. Segre, K. Zhang, and J.D. Grace, *Appl. Phys. Lett.*, 51 (1987) 57.
78. Y. Le Page, W.R. McKinnon, J.M. Tarascon, L.H. Green, G.W. Hull and D.M. Whang, *Phys. Rev.*, B35 (1987) 7195.
79. R. Beyers, G. Lim, E.M. Engler, V.Y. Lee, M.L. Ramirej, R.J. Savoy, R.D. Jacowitz, T.M. Shaw, S. La Placa, R. Boehme, C.C. Tsuei, Sung I. Park, M.W. Shafer, W.J. Gallagher and G.V. Chandrasekhar, *Appl. Phys. Lett.*, 51 (1987) 614.
80. G. Mie., "Considerations on the optic of turbid media, especially, colloidal metal sols" *Ann. Phys (Leipzig)* 25 (1908) 377.
81. H. Fujimoto; M. Murakami; S. Gotoh; N. Koshizuka; T. Oyama; Y. Shiohara; S. Tanaka; *Adv. Supercond.* 1990, pages 285-288.
82. T. Izumi; Y. Nakamura; Y. Shiohara; *J. Mater. Res.* 7 (1992) 1621.
83. J.W. Ekin, in *Processing and Properties of High Tc superconductors*, vol 1, ed. By S. Jin, World scientific, Singapore (1993) 371.
84. H.J. Jensen, A. Brass, A.J. Berlinsky, *Phys. Rev. Lett.* 60 (1988) 1676.
85. M.C. Faleski, M.C. Marchetti, A.A. Middleton, *Phys. Rev. B* 54 (1996) 124-27.

Chapter 3

86. M. Leskela, C. Mueller, J.K. Truman, and P. Holloway,
Mater. Res. Bull. 23 (1988)1469.
87. U. Balachandran, R. Poeppel, J. Emerson, S. Johnson, M. Lanagan, C.
Youngdahl, K. Goretta, and N. Eror, Mater. Lett. 8 (1989) 454
88. N. Chen, D. Shi, and K. Goretta, J. Appl. Phys. 66 (1989) 2485.
89. E. Ruckenstein, S. Narain, and N.L. Wu, J. Mater. Res. 4 (1989) 267.
90. P. Barboux, J. Tarascon, L. Greene, G. Hull, B. Bagley,
J. Appl. Phys. 63 (1988) 2725.
91. M.P. Pechini, U.S. Patent 3,330, (July 11, 1967) 697
92. E. Hayri, M. Greenblatt, K. Ramanajachary, M. Nagano, J. Oliver, M. Miceli and
R. Gerhadt, J. Mater, Res.4, (1989) 1099.
93. J. Subrahmanyam and M. Vijayakumar, J. Mater. Sci. (1992) 6249.
94. J. Lebrat and A. Varma, Physica C 184 (1991) 220.
95. T. Kodas, E. Engler, V. Lee, R. Jacowitz, T. Baum, K. Roche, S. Parkin, W.
Young, S. Hughes, J. Kledr, and W. Auser, Appl. Phys. Lett.52(1988) 1622.
96. Y. Kimura, T. Ito, H. Yoshikawa, and A. Hiraki,
Jap. J. Appl. Phys.30 (1991) 798.
97. G.J. Yurek, J. Vander Sande, W. Wang, D. Rudman, Y. Zhang, and M.
Matthiesen, Met. Trans. 18A (1987) 1813.
98. T. Dinger, T. Worthington, W. Gallagher, and R. Sandstrom,
Phys Rev. Lett. 58 (1987) 22.
99. V. Selvamanickam and K. Salama, Appl. Phys. Lett. 57, (1990) 1575.
100. I.W. Chen, X. Wu, S. Keating, C. Keating, P. Johnson, and T.Y. Tien, J. Am.
Ceram. Soc. 70 (1987) 388.

101. K. Matsuzaki, A. Inoue, and T. Masumoto, *Jap. J. Appl. Phys.* 29, (1990) L1789.

Chapter 4

102. S. Jin et al., *Phys. Rev. B* 37 (1989) 1859.

103. K. Salama et al., *Appl. Phys. Lett.* 54 (1989) 2352.

104. M. Murakami et al., *Jpn. J. Appl. Phys.* 28 (1989) 1189.

105. L. Zhou et al., *Supercond. Sci. Technol.* 3 (1990) 490.

106. M. Murakami, *Supercond. Sci. Technol.* 5 (1992) 185.

107. M. Murakami, in: M. Murakami (Ed.), *Melt Processed High-Temperature Superconductors*, World Scientific, Singapore, (Chapter3).1992, pp. 21-44.

108. M.P.Delamare, H.Walter, B.Bringmann ,A.Leenders,*Physica C* 329 (2000)160.

109. Murakami, Fujitomo,S.Yaamaguchi,S.Tanaka, *Physica C* 254 (1995) 249.

110. S.Salib.Cvipulanandan and T.Stone, *proc. MRS Fall Mtg. Boston, MA Nov 1989*
169 (1990) 1217.

111. C.Vipulanandan, S.Sailb, and K. Ravi-chandar, *Teter. Res. Bull.* 24 (1989) 1059.

112. K.C. Goretta, M.Kulberg, D Bar, S.E. Dorris, U.Balchandran, J.C. Routbort,
Proc. TMS Spring Mtg., Anaheim, CA, (1990) 3154

113. S. Jin, R.C. Sherwood, T.M. Tiefel, R.B. van Dover and D.W. Johnson, *Appl. Phys. Lett.* 51 (1987) 203.

114. D. Pavuna, H. Berger, J.L. Tholence, M. Affronte, R. Sanjines, A. Dubas, Ph. Bugnon and F.Vasey, *Physica C* 153-155 (1988) 1339.

115. B.R. Weinberger, L. Lynds, D.M. Potrepka, D.B. Snow, C.T. Burila, H.E. Eaton Jr. and R. Cipolli, *Physica C* 161 (1989) 3154.

116. J.P. Singh, H.J. Leu, R.B. Poeppel, E. Van Voorhees, G.T. Goudey, K. Winsley and D. Shi, *J. Appl. Phys.* 66 (1989)198.

117. T. Nishio, Y. Itoh, F. Ogasawara, M. Suganuma, Y. Yamada and U. Mizutani, J. Mater.Sci.24 (1989) 3228.
118. M.K. Malik, V.D. Nair, A.R. Biswas, R.V. Raghavan, P. Chaddah, P.K. Mishra, G. Ravi Kumar and B.A. Dasannacharya, Appl. Phys. Lett. 52 (1988) 1525.
119. T.H. Tiefel, S. Jin, R.C. Sherwood, M.E. Davis, G.W. Kammlott, P.K. Gallagher, D.W. Johnson Jr., R.A. Fastnacht and W.W. Rhodes, Mater. Lett.7 (1989) 363.
120. C.J. Kim, H.W.Park, K.B.Kim, G.W.Hong, Supercond. Sci. Technology, 8 (1995) 165.
121. C.J.Kim, K.B.Kim, H.W.Park, T.H.Sung, Supercond. Sci.Tech. 9 (1996) 76.

Chapter 5

122. I.W. Chen, X. Wu, S. Keating, C. Keating, P. Johnson, and T.Y. Tien, J. Am. Ceram. Soc. 70, (1987) C 388.
123. K. Matsuzaki, A. Inoue, and T. Masumoto, Jap. J. Appl. Phys. 29, (1990) 1789.
124. D. Farrell, B. Chandrasekhar, M. DeGuire, M. Fang, V. Kogan, J. Clem, and D. Finnemore, Phys. Rev. B 36 (1987) 4025.
125. R. Arendt, A. Gaddipati, F. Luborsky, and L. Schilling, in High Temperature Superconductors, ed. By M.R. Brodsky, R. Dynes, K. Kitazawa, and H. Tuller. Materials Research Society, Pittshurgh (1988), 203.
126. J.E. Tkaczyk and K.W. Lay, J. Mater. Res .5 (1990) 1368.
127. M. Lees, D. Bourgault, D. Braithwaite, P. de Rango, P. Lejay, A. Sulpice, and R. Tournier, Physica C 191 (1992) 414.
128. S. Jin, T. Tiefel, R. Sherwood, R. van Dover, M. Davis, G. Kammlott, and R. Fastnacht, Phys. Rev. B 37 (1988) 7850.

129. S. Jin, T. Tiefel, R. Sherwood, M. Davis, R. van Dover G. Kammlott, R. Fastnacht, and H. Keith, *Appl. Phys. Lett.* 52(1988) 2074.
130. S. Jin, R. Sherwood, E. Gyorgy, T. Tiefel, R. van Dover, S. Nakahara, L. Schneemeyer, R. Fastnacht, and M. Davis, *Appl. Phys. Lett.* 54 (1989) 584.
131. T.H.Tiefel,S.Jin, R.A.Fastnacht, Presentation in Meter.Res. Soc. Fall Meeting , Boston, 1991.
132. Z.Lain, Presentation at New Orleans, 1991.
133. H. Fujimoto, M. Murakami, S. Gotoh, T. Oyama, Y. Shiohara, N. Koshizuka, and S. Tanaka, in *Advances in Superconductivity II*, Springer-Verlag, Tokyo (1990) 85.
134. M. Murakami, *Mod. Phys. Lett.* 4 (1990)163.
135. Z. Lian, Z. Pingxiang, J. Ping, W. Keguang, W. Jingrong, and W. Xiaozu, *Supercond. Sci. Tech.* 3 (1990) 490.
136. M. Murakami, M. Morita, and N. Koyama, *Jap. J. Appl. Phys.* 28 (1989) 1125.
137. M. Murakami, M. Morita, K. Doi, and K. Miyamoto, *Jap. J. Appl. Phys.*28 (1989) 1189.
138. M. Murakami, M. Morita, K. Doi, K. Miyamoto, and H. Hamada, *Jap. J. Appl. Phys.*28 (1989) 399.
139. S. Jin, T. Tiefel, R. Sherwood, R. van Dover, M. Davis, G. Kammlott, and R. Fastnacht, *Phys. Rev. B* 37(1988) 7850.
140. S. Jin, T. Tiefel, R. Sherwood, M. Davis, R. van Dover G. Kammlott, R. Fastnacht, and H. Keith, *Appl. Phys. Lett.* 52 (1988) 2074.
141. S. Jin, R. Sherwood, E. Gyorgy, T. Tiefel, R. van Dover, S. Nakahara, L. Schneemeyer, R. Fastnacht, and M. Davis, *Appl. Phys. Lett.* 54 (1989) 584.

142. K. Salama, V. Selvamanickam, L. Gao, and K. Sun, *Appl. Phys. Lett.*, 54, (1989) 2352.
143. M. Cima, M.C. Fleming, A.M. M. Figueredo, Nakade, H. Ishii, H.D. Brody, and J.S. Haggerty, *J. Appl. Phys.*, 72 (1992) 179.
144. W. M. Yang; L. Zhou; Y. Feng; P. X. Zhang; C.P. Zhang; Z.M. Yu.; X.D. Tang; R. Nicolsky; R. Andrade; *Cryogenics*, vol.42, Num.10 (2002) 589.
145. D. Cardwell, *Am Mater. Sci. Eng. B.* 53(1998) 1.
146. D. Shi, K. Lahiri, S. Sagar, D. Qu, V. Pan, V.F. Solovjov, and J.R. Hull, *J. Mater. Res.* 12 (1997) 3036.
147. R.E. Sudhakar, and G.J. Schmitz, *Supercond. Sci. Technol.* 15(2002) L21.
148. P.G. Picard, X. Chaud, E. Beaunon, A. Erruad, and R. Tournier, *Mater. Sci. Eng. B.* 53 (1998) 66.
149. Y.-A. Jee; C.-J. Kim; T.-H. Sung; G.-W. Hong; *Supercond. Sci. Technol.* 13 (2000) 195.
150. D.A. Cardwell; W. Lo; H.D.E. Thorpe; A. Roberts; *J. Mater. Sci.* (1995) 1444.
151. A.D Bradley; W. Lo; M. Mironova; N.H. Babu; D.A. Cardwell; A.M. Campbell; K. Salama; *J. Mater. Res.* 16 8 (2001) 2298.
152. C. Cai, H. Mori; H. Fujimoto, H. Liu; S. Dou, *Physica C*, 357, (2001) 734.
153. Y.A. Jee; C.-J. Kim; T.-H. Sung; G. W. Hong; *Supercond. Sci. Technol.*, 13, 2 (2000) 195.
154. C.J. Kim; G.-W Hong.; Y.A. Jee; Y.-H. Han; S.-C. Han; T.-H. Sung; *IEEE Transaction on Magnetics.* 35 (1999) 4070.
155. J. Whitler and R. Roth, *Phase Diagrams for High Tc Superconductors*, The American Ceramic Society, Westerville, Ohio (1991).
156. T. Asselage and K. Keefer, *J. Mater. Res.* 3, (1988) 1279.

157. D.H. St. John, Acta Metall. Mater. 38 (1990) 631.

158. D.H. St. John, L.N. Logan, Acta. Metall. Mater. 35 (1987) 171.

Chapter 6

159. Istvan Vajda, Sandor “Semperger Simulation of electrical, magnetic and thermal properties of inductive fault current limiters made of YBCO ceramics superconductors” J. of the European ceramics society. 25 (2005) 2925.

160. A. Gyore, I. Vajda, M.R. Gonal, D.K. Pandya, IEEE transaction on applied superconductivity. 17 (2007) 1899.

161. Y. Shiohara, A. Endo, Materials Science and Engineering, R 19 (1997) 86.

Publications

Journal

- 1) Experimental Analysis of Different Type HTS Rings in Fault Current limiter
A.Gyore, I . Vajda, **M R Gonal**, K. P. Muthe, S C Kashyap, and D K Pandya.
IEEE transactions on Applied Superconductivity 17, 2. (2007),1899-1903.

- 2) Bulk High Temperature Superconductors Prepared by Melt Textured Growth
Technique- Effect of Y_2BaCuO_5 Particle Size
M. R. Gonal, R.C. Hubli and A.K. Tyagi
AIP Conf. Proc. **1349**, (2011) 833-834

- 3) Study of Superconducting Properties in Melt Textured YBCO samples
M. R. Gonal K.G.Bhushan, S Ramanathan, R.C. Hubli, A.K. Tyagi, and
G.P.Kothiyal
AIP Conf. Proc. 1447, pp. 911-912

- 4) The Effect of Addition of Y-211 with two Different Particle Sizes on the
Properties of Melt Processed $YBa_2Cu_3O_{7-\delta}$ (YBCO) Bulk Superconductors
M. R. Gonal, R.C. Hubli, A.K.Suri, A.K. Tyagi, Atila Gyore and Istvan Vajda
IEEE transactions on Applied Superconductivity (Communicated)

Symposium

- 1) Characterisation of Bulk High Temperature Superconductors Prepared by Melt
Textured Growth Technique
M. R. Gonal, R.C. Hubli and A.K. Tyagi[†]
Proceedings of the 54th DAE Solid State Physics Symposium (2009)